160
5/23/78

Qc-92

UCRL-52302

PRELIMINARY DESIGN STUDY OF THE TANDEM MIRROR REACTOR (TMR)

R. W. Moir, W. L. Barr, G. A. Carlson, W. L. Dexter,
J. N. Doggett, J. H. Fink, G. W. Hamilton, J. D. Lee,
B. G. Logan, W. S. Neef, Jr., M. A. Peterson, and M. E. Rensink

July 15, 1977

Work performed under the auspices of the U.S. Department of Energy by the UCLLL under contract number W-7405-ENG-48.

LAWRENCE
LIVERMORE
LABORATORY
University of California/Livermore

Distribution Category:
UC 20 a b d

LAWRENCE LIVERMORE LABORATORY
University of California / Livermore, California / 94550

UCRL-52302

PRELIMINARY DESIGN STUDY OF THE TANDEM MIRROR REACTOR (TMR)

R. W. Moir, W. L. Barr, G. A. Carlson, W. L. Dexter,
J. N. Doggett, J. H. Fink, G. W. Hamilton, J. D. Lee,
B. G. Logan, W. S. Neef, Jr., M. A. Peterson, and M. E. Rensink

MS date: July 15, 1977

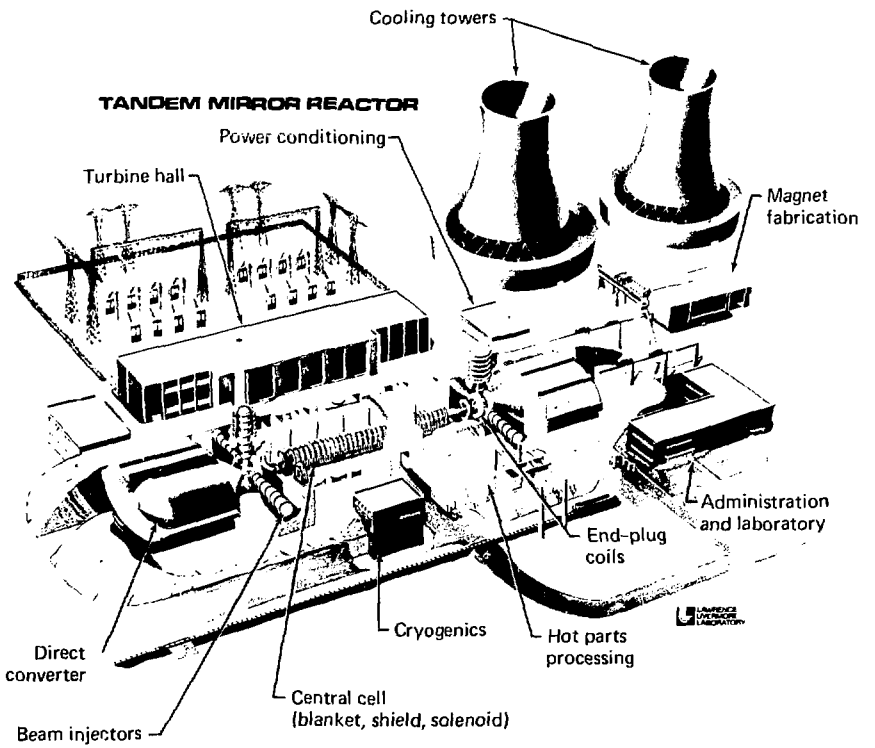
TANDEM MIRROR REACTOR
Cooling towers
Power conditioning
Turbine hall
Magnet fabrication
Administration and laboratory
End-plug coils
Cryogenics
Hot parts processing
Direct converter
Central cell (blanket, shield, solenoid)
Beam injectors

CONTENTS

PRELIMINARY DESIGN STUDY OF THE TANDEM MIRROR REACTOR (TMR)

ABSTRACT

The concept of tandem mirror confinement employs the positive electrostatic potential of two ordinary (standard) mirrors to plug the end losses from a long, power-producing solenoid. A proof-of-principle evaluation of the concept will be provided by the Tandem Mirror Experiment (TMX), now under construction at Lawrence Livermore Laboratory (LLL).

This report describes work done in Fiscal Year 1977 by the Fusion Reactor Studies Group of LLL on the conceptual design of a 1000-MW(e) Tandem Mirror Reactor (TMR). The high Q (defined as the ratio of fusion power to injection power) predicted for the TMR (~5) reduces the recirculating power to a non-dominant problem and results in an attractive mirror fusion power plant.

The fusion plasma of the TMR is contained in the 100-m-long central cell where the magnetic field strength is a modest 2 T. The blanket for neutron energy recovery and tritium breeding is cylindrical and, along with the solenoidal magnet, is divided into 3-m-long modules to facilitate maintenance. The central cell is fueled (but not heated) by the injection of low-energy neutral beams near its ends. Thus, the central cell is simple and of low technology. The end-cell plasmas must be of high density and high energy in order to plug and heat (via the electrons) the central-cell plasma. The present conceptual design uses 1.2-MeV neutral-beam injection for the end plugs and a cryogenic-aluminum, Yin-Yang magnet that produces an incremental field of about 1 T over a field of 16 T produced by a pair of Nb_3Sn superconducting solenoids. Important design problems remain in both the neutral-beam injector and in the end-plug magnet. Also remaining are important physics questions such as alpha-beam particle transport and end-plug stability. These questions are discussed at length in the report and suggestions for future work are given.

CHAPTER 1. INTRODUCTION

The concept of the Tandem Mirror Reactor (TMR), as developed by Dimov *et al.*[1-1] and by Fowler and Logan,[1-2] employs the positive electrostatic potential of two ordinary (standard) mirrors to plug the loss of plasma from a long solenoid. The combination results in Q values of 5 or so (where Q = fusion power/injection power), whereas the standard mirror Q is at most slightly more than 1. The concept looks sufficiently interesting that a major experiment called the Tandem Mirror Experiment (TMX) has been initiated to check out and explore the underlying physics questions.

A reactor based on this concept that produces 1000 MW(e) consists of a solenoidal magnet about 100 m long. A cylindrical blanket is used for energy recovery and tritium breeding. Thus, the reactor itself is simple and of low technology. The end plugs, however, are of high technology, having the high magnetic fields needed to confine the high-pressure plasma and the high injection energy (~1.2 MeV) needed to achieve good magnetic confinement. The plasma density in the plug ($\sim 8 \times 10^{14}$ cm^{-3}) is considerably higher than that in the central cell ($\sim 1 \times 10^{14}$ cm^{-3}) to provide a potential barrier at each end [$\phi = T_e \ln(n_{plug}/n_{solenoid})$]. Because the function of the end-plug plasma is to provide a potential barrier and not to produce plasma, only deuterium (or even hydrogen) need be injected. Therefore, neutron production in the end plugs is quite low. The end-plug magnets are very small [the size of the Mirror Fusion Test Facility (MFTF) coil] but of high field strength (17 T). Thus, what high technology is required for the TMR is concentrated in the end plugs.

This report describes how a 1000 MW(e) TMR would look based on our present understanding. However, because the design is based on physics and engineering ideas that are rapidly evolving, this report is a preliminary description of a TMR; several design problems will be addressed by us in a later version of the design. For example,

- At the beginning of this study, we did not understand the problem of ash (^{4}He) buildup; consequently, ash buildup was ignored in most of the design. However, on the basis of much new understanding of steady-state equilibrium concentrations of ash as discussed in the chapter on physics (Chapt. 3), we believe steady state may be possible from the ash buildup point of view. However, the design consequences are as yet unknown.

• The high-field superconducting magnet, for example, is in principle feasible based on measured properties of superconductors; however, there is no experience with such large (3-m-diam), high-field (17-T) coils.

As an example of evolving high-level technology, on the other hand, this report includes a description (Chapt. 7) of an invention, the arc snubber, that allows us to hold high voltages over large areas, thereby making feasible 1-MeV injectors for the end plugs.

The report is organized into chapters covering each major component or topic area; a Summary follows this Introduction.

REFERENCES

1-1. G. I. Dimov, V. V. Zakaidakov, and M. E. Kishinevsky, Fiz. Plasmy 2, 597 (1976); also G. I. Dimov, V. V. Zakaidakov, and M. E. Kishinevsky, "Open Trap with Ambipolar Mirrors," in *Proc. 6th Inter. Conf. Plasma Physics and Controlled Nuclear Fusion Research, Berchtesgaden, Fed. Rep. of Germany, 1976* (IAEA, in preparation), Paper C4.

1-2. T. K. Fowler and B. G. Logan, "The Tandem Mirror Reactor" *Comments on Plasma Physics and Controlled Fusion Research*, 2, 167 (1977).

1-3. F. H. Coensgen, Project Leader, *TMX Major Project Proposal*, Lawrence Livermore Laboratory, Rept. LLL-Prop-148 (1977).

1-4. F. H. Coensgen, Project Leader, *MX Major Project Proposal*, Lawrence Livermore Laboratory, Rept. LLL-Prop-142 (1976). [Note: The "MX" designation was subsequently changed to "Mirror Fusion Test Facility" (MFTF)].

CHAPTER 2. SUMMARY OF REPORT

INTRODUCTION

This report describes the results of a 6-month study of a 1000-MW(e) fusion reactor based on the tandem mirror confinement concept. Our objective was to uncover the major problem areas in the design of a Tandem Mirror Reactor (TMR) as well as to determine the feasibility of the concept. An artist's conception of an electric power plant based on TMR is shown in the Frontispiece to this report; general parameters for the TMR analyzed in this study are given in Table 2-1.

Table 2-1. General parameters for 1000-MW(e) Tandem Mirror Reactor.

Parameter	Value
P_{net}	1000 MW(e)
Q	4.8
Recirculating power	43%
Plant efficiency	34%
Direct capital cost	\$1.3/W(e)
Length of solenoid	100 m
Wall loading	2 $MW \cdot m^{-2}$
Fusion power density	5 $MW \cdot m^{-3}$

PLASMA CONFINEMENT AND HEATING

In the TMR configuration shown in Fig. 2-1, the plugs are assumed to be classical mirror machines sustained by the injection of high-energy neutral beams. Ion losses from the central cell are replenished by the injection of low-energy neutral beams, pellets, or gas at the thin plasma fans in the inner mirror throat. The design

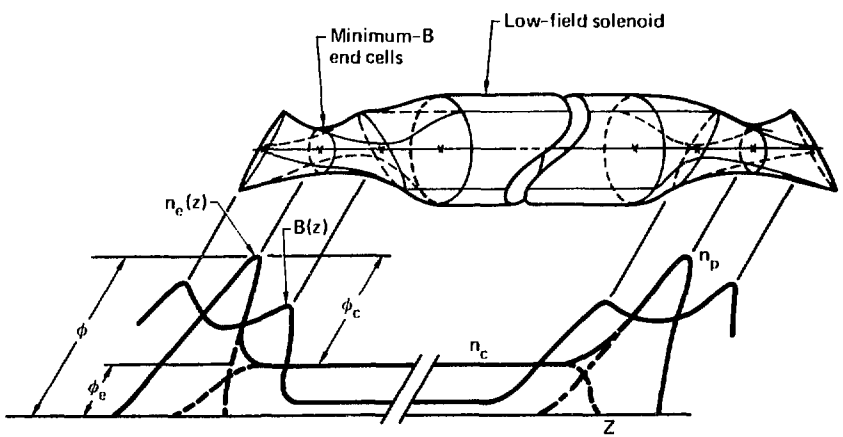

Fig. 2-1. Tandem mirror with ambipolar barriers at the ends.

considerations given in Chapt. 3 lead to the parameters shown in Table 2-2. For these values, we assume that impurities and alpha particles do not accumulate; however, in Chapt. 3 we also present detailed calculations for the steady-state equilibrium alpha density and cross-field transport.

MECHANICAL DESIGN

Table 2-3 lists some key mechanical design parameters for the TMR. As shown in the Frontispiece, the reactor is composed of a power-producing central cell, end-plug magnets, 1.2-MeV D^0 injectors to sustain the

Table 2-2. TMR physics parameters.

Parameter	Value
End Plug:	
Injection energy	1200 keV
Mean ion energy	880 keV
Plasma density	$8.6 \times 10^{14} cm^{-3}$
Trapped current into each plug	220 A
Electron temperature	42 keV
β_{plug} $\left(\beta \equiv \frac{P_\perp}{B_{vac}/2\mu_0}\right)$	1
Plasma radius	0.5 m
B_{vac} plug (midplane)	16.5 T
R_{vac}	1.07
Potential at midplane	350 keV
Particle $n\tau$	2.5×10^{14} s·cm^{-3}
Central Cell:	
Current injected	1570 A
β	0.7
Length	100 m
Plasma radius	1.2 m
B_{vac} (midplane)	2.4 T
Electron temperature	42 keV
Ion temperature	30 keV
Plasma density	$1.1 \times 10^{14} cm^{-3}$
Particle $n\tau$	7.7×10^{14} s·cm^{-3}
Potential of plasma	260 keV

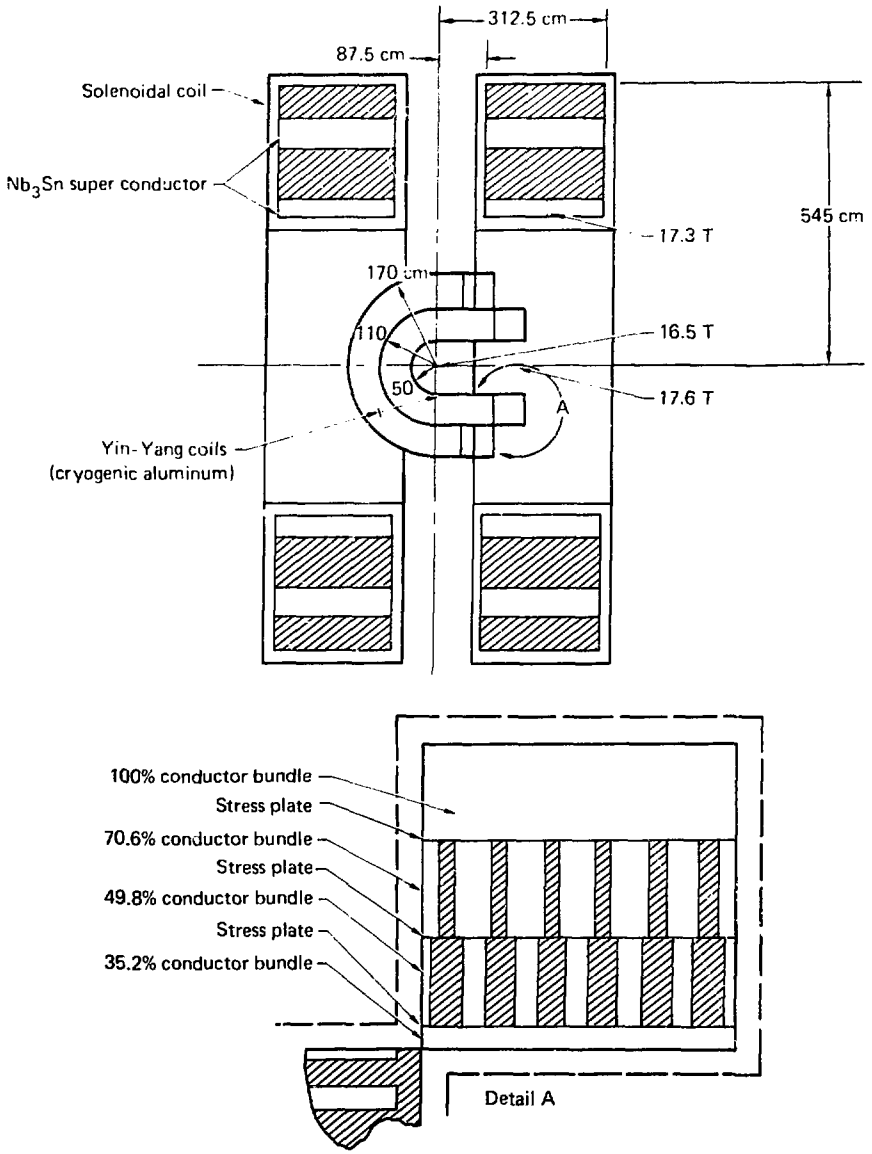

Fig. 2-2. Plug coil set (16.5 T).

Table 2-3. Mechanical design parameters for the central cell.

Parameter	Value
First-wall radius	1.56 m
Length	100 m
No. of modules	36
No. of parallel heat-exchange loops	6
Magnetic field	2.4 T
Blanket coolant	Helium
Inlet temperature	300°C
Exit temperature	530°C
Inlet pressure	50 atm
Helium pressure drop	2 atm
Blanket structure	Inconel 718
Average power density into direct converter	100 $W \cdot cm^{-2}$

end-plug plasma, and direct converters at each end to recover the charged particles that leak out the ends. The power-producing section is a 100-m-long cylinder. The power production in the end plugs is low because they are not supplied with D-T ions, but rather only with D ions. Thus, the energy-recovery blanket is in the cylindrical section, and only shielding is provided in the plug region. The reactor is modular in construction, with sections of the solenoidal magnet, cylindrical blanket, and vacuum chamber all being of modest size. The blanket is helium cooled with a standard, high-temperature, gas-cooled, reactor power-conversion system. Waste heat is dumped to the atmosphere via wet cooling towers.

MAGNET DESIGN

The plug magnet shown in Fig. 2-2 is a hybrid superconducting and cryogenic magnet; its parameters are given in Table 2-4. The complex-shaped Yin-Yang magnet is about the size of the magnet for the Mirror Fusion Test Facility (MFTF) and produces an incremental field of about 1 T over the field of 15.5 T produced by the pair of Nb_3Sn superconducting solenoids. The joule heating in the coil is about 0.5 MW and requires about 25 MW of refrigeration power.

This hybrid magnet was initially thought to require a lower level of technology than would an all-superconductor approach; however, we now conclude the reverse for two reasons:

Table 2-4. Magnet parameters.

Parameter	Value
Center-cell solenoid:	
B_{axis}	2.4 T
Material	Nb-Ti
Bore	8.4 m
Length	100 m (36 segments)
End-plug solenoidal pair:	
Bore	5.75 m
B_{axis}	16.5 T
$B_{conductor}$	17.3 T
Material	Nb_3Sn
End-Plug cryogenic Yin-Yang coil:	
Length	2.8 m (mirror to mirror)
B_{mirror}	17.6 T
Material	Al
R_{vac}	1.07
Resistive power	0.25 MW (each plug)

• Our parametric analysis has shown that reducing the central field of the plug from 16.5 T to 15 T increases the plant unit cost by only 3 or 4%, and a lower field considerably improves the usefulness of Nb_3Sn.

• The structural support for the cryogenic aluminum design was much more difficult than originally thought.

Because of our desire for a compact design, the shielding against neutrons is an important aspect of the design. We conclude in this study that the shielding in the present design is not adequate and that the magnet must be increased to allow for more shielding.

NUCLEONICS

Blanket

In our preliminary appraisal of TMR nucleonics, we conclude that the high Q and favorable geometry of the central cell allow us to contemplate a blanket of modest performance. The high Q eliminates the need for energy multiplication to achieve a favorable power balance; the very low area for neutron streaming (from the large

length-to-diameter ratio of the cylindrical central cell) coupled with no requirement for energy multiplication leads to only a minimal requirement for neutron multiplication in the blanket. Thus, no beryllium is needed in the blanket.

Our overall objective is to keep the blanket as simple and inexpensive as possible. In this light, we are considering a liquid-lithium (natural) and stainless-steel blanket cooled by helium. The blanket is 84 cm thick, its tritium breeding ratio is 1.10, and its energy multiplication is 1.20.

Shielding

Between the blanket and the central-cell coils is 90-cm thick steel- and lead-loaded concrete shielding. Our appraisal indicates that this shielding plus the blanket should provide more than enough shielding for the superconducting, central-cell coils.

Protecting the cryogenic-aluminum Yin-Yang coils is the major shielding challenge in this TMR design. The critical area appears to be at the inner mirror of the plug where D-T plasma leaking from the central cell generates 14-MeV neutrons at a significant rate. According to preliminary calculations, 64-cm-thick, tungsten-based shielding is needed in the inner mirror region. Because the present plug design allows for only 15 cm of shielding in this region, the magnet must be redesigned to provide for more shielding. With the possible exception of the outer mirror and the injection beam lines, the rest of the plug can use iron- and lead-based shielding.

NEUTRAL-BEAM INJECTOR

In Fig. 2-3, we show a conceptual design of a high-current, 1.2-MeV D^0 injector with an anticipated operating efficiency of 70%. Parameters for the injector design are given in Table 2-5. All of the components in the proposed beam line are elaborations of physics experiments that have already been reported in the literature. However, major advances in all phases of neutral-beam technology are needed to meet the requirements of the TMR. These include a continuous source of negative ions, an efficient electron-stripping cell, and the development of associated power conditioning and control equipment. We believe that the neutral-beam requirements of the TMR provide a realistic goal for the not-too-distant future.

DIRECT ENERGY CONVERTER

Direct converters to recover power from the plasma lost from the ends

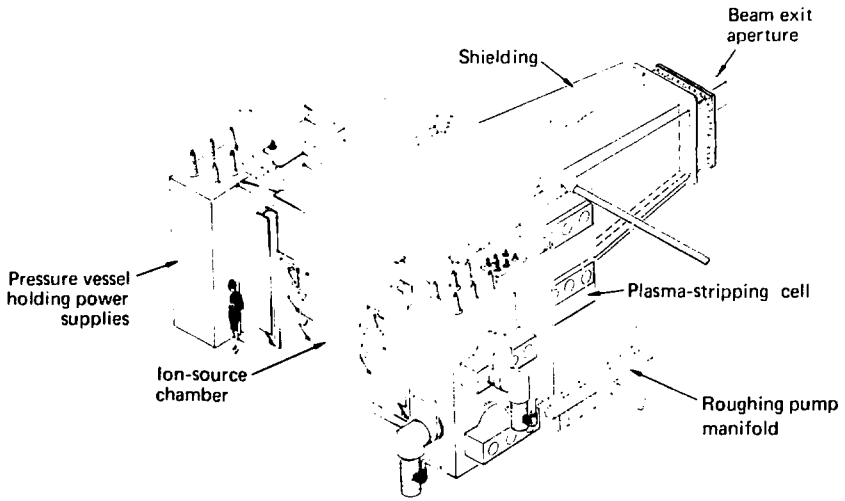

Fig. 2-3. A 1.2-MeV neutral-beam injector.

Table 2-5. Parameters for the neutral-beam injector.

Parameter	Value
Beam energy	1200 keV
Equivalent D^0 current (per injector)	122.5 A
Total injected power (4 units)	588 MW
Operating mode	Continuous
Type of beam line	Negative Ions
Source of negative ions	Ce double charge-exchange cell
Type of stripping cell	Ce plasma
System efficiency[a]	80%
System cost[a]	$200/W of beam output

[a]The values shown in this table are preliminary estimates used in the body of this study. Upon subsequent analyses, we estimated that the efficiency of the injector system would be 73% and the cost of the neutral-beam injector per kilowatt would be $320 divided by the efficiency. This iteration results in an approximate increase of 13% in the direct cost of the electric kilowatt supplied by the TMR.

of the TMR can be effective. The high ambipolar potential and the low ion temperature result in good efficiency even with a single collector stage. About 60% of the total efflux power (carried by escaping fuel ions, alpha particles, and electrons) can be directly recovered after allowing for losses due to incident electrons, grid interception, and secondary and thermionic electrons.

The two types of regions in the TMR - the central cell and the end plugs -- result in two distinct energy groups of ions and suggest a two-stage direct converter. The addition of a second collector stage in the direct converter raises its efficiency to about 70%. The direct converter would also control the recycling of cold electrons from the end walls. Problems associated with space charge, voltage holding, and capacitively stored energy appear to be solvable. Figure 2-4 shows a cross section of the direct converter electrodes, and Table 2-6 gives some typical parameters.

ELECTRICAL DESIGN

The electrical aspects of the plant are divided into standard power plant equipment such as the generator and power-conditioning equipment for transmission and the aspects unique to this fusion reactor such as power supplies for the neutral-beam injector and power-conditioning equipment for the direct energy converter. About 43% of the gross electrical power is recirculated in the plant to power the injector; this aspect of the plant is thus very important. Over

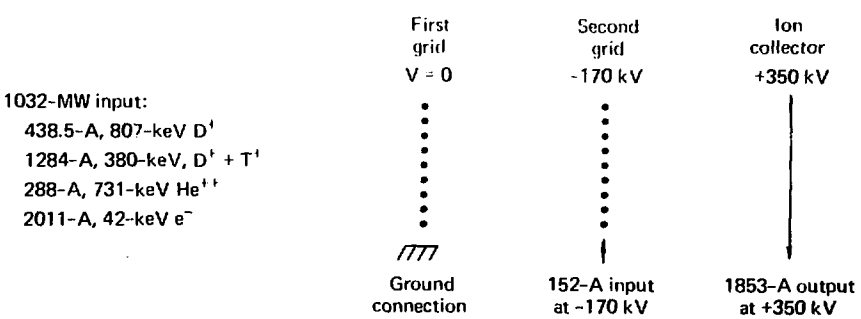

Fig. 2-4. Power and current flow in a single-stage direct converter on the TMR, where $\eta_{DC} = \frac{(1853 \times 350) - (152 \times 170)}{1.032 \times 10^6} = 0.603$.

Table 2-6. Typical parameters for the direct energy converter.[a]

Mean ion energy	470 keV
Mean electron energy	42 keV
Power in ions	950 MW
Power density	100 W/cm^{-2}
Efficiency (one-stage)	60%
Cost per kilowatt of incident power	$130

[a]The energies quoted are at the direct converter.

three fourths of this recirculated power comes in the form of direct-current power from the direct converter.

The startup electrical system uses power-conditioning equipment to bring power off the line during the brief time (~3 s) during startup. After the approximately 3-s startup period, this equipment is gradually (during a 10- to 30-min period) switched over to use for putting power into the line.

PARAMETRIC ANALYSIS

The analytic model of the TMR used in the parametric study begins with a self-consistent description of tandem mirror physics. The physics model relates the densities, energies, and containment times of the ions and electrons in the plugs and central cell. We assume that the plugs are mirror machines with classical end losses sustained by high-energy, neutral-beam injection. The central cell is fueled by low-energy neutral beams of deuterium and tritium. Electrons heated by the energetic ions in the plugs in turn heat the cold ions in the central cell. In the parametric study, the equations of the physics model are solved by specifying the plug injection energy, the plug mirror ratio, the mirror ratio between the plugs and the plugs and in the central cell, and the ion temperature of the central cell. The physics output consists of the various energies, containment parameters ($n\tau$'s), density ratios, and Q.

Next, the specification of a single magnetic field strength (usually the central field of the plug) allows us to calculate all the plasma densities and the fusion power density in the central cell. Then, specification of the blanket energy multiplication factor M and various efficiencies (thermal conversion, direct conversion, and neutral-beam injection) allows calculation of power flows. At this point, the power quantities are only relative because we have not yet selected an absolute power level.

Finally, specification of a single power quantity (usually the net electric power) allows complete design of the reactor. The dimensions of

the cylindrical, central-cell plasma and the approximately spherical plug plasmas are completely determined by the central cell-to-plugs volume ratio, the fusion power density of the central cell, the desired total fusion power, and the requirement for magnetic flux conservation throughout the machine. The plug magnets are designed to provide the specified magnetic field and to be large enough to contain the plug plasma. The central-cell design begins at the cylindrical first wall (three alpha radii away from the plasma) and proceeds outward through the blanket, shield, magnet, support structure, handling and maintenance equipment, and finally the reactor building.

There is an optimum set of values for plug injection energy, plug-to-central cell mirror ratio, and central cell-to-plugs volume ratio that minimizes the cost of power. For a 1000-MW(e) reactor with a plug having a central field strength of 16.5 T, a plug vacuum mirror ratio of 1.07, and β values of 1.0 and 0.7 in the plug and central cell, respectively, we have found the optimum values to be: plug injection energy (deuterium) = 1200 keV, plug-to-central cell mirror ratio = 7.0, and central-cell ion temperature = 30 keV. The blanket energy multiplication factor for this case was 1.2 (no beryllium), and the efficiencies for thermal conversion, single-stage direct conversion, and injection were 40%, 60%, and 80%, respectively. The total direct capital cost of this reactor is predicted to be $1300/kW(e). Characteristics of the optimized point design are listed in Tables 2-1 through 2-6. The cost estimate breakdown is given in Table 2-7.* Figure 2-5 shows the power flow diagram for the point design. Figures 2-6 through 2-8 show the effects on cost, on the recirculating power fraction, and on the neutron loading of the first wall of variations in injection energy, vacuum mirror ratio, and temperature of the ions in the central cell.

At the beginning of this study, we thought we could achieve an 80% efficient injector. The injector study, however, seems to show that 70% is more realistic. Further study will focus on this efficiency question.

We have also studied the direct heating of electrons in the TMR. This is an attractive idea for two reasons:

- It may ultimately be more efficient and less expensive than neutral-beam heating, and

*The cost estimate is not very accurate and should be interpreted in the context of the scope of the study.

Table 2-7. Cost estimate breakdown for the TMR point design.

Item	Cost (millions of $)	% of total
Central cell:		
Blanket	114	8.9
Shield	62	4.9
Vacuum vessel	11	0.9
Coil	35	2.7
Coil structure	21	1.6
Main structure	51	4.0
Crawler	22	1.7
Subtotal:	316	24.7
Plug coils	171	13.3
Reactor building	44	3.4
Injector system	147	11.5
Direct conversion system	134	10.5
Thermal conversion system	199	15.5
Other	270	21.1
Total:	1,281	100

• It may reduce the required neutral-beam injection energy in the end cell.

Since no particular electron heating method has been evaluated, we have assumed that the electrical efficiency of such heating, the coupling efficiency to the plasma, and its cost per unit power are the same as for the neutral-beam injectors. Figure 2-9 shows the optimum neutral-beam energy and the predicted cost of optimized 1000 MW(e) reactors as functions of F_e, the fraction of the total heating that goes directly to the electrons. For our point design with neutral-beam injection only, $F_e = 0$. There is an optimum value of F_e near 0.75 for which the cost of the reactor is reduced to $1160/kW(e). The neutral-beam injection energy for this optimized reactor is 500 keV.

To use this lower injection energy, it would be necessary to increase the plug mirror ratio R_p from 2 to 3 by

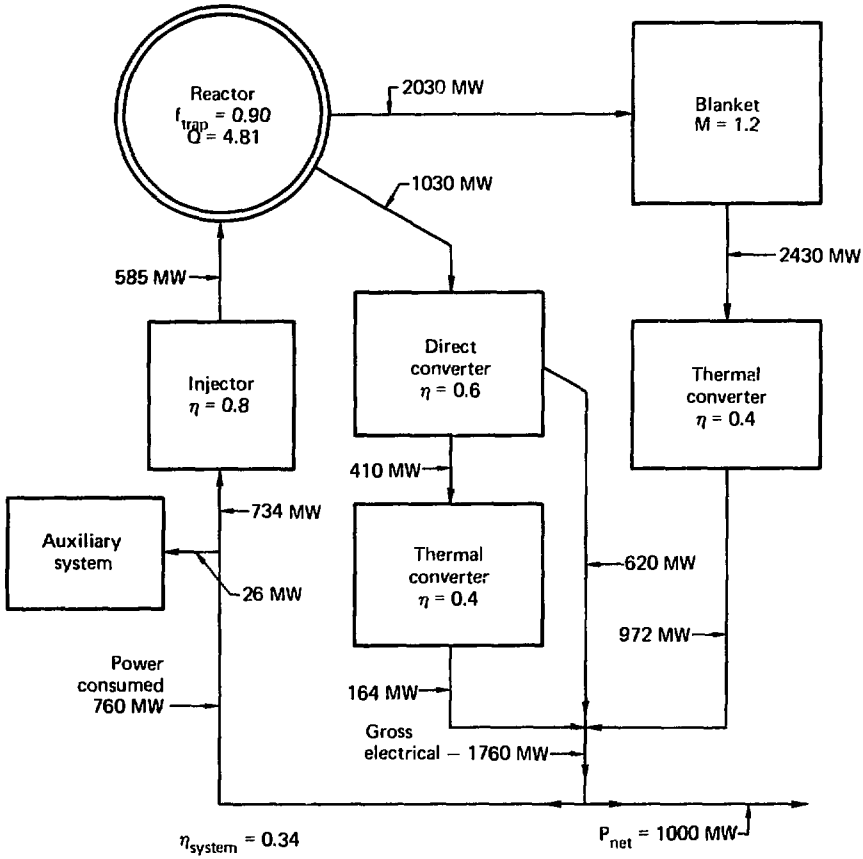

$$\text{Recirculating power fraction} = \frac{\text{power consumed}}{\text{gross electrical}} = 0.43$$

Fig. 2-5. TMR power flow diagram.

a combination of higher β_p and $R_{p\ vac}$, so as to reduce the ambipolar cutoff energy $(\phi_e + \phi_e)/(R_p - 1)$. (See arguments on minimum injection energies in Chapt. 10.) Increasing R_p should not entail a large increase in reactor cost, as indicated by Fig. 10-8.

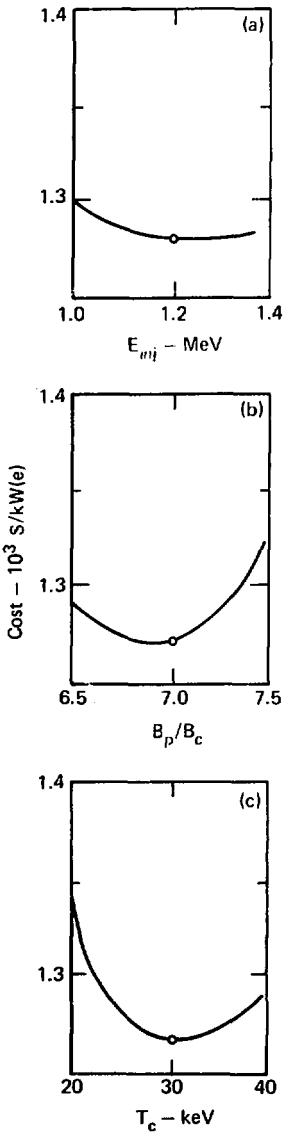

Fig. 2-6. Effect on cost of 1000-MeV(e) TMR's of variation in (a) injection energy E_{inj}, (b) vacuum mirror ratio between the center of the plug and the central cell B_p/B_c, and (c) temperature of the ions in the central cell T_c. *(Note: In Figs. 2-6 through 2-8, the data points identify the values selected for the point design.)*

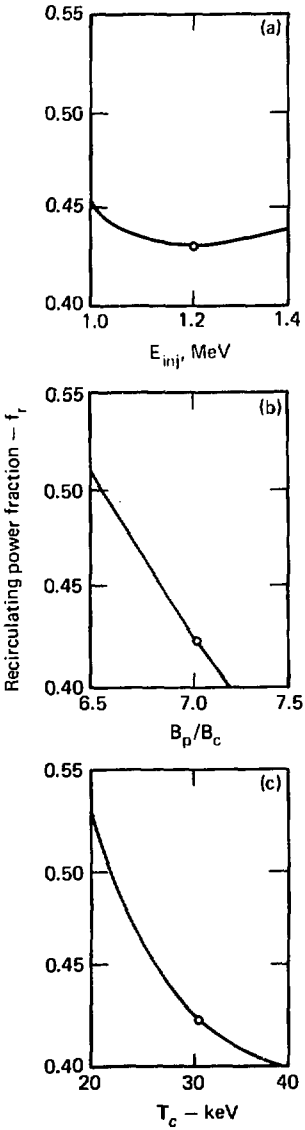

Fig. 2-7. Effect on recirculating power fraction f_r in 1000-MW(e) TMR's of variation in the parameters defined in Fig. 2-6.

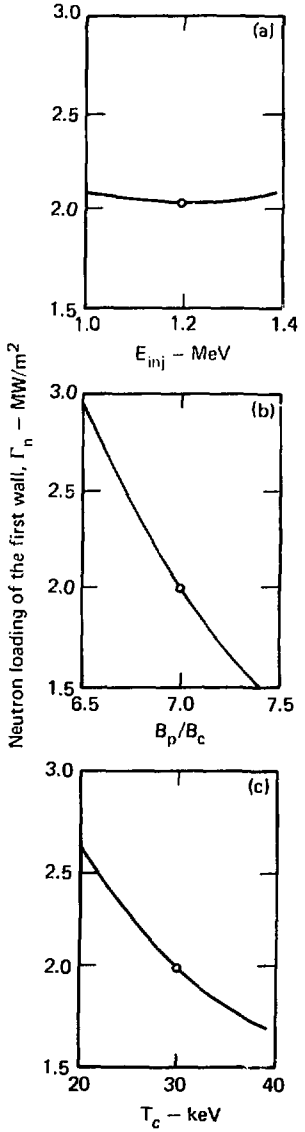

Fig. 2-8. Effect on the neutron loading of the first wall of 1000-MW(e) TMR's of variation in the parameters defined in Fig. 2-6.

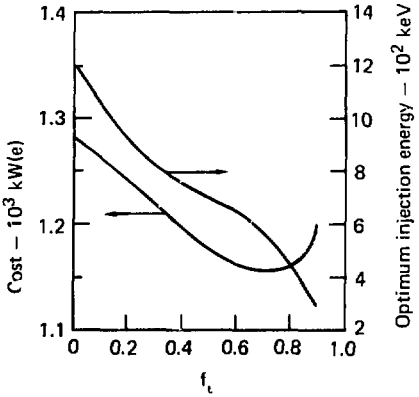

Fig. 2-9. Optimum neutral-beam injection energy and predicted cost of optimized 1000-MW(e) TMR's as functions of f_e, the fraction of the total heating that goes to the electrons.

SUGGESTIONS FOR FURTHER WORK

In the course of this work, the importance of ^{4}He (ash) buildup became apparent. We had originally envisioned a periodic plasma flush; however, more detailed analysis (see discussion in Chapt. 3) indicates a possible steady-state mode of operation in which the ^{4}He concentration is only 4%. Future work will focus on this question of impurity control and its implications to economics of the power cycle (i.e., a steady-state versus pulsed system).

Another area for further work is the increased size of the magnet to allow for more neutron shielding.

The most advanced component of the reactor is the 1.2-MeV neutral-beam injector. Its design rests on the production of negative-ion beams, their acceleration to high voltages, and their passage through a plasma stripping cell to make the neutral atoms. The neutral-beam injector thus has a high priority for future work. The design at present is not self-consistent in a number of significant ways. For instance, the injector efficiency of 80% was used in the power balance, whereas 70% comes out of the injector design work. The end-plug magnet must be enlarged to allow room for more shielding. The steady-state ^{4}He concentration will increase center-cell losses and reduce the power density. Extra power is expected to maintain proper radial boundary conditions for stability and ^{4}He removal. Each of these effects will increase the cost per unit net power and therefore needs further study.

The beneficial aspect of injecting energetic neutral D-T beams into the central cell is just beginning to be appreciated, and interesting reactors at smaller than 1 GW(e) with lower end-plug technology appear possible. Electron heating also appears promising if the efficiencies can approach that of the neutral-beam injector (~70 to 80%).

CONCLUSIONS

The TMR is a great improvement over the "standard" mirror reactor in a number of respects:

- The Q (~5) is about 5 times higher, thus greatly relieving the precarious power balance of the standard mirror.
- In large sizes [~1 GW(e)], the cost per unit power (~$1/W direct cost) is about 5 times lower.
- The technology of the reactor (the central-cell portion) is low by comparison to most other approaches to fusion in that low-field Nb-Ti superconducting coils in simple cylindrical geometry are employed.
- The reactor is highly modular in construction, which allows each component to be produced in a factory and shipped to and assembled on the site.

One major consequence of the modular construction is that a small demonstration prototype reactor would differ from the full-size plant only in the length of the central cell. That is, more central-cell modules would be added to the prototype to make a full-size reactor. Of course, small modifications would still be necessary, e.g., current from the injectors and size of the conventional part of the plant.

The biggest uncertainty in the technology appears to be the 1.2-MeV neutral injector. A number of physics uncertainties have been identified and are being addressed in the Tandem Mirror Experiment (TMX) and by theoretical analysis.

The tandem mirror concept is quite new and appears promising; however, it needs much more study.

CHAPTER 3. PLASMA CONFINEMENT AND HEATING

SUMMARY

The purpose of this chapter is to develop a physics model for calculating plasma confinement and heating in the tandem mirror reactor (TMR). Solutions are to be obtained from the physics model incorporated within the TMR cost-optimizer code, which includes the efficiencies and unit costs of the various energy-conversion systems external to the plasma (see Chapt. 10). Because there are numerous free parameters in the physics model, a wide, continuous spectrum of solutions for combined solenoid and plug parameters is always possible. However, only those particular solutions evaluated by the yardstick of minimum power cost in the TMR code are desired. The twin basic requirements for low power cost per kW(e) net are high Q (high $n\tau$) in order to reduce the cost of parasitic recirculating power, and high neutron flux at the vacuum wall (high fusion power density) in order to reduce the blanket and other costs per kW of fusion power. The general discussion of physics in the following section shows that the plasma confinement properties inherent to the TMR make very high Q and very high fusion power density mutually exclusive. The great value of including the reactor systems costs with solutions to the physics model in the TMR code is in finding the optimum trade-off between Q and wall loading for a minimum power cost at a given power output.

The physics model is simplified as much as possible to facilitate application of the TMR code over the widest range of parameter space. The goals of this first study are to determine the broad limits of economical operation of a TMR and to assess the basic trends and sensitivities of reactor cost to the various input parameters. While searching for the optimum operation regimes, the conditions for validity of several simplifying assumptions made in the model may be strained, resulting in errors in some quantities as large as 20%. This is acceptable for the present purpose of finding the zero-order operating parameters for a TMR, from which refinements in the physics model and more detailed reactor designs can be made in the future.

Energetic (3.5-MeV) fusion alpha particles are expected to provide a major portion of the energy input required to sustain the solenoid in a TMR. In the section on alpha heating, we discuss the containment and pressure of 3.5-MeV alpha particles and the partition of their energy to the plasma ions and electrons. The physics model is applied in the section on Q scaling to determine how the Q of a TMR varies with solenoid

length and density under conditions in which the energy input to alpha particles is not sufficient to sustain the solenoid (subignition). Conditions to achieve ignition in the solenoid are determined. Two of the most important simplifying assumptions made in the physics model are the neglect of thermalized alphas and the neglect of synchrotron radiation. Estimates of the radial transport of thermal alphas and power loss due to synchrotron radiation are made in the last two sections on radial alpha diffusion and synchrotron radiation.

GENERAL DESCRIPTION OF PLASMA CONFINEMENT, HEATING, AND STABILITY IN A TMR

Confinement in Potential Wells

In the tandem mirror configuration shown in Fig. 3-1, high-energy neutral beams sustain dense, mirror-confined plasmas in the minimum-B end cells. Neutral beams of generally larger current and lower energy replenish ion losses from the lower-density (but much larger-volume) central solenoid. The mirror plasmas in the end cells have the primary function of electrostatically plugging the solenoid via their positive ambipolar potentials. We assume the solenoid plasma is of much larger volume and produces much more fusion power than the plugs, and so we neglect the fusion power contributed by the plugs. We do include the neutral-beam power required to maintain the plugs as a primary power input to sustain the system.

In the solenoid as well as in the plugs, electrons tend to escape more rapidly than the ions, so that both the plugs and the solenoid charge up positive with respect to the end walls. Since electrons exchange rapidly between the plugs and solenoid during their lifetime, we can assume the electron temperature T_e in the plugs to be the same as in the solenoid. To satisfy charge neutrality with the electron density n_p in the plugs greater than the electron density n_c in the central solenoid, the plugs must be more positive than the solenoid by an amount

$$\phi_c = T_e \ell n(n_p/n_c). \qquad (3\text{-}1)$$

A larger potential drop $\phi_c + \phi_e$ from the plugs to the wall (Fig. 3-1) is set up to balance the electron loss rate with the combined ion loss rates from the solenoid and plugs (predominantly from the solenoid).

Since the plug ions see a larger outward potential drop $\phi_c + \phi_e$ than the inward potential drop ϕ_c, if the magnetic mirrors are of equal strength the loss boundary in velocity space (see Fig. 3-2) corresponding to the outward direction is closer to the

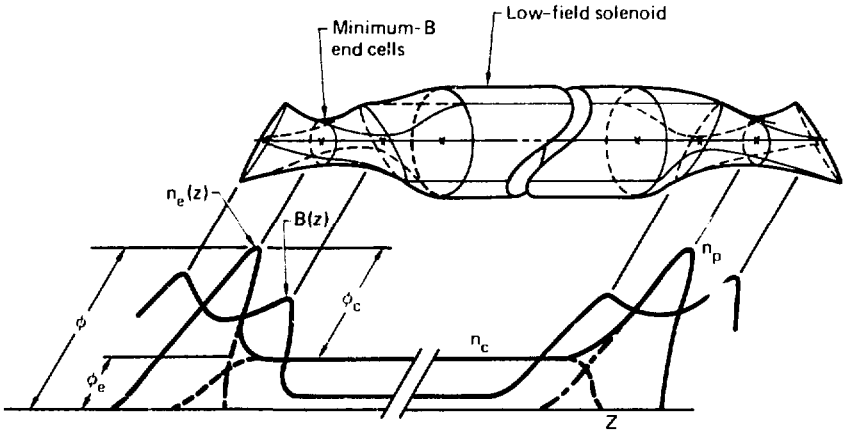

Fig. 3-1. Tandem mirror with ambipolar barriers at the ends.

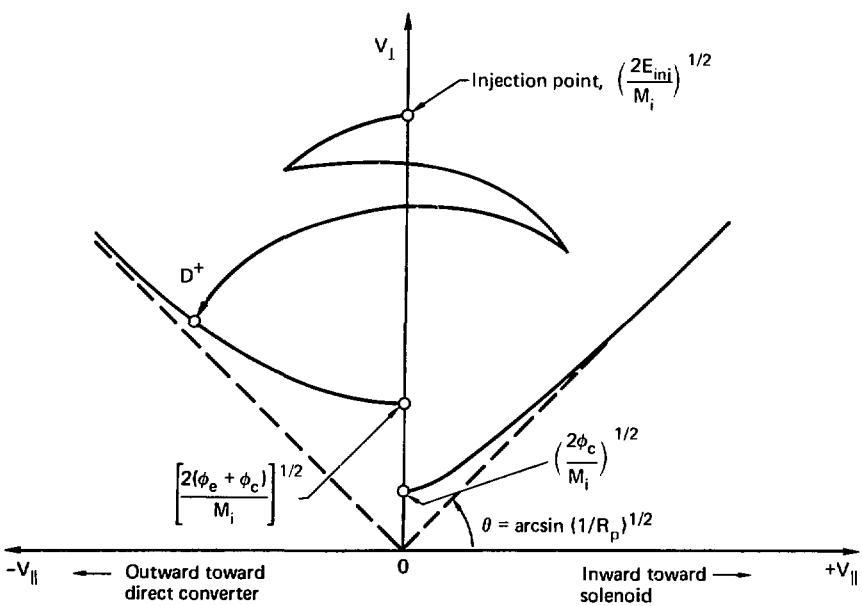

Fig. 3-2. Loss boundaries in velocity space for plug ions, showing asymmetric ambipolar cutoffs and typical ion trajectory.

injection point than to the loss boundary for inward motion. Since ions diffuse in small steps in velocity space, virtually all of the plug ions will exit away from the solenoid. Thus, the steady-state density in the solenoid is controlled only by the neutral-beam injection current into the solenoid, balancing the loss rate of central ions that are diffusing upward in energy over the potential barrier. The neutral-beam injection current in the plugs controls the plug density n_p independently; n_p together with n_c determines the potential barrier height ϕ_c. By suitably controlling the injection rates in the solenoid and in the plugs, an arbitrary density ratio and potential barrier can be maintained in steady state.

With relatively deep potential wells $\phi_c \gtrsim 3T_i$, where T_i is the central ion temperature, and with large central-cell mirror ratios R_c = (internal plug field B_{pi}/internal solenoid field B_{ci}) > 10, the confined ion distribution in the solenoid can be nearly Maxwellian. Since the density and temperature are both lower in the solenoid than in the plugs by typically a factor of 10 (solenoid pressure $\approx 10^{-2}$ plug pressure), the confining magnetic fields in the solenoid can be an order of magnitude smaller than the plug fields. With higher betas and diamagnetic field reduction inside the solenoid than inside the plugs, central-cell mirror ratios R_c as large as 20 to 40 are possible. A typical loss boundary in velocity space for central ions with $R_c = 20$ and $\phi_c = 3T_i$ is shown in Fig. 3-3. The dashed lines are the magnetic loss cones with angle $\theta_c = 13$ degrees, and the solid line is the loss boundary with combined magnetic mirrors and a potential barrier $\phi_c = 3T_i$. The circles are contours of constant $f_i(v, \theta)$ at $E_i = T_i$, $2T_i$, and $3T_i$. Close to 90% of the ions in the distribution have energies less than $3T_i$, the vertex of the loss hyperbolas. In addition, because a fraction $(1 - 1/R_c)^{1/2}$ of velocity space is occupied outside the magnetic loss-cone angle, more than 97% of the ions with energy above the potential barrier are still trapped magnetically. In the original tandem mirror scheme proposed by Kelley,[3-1] the central cell was a mirror machine with the ambipolar potential removed by having the outer cells at equal density with the center cell; therefore, the dashed lines in Fig. 3-3 became the loss boundary. We propose to go one step further by raising the density of the outer cell and imposing a potential barrier. With ions allowed to fill the loss cone below the potential barrier, the ion distribution can become nearly isotropic, eliminating loss-cone instabilities. In addition, the classical

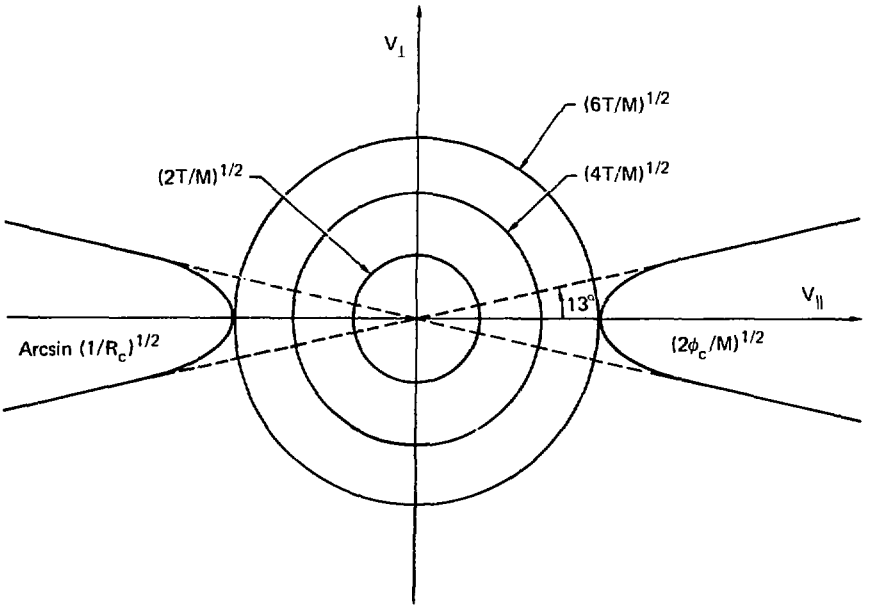

Fig. 3-3. Loss boundary in velocity space for solenoid ions for $\phi_c = 3T_i$ and $R_c = 20$.

ion confinement time is greatly enhanced by the addition of the potential well.

Depending on the ratio of potential barrier height ϕ_c to the central ion temperature T_i, the ion confinement time in the solenoid can be many collision times. For confinement of a single species of Z = 1 ions in a relatively deep potential well ($\phi_c \gtrsim 2T_i$) with magnetic mirrors, an approximate analytic formula by Pastukhov[3-2] can be written:

$$(n\tau)_i = \left[\frac{\sqrt{M_i}\, T_i^{3/2}}{\sqrt{2\pi}\, q^4 \ell n \Lambda_{ii}}\right] \cdot g\left(\frac{R_c}{2}\right)\left(\frac{\phi_c}{T_i}\right) \exp\left(\frac{\phi_c}{T_i}\right) , \quad (3\text{-}2)$$

where the quantity in brackets is the Spitzer self-collision time, and where $g(R) = \sqrt{\pi}\ (2R + 1)\ \ell n\ (4R + 2)/4R$ is a slow function of the central-cell mirror ratio R_c. For $R_c = 20$, $g(10) \approx 3.5$. For typical

ratios $\phi_c/T_i \approx 3$, Eq. (3-2) shows that the potential barrier together with a large mirror ratio provides ion confinement for over 100 ion-ion collision times. Also, the increase in $(n\tau)_i$ is much stronger than with the collision time factor $\propto T_i^{3/2}$. Thus, contrary to confinement with magnetic mirrors alone, confinement with a fixed potential barrier ($\phi > 2T_i$) increases as the ion temperature decreases. Using Eq. (3-1) to eliminate ϕ_c, and taking $M_i = 2.5$ amu for DT ions and $\ell n\lambda_{ii} \approx 22$, Eq. (3-2) can be written

$$(n\tau)_i \approx 8.7 \times 10^{10}\, T_i^{3/2} \left(\frac{T_e}{T_i}\right) \cdot \ell n\left(\frac{n_p}{n_c}\right)\left(\frac{n_p}{n_c}\right)^{T_e/T_i}, \qquad (3\text{-}3)$$

where T_i is in units of keV, and $(n\tau)_i$ is in cm^{-3}·s. Given a practical upper limit on the plug density that can be confined by a maximum plug field, Eq. (3-3) shows that to increase $(n\tau)_i$ for a given T_e/T_i ratio, one must decrease the solenoid density n_c. However, the fusion power density in the solenoid then decreases as n_c^2. This fundamental tradeoff between confinement and power density in a TMR will be discussed again later.

Ion Cooling by Charge Exchange

At central ion temperatures $T_i \approx 20$ to 40 keV, the probability for charge exchange of an injected neutral atom in the solenoid is several times greater than for ionization. Therefore, associated with the ionization rate needed to replace ion particle losses in the solenoid there is a charge-exchange energy loss per ion created of 3 to 10 times T_i, depending on T_i. Because of the scaling of electrostatic confinement of central-cell ions in a TMR, the improvement in $(n\tau)_i$ from a larger value of T_e/T_i can more than compensate for the lower reaction rate $\langle\sigma v\rangle$ due to charge-exchange cooling. Thus, for ions in a deep potential well ($\phi_c > 2T_i$), charge-exchange cooling is often beneficial. This ion cooling mechanism can be realized by supplying the solenoid losses with very low-energy beams (1 to 10 keV) injected *into the thin plasma fans near the* inner mirror throats. Since the potential barriers are co-located with the mirror-confined plug ions beyond the inner set of mirrors (see Fig. 3-1), the Maxwellian ions of the solenoid freely pass through the inner mirror fans at constant pressure. Therefore, with regard to confinement, creating an ion in the fan is as good as injecting the middle of the solenoid. Moreover, not only can the low-energy beams penetrate into the thin fans, but also the charge-exchange atoms can escape.

Electron Heating

For the same reason that ion confinement can be improved by ion cooling, ion confinement can also be improved by electron heating.[3-3,4] Electrons are heated by hot ions in the plugs, by ions in the solenoid if $T_i > T_e$, by 3.5-MeV fusion alpha particles in the solenoid, and as options, either by direct auxiliary heating such as with electron cyclotron resonance heating (ECRH) in the low-field solenoid or with intense relativistic electron beams injected from the ends. Increasing T_e/T_i by electron heating can increased at the same $(n\tau)_i$ for a given density ratio n_p/n_c; alternately, the power density can be increased at the same $(n\tau)_i$ with a lower density ratio. In Eq. (3-3), for example, the same factor of enhancement in $(n\tau)_i$ is obtained with $T_e = 3T_i$ and n_p/n_c of only 3 as with $T_e = T_i$ and $n_p/n_c = 27$. The power density in the solenoid with the former case would be nearly two orders of magnitude greater if T_i were kept constant and T_e were increased by heating. Unfortunately, the projected tube efficiences (20%) and the power output/unit (200 kW) of high-power microwave generators presently under development[3-5] for ECRH heating of 10^{14} cm^{-3} density plasmas ($f_c \simeq 100$ GHz, $\lambda_c < 3$ mm required) do not approach the capability already achieved by neutral beams (50% efficiency at > 1 MW per module on 2XIIB).

Whether microwave tube technology will ever catch up with neutral-beam development for fusion application is unclear. The situation with regard to intense relativistic electron beams is more hopeful; multi-megajoule pulses at production efficiencies comparable to or greater than neutral beams can probably be achieved with present technology.[3-6] Efficient absorption (>90% would be desired) of intense electron beams in $>10^{14}$ cm^{-3}, fully-ionized plasmas has yet to be demonstrated. However, extrapolation from theory[3-7] as well as from experimental measurement[3-8,9] of electron-beam absorption in short plasmas suggests that electron beams of 1 to 5 MeV at current densities of only 1 kA/cm^2 might be almost totally absorbed in 100 m of $10^{14}cm^{-3}$ plasma in a TMR. Many small pulses within the 5- to 8-s plasma lifetime can be used, each pulse supplying a small fraction of the plasma energy. Thus, perturbations of T_e, n_e, and beta are kept small, and the electron-beam heating would appear almost quasi-steady.

The benefits of auxiliary electron heating in a TMR are assessed in Chapt.10. However, since a detailed physics and engineering study of an electron-beam heating system has yet to be made for the TMR, such auxiliary electron heating is now considered only as an option.

Alpha-Particle Heating

Fusion alpha particles can supply a substantial fraction of the energy input needed to sustain the solenoid plasma in a TMR. Since the magnetic loss-cone angle is so small ($\lesssim 18°$) in the solenoid, more than 95% of the alpha particles born isotropically at 3.5 MeV have velocity vectors such that they are magnetically trapped by the central mirrors. Depending on the design of the field gradient length at the ends of the solenoid, a fraction $0.2 \lesssim f_\alpha \lesssim 1$ of the alphas can be adiabatically confined between the mirrors of the central cell for a sufficient time to thermalize, giving up their energy to the central ions and electrons (see "Heating by 3-5-MeV Alpha Particles").

With f_α near unity and with sufficient confinement $(n\tau)_i$, alpha particles alone can energetically sustain the central solenoid (ignition). An example of ignition is discussed under "Q Scaling in a TMR". Unfortunately, as the alphas slow down, they heat the central ions as well as the electrons, giving a larger fraction of their energy to the ions for $T_e > 33$ keV. Thus at high T_e, alpha heating tends to lower the ratio of T_e/T_i, increasing the density ratio n_p/n_c required for a given $(n\tau)_i$. If efficient methods of heating electrons alone are available, such as via hot ions in the plugs or by auxiliary electron heating, it is in fact desirable to reduce alpha heating (by using non-adiabaticity, so that $f_\alpha \ll 1$), and thereby to operate at smaller n_p/n_c and higher power density. However, reduced alpha input is an advantage only if the efficiency of direct electron heating is greater than about 50%; otherwise, the advantage of electron heating is wiped out because energy balance is recovered only at higher $(n\tau)_i$ and n_p/n_c.

The alphas which do survive to slow down below $2\phi_c$ energy become electrostatically trapped and quickly thermalize to the temperature of the solenoid ions. Their subsequent lifetime in a potential well of $2\phi_c$ is quite long; inspection of Eq. (3-2) shows that the lifetime of thermal alpha particles scattering on DT ions with $T_\alpha = T_i$, $\phi_c \to 2\phi_c$, and $q^4 \to Z_\alpha^2 Z_{DT}^2 q^4$, is longer than the DT ion lifetime by a factor of $\sqrt{4/2.5}\ Z_\alpha^{-2}\ 2 \exp(\phi_c/T_i)$. When $(n\tau)_i$ is large due to $\phi_c \gg T_i$, $(n\tau)_\alpha$ is very much larger still; therefore, the thermal alphas accumulate to a large equilibrium fraction $(n_\alpha/n_i \approx 1)$ even though their source strength due to DT burnup is small compared to the DT injection strength. Such large thermal alpha fractions would have a disastrous effect in reducing both $(n\tau)_i$ (enhanced scattering of DT ions by a factor of $(1 + Z_\alpha^2 n_\alpha/n_i)$ and power density (DT fuel density lower than the solenoid

electron density by a factor of $(1 + Z_\alpha n_\alpha/n_i)$. Fortunately, it appears that the classical radial diffusion of thermal alphas can greatly reduce their equilibrium fractions ($n_\alpha/n_i \ll 0.1$), as suggested by Dimov.[3-3] The equilibrium thermal alpha fractions can be reduced still further if $f_\alpha < 1$ due to nonadiabaticity; the source strength of thermal alphas is proportional to f_α. However, the alpha energy input to the solenoid is correspondingly reduced, favorably or unfavorably, depending on whether there is efficient electron heating to make up for the loss of alpha input.

Plug Injection Energies

For a TMR operating with high T_e, very high neutral injection energies E_{inj} are required to minimize the neutral-beam power required to maintain the plugs. In Fig. 3-2, the minimum ion energy $E_p(\min)$ that can be contained by the mirrors in the plugs is given by $(\phi_c + \psi_e)/(R_p - 1)$, where $\phi_c + \psi_e$ is the total expelling potential as seen by the plug ions, and R_p is the effective plug mirror ratio enhanced by the diamagnetism of the plug. High-vacuum mirror ratios are impractical due to the engineering difficulties associated with producing high magnetic fields in the mirrors; also, the very large factors of reduction in the internal field of the plug caused by high beta are counterproductive because the small magnetic flux linking the plug gives small cross-section solenoids by conservation of flux. Thus, R_p must always be modest: $R_p \approx 2$-3. We shall find that usually $\phi_c \gtrsim 6T_e$ and $\psi_e \gtrsim 2T_e$ as well. If $T_e \gtrsim T_i$, such as with electron heating, T_e must be a minimum of 40 to 60 keV if T_i is to be high enough for a practical fusion reaction rate. Thus, we are led to minimum plug ion energies $E_p(\min) \gtrsim 8T_e \gtrsim 300$ to 500 keV for $R_p = 2$, and $E_p(\min) \gtrsim 150$ to 250 keV for $R_p = 3$. Of course, a plug ion injected with only the energy $E_{inj} = E_p(\min)$ would be lost immediately. To have a useful plug ion lifetime, the injection energy should be three to four times the ambipolar cutoff. This will typically require $E_{inj} \approx 1$ MeV in a TMR.

A second reason for high injection energies in a TMR is to heat electrons. For ratios $E_{inj}/T_e \gtrsim 15$, plug ions transfer more energy to electrons than is carried out by the electrons accompanying those ions over the barrier $\phi_c + \psi_e$. In this way, a portion of the neutral-beam power required to maintain the plugs can be "reused" to heat the solenoid via electrons. The efficiency of heating electrons by the plugs increases with E_{inj}/T_e, exceeding 50% at $E_{inj}/T_e = 40$.

As a reference case for the TMR, we assume that the solenoid is

sustained solely by alpha particles and electron heating in the plugs. Since the plug neutral beams are then the only source of external power, the overall system Q = (fusion power/injection power) can be written, with $n_p = n_c = n_c/2$,

$$Q = \frac{\frac{1}{4} n_c^2 \langle \sigma v \rangle E_F V_c}{\left(n_p^2 \frac{E_{inj}}{\langle \sigma\tau \rangle_p} V_p \right)}$$

or

$$Q = \frac{1}{4} \langle \sigma\tau \rangle_p \langle \sigma v \rangle \left(\frac{E_F}{E_{inj}} \right) \left(\frac{n_c}{n_p} \right)^2 \left(\frac{V_c}{V_p} \right). \quad (5.4)$$

where $\langle \sigma\tau \rangle_p$ is the product of ion particle confinement time and density in the plugs, $\langle \sigma v \rangle$ is the fusion reaction rate in the solenoid, E_F is *the fusion energy release* which we take to be 17.6 MeV, and (V_c/V_p) is the ratio of solenoid volume to the volume of both plugs. As in classical mirror machines, $\langle \sigma\tau \rangle_p \propto E_{inj}^{3/2}$, so $Q \propto E_{inj}^{-1/2}$ by Eq. (5.4). In the *conventional single cell mirror* reactor, the DT fusion reaction rate $\langle \sigma v \rangle$ decreases as E_{inj} increases above 100 keV, so that the single cell Q has a maximum value near unity for *injection energies* ~ 100 keV. In the TMR however, $\langle \sigma v \rangle$ can be close to its maximum value in the solenoid, while at the same time $\langle \sigma\tau \rangle_p$ can be increased by injecting the plugs at a much higher energy. Since $n_p \propto 1/E_{inj}$ for *a maximum* plug field B_p and beta β_p, the solenoid density, following the plug density, must decrease as E_{inj} is increased. Here again we find a tradeoff between increasing confinement (in the plugs) and decreasing power density. Since an increasing plug line density $\int n_p \, dz$ is required to ionize the neutral beam as E_{inj} is increased, and since $n_p \propto 1/E_{inj}$, we *find that beam transmission* through the plugs sets a practical upper limit on E_{inj} at a little over 1 MeV.

MHD Stability

In addition to acting as electrostatic barriers, the plug plasmas have an essential role in anchoring the solenoid, which might otherwise be MHD unstable. Calculations[3,4,10] of pressure weighted $\int p_{\parallel} dz/B$ stability show that with plug pressures of about 100 times the solenoid plasma pressure (typical in a TMR), overall MHD stability can be easily obtained in a *time average sense*, even with weak radial magnetic well depths in the plugs. For long solenoids, a remaining concern is the central beta (β_c) limit above which local MHD modes driven by *bad curvature or by plasma* rotation resulting from a radial potential gradient might still grow despite plasma perturbations going to zero at the plugs (baffooning).

Ballooning mode beta limits neglecting the effects of conducting walls close to the plasma and the effects of finite Larmor radius have been calculated to range from $\beta_c \approx 0.5$ to 0.8, depending on the central mirror ratio R_c and on the detailed shape of the magnetic field profile at the ends of the solenoid.[5,10] These values of central beta would provide adequate fusion power density for the solenoid.

With regard to the beta limit of the EBR plug itself, we rely on 2XIIB experiments that show microstable plasma stability for beta values as high as 1.8[5,11]. Here beta is defined as the ratio of plasma energy density to the energy density of the local vacuum field. Such values of beta exceeding unity do not imply field reversal, since the 2XIIB plasma is short (nearly spherical in shape). A value $\beta_p = 2$ is estimated to result in zero internal magnetic field.[5,11] The values of beta achieved in 2XIIB substantially exceed the beta limits predicted for the *mirror mode*[5,12] and for the Alfven ion cyclotron mode,[5,13] possibly because of the short axial and radial scale lengths of the plasma. Moreover, because the 2XIIB plasma is so short compared to the length between the magnetic mirrors, the vacuum mirror ratio effectively confining the plasma is less than 1.04. We assume that such high betas and low vacuum mirror ratios can be used in the plugs of the EBR, even though the EBR plugs will be larger (in terms of ion gyroradii) than 2XIIB. It happens that the optimum plug beta is less than the maximum beta achieved in 2XIIB because of competition between maximizing plug magnetic flux (solenoid volume/length) and maximizing plug density. A minimum vacuum mirror ratio is required in the plugs to support the outward force on the plugs exerted by the solenoid plasma pressure. However, *since the solenoid pressure* is only 10^{-3} of the plug pressure and since the plug pressure is comparable to the midplane field pressure $B_p^2/8\pi$, the mirror field pressure of the outermost plug need only be greater than $B_p^2/8\pi$ by 1%. We assume that the plugs in the EBR will be nearly spherical in shape, similar to 2XIIB. Even shorter plasmas would be desirable to reduce the plug volume and power loss, but the constant B contours in the presence of high beta plasma are probably limited to aspect ratios $L_p/2r_p$ unity.

Plug Microstability

Of the various potential micro instabilities[1,14] in the EBR plugs, the drift cyclotron loss cone (DCLC) instability is of most concern, since it appears to be the principal cause of turbulence and low electron

temperatures in the 2XIIB experiment.[3-15] An important parameter for the DCLC mode is the scale length of the radial density gradient relative to the ion gyroradius $\Delta r_p/\rho_i$. At small $\Delta r_p/\rho_i \approx 3$ as in 2XIIB, marginal stability required that the loss cones be partially filled by low-energy ions streaming through the trapped ions, resulting in lower T_e and lower $(n\tau)_p$ by electron drag.[3-15,16] As $\Delta r_p/\rho_i$ is increased, the drive for the DCLC mode is weakened so that the streaming plasma required for marginal stability diminishes to insignificance for scale lengths $\Delta r_p/\rho_i \approx 40$. Such a scale length is comparable to the radial size of the plugs in a typical TMR of 1000 MW(e) output.

Precise conditions for DCLC stability in the TMR plugs must be determined by further theoretical and experimental investigation in the upcoming TMX experiments (plug-solenoid ion overlap effects) and in the MFTF experiments (scaling to larger $\Delta r_p/\rho_i$). For the present study, we assume classical loss as a reference case for the reactor. Should micro-instabilities enhance loss rates in the plugs, the overall TMR Q can be recovered by increasing the length of the solenoid (volume ratio) according to Eq. (3-4). The penalty is then an increase in reactor size for the same Q. However, practical reactor sizes will require that plug confinement not be degraded by large factors below classical.

Gradient Instabilities in the Solenoid

Although the uniform temperature and density region of the solenoid should be stable, a solenoid boundary layer of 2 to $4\rho_i$ scale length is subject to instabilities driven by density and temperature gradient. At present, little research has been done on such instabilities and the enhanced radial transport they may cause. However, a few comments can be made in light of recent work[3-17,18] on finite-beta effects in temperature and density gradient instabilities. With regard to low-frequency ($\omega \ll \omega_{ci}$) drift waves, a fully electromagnetic treatment by Berk and Domingues[3-17] shows stability above modest critical beta values $\beta_c \gtrsim 0.15$, depending on the gradients in temperature relative to gradients in density. Also for the higher frequency, lower-hybrid-drift instability ($\omega \gg \omega_{ci}$) Davidson *et al.*,[3-18] find that finite-beta effects are stabilizing above critical beta values $\beta_c \gtrsim 0.5$, depending on T_e/T_i and $\Delta r_p/\rho_i$. Of course, there will always be low-beta regions in the outer edges of the boundary layer which may be unstable. What result such instability in the outer fringes may have on bulk radial diffusion is unclear. We note that the hot-ion confinement

near the boundary need only be one electron drag time. On time scales of the same order, there is no observable radial diffusion in the 2XIIB experiment.

PHYSICS MODEL

In the following model of plasma confinement and heating in a TMR, we assume that the solenoid is energetically sustained primarily by 3.5-MeV alpha-particle heating in the solenoid and by electron heating from hot ions in the plugs. As an option, we shall also consider direct auxiliary electron heating by including a general electron energy input term energy-balance equation. We assume that the neutral beams supplying the ion particle losses from the solenoid are of negligible energy, and include the effects of charge-exchange cooling of the solenoid ions off the low-energy beam or gas neutrals supplying the solenoid. In the reference case, the neutral-beam power to the plugs is the only external power input to the system.

In taking credit for ion and electron heating by the fast alphas, we include their partial pressure in the solenoid when calculating the required confining field for the solenoid. However, since the equilibrium density of the hot alpha particles that are doing the heating is typically only 1% of n_e, their density is neglected. Also, in this model we assume (following Dimov[3-3]) that the radial diffusion of thermalized alphas will keep their density small compared to the density of the fuel ion. Thus, we set

$$n_e = n_i \equiv n_c \tag{3-5}$$

in the central solenoid and use Eq. (3-1) for the ion potential barrier ϕ_c and Eq. (3-3) for the DT ion confinement product $(n\tau)_i$. We assume that the fractional burnup in the solenoid is small and ignore the fact that the small portion of the injected fuel burned in the solenoid will exit radially in the form of Z = 2 alphas rather than as DT ions over the potential barrier. As it happens, the neglect of energy carried out by the thermal alphas ($\approx 3/2T_\alpha \approx 3/2T_i$) is pessimistic since ion cooling by alpha loss would improve confinement just as does charge-exchange cooling. Also burnup itself cools the ions, since the average energy of reacting ions is several times T_i. However, the neglect of the alpha density is an optimistic assumption that offsets the neglect of beneficial ion cooling by burnup and alpha loss.

The two ion species used for fuel in the solenoid, deuterium and tritium, are treated as one ion species

with an effective mass = 2.5 amu. To ease shielding requirements for the end cells, we assume that the plugs consist of a single injected species -- either protons, deuterons, or tritons. Thus, contributions of fusion power from the plugs are neglected, whereas the plug injection power is included in determining Q for the system. We take all mirror fields to be equal, so that few of the plug ions will exit into the center cell. The model then simplifies to one ion species in the center cell and one in the plugs, and one electron species throughout. The alphas then appear only as heating terms in the ion and electron energy-balance equations.

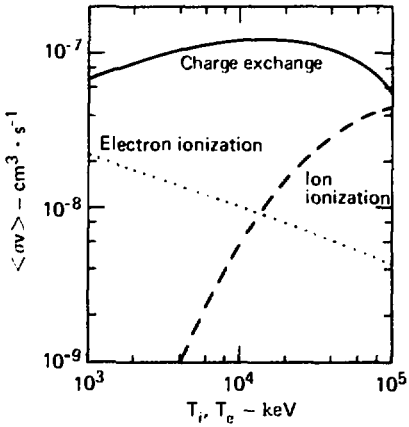

Fig. 3-4. Rate coefficients for electron ionization as a function of T_e and for charge exchange and ionization by DT ions as a function of T_i.

Ion Energy Balance

We assume that the low-energy neutral beams or gas feed maintain a constant average neutral density n_0 within the solenoid plasma. The ionization rate per cm^{-3} J_i required to replenish the DT-ion loss rate in steady state is given by

$$J_i = n_0 n_c \langle \sigma v \rangle_i = n_c^2/(n\tau)_i \ , \qquad (3\text{-}6)$$

where $\langle \sigma v \rangle_i$ is the sum of $\langle \sigma v \rangle_e (T_e)$, which is the rate coefficient for ionization by electron impact, and $\langle \sigma v \rangle_i (T_i)$, which is the rate coefficient for ionization by ion impact. These coefficients are given by the dotted and dashed curves, respectively, in Fig. 3-4. The rate of charge-exchange events per cm^{-3} J_{cx} is correspondingly given by

$$J_{cx} = n_0 n_c \langle \sigma v \rangle_{cx} \ , \qquad (3\text{-}7)$$

where $\langle \sigma v \rangle_{cx} (T_i)$ is the rate coefficient for charge exchange given by the solid curve in Fig. 3-4. Solving Eq. (3-6) for n_0 and substituting into Eq. (3-7), we can write

$$J_{cx} = \frac{n_c^2}{(n\tau)_i} \frac{\langle \sigma v \rangle_{cx}}{\langle \sigma v \rangle_i} \ . \qquad (3\text{-}8)$$

Pastukhov's calculation, and recent Fokker-Planck calculations[3-19,20] show that the average energy carried out by ions escaping over the potential barrier is $\phi_c + T_i$ per ion lost.

Assuming the injected neutral energy is small compared to the average ion energy, each charge-exchange event will result in approximately $3/2T_i$ loss of energy, with no corresponding loss of ion particles (charge exchange merely replaces a hot ion with a cold one). Thus, the total energy lost per ion lost is given approximately by

$$T_i \left(1 + 3/2 \frac{\langle\sigma v\rangle}{\langle\sigma v\rangle_i}\right) \approx 110\ T_i^{1/5}, \tag{3-9}$$

for T_i in keV, ±5% in the range $10 < T_i < 50$ keV. We have used *Fig. 3-4 in obtaining the fit* given by Eq. (3-9), setting $T_e = T_i$. Since ionization by electrons is significantly less than ionization by ion impact, the errors incurred in $T_e \neq T_i$ are small, permitting Eq. (3-9) to be given as a function only of T_i.

We can now express the ion energy balance in the solenoid as

$$\frac{n_c^2}{(n\tau)_i}\left[\phi_c + T_i\left(1 + \frac{3}{2}\frac{\langle\sigma v\rangle_{cx}}{\langle\sigma v\rangle_i}\right)\right] = \frac{n_c^2 \frac{3}{2}\left(T_e - T_i\right)}{(n\tau)_{ei}} + \frac{1}{4} n_c^2 \langle\sigma v\rangle_{DT} E_{\alpha 0} f_\alpha f_i. \tag{3-10}$$

In the right-hand side of Eq. (3-10), the first term is the energy transfer between ions and electrons by classical equilibration. The equilibration time multiplied by the electron density $(n\tau)_{ei}$ is given by

$$(n\tau)_{ei} = 1.25 \times 10^{12}\ T_e^{3/2} \text{cm}^{-3}\text{.s.} \tag{3-11}$$

for DT ions of average mass = 2.5 amu, for $\ell n\Lambda_{ei} = 20$, and for T_e in keV. The second term in the right-hand side of Eq. (3-10) is the energy input per cm^{-3} given to ions by the fusion alphas: $\langle\sigma v\rangle_{DT}$ is the DT fusion-reaction rate, $E_{\alpha 0} = 3520$ keV is the initial alpha energy, f_α is the fraction of alphas that are contained and thermalized, and f_i is the fraction of $E_{\alpha 0}$ energy given to ions by each alpha that thermalizes. According to subsequent discussion, f_α can be considered a parameter controlled by the design of the solenoid transition regions (adiabaticity control). The fraction f_i is a function of T_e as given in Fig. 3-5. An approximate formula for f_i is given by

$$f_i \approx 0.29\ \ell n(T_e) - 0.5, \tag{3-12}$$

for T_e in keV, ±5% in the range $20 \lesssim T_e \lesssim 60$ keV. An approximate formula for $\langle\sigma v\rangle_{DT}$ is given by

$$\langle\sigma v\rangle_{DT} \approx 5.1 \times 10^{-16}\left[\ell n(T_i) - 2.1\right] \tag{3-13}$$

for T_i in keV, ±5% in the range $10 < T_i < 50$ keV.

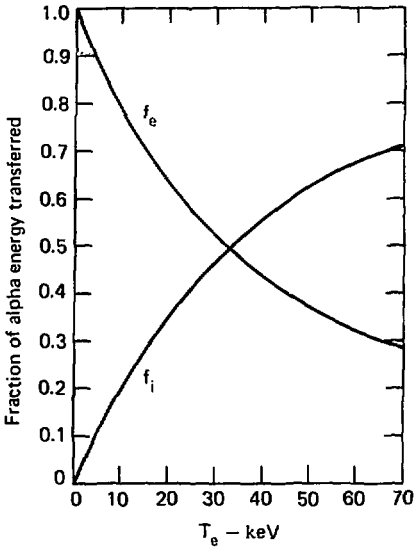

Fig. 3-5. Fraction of alpha energy transferred to electrons f_e and to DT ions f_i as a function of electron temperature.

Plug Heating of Electrons

Since electron heating beneficial in a TMR, the injection energy in the plugs is made as high as practical to allow a maximum fraction of the injected plug ion energy to be transferred to solenoid electrons by drag. For plug ion confinement dominated by electron drag, we use the approximate formula

$$(n\tau)_p \approx 1.5 \times 10^{10} M_p E_p^{3/2} \log_{10} R_p \cdot (cm^{-3} \cdot s), \quad (3\text{-}14)$$

which is derived from Fokker-Planck calculations[3-20] for plug injection energies $E_{inj} \approx 30$ to 40 T_e and modest plug mirror ratios $R_p \approx 2$ to 3. We assume either protons, deuterons, or tritons, for the plug ions, for which M_p is the appropriate mass number. The average plug ion energy in keV E_p is given by

$$E_p \approx 3.9 \left(T_e E_{inj}\right)^{1/2} \text{ (keV)}, \quad (3\text{-}15)$$

where T_e and E_{inj} are in keV. For $T_e \approx E_{inj}/15$ as in a conventional mirror machine, Eq. (3-15) gives $E_p \approx E_{inj}$. However, because for more drag-dominated plugs with lower T_e/E_{inj} the average plug ion energy is less than E_{inj}, $E_p^{3/2}$ gives a better fit to $(n\tau)_p$ in Eq. (3-14) than the usual $E_{inj}^{3/2}$. For the effective mirror ratio of short, 2XIIB-shaped plugs at high beta, we use an approximate empirical formula for R_p given by

$$R_p = R_{p\text{-vac}} / [1 - (\beta_p/2)]. \quad (3\text{-}16)$$

Data[3-18] from 2XIIB indicate that the diamagnetic reduction in plasma internal field ΔB is roughly linear with beta up to $\beta \approx 2$, hence the mirror ratio enhancement factor $[1 - (\beta_p/2)]$ in Eq. (3-16) rather than the usual $(1 - \beta)^{1/2}$ factor for long, thin plasmas. For lower ratios of E_{inj}/T_e and lower mirror ratios, Eq. (3-14) will tend to overestimate

$(n\tau)_p$; at the lowest $E_{inj}/T_e = 30$ and $R_p = 2$, the error is 20%. For most of the intended range of plug operation, however, Eq. (3-14) should give smaller errors. The rate at which hot plug ions of energy $E_p >> T_e$ transfer energy to electrons per cm^3 of plug volume is given by $n_p^2 E_p/(n\tau)_{ep}$, where the product of plug density and equilibration time in the plugs is given by

$$(n\tau)_{ep} = 5 \times 10^{11} M_p T_e^{3/2} \ (cm^{-3} \cdot s). \qquad (3\text{-}17)$$

In Eq. (3-17), M_p is the mass number for either protons, deuteron, or triton plug ions, T_e is in keV, and we have assumed that $\ell n \Lambda_{ep} = 20$. Each cold electron deposited with each neutral atom injected and ionized in the plugs escapes with an energy equal to the total plug potential $\phi_e + \phi_c$ (see Fig. 3-1) plus a transverse kinetic energy T_e. The fraction of plug ion energy available to heat the solenoid electrons is therefore given by

$$f_p = \left[\frac{n_p^2 E_p}{(n\tau)_{ep}} - \frac{n_p^2 (\phi_e + \phi_c + T_e)}{(n\tau)_p}\right] \cdot \left[\frac{n_p^2 E_{inj}}{(n\tau)_p}\right]^{-1};$$

or

$$f_p = \left[\frac{(n\tau)_p}{(n\tau)_{ep}} \left(E_p - \phi_e - \phi_c - T_e\right)\right]\left(\frac{1}{E_{inj}}\right). \qquad (3\text{-}18)$$

The fraction f_p can be considered as the efficiency by which high-energy neutral injection in the plugs heats the solenoid ions via electrons. Typically, $\phi_e \approx 6T_e$ and $\phi_c \approx 2T_e$ are required for adequate electron and ion confinement, respectively, in the solenoid. Using $(\phi_e + \phi_c + T_e) = 9\ T_e$, $M_p = 2$, $R_p = 2$, and using Eqs. (3-14), (3-15), and (3-17),

$$f_p = 0.27 \left(\frac{E_{inj}}{T_e}\right)^{1/4} - 9\left(\frac{T_e}{E_{inj}}\right) .$$

For a typical $T_e \approx 40$ keV, $f_p = 0$ at $E_{inj} = 660$ keV, 33% at 1.2 MeV, and 60% at 2.4 MeV.

Electron Confining Potential

We assume that the solenoid volume V_c is sufficiently large that the total ion loss current from the solenoid is much larger than the ion loss current from the plugs, even though the solenoid ion confinement is better than ion confinement in the plug. In steady state, quasi-charge neutrality requires the electron loss current I_{ec} from the solenoid to equal the ion loss current Iic from the solenoid: $I_{ec} = I_{ic}$, or approximately,

$$\frac{n_e^2 V_c}{(n\tau)_e} \approx \frac{n_c^2 V_c}{(n\tau)_i} , \qquad (3\text{-}19)$$

where $(n\tau)_e$ is the product of electron density and electron confinement time for those electrons in the solenoid

that see a confining potential of magnitude ϕ_e (see Fig. 3-1). The electron confinement product $(n\tau)_e$ is given by a formula similar to Eq. (3-2) for ions, with $M_i \to m_e$, $T_i \to T_e$, $R_c \to R_c$, and $\phi_c \to \phi_e$. The electron collision time is reduced by a factor of 2 due to collisions of electrons with plasma ions as well as self-collisions. Using $\ell n \Lambda_{ee} = 20$, and $g(R) = 4$, we can write Eq. (3-2) for electrons as

$$(n\tau)_e = 9 \times 10^8 \, T_e^{3/2} \left(\frac{\phi_e}{T_e}\right) \times \exp\left(\frac{\phi_e}{T_e}\right) \, (cm^{-3}.s) \, , \qquad (3\text{-}20)$$

where T_e is in keV. Equation (3-19) is only very roughly satisfied when the plug current is comparable to the solenoid current, as sometimes occurs for small TMR's. The inexactness of Eq. (3-20) is because the plug electrons see a larger confining potential $\phi_e + \phi_c$ and become part of the solenoid electron density (passing electrons between the plugs and solenoid) before escaping to the ends. Thus, the appropriate $(n\tau)_e$ to insure that the total electron loss equals the sum of plug and solenoid ion currents is somewhat different from Eq. (3-20). However, the magnitude of ϕ_e that adjusts to ensure quasi-charge neutrality can be determined to sufficient accuracy (within 5% by substituting Eq. (3-20) into Eq. (3-19) and using $n_e = n_c$ from Eq. (3-5) to obtain

$$\left(\frac{\phi_e}{T_e}\right) = \ell n \left[\frac{(n\tau)_i}{9 \times 10^8 \, T_e^{3/2} \left(\frac{\phi_e}{T_e}\right)} \right] . \qquad (3\text{-}21)$$

For all cases of interest, ϕ_e/T_e will be between 5 and 7; therefore, setting $\phi_e/T_e = 6$ within brackets of Eq. (3-21) will suffice to give an accurate value of ϕ_e/T_e as a function of T_e and $(n\tau)_i$.

Electron Energy Balance

Each electron escaping from the solenoid carries out an energy equal to ϕ_e plus a transverse kinetic energy T_e. Correspondingly, each electron injected with a plug ion escapes with $\phi_e + \phi_c + T_e$ energy. The electron temperature is determined by this electron energy loss out the ends by equilibration with ions, by the electron heating from hot plug ions and fusion alphas, and by external auxiliary heating (if any). We neglect bremsstrahlung and synchrotron radiation loss as small (see estimates at the end of this chapter). Using Eqs. (3-18) and (3-19), the electron energy balance can be expressed as

$$\frac{n_c^2}{(n\tau)_i} (\phi_e + T_e) + \frac{n_c^2 \, (3/2) \, (T_e - T_i)}{(n\tau)_{ei}} = f_p \left(\frac{n_p^2 \, E_{inj}}{(n\tau)_p}\right) \left(\frac{V_p}{V_c}\right) + \frac{1}{4} n_c^2 \langle \sigma v \rangle E_{\alpha o} f_\alpha f_e + P_{e\text{-}aux} . \qquad (3\text{-}22)$$

The first term on the left-hand side of Eq. (3-22) is the electron power loss/cm^3 carried out by electrons accompanying the ions lost from the solenoid; the second term on the left-hand side is the energy transfer rate/cm^3 to ions by equilibration when $T_e > T_i$. The first term on the right-hand side of Eq. (3-22) is the energy input to the solenoid via electrons heated by the plug ions. The volume ratio factor V_p/V_c in this term normalizes the heating of electrons in the plugs per unit of volume in the solenoid. Note that the electron energy carried out by the electrons accompanying the plug ions is included in the definition of f_p, Eq. (3-18). The second term on the right-hand side of Eq. (22) is the power density of electron heating by fusion alphas. The fraction of alphas adiabatically contained and thermalized is f_α, and f_e is the fraction of 3.5-MeV energy given to electrons by each alpha that thermalizes. The fraction f_e is a function of T_e as given in Fig. 3-5. An approximate formula for f_e is given by

$$f_e \approx 1.5 - 0.29\ \ell n(T_e), \quad (3\text{-}23)$$

for T_e in keV, $\pm 5\%$ in the range $20 < T_e < 60$ keV. Recall that, by definition, $f_e + f_i = 1$, for alphas which completely thermalize. As discussed later, some alphas initially slow down on electrons and then scatter into the loss cone before giving the remainder of their energy to ions. Therefore, electron heating by alphas is underestimated in Eq. (3-22) using Eq. (3-23), while ion heating in Eq. (3-10) is overestimated. Since confinement is sensitive to the ratio T_e/T_i, the approximation that alphas are either lost with no energy transfer or else completely thermalize is a pessimistic approximation with regard to the effects of alpha heating on confinement. The last term on the right-hand side of Eq. (3-22) represents the power input to the electrons by external auxiliary heating per cm^3 of solenoid volume. For a given value of E_{inj}, M_p, R_p, n_p/n_c, V_c/V_p, f_α and $F_{e\text{-}aux}$, and using Eq. (3-3) for $(n\tau)_i$ in the solenoid, Eq. (3-14) for $(n\tau)_p$ in the plugs, Eq. (3-1) for ϕ_c, and Eq. (3-21) for ϕ_e, the ion energy balance Eq. (3-10) and the electron energy balance Eq. (3-22) can be solved together to obtain the ion temperature T_i and the electron temperature T_e.

Pressure Balance

To relate the densities n_p and n_c to the fields B_p and B_c in the plugs and in the solenoid, respectively, we require pressure balance with the respective betas β_p and β_c as parameters. By definition, the plug beta

is given by

$$\beta_p \approx \frac{n_p (E_{p\perp} + T_e)}{(B_p^2/8\pi)} , \qquad (3\text{-}24)$$

where $E_{p\perp}$ is the average perpendicular energy of the plug ions, and B_p is the vacuum field in the centers of the plugs. The plug mirror field is then $B_{p\text{-}max} = R_{vac}\, B_p$. Fokker-Planck calculations show that for drag-dominated plugs ($E_{inj} >> T_e$) and injection perpendicular to the field lines as in 2XIIB, $E_{p\perp} \approx 0.9\, E_p$. That is, the plug pressure is anisotropic, peaked in the perpendicular direction. Then, neglecting T_e compared to E_p, the plug density can be expressed as

$$n_p = 2.8 \times 10^{15} \frac{\beta_p B^2_{p\text{-}max}}{R^2_{vac}\, E_p} \text{ cm}^{-3}, \qquad (3\text{-}25)$$

where $B_{p\text{-}max}$ is in teslas and E_p is in keV. By definition, the central solenoid beta is given by

$$\beta_c = \frac{n_c (T_e + T_i + p_\alpha/n_c)}{(B_c^2/8\pi)} \qquad (3\text{-}26)$$

where p_α/n_c is the perpendicular alpha pressure per unit central density given by Eq. (3-58), and where B_c is the external (vacuum) field in the central solenoid. Using Eq. (3-58) for p_α/n_c, the solenoid density can be expressed as

$$n_c = \frac{2.5 \times 10^{15}\, \beta_c B_c^2}{\left(T_e + T_i + 10^{11}\, T_e^{3/2} \langle\sigma v\rangle_{E_{\alpha 0}} f_\alpha f_e\right)^{-1}} , \qquad (3\text{-}27)$$

where B_c is in teslas and T_e, T_i, and $E_{\alpha 0}$ are in keV. Given the density ratio n_p/n_c, the betas β_p and β_c, and either one of the fields B_p or B_c, Eqs. (3-25) and (3-27) can be used to obtain the other field. Alternatively, given both fields, Eqs. (3-25) and (3-27) can be used to obtain the densities n_p and n_c and the density ratio n_p/n_c.

Plasma Dimensions

The dimensions of the plugs and the solenoid in a TMR are related by conservation of magnetic flux through the plugs and solenoid and by the volume ratio V_c/V_p. If we assume uniform plasma pressure across the cross sections of the plug midplanes and the solenoid, the condition for flux conservation can be written as

$$\pi r_c^2 B_{ci} = \pi r_p^2 B_{pi}, \qquad (3\text{-}28)$$

where B_{ci} and B_{pi} are the fields inside the solenoid and plug plasmas, respectively, given by

$$B_{ci} = B_c\, (1 - \beta_c)^{1/2} \qquad (3\text{-}29)$$

(the long, thin approximation for the solenoid) and

$$B_{pi} = B_p \left[1 - (\beta_p/2)\right] \qquad (3\text{-}30)$$

(the short, fat approximation for 2XIIB-like plugs).

Using Eqs. (3-29) and (3-30) for B_{ci} and B_{pi}, and solving Eqs. (3-27) and (3-25) for the external fields B_c and B_p, respectively, Eq. (3-28) can be written

$$\frac{r_c}{r_p} = \left[\frac{1 - (\beta_p/2)}{(1 - \beta_c)^{1/2}}\right]^{1/2} \left[\left(\frac{\beta_c}{\beta_p}\right)\left(\frac{n_p}{n_c}\right) \cdot \left(\frac{0.9E_p}{T_e + T_i + 10^{11} T_e^{3/2} \langle\sigma v\rangle E_{\alpha 0} f_\alpha f_e}\right)\right]^{1/4}. \quad (3\text{-}31)$$

Equation (31) relates the radii of the plugs and the solenoid when the densities and temperatures are known and when the plug and solenoid betas are specified.

We assume that the equivalent volume of each plug corresponds to a uniform sphere of radius r_p at density n_p at density n_p and that the solenoid volume is that of a cylinder of radius r_c and length L_c:

$$V_p = 2\left(\pi\frac{4}{3} r_p^3\right) \text{(both plugs)} \quad (3\text{-}32)$$

and

$$V_c = \pi r_c^2 L_c \quad \text{(solenoid)}. \quad (3\text{-}33)$$

Given the volume ratio V_p/V_c, the solenoid length can be determined from Eqs. (3-31) through (3-33) when either the radius of the flux tube in the plugs (r_p) or the radius in the solenoid (r_c) is specified:

$$L_c = \left(\frac{V_c}{V_p}\right)\left(\frac{8r_p^3}{3r_c^2}\right) = \left(\frac{V_c}{V_p}\right)\left(\frac{8}{3} r_c\right)\left(\frac{r_c}{r_p}\right)^{-3}$$

$$= \left(\frac{V_c}{V_p}\right)\left(\frac{8}{3} r_p\right)\left(\frac{r_p}{r_c}\right)^2 . \quad (3\text{-}34)$$

The radius r_c will be usually be determined by the economic requirement for sufficient solenoid fusion power per square metre of blanket (which scales with r_c), balanced with the requirement for sufficient Q and a given total power output. Alternatively, depending on the injection energy E_{inj} and plug field B_p, the radius of the plug r_p might be determined by the requirement for having a reasonable fraction of the plug neutral beams trapped in the plugs. The trapping function f_t for the plug beam is given by

$$f_t = 1 - e^{-\gamma}, \quad (3\text{-}35)$$

where the attenuation ratio γ for a uniform density plug, using cross-section and energy distribution functions by Riviere,[3-21] is given by

$$\gamma = 1.85 \times 10^{-14} n_p r_p \left(\frac{M_p}{E_{inj}}\right)^{0.91} \quad (3\text{-}36)$$

with n_p in cm^{-3}, r_p in cm, and E_{inj} in keV. The competition between the need for high E_{inj} and small plugs may sometimes lead to f_t substantially

less than unity. In all cases, the untrapped portion of the beam is assumed to be disposed of with no energy recovery, a circumstance which increases the recirculating power fraction and $/kW(e) net for a given Q. (Q is by definition the fusion power over injection power actually trapped in the plasma.) Nonrecovery of the untrapped beam is a pessimistic assumption, since it may be cost-effective to directly convert, or at least thermally convert, the unused portion of the beam. However, a design for such a beam direct converter has not yet been made. For the reference case (Table 10-2), 90% of the beam is trapped; therefore, whatever is done with the untrapped portion of the beam will not affect the energy balance more than 10%. For the case of electron heating, the absorbed power $P_{e\text{-}aux}$ in Eq. (3-22) is assumed to be the same percentage of the injected electron power input as the trapped portion of the plug neutral beams is of the incident neutral beam.

HEATING BY 3.5-MeV ALPHA PARTICLES

Adiabatic Containment of Alpha Particles

Since nearly all the 3.5-MeV alpha particles are born with pitch angles greater than the magnetic loss-cone angle in the solenoid, the fraction f_α of contained 3.5-MeV alpha particles available to heat the plasma is determined mainly by adiabaticity. Adiabaticity is a function both of the particle energy and pitch angle, with alphas of greater pitch angle and lower energy being more adiabatic. The relative jumps in magnetic moment $\Delta\mu/\mu$ that occur when the alphas reflect at the ends of the solenoid can be expressed as [3-22]

$$\left(\frac{\Delta\mu}{\mu}\right)_{rms} = \frac{A_0}{2}\,\frac{V}{V_\perp}\exp(-\kappa/\varepsilon)\ , \qquad (3\text{-}37)$$

where the amplitude $A_0 \approx 4$ for the majority of off-axis alphas (A_0 is less for axis-encircling alphas). Assuming a quadratic field variation of the transition regions in the ends of solenoid,

$$\kappa = \frac{1}{2\lambda^2}\left[\frac{1+\lambda^2}{2\lambda}\,\ell n\left(\frac{1+\lambda}{1-\lambda}\right) - 1\right], \qquad (3\text{-}38)$$

where $\lambda = v_\perp/v$ in the uniform field region of the center of the solenoid. κ is an increasing function of λ (pitch angle); $\kappa \approx 0.70$ for the more nonadiabatic alphas near the loss-cone angle $\theta = 20°$ ($\lambda = 0.342$), and $k \approx 2.0$ for alphas with $\theta = 80°$ ($\lambda = 0.985$). The quantity ε is given by

$$\varepsilon = \frac{v}{\Omega_0 L_\parallel}\ , \qquad (3\text{-}39)$$

where v is the alpha velocity.

$$\Omega_0 = \frac{2qB_{ci}}{M_\alpha} \qquad (3\text{-}40)$$

is the alpha cyclotron frequency at the field $B_{ci} = B_c (1 - \beta_c)^{1/2}$ inside the solenoid plasma, and where L is the field gradient scale length in the transition (mirror) regions at the solenoid ends.

Since adiabaticity is strongly energy dependent through ε in Eq. (3-37), the condition for alpha containment can be approximately expressed as

$$\tau_{\alpha\theta} \gtrsim \tau_{\alpha e}, \tag{3-41}$$

where $\tau_{\alpha\theta}$ is the time for an alpha to diffuse in pitch angle by nonadiabaticity from its initial angle θ_α to the loss-cone angle θ_c, and where $\tau_{\alpha e}$ is the slowing-down time for an alpha by electron drag. Assuming an alpha makes a random (uncorrelated) pitch angle step of average magnitude

$$\Delta\theta_\alpha = \Delta(v_\perp/v) = \left(\frac{\lambda}{2}\right)\left(\frac{\Delta\mu}{\mu}\right)_{rms} \tag{3-42}$$

in each bounce time $\tau_{bounce} \equiv L_c/v_\parallel$, Eq. (3-41) can be expressed as

$$\frac{(\theta_\alpha - \theta_c)^2}{\langle\Delta\theta_\alpha\rangle^2/\tau_{bounce}} \gtrsim 5 \times 10^{11}\, T_e^{3/2}/n_c, \tag{3-43}$$

where we have written the alpha drag time $\tau_{\alpha e}$ in terms of T_e in keV and electron density $n_e = n_c$. Using Eq. (3-42) then, the condition for adiabaticity is

$$\left(\frac{\Delta\mu}{\mu}\right)_{rms} \lesssim \left(\frac{2}{\gamma}\right)\left(\frac{\theta_\alpha - \theta_c}{\sqrt{N}}\right), \tag{3-44}$$

where $N \equiv \tau_{\alpha e}/\tau_{bounce}$ is the number of longitudinal bounces an alpha makes in the solenoid in one slowing down time. Using Eq. (3-37) for $(\Delta\mu/\mu)_{rms}$ in Eq. (3-44), we obtain

$$\kappa/\varepsilon \gtrsim \ell n\left(\frac{\sqrt{2N}}{\theta_\alpha - \theta_c}\right) \tag{3-45}$$

for adiabaticity. Using Eq. (3-39) and (3-40), this can be written

$$B_{ci} L_\parallel \gtrsim v\left(\frac{M_\alpha}{2q}\right)\left(\frac{1}{\kappa}\right) \ell n\left(\frac{\sqrt{2N}}{\theta_\alpha - \theta_c}\right),$$

or

$$B_c L_\parallel (1 - \beta_c)^{1/2} \gtrsim \frac{0.27}{\kappa(\theta)}\, \ell n\left(\frac{\sqrt{2N}}{\theta_\alpha - \theta_c}\right), \tag{3-46}$$

for 3.5-MeV alphas ($v = 1.3 \times 10^9$ cm/s), and where B_c is in teslas, and $L_\parallel$ is in metres. Consider the two cases $\theta_\alpha = 20°$ and $\theta_\alpha = 80°$, for which $\kappa = 0.7$ and 2.0, respectively. For the reference case parameters, $N \approx 1.7 \times 10^5$ bounces at $\theta_\alpha = 20°$ and 3.2×10^4 bounces for $\theta_\alpha = 80°$. If we take a typical value for the loss-cone angle $\theta_c = 13°$, Eq. (3-46) gives $B_c L_\parallel (1 - \beta_c)^{1/2} \gtrsim 3.2$ T·m for containment of 20° alphas, and $B_c L_\parallel (1 - \beta_c)^{1/2} > 0.7$ T·m for containment of 80° alphas. If we assume the reference case $B_c = 2.2$ T and $\beta_c = 0.7$, the required

field gradient scale length $L_{\parallel}$ is 2.7 m for $\theta_{\alpha} = 20°$ and 0.6 m for $\theta_{\alpha} = 80°$. Since either field gradient length could probably be designed for the solenoid transition regions, the minimum alpha pitch angle $\theta_{\alpha min}$ for adiabatic confinement could be chosen anywhere between these limits, giving a fraction of contained alphas $f_{\alpha} = \cos\theta_{\alpha min}$ ranging from 94% to 17%. In the absence of nonadiabatic effects, Fokker-Planck calculations[3-20] indicate that 70% of the alphas thermalize for a mirror ratio $R_c = 10(\theta_c = 18°)$. The 30% alpha particle loss is due to Coulomb scattering on plasma ions after most of the alpha energy has been lost to electrons and ions by drag. Most of those alphas lost would have been those born near the loss-cone angle. For $f_{\alpha} < 1$ due to nonadiabaticity, alpha loss by Coulomb scattering will be less important. For the present physics model, we assume that all adiabatically contained 3.5-MeV alphas ($\theta_{\alpha} > \theta_{\alpha min}$) completely thermalize; i.e., we neglect Coulomb loss during thermalization of those alphas. Since the ion heating will thereby be overestimated compared to electron heating (an unfavorable effect), we may sometimes try to offset some of the disadvantage of this simplifying assumption by taking $f_{\alpha} = 1$ even though $f_{\alpha} \lesssim 0.95$.

Alpha Heating of Ions and Electrons

Assuming that those alpha particles that are adiabatically contained survive to thermalize completely, we wish to determine the fractions f_e and f_i of the initial alpha energy $E_{\alpha 0}$ that are transferred to electrons and DT ions, respectively. By definition, then,

$$f_e + f_i = 1 \qquad (3\text{-}47)$$

Following a treatment by Rose,[3-23] we can determine the functions f_e and f_i from the drag rates of alphas on electrons and ions. If we assume that $E_{\alpha} >> T_e, T_i$, the decay of alpha energy is given by

$$\frac{dE_{\alpha}}{dt} = -\frac{E_{\alpha}}{\tau_{\alpha e}} - \frac{E_{\alpha}}{\tau_{\alpha i}} , \qquad (3\text{-}48)$$

where

$$\tau_{\alpha e} = 5 \times 10^{11}\, T_e^{3/2}/n_c \qquad (3\text{-}49)$$

is the drag time on electrons and where

$$\tau_{\alpha i} = 1.7 \times 10^{9}\, E_{\alpha}^{3/2}/n_c \qquad (3\text{-}50)$$

is the drag time on DT ions in the solenoid. (All energies are in keV; $\ell n\Lambda_{\alpha e} = \ell n\Lambda_{\alpha i} = 20.$) Equation (3-48) can be expressed as

$$\frac{dE_{\alpha}}{dt} = -\frac{E_{\alpha}}{\tau_{\alpha e}} \left[1 + k\left(\frac{E_{\alpha 0}}{E_{\alpha}}\right)^{3/2}\right] , \qquad (3\text{-}51)$$

where

$$k = 1.43 \times 10^{-3} T_e^{3/2}, \qquad (3\text{-}52)$$

and where $E_{\alpha 0} = 3500$ keV is the initial alpha energy. Note that as long as $E_\alpha \gg T_e, T_i$, the rate of alpha energy loss depends only on T_e and E_α. The ion temperature T_i does not matter until the alpha velocity approaches the ion velocity, by which time the alpha has lost nearly all its energy. The alpha energy decay is initially exponential with a time constant $\tau_{\alpha e}$, but when $E_\alpha \lesssim 30\ T_e$, the ion drag term [the second term in brackets in Eq. (3-51)] becomes dominant, and the alpha rapidly loses its remaining energy to the ions.

The solution to Eq. (3-51) for the alpha energy is given by

$$E_\alpha(t) = E_{\alpha 0}\ [(k+1)\, e^{-t'} - k]^{2/3}, \qquad (3\text{-}53)$$

where

$$t' \equiv \frac{3t}{2\tau_{\alpha e}} \quad . \qquad (3\text{-}54)$$

Note that the alpha completely thermalizes ($E_\alpha \to 0$) when $t' = \ell n[(k+1)/k]$. The fraction of alpha energy transferred to electrons is then given by

$$f_e = \frac{1}{E_{\alpha e}} \int \left(\frac{E_\alpha}{\tau_{\alpha e}}\right) dt = \frac{2}{3} \int_0^{\ell n[(k+1)/k]} \cdot \left[(k+1)e^{-t'} - k\right]^{2/3} dt' \quad . \qquad (3\text{-}55)$$

The fraction of alpha energy transferred to ions is correspondingly given by

$$f_i = \frac{1}{E_{\alpha 0}} \int \frac{E_\alpha}{\tau_{\alpha i}}\, dt$$

$$= \frac{2}{3} \int_0^{\ell n[(k+1)/k]} \frac{k\, dt}{[(k+1)e^{-t'} - k]^{1/3}} \qquad (3\text{-}56)$$

A plot of f_e and f_i as a function of T_e is shown in Fig. 3-5. Note that alphas transfer more energy to ions than to electrons for $T_e \gtrsim 33$ keV. Ratios of $T_e/T_i > 1$ improve electrostatic confinement in a TMR, a process which requires more energy into electrons than ions. However, because alphas heat the electrons less than ions for $T_e \gtrsim 33$ keV, ignition at such temperatures occurs only with $T_e/T_i \lesssim 1$ and requires fairly large density ratios (see "Q Scaling in a TMR"). Additional electron energy input, either by plug ions or other external sources, is required to obtain $T_e/T_i > 1$.

Hot-Alpha Pressure

Associated with the instantaneous power input per cm^3 to electrons from fast alphas is a required alpha pressure p_α giving a stored energy density $\approx 3/2\ p_\alpha$ in the form of hot

alphas slowing down. Assuming that the average energy of the slowing-down alphas is much greater than T_e, one can express power balance between fusion production of alpha energy and alpha energy loss by drag from the electron component as

$$\frac{\frac{3}{2} p_\alpha}{\tau_{\alpha e}} = \frac{1}{4} n_c^2 \langle\sigma v\rangle E_{\alpha 0} f_\alpha f_e, \qquad (3\text{-}57)$$

where $\tau_{\alpha e}$ is given by Eq. (3-49), and f_e is given either by Eq. (3-55) or more conveniently by Eq. (3-23). Using Eq. (3-49), Eq. (3-57) can be solved for the hot-alpha pressure per unit density in the solenoid:

$$\frac{p_\alpha}{n_c} \approx 10^{11} T_e^{3/2} \langle\sigma v\rangle E_{\alpha 0} f_\alpha f_e. \qquad (3\text{-}58)$$

For the reference case parameters (Table 10-2), the ratio of alpha pressure to electron plus ion pressure $p_\alpha / [n_c(T_e + T_i)] \approx 36\%$.

Q SCALING IN A TMR

The Q in a TMR depends on a number of independent plasma parameters — E_{inj} M_p, n_p/n_c, V_c/V_p, and f_a —and also depends weakly on the plasma betas β_p and β_c insofar as they affect the mirror ratios R_p and R_c seen by the plug and solenoid ions. For the case with auxiliary electron heating, the Q given by Eq. (3-4) can be generalized to include the electron heating power:

$$Q = \frac{1}{4} (n\tau)_p \langle\sigma v\rangle \left(\frac{E_F}{E_{inj}}\right)\left(\frac{n_c}{n_p}\right)^2 \cdot \left(\frac{V_c}{V_p}\right) (1 - F_e), \qquad (3\text{-}59)$$

where

$$F_e \equiv \frac{P_{e\text{-}aux} V_c}{\left(\frac{n_p^2 E_{inj} V_p}{(n\tau)_p}\right) + P_{e\text{-}aux} V_c} \qquad (3\text{-}60)$$

is the ratio of direct electron heating power to the total power (neutral beam plus electron) injected into the plasma. In the limit $F_e \to 1$ (dominant electron heating), $Q \to \frac{1}{4} n_c^2 \langle\sigma v\rangle E_f P_{e\text{-}aux}$, so that Q no longer depends on the plug parameters or V_c/V_p.

For an economic TMR, the goal is not just to maximize Q, but to minimize capital cost per kilowatt. If there were no restrictions on n_p/n_c or $V_c V_p$, Q could be made arbitrarily large according to Eq. (3-59). However, increasing n_c/n_c generally increases blanket cost per kW; higher V_c/V_p generally requires larger reactor size and power. Nevertheless, a high Q is necessary also to keep the recirculating power small. One of the most uncertain reactor cost estimates at the time of this study

is the cost of the MeV neutral-beam injectors for the plugs. Depending on how large the $/kW of recirculating power by those beams is in the final analysis, Q may possibly need to be increased to ten or more for economic operation. In that event, it is desirable to know the various ways to scale up Q in a TMR.

Subignition Case

Let us consider first the situation where alpha heating alone is not sufficient to energetically sustain the solenoid. The solenoid requires additional energy input in steady state, preferably in electron heating of some form rather than in ion heating. In the reference case, the extra energy comes from plug ions heating the electrons, parameterized by the fraction f_p of neutral-beam power that is available to the solenoid electrons. Auxiliary direct heating of electrons is parametrized by the fraction F_e of total injection power that is direct electron heating. The plug parameters are coupled to solenoid parameters though the electron energy balance Eq. (3-22). Equation (3-22) can be solved for the volume ratio, giving

$$\frac{V_c}{V_p} = \left(\frac{n_p}{n_c}\right) \frac{(n\tau)_i}{(n\tau)_p} \left(f_p + \frac{F_e}{1 - F_e}\right) \left[\frac{E_{inj}}{\frac{1}{2}T_e + T_e + \frac{(n\tau)_i}{(n\tau)_{ei}}\left(\frac{3}{2}\right)(T_e - T_i) - \frac{1}{2}f_b f_\alpha f_e E_{\alpha 0}}\right], \tag{3-61}$$

where

$$f_b = \frac{\frac{1}{2}(n\tau)_i \langle\sigma v\rangle}{1 + \frac{1}{2}(n\tau)_i \langle\sigma v\rangle} \tag{3-62}$$

is the burnup fraction. Substitution of Eq. (3-61) into Eq. (3-59) then gives

$$Q = \frac{1}{2}\left(\frac{f_b}{1 - f_b}\right)\left[f_p(1 - F_e) + F_e\right] \left[\frac{E_F}{\frac{1}{2}T_e + T_e + \frac{(n\tau)_i}{(n\tau)_{ei}}\left(\frac{3}{2}\right)(T_e - T_i) - \frac{1}{2}f_b f_\alpha f_e E_{\alpha 0}}\right]. \tag{3-63}$$

Note that Q is directly proportional to the burnup $(f_b/1 - f_b)$, hence proportional to $(n\tau)_i$, a dependence not apparent in Eq. (3-59). When *there is no auxiliary electron heating* ($F_e = 0$), Q is directly proportional to the plug heating fraction f_p. The way to increase Q with f_p is to raise the injection energy E_{inj} according to Eq. (3-18). However, raising E_{inj} at fixed β_p and B_p decreases plug density and solenoid fusion power density. When E_{inj}/T_e is such that $f_p = 0$ by Eq. (3-18), Q is directly proportional to F_e.

Compared to the reference case with $f_p \simeq 1/3$, a case with electron heating and $f_p = 0$ would need $F_e \geq 1/3$ to do as well, assuming the generating and injection efficiency for electron heating were the same as the neutral-beam efficiency.

For the case of no electron heating ($F_e = 0$), Fig. 3-6 shows the variation of Q, T_e, and T_i with volume ratio V_c/V_p (i.e., solenoid length) for a fixed plug injection power, a fixed injection energy $E_{inj} = 1$ MeV, and a fixed density ratio $n_p/n_c = 10$. Deuterium plugs, $R_p = 2.5$, and an alpha containment fraction $f_\alpha = 1$ are assumed. As the volume ratio is increased, the power input per unit volume of solenoid from the plugs is decreased, so that the equilibrium electron and ion temperatures decrease monotonically with V_c/V_p. However,

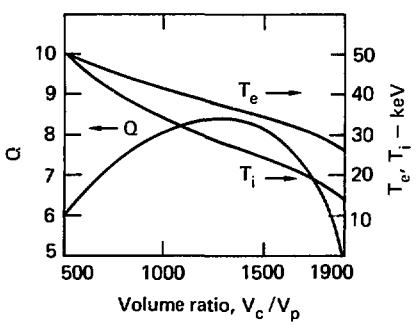

Fig. 3-6. Variation of Q, T_e, and T_i with volume ratio V_c/V_p (subignition) for $n_p/n_c = 10$, $E_{inj} = 1$ MeV, $f_\alpha = 1.0$, and $F_e = 0$.

the total solenoid fusion power is increasing faster due to the volume increase than it is decreasing due to the decrease in T_i and $\langle\sigma v\rangle$. Beyond a certain volume ratio, however, the rate of decline in $\langle\sigma v\rangle$ with T_i cannot be compensated for by increases in volume, and Q decreases.

Condition for Ignition

The conditions for alpha heating alone to sustain the solenoid (ignition) can be expressed as

$$\frac{1}{4} n_c^2 \langle\sigma v\rangle E_{\alpha 0} f_\alpha f_e = \frac{n_c^2}{(n\tau)_e} (\phi_e + T_e) + \frac{n_c^2}{(n\tau)_{ei}} \left(\frac{3}{2}\right) (T_e - T_i) \quad (3\text{-}64)$$

and

$$\frac{1}{4} n_c^2 \langle\sigma v\rangle E_{\alpha 0} f_\alpha f_i = \frac{n_c^2}{(n\tau)_i} (\phi_c + T_i) - \frac{n_c^2}{(n\tau)_{ei}} \left(\frac{3}{2}\right) (T_e - T_i). \quad (3\text{-}65)$$

Adding Eq. (3-64) and (3-65) and using $f_e + f_i = 1$ and $(n\tau)_i = (n\tau)_e$, we obtain

$$\frac{1}{4} n_c^2 \langle\sigma v\rangle E_{\alpha 0} f_\alpha = \frac{n_c^2}{(n\tau)_i} (\phi_e + \phi_c + T_e + T_i), \quad (3\text{-}66)$$

or

$$(n\tau)_i = \frac{4(\phi_e + \phi_c + T_e + T_i)}{\langle \sigma v \rangle E_{\alpha 0} f_\alpha} \quad (3\text{-}67)$$

For ignition, $(n\tau)_i$ has a minimum $\approx 7 \times 10^{14}$ cm^{-3} at $n_p/n_c \approx 17$, $T_e \approx T_i \approx 40$ keV, $f_\alpha \approx 1$. The required $(n\tau)_i$ for ignition in a TMR is higher than in tokamaks because the energy carried out per ion-electron pair is greater than $\frac{3}{2}(T_e + T_i)$ due to the potentials. On the other hand, the ions fall through the combined potential $\phi_e + \phi_c$ on escape, making efficient direct conversion possible in a simple one-stage direct converter with a collector potential at $\phi_e + \phi_c$.

Ideally, the plugs should not input any net electron energy to the solenoid under conditions of ignition; i.e., $f_p = 0$. The solenoid parameters can then become uncoupled from those plugs; T_e and T_i become independent of $V_c V_p$. In Eqs. (3-61) and (3-62), this means that the denominators of the energy ratios in brackets go to zero, in accordance with Eq. (3-64). $V_c V_p$ and Q can then assume any value. Although the effective Q of the solenoid alone is infinite at ignition, a fixed neutral-beam power must always be injected to maintain the plugs. The tandem mirror system Q according to Eq. (3-59) then scales up linearly with V_c/V_p, or solenoid length.

Development of such a reactor would have the attractive possibility of starting out at small power levels with a short solenoid, which could later be lengthened by simply adding solenoid modules to increase both Q and power output without changing plug or solenoid parameters. As an example, Fig. (3-7) shows Q as a function of volume ratio at a density ratio sufficient for ignition, $n_p/n_c = 16.5$. All other parameters are the same as in Fig. 3-6. Q is seen to increase indefinitely with volume ratio. T_e and T_i approach constant asymptotic values = 40 keV at large volume ratios, so fusion power is also increasing proportional to volume. T_e and T_i actually vary slowly with the smaller values of V_c/V_p because the assumed injection

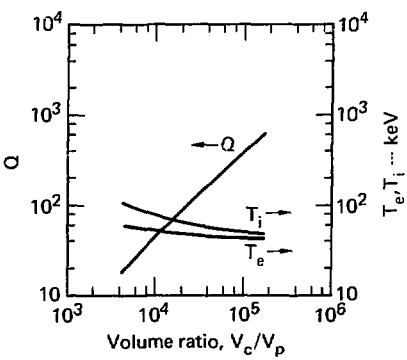

Fig. 3-7. Variation of Q, T_e and T_i with volume ratio V_c/V_p (ignition) for $n_p/n_c = 16.5$, $E_{inj} = 1$ MeV, $f_\alpha = 1.0$, and $F_e = 0$.

energy E_{inj} = 1 MeV is too high for f_p to be exactly zero at the asymptotic ignition temperatures of 40 keV. Some unnecessary energy is being input by the plugs. The energy input is significant only at small solenoid volumes, at which T_e heats up to approximately satisfy $f_p \sim 0$. An injection energy $E_{inj} \approx 660$ keV would allow the plugs to completely decouple.

Unfortunately, the constraint of a maximum plug density at practical plug magnetic fields makes the fusion power density in the solenoid uneconomically low at the density ratio $n_p/n_c \approx 17$ required for ignition and at a total net power output of 1000 MW(e). The plasma radius in the plugs and solenoid can be scaled up to achieve any desired wall loading on the blanket, but only at an increase in total power. The parametric analysis in Chapt. 10 shows that minimum reactor cost at a power level of 1000 MW(e) occurs at $n_p/n_c \approx 9$, at which the power input to the solenoid from the plugs is comparable to the input by alpha particles. The percentage of alpha heating increases asymptotically to 100% (ignition) as the reactor power is increased.

RADIAL DIFFUSION OF THERMAL ALPHA PARTICLES AND IMPURITIES

Here we consider the removal of thermal alpha particles and higher-Z impurities in a TMR by classical radial diffusion across the solenoid field, as suggested by Dimov.[3-3] Such diffusion can occur by collisions between the higher-Z ions and the majority species of DT ions much more rapidly than the usual diffusion of ions by momentum-transfer collisions with electrons. For the moment, let us consider only thermal alphas as impurities. We assume flat radial density and temperature profiles in both the plugs and in the solenoid, as shown in Fig. 3-8. Thermal alphas generated by fusion reactions and cooling down within the interior diffuse to the boundary, sustaining a negative radial density gradient of alphas $dn_\alpha/dr < 0$. Let us assume there is some mechanism of removing thermal alphas preferentially from the boundary layer, so that the alpha density at the boundary is small, $n_\alpha(r_c) \approx 0$. One such mechanism is to inject high-energy neutral beams tangentially into the boundary layer, heating the ions T_i, $T_\alpha > \phi_b$, where ϕ_b is a small boundary layer potential barrier reduced by a lower T_e in the layer. The DT ions in the layer are contained for a collision time as in a high-temperature, Q = 1 conventional mirror machine. Alphas with Z = 2 and higher-Z impurities are then preferentially expelled from the layer because of their higher scattering rate.

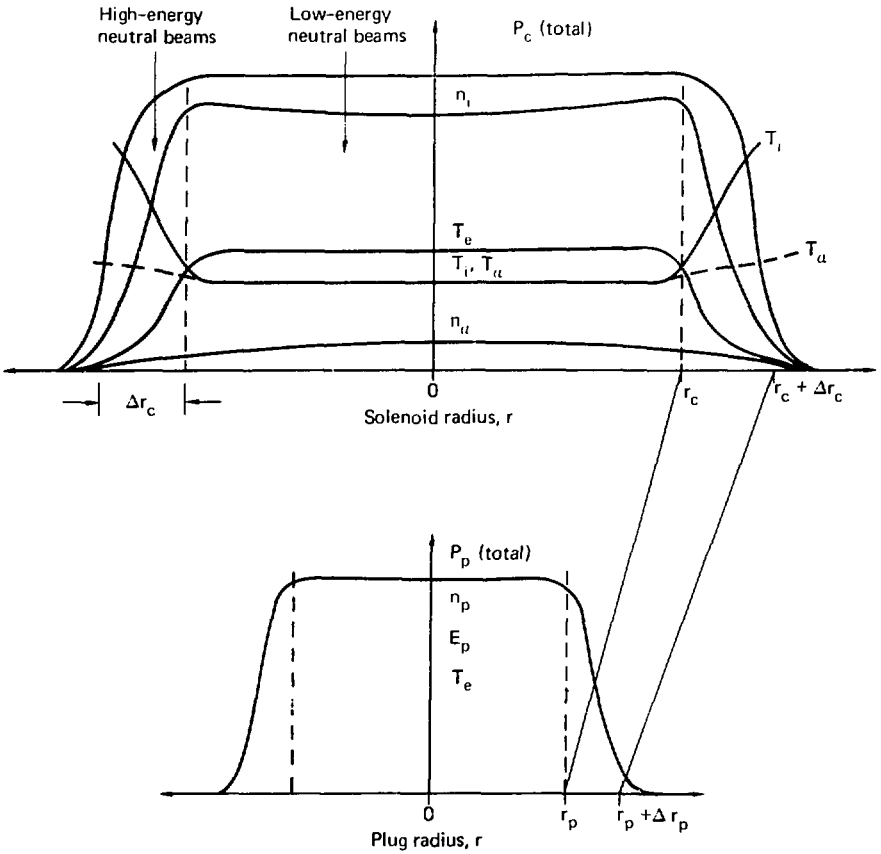

Fig. 3-8. Radial profiles of solenoid and plug.

For the case where there are no thermal gradients ($\partial T/\partial r = 0$), Longmire and Rosenbluth[3-24] derive the flux Γ_{12} of Species 1 due to the collisions with Species 2, which can be written for $T_1 = T_2$ as

$$\Gamma_{12} = \frac{4}{3}\left(\frac{2\pi M_{12} c^2}{kT}\right)^{1/2} \frac{cq_2^2}{B^2} \ell n\Lambda_{12} \times \left(\frac{q_1}{q_2} n_1 \frac{\partial n_2}{\partial r} - n_2 \frac{\partial n_1}{\partial r}\right), \quad (3\text{-}68)$$

where M_{12} is the reduced mass. Equation 68 predicts that the net charge flux is zero

$$q_1\Gamma_{12} + q_2\Gamma_{21} = 0 \qquad (3\text{-}69)$$

Rose[3-25] shows this to be a direct consequence of momentum conservation for guiding-center displacements due to individual collisions. Thus, no radial electron transport is required for charge neutralization of alphas diffusion outward on DT ions, since there is a flux of DT ions diffusing inward that is twice as large. This also means that in steady state, the diffusion of DT fuel into a local volume exactly balances the radial loss of thermal alpha from that volume. Thus, if most alphas thermalize, a local injection strength equal only to the unburned DT fuel loss is required. Of course, the extra fuel diffusing inward must be supplied by injection in the plasma boundary to compensate for fuel loss by burnup in the plasma interior.

Letting Species 1 be thermal alphas and Species 2 be DT ions with an effective mass of 2.5 amu, the flux of alphas by Eq. (3-69), with $\ell n\Lambda_{\alpha i} \approx 22$, becomes

$$\Gamma_{\alpha i} = \frac{6.1 \times 10^{-12}}{\sqrt{T_i}\, B_{ci}^2} \cdot \left(Z_\alpha n_\alpha \frac{dn_i}{dr} - n_i \frac{dn_\alpha}{dr} \right). \qquad (3\text{-}70)$$

where $T_i = T_\alpha$ is the ion temperature in keV, and B_{ci} is the field inside the plasma of the solenoid in teslas. Note that if the majority species of DT ions had a sufficient negative radial gradient, the flux of alphas could be inward $\Gamma_{\alpha i} < 0$ even though the alpha gradient were negative $dn_\alpha/dr < 0$. Thus, it is important to keep dn_i/dr zero or positive, as in the central zone in Fig. 3-8.

If there were no axial loss of the majority DT fuel ion species, cross-field diffusion of DT ions diffusing on electrons and on the alphas would proceed irreversibly to a negative DT ion density gradient $dn_1/dr < 0$. The outward diffusion of alphas would then be shut off until the alphas built up in the center to a point where the alpha density gradient term $n_i \partial n_\alpha/\partial r$ in Eq. (3-70) exceeded $Z_\alpha n_\alpha \partial n_i/\partial r$. For small burnup fractions $f_b \approx 0$, the net alpha flux would be small, so that in steady state

$$Z_\alpha n_\alpha \frac{\partial n_i}{\partial r} - n_i \frac{\partial n_\alpha}{\partial r} \approx 0 . \qquad (3\text{-}71)$$

Equation (3-71) can be integrated to give

$$\ell n \left(\frac{n_{\alpha 0}}{n_{\alpha b}} \right) = Z_\alpha \ell n \left(\frac{n_{i0}}{n_{ib}} \right),$$

or

$$\frac{n_{\alpha 0}}{n_{\alpha b}} = \left(\frac{n_{i0}}{n_{ib}} \right)^{Z_\alpha}, \qquad (3\text{-}72)$$

where $n_{\alpha 0}$, n_{i0} are the alpha and DT ion densities at r = 0, and $n_{\alpha b}$, n_{ib} are the corresponding densities at the plasma boundary $r = r_c$. If the DT ion density decreased by a ratio of 10 from the center to the boundary, and the alpha fraction was 1% at the boundary, the resulting alpha fraction in the center would be unity by Eq. (3-72). Higher-Z impurities would concentrate even more. Only because the dominant loss of DT ions is axial is it possible to preserve $dn_i/dr \gtrsim 0$ by an appropriate distribution of neutral injection in the solenoid, giving rapid outward diffusion of alphas and impurities.

We now wish to calculate the steady-state alpha fraction $C_\alpha \equiv n_\alpha/n_i$ at r = 0 using Eq. (3-70) under conditions of a constant radial pressure profile as in Fig. (3-8), such that the internal field $B_{ci} = B_c (1 - \beta_c)^{1/2}$ is uniform in radius. The condition that the total solenoid pressure p_c be constant can be written

$$p_c \equiv n_i T_i + n_\alpha T_\alpha + n_e T_e \left(1 + \frac{p_\alpha}{n_e T_e}\right)$$

$$\equiv \text{constant} \quad (r < r_c), \qquad (3\text{-}73)$$

where p_α is defined in Eq. (3-57). Since equilibration between thermal alphas and DT ions is rapid, we can take $T_\alpha = T_i = \text{constant}$. We assume nearly uniform $(n\tau)_i$ in radius, so we can also approximate $T_e \approx$ constant, with radius. Assuming T_e = 40 keV and T_i = 30 keV (reference case) and using Eq. (3-58) for p_α/n_e, we can write Eq. (3-73)

$$n_i + n_\alpha + (n_i + 2n_\alpha)\ (1.33) \cdot \left[1 + \frac{0.58 n_i^2}{(n_i + 2n_\alpha)^2}\right] = \text{constant}. \qquad (3\text{-}74)$$

Taking the derivative of Eq. (3-74) with respect to r and assuming $C_\alpha \ll 1$, we obtain

$$\frac{dn_i}{dr} \approx -0.68 \frac{dn_\alpha}{dr}, \qquad (3\text{-}75)$$

to first order in C_α. By substituting Eq. (3-75) into Eq. (3-70), the alpha flux can be written

$$\Gamma_{\alpha i} \approx -D_\alpha \frac{dn_\alpha}{dr} \quad \frac{\text{alphas}}{\text{cm}^2 \cdot \text{s}}, \quad (r < r_c), \qquad (3\text{-}76)$$

where the diffusion coefficient D_α is given by

$$D_\alpha = \frac{6.1 \times 10^{-12}\ n_i\ (1 + 1.36 C_\alpha)}{\sqrt{T_i}\ B_c^2\ (1 - \beta_c)}\ \text{cm}^2/\text{s}. \qquad (3\text{-}77)$$

In Eq. (3-77) we have used $B_{ci}^2 \approx B_c^2 (1 - \beta_c)$. Anticipating small alpha fractions $C_\alpha \ll 1$ over $r < r_c$, and

because the radial profile is kept at constant pressure by appropriate neutral-beam injection, we note that D_α is approximately constant with radius. We obtain the steady-state alpha density profile from the diffusion equation

$$D_\alpha \frac{d^2 n_\alpha}{dr^2} + J_\alpha = 0 , \qquad (3\text{-}78)$$

where

$$J_\alpha = f_\alpha \left(\frac{1}{4} n_i^2 \langle\sigma v\rangle\right) \qquad (3\text{-}79)$$

is the source strength of the thermal alphas. For the same reasons noted above, J_α is nearly constant with radius, so $d^2 n_\alpha / dr^2 \approx$ const. The solution to Eq. (3-78) is then

$$n_\alpha (r) = C_1 r^2 + C_2 , \qquad (3\text{-}80)$$

where the constants C_1 and C_2 are determined by the boundary condition at $r = r_c$ on the total alpha flux;

$$-D_\alpha \left.\frac{dn_\alpha}{dr}\right|_{r=r_c} \cdot 2\pi r_c \ell = J_\alpha \pi r_c^2 \ell ,$$

or

$$C_1 = -\frac{J_\alpha}{4D_\alpha} , \qquad (3\text{-}81)$$

and by the boundary condition that the alpha density go to zero at $r = r_c$;

$$n_\alpha(r) \Big|_{r=r_c} = 0,$$

or

$$C_2 = -\left(\frac{J_\alpha}{4D_\alpha}\right) r_c^2 . \qquad (3\text{-}82)$$

Thus the density profile of the thermal alpha is

$$n_\alpha(r) \quad \frac{J_\alpha r_c^2}{4D_\alpha} \left(1 - \frac{r^2}{r_c^2}\right). \qquad (3\text{-}83)$$

We are interested in the average alpha fraction over $0 < r < r_c$:

$$\bar{C}_\alpha \approx \frac{J_\alpha r_c^2}{8 D_\alpha n_i} . \qquad (3\text{-}84)$$

Using Eq. (3-77) for D_α, assuming C_α in the range of 10%, and using Eq. (3-79) for J_α, we obtain

$$\bar{C}_\alpha \approx 4.5 \times 10^9 f_\alpha \langle\sigma v\rangle \cdot \sqrt{T_i}\, (r_c B_c)^2 (1 - \beta_c). \qquad (3\text{-}85)$$

For the reference case parameters at $\beta_c = 0.7$ and taking $f_\alpha = 0.7$ for the actual thermalization fraction (see "Alpha Heating of Ions and Electrons"), Eq. (3-85) gives $\bar{C}_\alpha = 20\%$. However, with the same parameters except for $\beta_c = 0.95$, $\bar{C}_\alpha = 3\%$. Thus, high beta in the solenoid is important for efficient alpha removal. At any beta, a re-optimization of power cost with a self-consistent alpha fraction would probably result in lower values of C_α by compromising f_α, T_i, and r_c.

Probable values of $\bar{C}_\alpha$ in the neighborhood of 5%, depending on β_c, would result in lower $(n\tau)_i$ by a factor of $Z_\alpha^2 \bar{C}_\alpha \approx 20\%$ due to enhanced DT ion scattering on the alphas. However, as noted in previous discussion, favorable ion cooling effects by burnup and alpha loss have also been neglected as well as the thermal alpha fraction in this study.

Should higher-Z impurities somehow manage to get into the solenoid, Eq. (3-68) shows that the radial diffusion flux Γ_Z and diffusion coefficient D_Z for impurities increase proportionally to Z. In addition, the source strength of high-Z impurities will likely be very much smaller than the DT fuel burnup rate (20%), therefore, we may conclude that under conditions in which thermal alphas can diffuse out, higher-Z ions will do so also, at concentrations that will always be much smaller than alpha concentrations.

SYNCHROTRON RADIATION LOSSES

Since high electron temperatures are desirable in a TMR, synchrotron radiation losses would appear, at first sight, to be important. However, the plasma beta in the solenoid is also expected to be high, reducing the magnetic field in the plasma. Radiation in the plugs should not be dominant because although the density and field are higher there, the volume of the plugs is sufficiently small compared to the solenoid volume. Bremsstrahlung is negligible compared to the fusion power since the ion temperature in a TMR is always well above the bremsstrahlung ignition temperature of 4.5 keV for DT.

To evaluate synchrotron radiation loss, we make use of formulas by Trubnikov,[3-26] using an effective plasma radius $r_p/(1 - R_w)$ in the presence of conducting walls having reflectivity R_w, as suggested by Drummond and Rosenbluth.[3-27] The synchrotron radiation loss per cm^3 of plasma is

$$P_{sync} = 6.2 \times 10^{-17} B_i^2 n_e T_e \cdot \frac{K_3 (mc^2/T_e)}{K_2 (mc^2/T_e)} K_L \left(W \cdot cm^{-3}\right), \qquad (3\text{-}86)$$

where B_i is in teslas, n_c is in cm^{-3}, and T_e is in keV. K_3 and K_2 are modified Bessel functions with arguments mc^2/T_e, the electron rest mass energy over the electron temperature. The ratio K_3/K_2 can be expanded for large argument to give

$$\frac{K_3(mc^2/T_e)}{K_2(mc^2/T_e)} = 1 + \frac{T_e}{204} \cdots, \qquad (3\text{-}87)$$

for T_e in keV. The dimensionless coefficient K_L for plasma reabsorption of radiation can be expressed by an approximate formula given by Rose,[3-23]

which fits Trubnikov's exact calculations within 10% up to T_e = 150 keV:

$$K_L = 2.1 \times 10^{-3} \, T_e^{7/4} / \sqrt{\mathscr{L}} , \qquad (3\text{-}88)$$

for T_e in keV. Equation (3-88) is valid only for $K_L \ll 1$, or strong reabsorption, as is usually the case. The dimensionless plasma length $\mathscr{L}$ with reflecting walls can be approximated by

$$\mathscr{L} \approx \left(\frac{r_p}{1 - R_w} \right) \left(\frac{\omega_{pe}^2}{c\omega_{ce}} \right) . \qquad (3\text{-}89)$$

The internal field B_i is determined by the plasma beta β and pressure balance:

$$\frac{\beta}{1-\beta} \left(\frac{B_i^2}{8\pi} \right) = n_e T_e + n_i T_i . \qquad (3\text{-}90)$$

Assuming $n_e = n_i$ and $T_e = T_i$, Eq. (86) can be written, using Eqs. (87) through (90):

$$P_{sync} \approx 3.8 \times 10^{-37} \, n_e^2 \, T_e^{17/4} \cdot \left(1 + \frac{T_e}{204} \right) \left(\frac{1 - R_w}{\langle r_p B \rangle} \right)^{1/2} \cdot \left(\frac{1 - \beta}{\beta} \right)^{3/2} , \qquad (3\text{-}91)$$

where $$\langle r_p B \rangle \equiv \int_0^{r_p} B_i(r) \, dr \qquad (3\text{-}92)$$

is a quantity proportional to the number of ion gyroradii across the plasma (which may have some minimum value). For the solenoid, the effective wall reflection coefficient with holes at the ends for the low-energy neutral beams and connection to the plugs averages out to $R_w \approx 0.99$. In the plugs, the end holes have relatively more area, so $R_w \approx 0.90$. The product $\langle r_p B \rangle \approx 1$ T·m in the solenoid and 4 T·m in the plugs. For the reference TMR reactor parameters at T_e = 43 keV, T_i = 30 keV, the ratio of fusion power to synchrotron radiation power $P_{fusion}/P_{sync} \gtrsim 5 \times 10^3$ at $\beta_c = 0.7$ in the solenoid. Thus, synchrotron radiation would be small even if T_e were higher. In the plugs, the ratio of the neutral-beam power in the plug to synchrotron radiation $[n_p^2 E_{inj}/(n\tau)_p]/P_{sync} \gtrsim 40$, so radiation is small there also.

REFERENCES

3-1. G. G. Kelley, "Elimination of Ambipolar Potential-Enhanced Loss in a Magnetic Trap," *Plasma Phys.* 9, 503 (1967).

3-2. V. P. Pastukhov, "Collisional Losses of Electron from an Adiabatic Trap in a Plasma with a Positive Potential," *Nucl. Fusion* 14, 3 (1974).

3-3. G. I. Dimov, V. V. Zakaidakov, and M. E. Kishinevsky, *Fiz. Plasmy* 2, 597 (1976); also G. I. Dimov, V. V. Zakaidakov,

and M. E. Kishinevsky, "Open Trap with Ambipolar Mirrors," in *Proc. 6th Inter. Conf. Plasma Physics and Controlled Nuclear Fusion Research, Berchtesgaden, Fed. Rep. of Germany, 1976* (IAEA, in preparation), Paper C4.

3-4. T. K. Fowler and B. G. Logan, "The Tandem Mirror Reactor" *Comments on Plasma Physics and Controlled Fusion Research*, 2, 167 (1977).

3-5. R. A. Dandle, *Research Program for Plasma Confinement and Heating in Elmo Bumpy Torus Devices*, Oak Ridge National Laboratory, Rept. ORNL-TM-4941, Appendix G (1975).

3-6. See discussion by S. Putnam *et al., in Proc. of High Beta Workshop, Los Alamos Scientific Laboratory, 1975* (ERDA Rept. 76/108, 1975) 411.

3-7. L. E. Thode, "Plasma Heating by Scattered Relativistic Electron Beams: Correlations Among Experiment, Simulation, and Theory," *Phys. Fluids* 19, 831 (1976).

3-8. D. Prono, B. Ecker, N. Bergstrom, and J. Benford, "Plasma-Return-Current Heating by Relativistic Electron Beams with $\nu/\gamma \sim 10$," *Phys. Rev. Lett.* 35, 438 (1975).

3-9. G. C. Goldenbaum, W. F. Dove, K. A. Gerber and B. G. Logan "Plasma Heating by Intense, Relativistic Electron Beams," *Phys. Rev. Lett.* 32, 830 (1974).

3-10. F. H. Coensgen, Project Leader, *TMX Major Project Proposal*, Lawrence Livermore Laboratory, Rept. LLL-Prop-148 (1977), Appendix A2, p. 47.

3-11. B. G. Logan, J. F. Clauser, F. H. Coensgen, D. L. Correll, W. F. Cummins, C. Gormezano, A. W. Molvik, W. E. Nexsen, T. C. Simonen, B. W. Stallard, and W. C. Turner, "High-B, Gas-Stabilized, Mirror-Confined Plasma," *Phys. Rev. Lett.* 37 1468 (1976).

3-12. L. S. Hall, "Magnetostatic Equilibria of Finite-Pressure Minimum-B Plasma Configurations," *Phys. Fluids* 15, (1972).

3-13. R. C. Davidson and J. M. Ogden, "Electromagnetic Ion Cyclotron Instability Driven by Ion Energy Anisotropy in High-Beta Plasmas," *Phys. Fluids* 18, 1045 (1975).

3-14. H. L. Berk, D. E. Bladwin, T. A. Culler, L. L. Lodestro, N. Maron, L. D. Pearlstein, T. D. Rognlien, J. J. Stewart, and D. C. Watson, "Theoretical Explanation of Present Mirror Experiments and Linear Stability

of Larger Scaled Machines," in *Proc. Sixth Inter. Conf. Plasma Physics and Controlled Nuclear Fusion Research, Berchtesgaden, Fed. Rep. of Germany, 1976* (IAEA, in preparation), Paper CN-35/C2.

3-15. F. H. Coensgen, W. F. Cummins, B. G. Logan, A. W. Molvik, W. E. Nexsen, T. C. Simonen, B. W. Stallard, and W. C. Turner, "Stabilization of a Neutral-Beam-Sustained, Mirror-Confined Plasma," *Phys. Rev. Lett.* 35, 1501 (1976).

3-16. D. E. Baldwin, H. L. Berk, and L. D. Pearlstein, "Turbulent Lifetimes in Mirror Machines," *Phys. Rev. Lett.* 36, 1051 (1976).

3-17. H. L. Berk and R. R. Dominguez, *Variational Method for Electromagnetic Waves in a Magneto-Plasma*, Lawrence Livermore Laboratory, Rept. UCRL-78607 (1976).

3-18. R. C. Davidson, N. T. Gladd, C. S. Wu, and J. D. Huba, "Influence of Finite-B Effects on the Lower-Hybrid-Drift Instability in Post-Implosion θ Pinches," *Phys. Rev. Lett.* 37, 750 (1976).

3-19. R. H. Cohen, Lawrence Livermore Laboratory, private communication (1977).

3-20. M. E. Rensink, Lawrence Livermore Laboratory, private communication (1977).

3-21. A. C. Riviere, "Penetration of Fast Hydrogen Atoms into a Fusion Reactor Plasma," *Nucl. Fusion* 11, 363, (1971).

3-22. R. H. Cohen, G. Rowlands, and J. H. Foote, UCRL preprint 78889, (Dec. 1976).

3-23. D. J. Rose, *Feasibility of Power by Nuclear Fusion*, Oak Ridge National Laboratory, Rept. ORNL-TM-2204 (1968).

3-24. C. L. Longmire and M. N. Rosenbluth, *Ann. Phys. (N.Y.)* 1, 120 (1957).

3-25. D. J. Rose and M. Clark, *Plasmas and Controlled Fusion Research*, Wiley, N.Y. (1961), p. 221.

3-26. B. A. Trubnikov and V. S. Kudryavtsev, "Plasma Radiation in a Magnetic Field," in *Proc. 2nd U. S. Conference on Peaceful Uses of Atomic Energy, Vol. 31*, (United Nations, Geneva 1958), p. 93.

3-27. W. E. Drummond and M. N. Rosenbluth, "Cyclotron Radiation from a Hot Plasma," *Phys. Fluids* 3, 45 (1960).

CHAPTER 4. MECHANICAL DESIGN ASPECTS OF A TANDEM MIRROR REACTOR

W. L. Hogg, Jr.

SUMMARY

The new concept for a mirror fusion power plant, the tandem mirror reactor (TMR), calls for two plugs of dense plasma at either end of a central solenoid cell. A blanket design for the central cell is presented. Because of their linear, axisymmetric geometry, blanket modules can be permanently mounted on crawler tracks and serviced by remote welding and handling machines of very simple design. Three blanket designs are considered; the best, presented in some detail, has lithium as the breeder material and is helium-cooled.

The plug magnet must have high field strengths. A novel magnet composed of a simple mirror pair surrounding a small Yin-Yang pair satisfies the physics of the end plugs. Because 1,200-keV beam sources present special problems, methods of voltage standoff, arc damage control, and neutralization are discussed. New secondary containment ideas are presented that allow removable roof sections of balanced design.

INTRODUCTION

In a new concept for a mirror fusion reactor proposed by Fowler and Logan[4-1] and Dimov *et al.*,[4-2] the power output comes from a central, axisymmetric solenoidal cell of length appropriate to the desired total electrical power of the reactor. Losses from the ends of the central cell are prevented by a dense plasma plug at each end.

Each plug requires a Yin-Yang or Baseball coil having a low mirror ratio but a field strength in the 16-T to 20-T range. Neutral-beam injection is required to maintain the plug plasma; our calculations indicate that the best injection energy is 1,200 keV. The ambipolar potential of each plug provides electrostatic stoppering for central-cell ions and allows reactor designs with large values of Q (fusion power/injected power). The field strength of the central-cell solenoid is about one-tenth that of the plugs, well within today's superconducting-magnet technology.

Fusion reactor designs abound. The fusion community appears to agree that a demonstration reactor must be presented in about two decades. Any new approach to plasma containment must stand firm before the question, "Can a mechanically and operationally reasonable power reactor be designed using this physics concept?"

The Tandem Mirror Reactor stands up well to this engineering critique. The central-cell technology is largely state-of-the-art. Only in the consideration of first-wall life

are we forced to admit that our projections are uncertain; however, we note that the wall loading of 2 MW/m^2 is about the same as that in other fusion reactor designs. Only the construction of a reactor will allow design data to be obtained. In all other areas of design, the construction and successful operation of similar equipment have been accomplished by others and/or ourselves. General Atomics has operated a reactor cooled by helium gas. Lawrence Livermore Laboratory (LLL) and other laboratories have operated large superconducting coils in the 2-T regime. The Apollo space capsules were welded automatically by the same methods proposed here. Remote assembly tools of greater complexity than needed here have seen service in several fission-power plants.

CENTRAL-CELL BLANKET MODULE

Design, Installation, and Replacement

This solenoidal, axisymmetric portion of the reactor is probably the simplest to construct and service of any fusion reactor design yet proposed. The total length is 100 m, and that is composed of 36 blanket modules, each 2.78 m thick and weighing ~620 tonne.

Each blanket module has the following components:

- Vacuum wall cylinder with weld flanges,
- Superconducting solenoid coil in its vacuum jacket,
- Support frame,
- Main helium supply and return ring-manifolds and distribution pipes, and
- Blanket/shield segments (24 per assembly).

All items except the blanket/shield segments can be assembled outside the main access door and conveyed into location on air pallets. The weight prior to blanket/shield installation is approximately 313 tonne. The assembly can then be completed inside the central-cell bay using the automatic tools described below.

Each module (see Fig. 4-1) is permanently mounted on a "crawler" transporter of the type now used to transport reactor pressure vessels and other heavy items. The motor-driven crawler can move the blanket module about 12 m perpendicular to the cell axis after two circumferential welds joining the module to its neighbors have been ground off and the two helium manifolds disconnected. A guide I-beam (part of the building structure) prevents the module from toppling while in the service position. The weld is removed and rejoined by a "skate" that is remotely and automatically driven around the cell circumference. A very similar

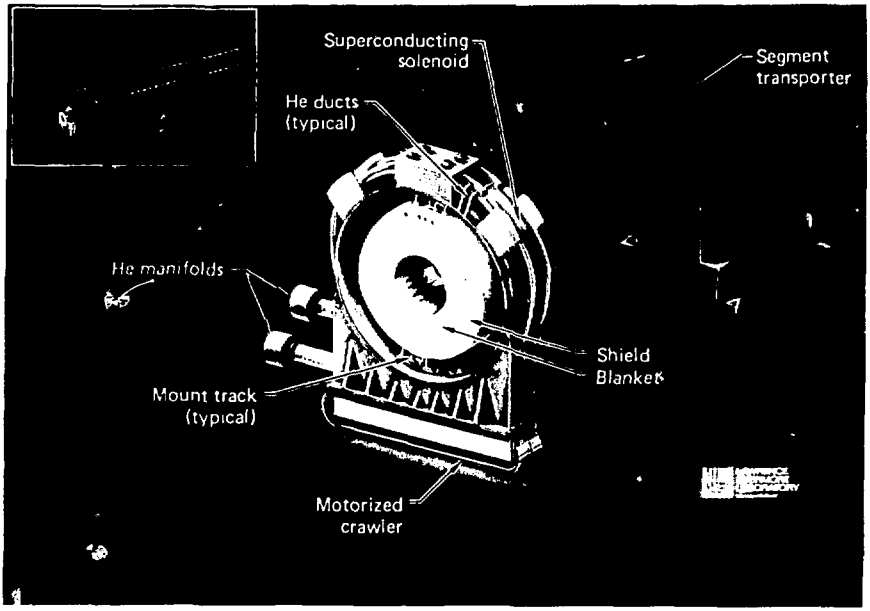

Fig. 4-1. Blanket module for the TMR.

system was used by Skiaky Bros. Inc.[4-3] in welding the Apollo re-entry capsule.

After being withdrawn from the solenoid, the blanket module is approached from each side by remote servicing machines. On one side, a machine removes helium manifold welds (and re-welds during re-assembly). On the other side, a rotating fork indexes to the particular blanket section being removed and withdraws it from the mounting slots fixed to the cylindrical vacuum wall.

The blanket module is divided into 24 identical, wedge-shaped blanket/shield segments. Removed blanket/shield segments are delivered by the fork assembly machine to a conveyor for transport to a hot-parts storage and processing area where blanket and shield can, in due time, be separated. The shield can be reused. Old blanket components are removed in special railroad cars for appropriate disposal.

An alternate method for replacing the blanket module, which will be considered in future refinements of this reactor, is replacement of a complete 620-tonne module. At this time, maneuvering such an unstable

mass to an exit door and then reversing the process with a new module seems unnecessary and fraught with difficult design problems affecting what now is a simple building structure.

Energy Conversion in the Blanket/Shield Segments

There are many ways to build a blanket/shield for use in fusion-neutron energy-conversion. The following simple and most obvious were selected for comparison:

- Liquid lithium circulated to a heat exchanger.
- Quasi-static liquid lithium slowly circulated only to remove bred tritium and cooled by helium carried in buried pipes.
- A static breeder — such as lithium aluminate, lithium beryllate, or liquid lithium — cooled by high-pressure helium gas.

Circulated Liquid Lithium. We considered using liquid lithium circulated to a heat exchanger as one technique for converting fusion-neutron energy. Figure 4-2 shows a possible design. We found two major drawbacks to this technique:

- The electrical power required to drive the lithium-circulating pumps, and
- The required purging, special valves, and auxiliary heating systems.

The chief obstacle to flowing lithium results from the magnetohydrodynamic (MHD) pressure drop required to force the conducting fluid across magnetic field lines. Every gram of lithium must flow twice across the solenoid flux. The space occupied by the coil is two-thirds of the module length; the weld flanges and welding skate take much of the remaining space. The resulting diameter of the channel in which the lithium flows from the manifold ring to the blanket segment is 15 cm, and the resulting flow velocity is 0.24 m/s. Using this value, we evaluated the lithium circuit for MHD pressure drop:

$$\Delta P_{MHD} = \sigma_{\ell} L V B_c^2 \frac{c}{1+c} \quad 235 \text{ psi},$$

where

σ_{ℓ} = 3.05(10)6 mhos/m conductivity of lithium

L = flow length,

V = flow velocity,

B_c = magnetic field strength perpendicular to flow,

c = [σ_{wall} × (wall thickness)]/[$\sigma_{lithium}$ × (radius of flow channel)]

When the MHD and hydraulic pressure drops are summed,

MHD ΔP	235 psi
Hydraulic ΔP	50 psi
Total circuit ΔP	285 psi

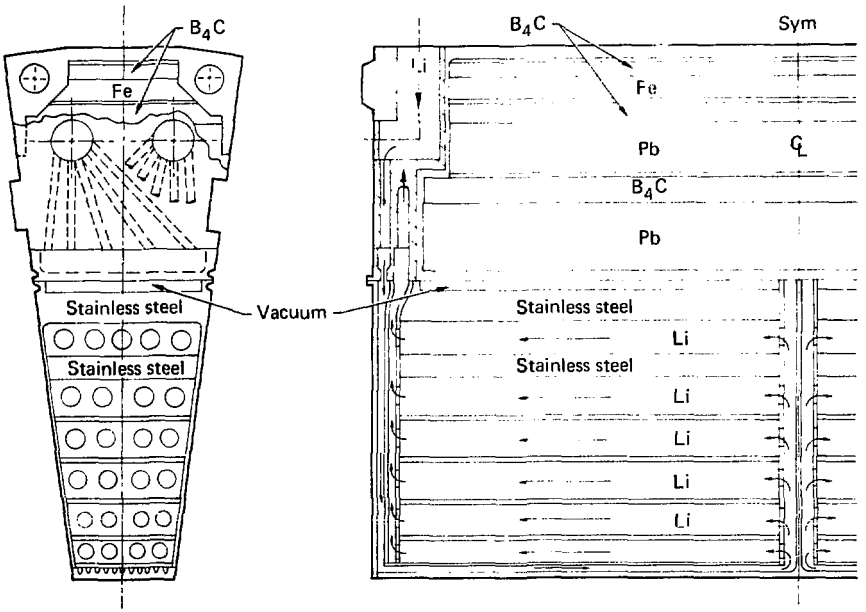

Fig. 4-2. Possible design for a circulating-lithium blanket/shield segment. Arrows show lithium flow.

the total is equivalent to about 15 MW of electrical power needed to drive the lithium circulating pumps, or 1.5% of the net electricity output of the plant.

Although large, that amount of power is not what caused us to choose another system. The main factor influencing the decision was the requirement for elaborate purging and valve systems and large auxiliary heater systems. These systems would be necessary for valving-off and subsequent decoupling of large lithium supply and return ducts, removing blanket segments, and preparing for lithium circulation after reassembly, all procedures that require opening internal piping in the blanket module assembly.

Quasi-Static, Helium-Cooled Lithium. The second system considered was one in which slowly circulated, helium-cooled lithium would remove only bred tritium. It was reasoned that the plumbing problems could be greatly reduced by reducing line size and circulation rate to those necessary to hold the tritium inventory of the blanket to about 1 kg. In this technique, a separate cooling circuit

would be used to extract blanket energy. After considering a number of coolants such as Princeton's flibe (a molten salt mixture of F, Li, and Be),[4-4] a separate lithium circuit, and various gases, we concluded that the most reasonable method would be helium gas at about 50 atm.

We studied several mechanical blanket configurations. The most difficult thing to achieve was first-wall cooling with the coldest gas, then subsequent circulation of that gas to the rest of the blanket. Since energy deposition in the space behind the first wall varies with distance from the first wall, the spacing of coolant tubes (or their size) can be varied with distance from the first wall. An example of our calculated results is shown in Table 4-1. These results apply for "hot-spot" lithium temperature of 613°C, a 15°C temperature drop across the tube wall, and a 48°C film temperature drop in the helium film.

Table 4-1. Variation of tube spacing with distance from first wall (2-in. o. d. × 0.040-in.-wall-thickness stainless-steel tubes).

Radial distance from first wall (cm)	Cooling tube spacing (cm)
10	9
25	10.5
40	11.5

Constructing blanket segments using gas-cooled lithium becomes a difficult and costly fabrication problem. Flow patterns are complex, and tube-support bulkheads almost eliminate access for welding. We sought a better solution.

Static, Gas-Cooled Breeder. J. D. Lee *et al.*,[4-5] proposed the third approach to an energy-conversion blanket — use of a solid, tritium-breeding material such as lithium aluminate or lithium beryllate contained in an envelope of thin alloy that would limit tritium permeation. In this design (Figs. 4-3 and 4-4), coolant gas is circulated past the envelope so that it contacts both the outer wall and the alloy tubes that run through the envelope at a spacing appropriate to good heat transfer. A blanket of this design appears reasonable to fabricate and easy to assemble and take apart, and permits simple extraction of the bred tritium.

However, an attempt to use pure lithium aluminate showed that a sufficient breeding ratio could not be obtained. Even addition of a neutron multiplier such as lead did not make lithium aluminate acceptable. Although lithium beryllate would make a good blanket, we did not want beryllium in the design at this time because of limited availability and cost. Lithium alone, encapsulated in

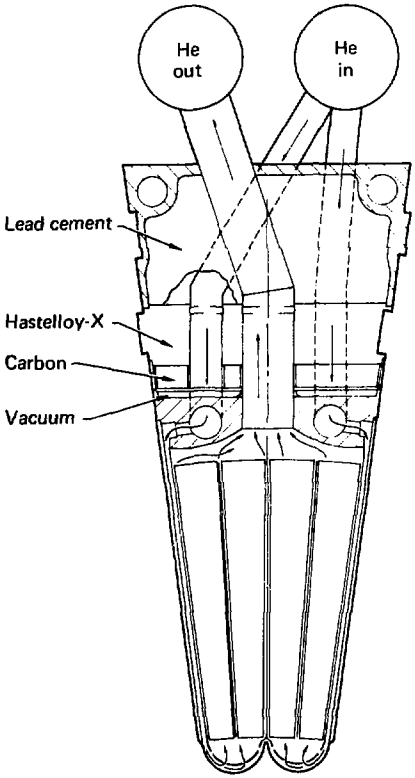

Fig. 4-3. Blanket/shield segment. Arrows show helium flow.

stainless-steel cans, provides an adequate breeding ratio.

Of course, when the neutronics of lithium aluminate were proven poor and pure lithium was selected, the blanket was no longer "solid." However, the concept of a static blanket was retained with helium gas as the coolant for the envelopes in the breeding blanket. Tritium could be removed from such metal envelopes in several ways:

- By allowing tritium inventory to build up in the envelope until blanket replacement time and then processing the extracted breeder envelopes to remove accumulated tritium.
- By slowly circulating helium through capillary tubes contained within the breeding envelope. The capillary tubes would be made of material that permits tritium permeation. As bred tritium permeates into the tubes, the separate helium flushing circuit sweeps it away.

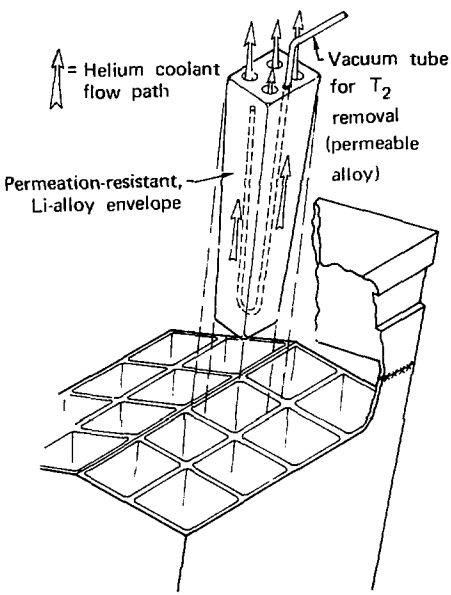

Fig. 4-4. Static lithium container in blanket for TMR. Arrows show flow path of helium coolant.

• By using the permeable capillary tubes suggested above, but merely evacuating the tubes and processing the collected tritium from the auxiliary vacuum system.

The last method appears most attractive economically, but the vacuum conductance of small tubes may be so low that a penalty is paid in higher tritium blanket inventory than the helium flushing method.

Structure of the Blanket/Shield Segments

Our paramount objectives were simplicity of structure, ease of disassembly and change-over, and as a result, low cost of blanket/shield segments.

We plan a vacuum-cast structure with an egg-crate cross section; to it will be welded a curved first-wall of 0.5-cm-thick Inconel 718 sheet and a shield structure enclosing Hastelloy-X plate and lead-cement. The whole assembly will be a pressure vessel for helium at 50-atm, and as such would be exhaustively radiographed around all perimeter walls and welds. Each unit will be subjected to high-temperature pressurization tests at 150% design pressure before installation in a blanket module. Thus, the assembly of the segments to make a full circle does *not* imply that we would rely on side support from adjacent segments while under pressure.

PLUG DESIGN

The magnet used to contain the plug plasma is a more challenging design problem than the basic, low-field solenoid employed by the central cell. The vacuum field required at the center of the plug is 16.5 T, but the vacuum mirror ratio is a modest 1.07. Superconducting materials have been found which, in laboratory samples, show promise of satisfactory performance at the required field strength. A small, 17.5-T coil has already been built.

Figure 4-5 shows the plug coil, a simple mirror pair surrounding a small Yin-Yang coil pair. The total amount of superconducting material required is 5000 tonnes at each end of the TMR. It is not known at this time whether the small Yin-Yang should be superconducting or be made of cryogenic aluminum. Detailed field calculations will determine whether Nb_3Sn wire could be safely operated here or whether the price of normal coil refrigeration should be paid to operate conventional conductors in very high-field regions of the Yin-Yang pair. This geometry looks comparatively attractive from the standpoint of fabrication cost.

In conjunction with this plug magnet, a transition coil will probably be needed to smooth the flux path between the solenoid and the

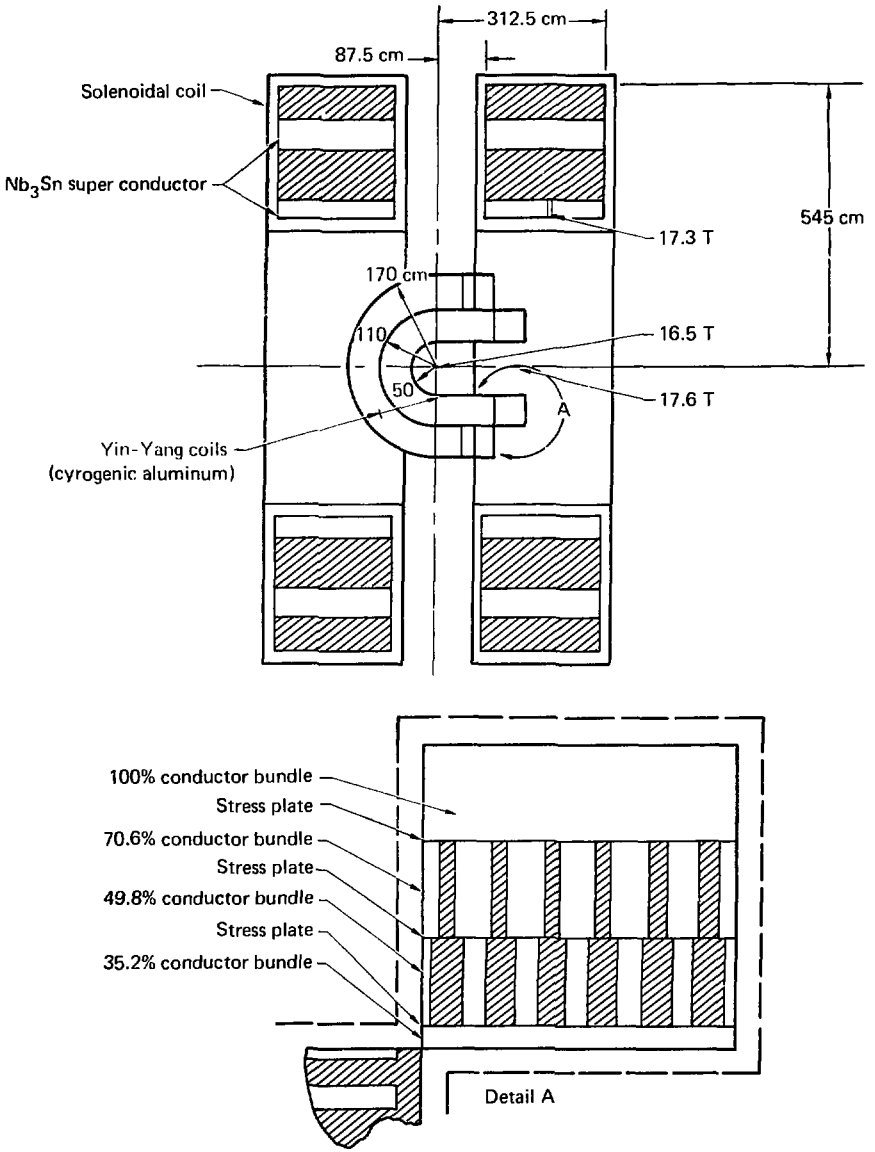

Fig. 4-5. Plug coil set (16.5 T).

plug. The flux bundle emerging from the plug is elliptical in cross section with an aspect ratio of 2.0. The shape of this transition magnet has only been estimated. The flux leaving the plug and entering the direct convertor has this same elliptical aspect ratio (2.0). The orientation of the Yin-Yang pair about the long axis of the machine will be such as to make the long dimension of the exit fan parallel to the building floor at both ends. This has a dramatic effect on the design and cost of the direct convertor.

NEUTRAL-BEAM INJECTORS

The plasma density of the plugs must be maintained by the continuous injection of deuterium ions.[4-6] Magnet shielding requirements will be less severe if no tritium ions are injected into the plug. (There will be tritium present in the plugs, fugitive from the central cell.) The ambipolar property of the plug plasma can be achieved with 1,200-keV deuterium injectors supplying 490 A total into both plugs.

Lawrence Berkeley Laboratory (LBL) is developing sources for neutral-beam injectors for continuous operation at 120 keV. Fifty amperes of pulsed current has been obtained from an extraction grid area 10 cm by 35 cm at a few tens of kilovolts. When the extractor grid cooling problem is solved, we shall be left with only the voltage isolation and spark damage suppression problems. A design for progressive shielding in steps of 200 kV is being developed. Figure 4-6 shows the beam line arrangement with nested shields. Two of these source arrays are planned for each plug. Three of the above described 50-A sources supply the current for each injector.

Spark-down during initial operation of such high-voltage equipment is inevitable. By controlling the energy in the spark it can be advantageous, smoothing out sharp points or edges, minimizing subsequent arcs. To control the spark energy to about 10 J, the shield must be subdivided into areas of a few square meters that must be electrically separated by large lossy elements such as transformer cores or resistors. Careful design will allow a small arc to occur and extinguish before current from adjacent panels can make it through the "choke" to compound the damage at the original arc site. Constant potential during normal operation is assured by electrical continuity.

To accomplish the 1,200-keV ion acceleration, the positive-ion source is held at -600 kV and the ions are

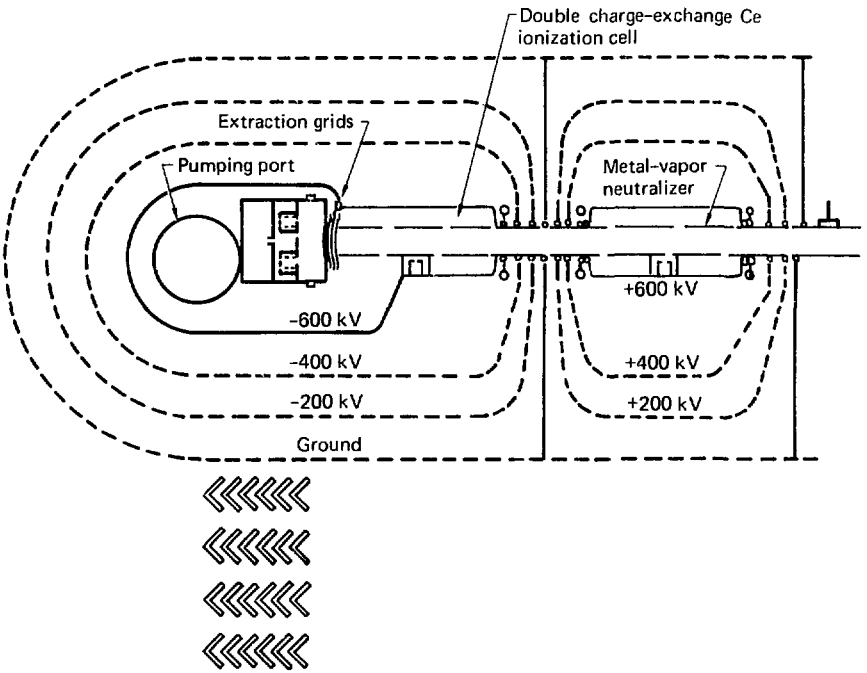

Fig. 4-6. 1,200-keV neutral-beam source.

neutralized in a stripping cell at +600 kV (see Fig. 4-6).

A cesium cell will be used to double charge exchange the positive ions from the source. The D^- ions thus formed can be further accelerated and then neutralized by one of several techniques:

- By laser photodetachment with estimated efficiency about 95%,
- By a metal vapor stripping cell with efficiency approximately 62%, or
- By a high-density plasma-stripping cell using cesium ions with estimated efficiency of 82%.

The laser-photodetachment technique has a serious drawback for this application: the length of a beam source. The cross section of the beam is such that a very large array of lasers and focusing lenses and also a lengthy (thick) photon-reflection region would be required. The total length of a beam source

thus becomes about 25 m, and this has an undesirable effect on reactor and building size and cost. We are evaluating the other two methods, both of which occupy about the same space and reduce the neutralizer length from 10 m to 2 m.

The large pumping loads for a 125-A steady-state beam line can be met by cryopanels on both sides of and parallel to the beam line. Periodically, the panels must be warmed and evolved gas must be pumped out of the system. A bank of tubes, whose centerlines lie in the plane of a wall, is allowed to protrude half into the beam line and half into the vacuum space on the far side of the bulkhead. When loaded with frozen deuterium, the tubes are rotated 180 degrees on their centerlines and are heated. The gas load represented by the frozen deuterium is released into the vacuum space, and the tube is then rotated back to its original position and cryogenically cooled. Conventional diffusion pumps evacuate the volume behind the pumping wall. The source extraction grid imposes a large gas load at the grid end of the beam line. Cryopumps are not used there because of space limitations. Through careful design of the insulator and shield, two large pumping apertures will be provided near the origin of the heaviest gas load, one opening above and one below the vertical column of beam sources.

DIRECT CONVERTER

Not all of the injected beam will be trapped by the plasma plug. It appears that a direct convertor on the far side of each beam line would substantially improve the overall efficiency of the power plant. This convertor will be a single-stage device similar to the venetian-blind convertor proposed by Moir *et al.*,[4-7] and the housing will include cryopump panels sufficient to continuously pump the expected residual beam. The plug plasma will thus have better vacuum environment, and the unavoidable need for a beam dump can be met by proper design of the thermal conversion elements in the direct converter.

When the TMR was first envisioned, we considered using another magnet outside the plug magnet set to recircularize the flux fan. We were motivated by the desirability of an economical cylindrical vacuum tank for the main direct converters. However, as the design for the plugs developed (particularly the 1,200-keV beam sources), another problem appeared that caused a different design to be considered. As mentioned previously, the spark-down damage

problem related to the capacitance of large electrostatic shield surfaces became a great concern. If the direct-convertor grids were subdivided into regions of acceptable capacitance (a few square metres) severe blockage of flux would occur. The structural frame supporting the grid would have to be convectively cooled, and any transformer or choke assembly used to electrically separate such regions would itself block much ion flux. This would further degrade convertor efficiency and create another severe cooling problem.

It seemed best to eliminate all blockage except the grid itself by confining all tensioners and chokes to the annular space around the flux bundle. One could design a circular direct converter to meet this objective, but the maximum length of a grid or vane is less if the flux bundle is elliptical and the length of the vane is parallel to the minor axis. Simply eliminating the outside circularizing magnet allows a flux bundle of elliptical cross section with an aspect ratio of about 2:1 to enter the direct converter. If the minor axis of the ellipse is vertical, and all vanes or grids run in the vertical direction, we can have the shortest, straightest grid structure (see Fig. 4-7).

One must design a vacuum tank to encompass such an elliptical grid arrangement. A membrane of stainless steel periodically anchored to the heavy post-tensioned concrete secondary containment structure can serve as the vacuum vessel. This membrane can also serve as the "form" for the concrete of the containment shell.

CONTAINMENT BUILDING

This TMR is long and relatively slim. The configuration of the containment building differs greatly from any previous power reactor concepts. In size, it approximates a drydock for a large passenger ship. The reactor fits its enclosure more efficiently than competitive designs. Roof spans are limited to about 40 m, and portions of the secondary containment structure can be moved by a large gantry crane. (The same crane is used to install the plug magnets.) No large crane inside the building is required, hence, no lift-space and crane clearance. This is a blessing in reducing the building cost, but the smaller volume exacts a penalty: accident pressures in the building can be higher than designs with large containment shells. We propose pressure relief diaphragms on the direct-converter portion of the vacuum system. They must relieve *inward* to prevent excess pressurization resulting from a primary heat exchange loop accident. The entire reactor vacuum

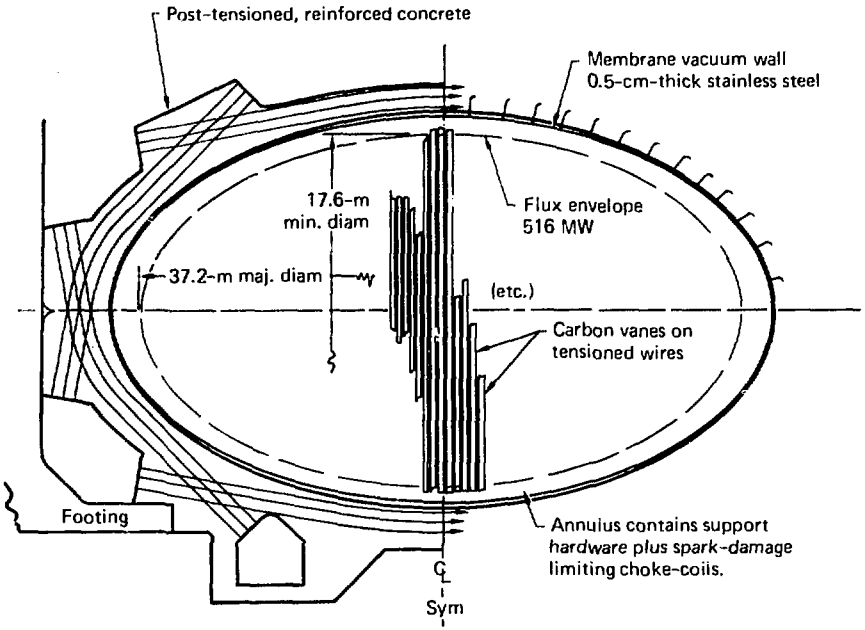

Fig. 4-7. Cross section of TMR at the direct converter. Detail A shows variation of conductor percentage through thickness of coil.

tank then forms part of the containment volume, and the pressure increase can be maintained below 2 atm. These relief diaphragms should be located on the ellipso-conical transitions between the plugs and the direct converters at both ends of the machine.

Any accidental releases of primary coolant must be confined within a secondary containment shell. It has been proposed by ORNL and by researchers in Europe that evacuation of the containment building offers some safety advantages at a negligible increase in cost. Plumbrook Station,[4-8] near Lake Erie, which has been operated successfully by NASA as a test station for space power reactors, is an evacuated building of dimensions quite similar to those proposed for an Experimental Fusion Power Reactor.

An evacuated secondary containment shell presents one significant structural advantage. The side walls and roof of the TMR building are all basically flat plates (with the

possible exception of a slightly arched roof). They can be more economically designed if the pressure differential varies from 1 atm "inward" to 1 atm "outward" rather than from zero to 2 atm in one direction. We plan to size the evacuated containment building so the pressure increase will in no accident circumstance exceed 2 atm. In the case of a 2-atm pressure change, the wall will experience a stress reversal. A reinforced concrete wall can be considerably thinner if designed to meet the reversed load condition. Calculations show that for the same weight of reinforcing steel, only 60% as much wall thickness is required in the case of 1-atm pressure difference in either direction. On a concrete structure of this size, that represents an estimated 20% of the cost of the containment shell.

REFERENCES

4-1. T. K. Fowler and B. G. Logan, *The Tandem Mirror Reactor*, Lawrence Livermore Laboratory, Rept, UCRL-78740 (1976).

4-2. G. I. Dimov, V. V. Zakaidakov, and M. E. Kishinevsky, *Fiz. Plasmy* 2 597(1976).

4-3. P. Tade, Western Region Representative of Sciaky Bros. Inc., Los Angeles, CA, private communication (1977).

4-4. *[illegible]*, R. G. Mills, Ed., Princeton Plasma Physics Laboratory, Rept. MATT-1050 (1974).

4-5. J. D. Lee, W. L. Barmore, D. J. Bender, J. N. Doggett, and J. R. Galloway, *[illegible]*, Lawrence Livermore Laboratory, Rept. UCID-17083, Rev. 1 (1976).

4-6. J. H. Fink, *[illegible]*, Lawrence Livermore Laboratory, Rept. UCID-17303 (1976).

4-7. W. L. Barr, R. J. Burleigh, W. L. Dexter, R. W. Moir, and R. R. Smith, *A Preliminary Engineering Design for a "Venetian Blind" Direct Energy Convertor for Fusion Reactors*, Lawrence Livermore Laboratory, Rept. UCRL-74636, Rev. 1 (1974).

4-8. *Space Power Facility, Description and Capabilities*, NASA Lewis Research Center, Plum Brook Station, Sandusky, Ohio (1974).

CHAPTER 5. DESIGN OF THE COIL SYSTEM FOR THE TMR PLUG

M. A. Peterson

SUMMARY

Each plug coil in the Tandem Mirror Reactor (TMR) is a hybrid superconducting and cryogenic magnet set consisting of a cryogenic-aluminum Yin-Yang magnet placed within a niobium-tin solenoidal pair. The strength of the central vacuum magnetic field of the plug coil is 16.5 T, and its vacuum mirror ratio is 1.07. The niobium-tin superconducting solenoids have an inside diameter of 5.8 m and an outside diameter of 11 m. The magnetic forces of these coils are restrained by periodic bands of stainless steel. The cryogenic-aluminum Yin-Yang magnet is about the size of the magnet for the Mirror Fusion Test facility (MFTF) and produces a field of about 1 T which adds to the field produced by the solenoids. The resistive heating in the Yin-Yang magnet is 0.25 MW, which requires about 12 MW of refrigeration power. Structural integrity of the Yin-Yang magnet requires a layered construction of pure-aluminum conductor plus aluminum-alloy columns and stress plates to transfer the magnetic forces to an external clamping structure.

INTRODUCTION

General Description of the Plug Coil Design

Figure 5-1 shows the preliminary design of the TMR plug coil. In addition to the high-field design $|B_0|$ = 18 , design ($|B_0|$ = 18-T) shown in Fig. 5-1, two lower-field cases ($|B_0|$ = 16.5 T and $|B_0|$ = 15 T) were developed from the high-field case by suitably scaling down the winding current. Although the intermediate — field strength ($|B_0|$ = 16.5 T) was eventually selected as the point value for the TMR reactor study, primary emphasis throughout the development of the preliminary plug coil design was placed on the high-field case ($|B_0|$ = 18 T) in order to define and explore the design problems that limit the attainable field strength in the plug coil system.

The plug coil system uses a relatively small Yin-Yang coil pair with a square conductor cross section located inside two solenoid coils to generate a shallow minimum-$|B|$ well (mirror ratio R = 1.07). The solenoid coils are superconducting; the Yin-Yang coil set carries about 12% of the total current in the plug coil system, while the superconducting solenoid windings carry the remaining 88% of the total current. The solenoid coil is separated into two winding layers, each with its own external, structurally independent support structure. This support structure carries the principal component of the magnetic force, which is directed radially outward, in tension. Depending on the stress and/or strain

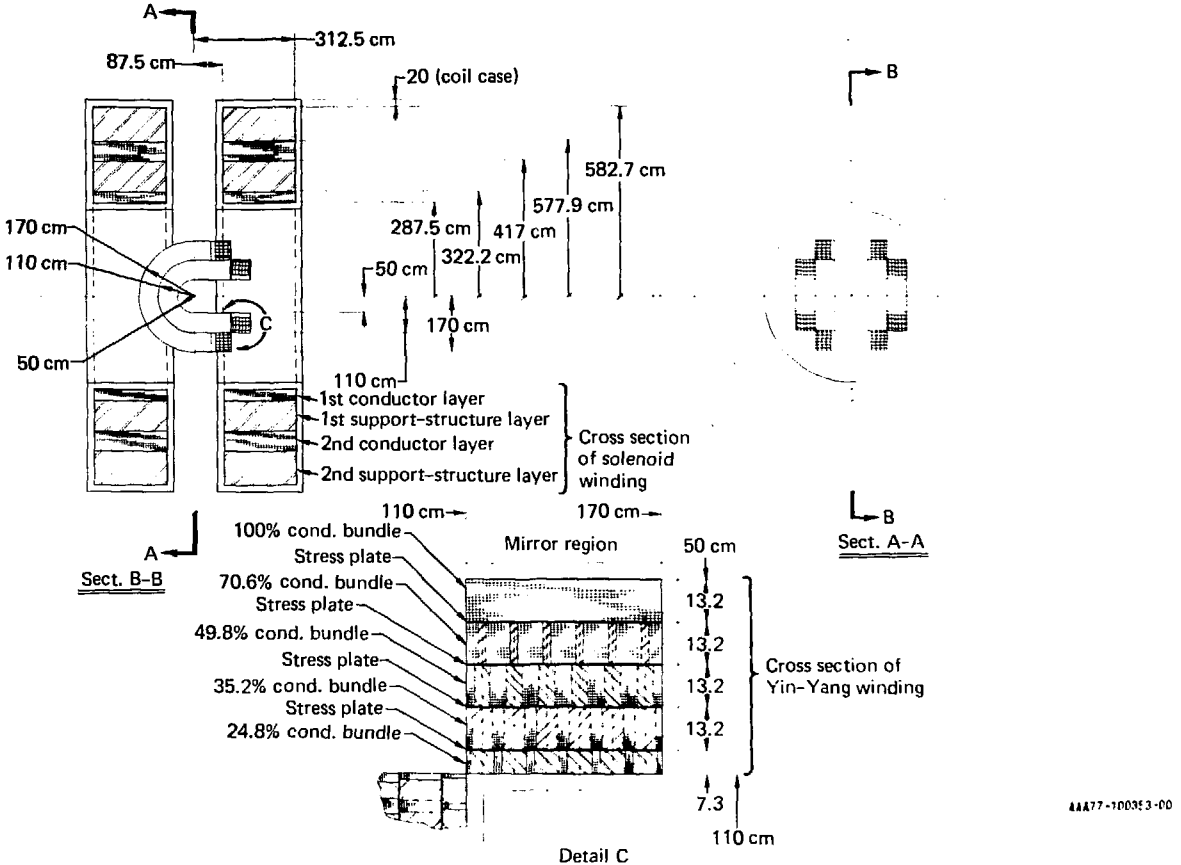

Fig. 5-1. Preliminary design of the 18-T coil bundle for the TMR plug coil.

limits of the copper-stabilized, Nb_3Sn superconductor, the inner support structure may have to be prestressed. The maximum allowable current density in the winding of the superconducting solenoid is determined by requiring that cryostatic stability be maintained locally throughout the winding. The detailed conductor configuration used in the cryostatic stability analysis is based upon the conductor design proposed for the MFTF.[5-1]

The Yin-Yang coil (Fig. 5-1) incorporates an internal support structure that transmits to an external structure the magnetic forces distributed over the conductors. The internal structure is necessary to limit the compressive stress on the relatively weak, high-purity aluminum conductors. As discussed later in this chapter, in this report we do not consider the external structure supporting the Yin-Yang coil pair.

The cryogenic, high-purity-aluminum conductor is convectively cooled by gaseous helium pressurized to about 4 atm. Although it appears to present a formidable design challenge, the design of a manifolding system for the helium coolant has not been considered thus far in this preliminary study.

Design Considerations

Before beginning a detailed discussion of the design of the TMR coil system, we shall review several important conclusions that emerged from the iterative search for a coil design.

If very high magnetic field strengths are desired (>20 T), coil systems incorporating both superconducting and cryogenic-aluminum conductors appear necessary for the following reasons:

- The critical current density of available superconducting materials is quite low at high flux densities, and
- The refrigeration power for a coil system composed entirely of cryogenic aluminum is prohibitive.

Thus, if field strengths above about 20 T are specified, the coil winding would probably incorporate cryogenic aluminum in the portion of the winding where the field strength was very high ($|B| \gtrsim 20$ T), whereas the remainder of the winding would be superconducting in order to minimize the refrigeration power required. Because of the extremely large magnetic forces generated by the high field strengths and the relatively low yield stresses of the conductor materials — especially the high-purity aluminum used in the cryogenic-aluminum conductor ($\sigma_{yp} = 1 \times 10^8$ N/m^2, 14.5 ksi) an internal structural system is required to transmit the magnetic forces through the winding itself to an external structure supporting the Yin-Yang coils. The choice of

materials for the internal support structure is severely limited by the wide temperature range from the room-temperature environment in which it is assembled to its cryogenic operating temperature. Thus, the material from which the internal coil structure is constructed must be selected on the basis of having a thermal expansion coefficient compatible with the conductor material rather than for maximum strength. As with the conductor yield stress previously mentioned, this limitation on the material used in the internal structure is much more serious for cyyogenic aluminum windings (aluminum-alloy structure ($\sigma_{yp} \approx 3.4 \times 10^8$ N/m^2, $\approx$ 49.2 ksi) than for the copper-stabilized superconducting windings (stainless-steel structure, $\sigma_{yp} \approx 6.9 \times 10^8$ N/m^2 $\approx$ 100 ksi).

When we sized the internal structure by the analysis described later in this chapter, and when we assumed reasonable current density values within the conductor itself, it became apparent that the large amount of conductor displaced by the internal structure severely limited the average current density [current density averaged over the cross section of the entire winding (conductor and internal structure)] that could be realized.

An economic analysis of the entire TMR reactor system[5-2] indicates that the central field strength must be maintained as high as possible if the relative cost [$/kW(e)] of the TMR system is to be reasonable. There is a clear economic incentive towards high central field strength and low mirror ratio in the plugs. Experiments in 2XIIB suggest that a plasma can be confined by a mirror-ratio of a few percent.

Although the preliminary design described in this report ($R \approx 1.07$) certainly does not represent the highest possible mirror ratio design with adequate central field strength ($|B_0| \gtrsim 15$ T), it should be emphasized that the increased conductor field strengths resulting from even relatively small increases in the mirror ratio will render the design of a viable coil system much more difficult.

The configuration of the internal structure and the local current density in each layer of the winding depend upon the magnetic field strength throughout the winding volume and upon the winding geometry. Since the magnetic field is itself dependent upon the geometry of the coil system, the configuration of the internal structure, and the local current densities within the winding, the development of a coil system design in which the average current densities used in the magnetic calculations are consistent with the local maximum current densities limitations in the

conductor is an iterative process. To develop the coil system design presented in this chapter, we first developed a "first-cut" coil geometry with suitable magnetic parameters based upon an assumed value of the average current density. Then, with the coil geometry and field strengths determined from the first-cut design, we calculated the actual value of the average current density from the local maximum allowable current density values in the conductor. If the assumed values of the average current densities were significantly different than the calculated achievable values based on local conductor limits, another iteration was made by altering the initial first-cut coil geometry.

The coil design presented in this chapter represents a preliminary design whose magnetic parameters fall within the magnetic design goals and whose bulk current densities closely approximate the maximum allowable current density values calculated from the preliminary analyses also described in this chapter. Thus, while further changes will probably be required when a more detailed analysis is made, the coil design presented here should provide a reasonably self-consistent picture of a viable TMR coil system.

In the remaining portion of this Introduction, we shall briefly discuss several key aspects of this preliminary TMR coil design that requires more investigation.

Unfinished Business

Although the solenoid coil must be superconducting in order to limit the refrigeration power required, the relatively small share of the current carried by the Yin-Yang coil winding permits the use of cryogenic-aluminum conductors. Although cryogenic-aluminum Yin-Yang conductors were initially chosen because of their capability for relatively high current densities at high field strengths, it may be feasible to use superconductors for both the Yin-Yang and solenoid coils. However, the very strong, spatially uniform, magnetic fields present throughout the volume of the Yin-Yang coil windings limit the average current density achievable in a coil that incorporates superconducting conductors. Although achieving the desired current densities may be difficult with superconducting windings, their potential advantages — reduced refrigeration power requirements, reduction in the relative size of the internal structure (stronger conductor and structural material), and a potentially simpler cooling system — provide a strong incentive for investigating their feasibility.

If further investigation eliminates the superconducting Yin-Yang option, a substantial design effort would be

required to verify the feasibility of a cryogenic-aluminum, Yin-Yang coil system. Because of the limited time available, only the magnetic, structural, and internal thermal design of the aluminum Yin-Yang coil have been considered here. Since the thermal analysis (see subsequent discussion under "Thermal Analysis of the Cryogenic Yin-Yang Coil") indicated that many relatively short coolant passages would be required, the development of a coolant manifold design that is compatible with structural, electrical, and construction requirements may be quite difficult. To fully validate the feasibility of a cryogenic-aluminum, Yin-Yang coil option, we must develop a coil winding design, including electrical connections and coolant manifolds, that is compatible with the internal structure and coolant passage configurations described later in this chapter. Since the design of the electrical and coolant passages involves consideration of fine-scale, local aspects of the winding design, a fully feasible aluminum Yin-Yang coil design must be rather detailed, and thus requires a substantial design effort.

Thus far in this design study, we have not considered the external structure required to support the Yin-Yang coil winding because, in contrast with past reactor coil systems, it does not appear to present a particularly difficult design challenge. Several different factors have contributed to the simplification of the coil support structure for the TMR reactor concept relative to past reactor designs. Because of the low TMR mirror ratio ($R = 1.07$), the nearly cylindrical plasma volume (approximately defined by the mirror-to-mirror extension of all the field lines passing through the last closed surface of constant $|B|$) fills only a relatively small central portion of the mirror region of each Yin-Yang coil. Thus, a large portion of the major arcs (Fig. 5-1) of each Yin-Yang coil can be locally supported by a tension structure connecting the upper and lower coil winding. This contrasts with previous Yin-Yang designs in which structural material was excluded from a large portion of the mirror by the fan regions of the plasma volume. In addition to the large portion of the mirror region available for structure, the small size of the Yin-Yang coil winding relative to the solenoid winding surrounding it appears to allow ample space external to the Yin-Yang coil set for a supporting structure.

In any further design work on the TMR plug coil system, considerable emphasis should be placed on determining whether the solenoid coil structure requires prestressing, and

if so, how to do it. To determine the need for prestressing the solenoid coil structure, its stress state must be more precisely defined through a more detailed structural analysis, and the maximum allowable conductor strain limits must be clarified from a wider range of experimental data. If prestressing is required, a preliminary structure design incorporating the desired amount of prestressing should be developed.

In the remaining sections of this chapter, the assumptions, design models, and calculations upon which this preliminary design is based are discussed in greater detail. First, we discuss the magnetic design of the TMR plug coil system shown in Fig. 5-1. Then we review the design of the superconducting solenoid winding conductor and its supporting structure. Finally, we discuss the design of the conductor and the internal support structure for the cryogenic-aluminum, Yin-Yang coil pair.

MAGNETIC DESIGN

The preliminary plug coil design developed to meet TMR magnetic design goals ($1.05 \lesssim R \lesssim 1.10$; $|B_0| \gtrsim 15$ T) is shown in Fig. 5-1. This system utilizes a relatively small Yin-Yang coil set with a square conductor cross section located inside two solenoid coils to generate a shallow minimum-$|B|$ well. The solenoid coils are superconducting; the Yin-Yang coil sets uses cryogenic-aluminum conductors. The Yin-Yang coil set carries about 12% of the total current in the plug coil system, and the superconducting solenoid windings carry the remaining 88% of the total current.

The solenoid coils are separated into two layers of windings, each with its own external support structure.

Although it is not shown in Fig. 5-1, the solenoid windings are subdivided into five layers of conductor, each with a different current density and superconductor-stabilizer ratio (see Fig. 5-4, Table 5-2). The Yin-Yang coil (detail, Fig. 5-1) incorporates an internal support structure that transmits the magnetic forces distributed over the conductors to an external structure. The internal structure is necessary to limit the compressive stress on the relatively weak pure-aluminum conductors. As discussed later in this chapter, in this report we have not considered the external structure supporting the Yin-Yang coil pair.

The geometry and magnitude of the magnetic fields generated by the plug coil design were evaluated with the computer code EFFI. To simplify the magnetic calculations, the Yin-Yang conductors shown in Fig. 5-1 were simulated by a number of circular arc

conductors with the same external dimensions, but with the complex internal structure and coil bundles replaced by a homogeneously distributed, average current density. Because the local value of the current density within the cryogenic-aluminum conductor is constant, and because the inner conductor layers (those nearest the mirror region) of the Yin-Yang winding have less conductor displaced by the internal structure, the constant current density approximation should tend to slightly underestimate both the mirror field strength and the mirror ratio.

The solenoid coils were modeled by constant current density conductors with the dimensions given in Fig. 5-1 for each conductor layer. Since in the actual solenoid winding the current density increases radially outward through the winding (lower field strength, higher critical current density) the constant current density approximation over-predicts the strengths of the mirror and central fields. This was confirmed, and we used a magnetic calculation performed with the correct current density distribution in the solenoid winding to determine that the error was less than 2%. We found that the average current density values initially chosen for the solenoid ($J = 3000\ A/cm^2$) and for the Yin-Yang coil ($J = 2337\ A/cm^2$) were in reasonable accord with the maximum allowable current density value determinations described later in this chapter. Thus, at least for a preliminary design study, no further iterations are necessary on the plug coil system design shown in Fig. 5-1. Table 5-1 lists the EFFI-compatible input data required to specify the geometrical configuration of the four circular loop conductors and the eight circular arc conductors used to simulate the plug coil system.

The magnitude of the axial magnetic field strength along the z-axis of the coil system as calculated by EFFI is displayed in Fig. 5-2 superimposed on the outline of the conductor cross sections in the xz-plane (from Fig. 5-1). From this plot, it may be seen that the central field strength is very close to 18 T and the mirror ratio is about 1.07.

Since past experience with similiar geometries has shown that for such small mirror ratios the existence of a minimum-$|B|$ well cannot be taken for granted, we used EFFI to obtain a plot of contours of constant field strength in the central plasma region. From the contour plot shown in Fig. 5-3, it appears that a closed, minimum-$|B|$ well does exist, although it is very small (radial mirror ratio $\lesssim 1.002$). Since the solenoid coil is superconducting, the magnitude of the field within the winding is of considerable interest. Since (unlike

Table 5-1. TMR plug coil system/EFFI input.

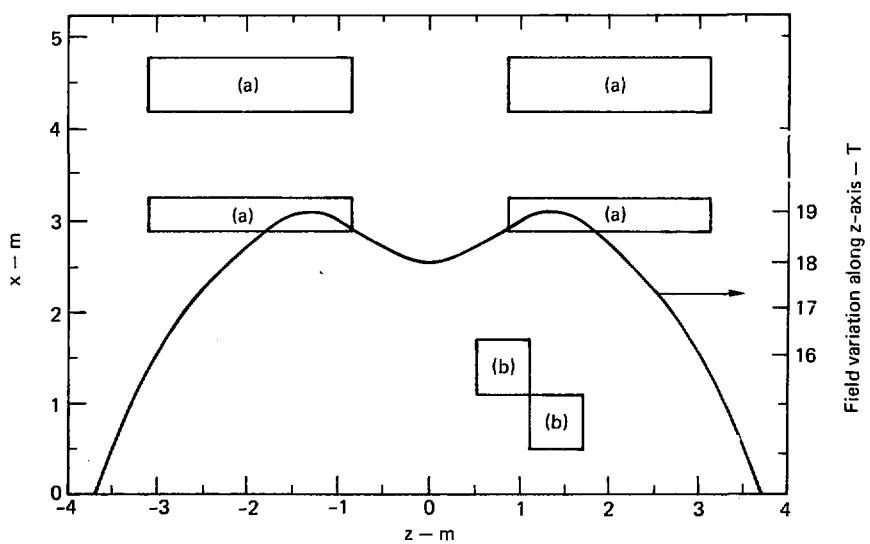

Fig. 5-2. Plot of on-axis magnetic field strength |B|. Items (a) are cross sections through the solenoid winding; items (b) are cross sections through the Yin-Yang winding.

the fields in the central plasma region) the field strength within the solenoid winding itself is sensitive to the actual details of the current density distribution, we calculated the field using the actual current density distribution determined later in this chapter.

The plot of constant field strength contours across the solenoid winding obtained with the actual current density distribution is shown in Fig. 5-4. From the values of the contours in Fig. 5-4, it can be seen that the peak field strength within the solenoid winding is actually less than the mirror field strength (17.8 T vs $|B_{mp}|$ = 19.2 T) because the magnetic flux vector components generated by the solenoid and by the Yin-Yang coil are oppositely directed in the region of the solenoid.

To investigate the effects of lowering the central field strength while maintaining an approximately constant mirror ratio, we developed

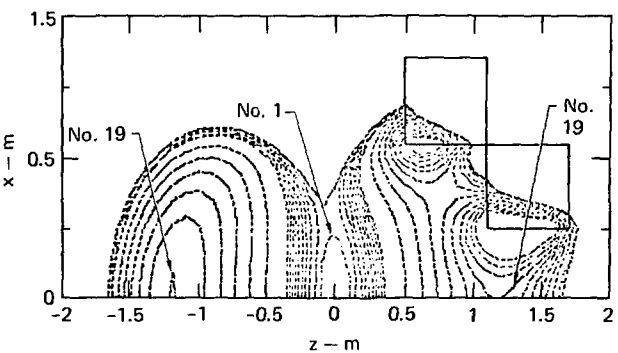

Contour No.	|B| value (T)
$\|B_0\|$	18.036
1	18.054
2	18.072
3	18.090
4	18.108
5	18.126
6	18.144
7	18.162
8	18.180
9	18.198
10	18.216
11	18.396
12	18.577
13	18.757
14	18.937
15	19.118
16	19.298
17	19.473
18	19.659
19	19.836

Fig. 5-3. Constant field strength contours of the minimum-|B|well.

two additional design cases based upon the coil system shown in Fig. 5-1. In these two design cases, all the field strengths were reduced by scaling down the total current in the solenoids and in the Yin-Yang coil set. In the first case, the currents were reduced by 20% to yield a central field strength of 16 T; in the second case, a 10% reduction in the currents and fields yielded a central field strength of 16.5 T.

Although this linear scaling of the field with the winding currents is strictly correct only if the geometry of the coil system is unaltered, the reduced currents in the solenoids were obtained by reducing the radial thickness of the solenoid winding rather than the current density. Thus, the magnetic parameters of these two additional cases as determined by linear scaling from the original high field strength case are not exactly

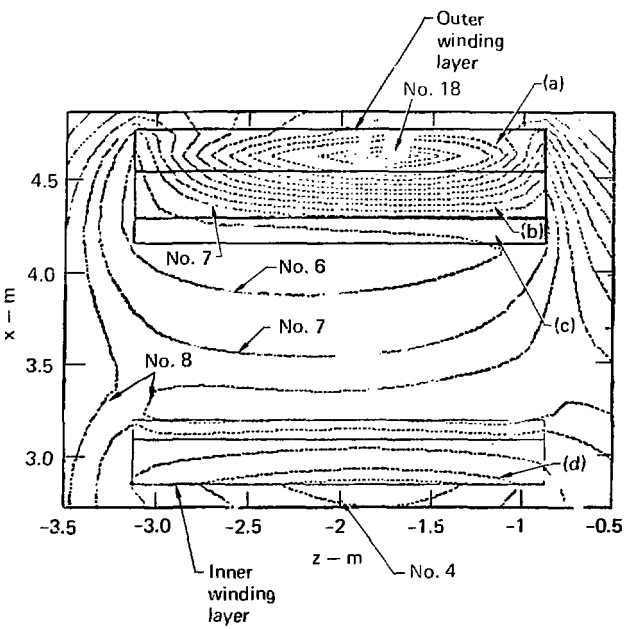

Contour No.	|B| value (T)
1	19.961
2	19.100
3	18.060
4	17.109
5	16.159
6	14.258
7	12.357
8	11.406
9	18.456
10	95.050
11	85.550
12	76.040
13	66.540
14	57.030
15	47.530
16	28.520
17	19.010
18	95.000

Fig. 5-4. Constant field-strength contours across the solenoid winding for the actual current-density distribution. Item (a) is the conductor layer at j_4, item (b) the conductor layer at j_3, item (c) the conductor layer at j_2, and item (d) the conductor layer at j_1.

correct. However, the small relative magnitude of the cross-sectional changes and the distant location of the solenoid winding from the central plasma region should cause the error resulting from the altered radial thickness of the solenoid winding to be insignificant.

SUPERCONDUCTOR DESIGN

In the initial design of the two identical solenoid coils used in each plug coil system (Fig. 5-1), we assumed that we could achieve a bulk average current density J (averaged over the superconductor and copper stabilizing material for the entire cross sectional area of the winding) of approximately 3000 A/cm^2. This value was not based directly on any particular calculations, but rather represented a first guess of what should be possible using Nb_3Sn superconductor at the contemplated field strengths.

For a particular desired value of the central field strength and a given superconductor, the bulk average current density that can actually be achieved depends upon the strength of the magnetic field throughout the entire conductor. Since the magnetic field strength can not be determined without specifying the geometrical configuration of the entire coil system and an assumed current density, an iterative process is necessary if the bulk average current density value initially assumed is much different than the actual allowable value. In addition, since the structural analysis of the solenoid coil is based on the initially assumed value of the average current density, a substantial change in that value would also render the structural analysis inconsistent. However, if the initially assumed current-density value can actually be achieved, the plug coil system shown in Fig. 5-1 will be capable of generating the calculated central field strength of 18 T.

Since the two lower field strengths cases considered in the magnetic design section ($|B_0|$ = 15 T and $|B_0|$ = 16.5 T) were developed by reducing the radial thickness of the solenoid winding while maintaining the current density used in the high-field case ($|B|$ = 18 T, J = 3000 A/cm^2), their viability will also be assured if the initially assumed current density can actually be achieved. Since the following analysis will indicate that the bulk current density value initially assumed is indeed viable, an iterative redesign is not required, and the plug coil design shown in Fig. 5-1 is an acceptable preliminary design.

In this analysis, we assume that the bulk average current density of the superconducting solenoid is determined by the requirement that all the

conductors in the winding be cryostatically stable. The cryostatic stability criterion requires that at any point along the conductor the natural convective heat-transfer rate to the helium coolant must be sufficient to transfer the Joule dissipation power resulting from having current locally flow in the copper stabilizing material. Since this criterion applies locally at each point along the entire length of every conductor, we must begin the determination of its effect on the bulk average current density by locally examining a single conductor.

The cryostatic stability criterion can be formulated analytically in terms of a generalized conductor design (rectangular cross section defined by d and b, Fig. 5-5) by imposing the requirement that the Joule dissipation (δP) in an incremental length ($\delta \ell$) of conductor be equivalent to the thermal power (δP_c) removed from the conductor surface [$2d(1 + b)\ \delta\ell$] by the helium coolant. With the conductor geometry specified by the dimension of its largest side d, its aspect ratio b, and the fraction of its cross-sectional area occupied by each conductor component (copper stabilizer f_{cu}, superconductor f_{sc}, coolant f_{he} and insulation f_{in}, Fig. 5-5), the Joule dissipation induced by the entire conductor current flowing in the copper stabilizer is given by the following expression:

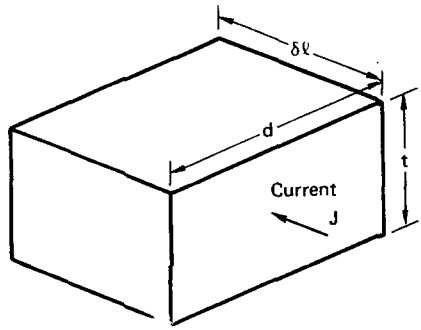

Fig. 5-5. Generalized conductor design, where

b = aspect ratio of cross section = t/d,
d = dimension of largest side,
α = fraction of conductor surface area interfacing with coolant,
f_{sc} = fractional cross sectional area of superconductor $\equiv A_{sc}/A_{tot}$,
f_{cu} = fractional cross sectional area of copper stabilizer $\equiv A_{cu}/A_{tot}$,
f_{in} = fractional cross sectional area of insulator $\equiv A_{in}/A_{tot}$,
f_{he} = fractional cross sectional area of He coolant $\equiv A_{he}/A_{tot}$,
ρ_{cu} = $\rho(|B|, T)$ = resistivity of copper stabilizer
j_{sc} = $j(|B|, T)$ = critical current density in super conductor,
$\bar{q}$ = average heat transfer rate per unit of coolant passage-conductor contact area,

$A_{tot} = A_{he} + A_{sc} + A_{cu} + A_{in}$,
and
$I = f_{he} + f_{sc} + f_{cu} + f_{in}$

$$\delta P = I^2 \delta R = j_{sc}^2 \left(\frac{A_{sc}^2}{A^2}\right)\left(\frac{A}{A_{cu}}\right) \rho_{cu} A \delta \ell$$

$$= j_{sc}^2 \left(\frac{f_{sc}^2}{f_{cu}}\right) \rho_{cu} (bd^2) \delta \ell \quad . \qquad (5\text{-}1)$$

The power δP_c removed from the same incremental conductor by the coolant is given by the following relationship in terms of $\bar{q}$, the average heat transfer rate per unit of coolant passage-conductor contact area and α, the fraction of the conductor surface that interfaces with the coolant passage:

$$\delta P_c = \bar{q}\alpha \left[(2d + 2T)\ \delta \ell\right]$$

$$= \bar{q}\alpha 2d\ (1 + b) \delta \ell \quad . \qquad (5\text{-}2)$$

Since the thermal power removed by the coolant is proportional to the conductor surface area and the Joule dissipation power is proportional to the conductor volume, cryostatic stability can in principle be achieved by reducing the conductor size d. However, pragmatic considerations associated with conductor fabrication and coil winding limit the conductor size to reasonable levels ($d \gtrsim 1$ cm). When the cryostatic criterion is enforced by equating the dissipated power δP, Eq. (5-1) to the thermal power removed by the coolant δP_c, Eq. (5-2), the following relationship is obtained:

$$\frac{f_{sc}^2}{f_{cu}} = \left[\frac{\bar{q}}{\rho_{cu} j_{sc}^2}\right]\left[\frac{\alpha}{d}\left(\frac{1 + b}{b}\right)\right] . \qquad (5\text{-}3)$$

The terms inside the first brackets on the right-hand side of Eq. (5-3) are determined by physical properties of the helium coolant, the copper stabilizing material, and the superconducting material for a particular magnetic field strength and temperature. The geometrical terms inside the second set of brackets are determined by the detailed design configuration of the actual conductor. Thus, when we have chosen a particular conductor design (α, d, b) and determined the appropriate set of material properties ($\bar{q}$, λ_{cu}, j_{sc}), the fractional area of the superconductor f_{sc} and the fractional area of the copper stabilizer f_{cu} must satisfy Eq. (5-3) if the cryostatic stability criterion is to be observed.

From the definitions of the fractional areas (Fig. 5-5) we may use the following relationship to express the fractional area of the copper stabilizing material f_{cu} in terms of the fractional areas of the helium coolant f_{he} and insulation f_{in}:

$$f_{cu} = 1 - (f_{in} + f_{he}) - f_{sc}. \qquad (5\text{-}4)$$

If we assume that the fractional areas required by the helium coolant and the insulation are fixed for a

particular conductor and winding design, we may use Eq. (5-4) to eliminate the fractional area of the copper stabilizing material from the cryostatic stability criterion [Eq. (5-3)]. Thus, for a set of material properties at a particular temperature and field strength and a particular conductor design, the maximum allowable fractional area of the superconductor F_{sc} is locally set by the cryostatic stability criterion.

When Eq. (5-3) and (5-4) are combined and the quadratic rule invoked, the maximum allowable value of the fraction of conductor cross-sectional area devoted to the superconductor is given by the following relationship:

$$F_{sc} = \left\{ \left[\frac{\bar{q}}{\rho_{cu} j_{sc}^2} \right] \left[\frac{\alpha (1 + b)}{bd} \right] \right\} \times \left(-1 + \left\{ 1 + 2 \left[\frac{\rho_{cu} j_{sc}^2}{\bar{q}} \right] \left[\frac{bd}{\alpha(1 + b)} \right] (1 - f_{in} - f_{he}) \right\}^{1/2} \right) . \quad (5\text{-}5)$$

The local value of the conductor current density j at any point along the conductor is given by the product of the superconductor current density and the maximum allowable superconductor fractional area F_{sc} as set by the cryostatic criterion Eq. (5-5):

$$j = j_{sc} F_{sc} . \quad (5\text{-}6)$$

Having determined the allowable local current density in the conductor, we must consider the relationship of the conductor to the winding in order to determine the maximum achievable bulk current density j.

Although the absolute maximum bulk current density would occur when the superconductor fractional area f_{sc} is continuously varied to maintain all the conductors at the local maximum allowable current density value, the obvious constructional difficulties of such a design suggest that a discrete approximation to the continuously varying case provides a more realistic estimate of maximum achievable bulk current density. We develop this approximation by dividing the solenoid winding into a number of layers of conductors N in which the conductor current density j is fixed throughout each layer at the lowest value of the allowable current density in the entire layer.

To apply this approximation to the solenoid winding design previously developed (Fig. 5-1), the total thickness in the radial direction of both the inner and outer windings of each solenoid (T_t = 0.987 m) is divided into four layers of equal thickness.

[The second layer of constant current density conductors is split between the inner and outer winding layers (Fig. 5-4 and 5-9).] We assume that the magnetic field strength varies through the winding in a linear manner from the peak strength at the inner radial surface (the surface normal to the inside radius of the solenoid) to zero field strength at the outer radial surface of the winding. From the following relationship, it may be seen that this linear variation of $|B|$ is based upon the distance β through the winding from the inner radial surface, with the region occupied by the inner support structure (Fig. 5-1) being neglected:

$$|B| = |B_{mc}| \, [1 - \beta/T_t], \qquad (5\text{-}7)$$

where

$\beta \equiv$ the distance through the winding from the inner surface (neglecting the inner coil-support structure), and

$T_t \equiv$ the total winding thickness (neglecting the inner coil-support structure).

Since the assumed linear variation of the magnetic field inside the winding is correct only for a solenoid of infinite axial length and uniform current density, it provides only a first-order approximation to the more complex spatial variation of the field within the finite-length, variable-current-density solenoids in the plug coil. Because the maximum allowable current density decreases with increasing field strength, the lowest value of the maximum allowable current density in a particular layer of conductor occurs at the location of maximum field strength within that layer of conductor.

Thus, with the assumed field variation [Eq. (5-7)], the limiting value of the maximum allowable current density for a given layer of conductor occurs at the inner radial surface of the conductor layer where the magnetic field strength is highest. Since the current density within a conductor layer is less than the maximum allowable value everywhere within that layer except at its innermost surface, the layered approximation tends to underestimate the value of maximum allowable bulk current density J. However, with a reasonable number of layers ($N \geq 3$), it provides an adequate estimate of the maximum achievable bulk current density, considering the preliminary nature of this analysis and the obvious constructional problems associated with a large number of conductor layers.

To estimate the maximum allowable bulk current density J with the

computational model discussed in the preceding test, we need a conductor design configuration. For the purposes of this analysis, we adopted the conductor design developed for the Mirror Fusion Test Facility (MFTF) experiment 5-1 (Fig. 5-6). To allow the relatively large superconductor fractional areas required by the high field strength levels inherent in the TMR concept, we modified MFTF conductor design by removing the restriction that the superconductor be confined to only one quadrant of the conductor (Fig. 5-6). We then evaluated the values of the parameters d, b, α, and f_{he} describing the generalized conductor about which the preceding analysis was formulated for the MFTF conductor geometry (Fig. 5-6).

In addition to a conductor design, we must evaluate the material property values ρ_{cu}, j_{sc} and $\bar{q}$ for the appropriate temperature (~4 K) over the relevent range of magnetic field strengths ($0 \leq |B| \leq 19$ T) in order to calculate the maximum allowable bulk current density from the model previously developed. For this analysis, we took the value of the average heat-transfer rate per unit of coolant-passage contact area used in Ref. 5-1: $\bar{q} = 0.36$ W/cm^2. Although the relatively low field strengths associated with the MFTF experiment allowed the utilization of a NbTi superconductor, the high field strengths required in the TMR concept necessitate the use of Nb_3Sn superconductor. In estimating the allowable current density in the Nb_3Sn superconductor, we used a plot of the critical current density for pure Nb_3Sn as a function of magnetic field strength (Fig. 5-7) to provide the

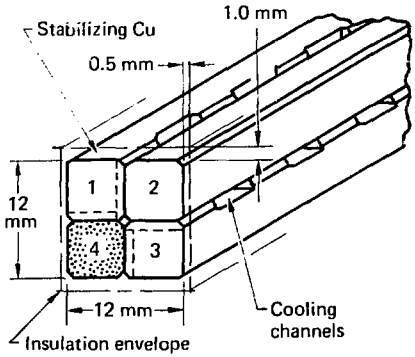

Fig. 5-6. Design of the MFTF conductor, where the variables defined in the caption to Fig. 5-5 have the following values:

$\bar{q} = 0.36$ W/cm^2,

Coolant passage-conductor interface area/unit length = 53 mm^2/mm,

$d = 12 + 1.0 + 1.0 = 14$ mm

$$b = \frac{12 + 0.5 + 0.5 \text{ mm}}{14 \text{ mm}} = 0.93,$$

$$\alpha = \frac{53 \text{ mm}^2/\text{mm}}{2(12 + 2) + 2(12 + 1) \text{ mm}^2/\text{mm}} = 0.98,$$

and

$f_{in} = 0.15$

$f_{he} = 0.005$

} assumed values.

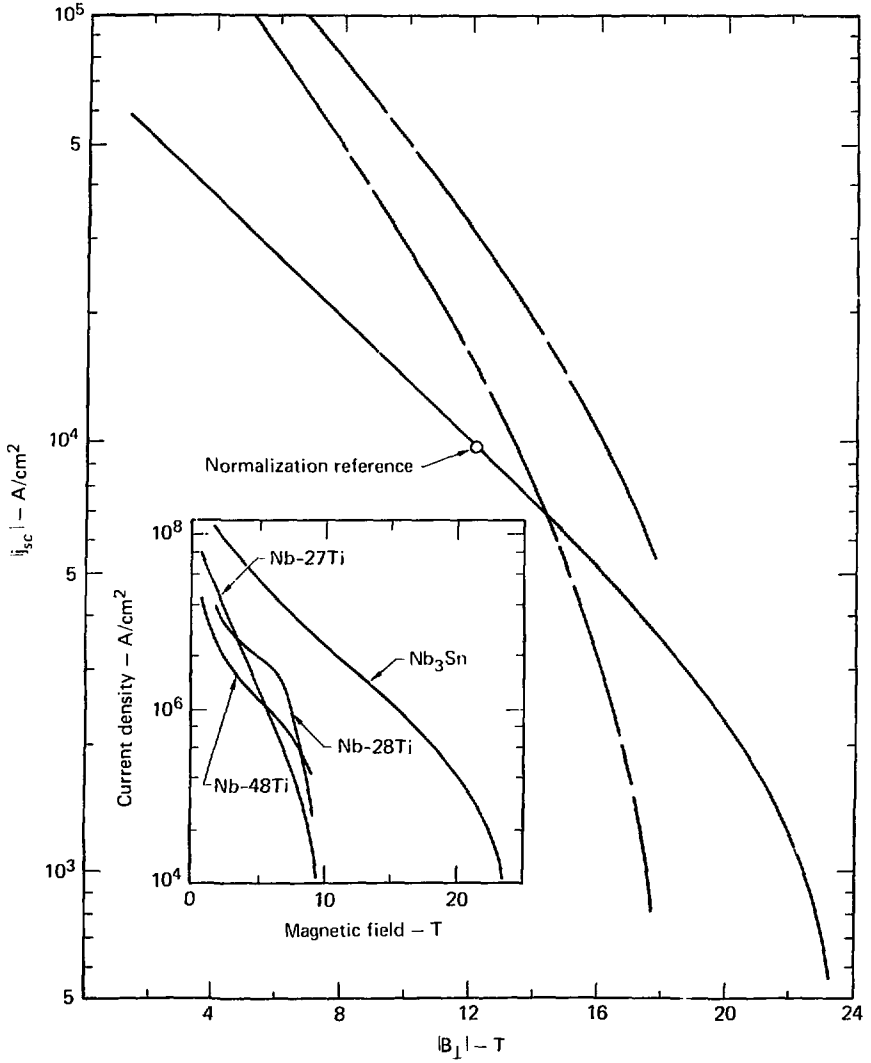

Fig. 5-7. Critical current density for pure Nb_3Sn superconductor as a function of magnetic field strength. The shaded area represents critical current density data from Ref. 5-3 for Nb_3Sn multifilimentary conductors with different heat treatments. The solid line is the normalized critical current density j_{sc}. The normalization point, from Ref. 5-4, is $j_{sc} = 1 \times 10^4$ A/cm^2 at 12 T. Insert (taken from Ref. 5-5) shows un-normalized critical current density for three ductile alloys of Nb and Ti as well as for the Nb_3Sn.

scaling of the critical current density with field strength. To include the various deleterious effects that reduce the critical current density of actual fabricated Nb_3Sn superconductors, the critical field plot for pure Nb_3Sn was normalized to a critical current density value representative of actual fabricated Nb_3Sn superconductor ($j_{sc} = 1 \times 10^4$ A/cm^2 at 12 T.

The substantial reduction in the critical current density for fabricated Nb_3Sn superconductor relative to pure Nb_3Sn (about an order of magnitude) results from several different factors associated with the diffusion process used to fabricate the Nb_3Sn superconductor. This deterioration in critical current density for the Nb_3Sn superconductor is not related to the current density limitations imposed on the complete conductor (Nb_3Sn conductor and copper-stabilizing material) by the cryostatic stability criterion [Eq. (5-5)].

The resulting curve of the critical current density for a Nb_3Sn conductor that was utilized throughout the remainder of this analysis is also given in Fig. 5-7. In addition, some more recent experimental data[5-3] for Nb_3Sn filamentary conductors are included in Fig. 5-7.

The electrical resistivity of copper is a function of both the temperature and magnetic field strength at cryogenic temperatures. The resistivity of copper immersed in a magnetic field $|B|$ at a particular temperature $\rho(|B|, T)$ may be related to its resistivity in the absence of a magnetic field $\rho(0,T)$ by Kohler's law [Eq. (5-8)], which copper closely follows over a wide range of conditions:[5-6]

$$\Delta R \equiv \frac{\rho(|B|, T) - \rho(0,T)}{\rho(0,T)} = f\left(\frac{|B|}{\rho(0,T)}\right) \qquad (5\text{-}8)$$

From the definition of the magnetoresistance parameter ΔR used in Kohler's law we can develop the following relationship for the resistivity:

$$\rho(|B|, T) = \rho(0,273)[\Delta R + 1]/R$$

where R is the resistance ratio,

$$R \equiv \rho(0,273/\rho(0,T) \quad . \qquad (5\text{-}9)$$

With the magnetoresistance parameter evaluated from the appropriate plot for copper,[5-6] we calculated the resistivity of copper [$\rho(|B|,$ T)] as a function of the magnetic field strength $|B|$ for several different resistance ratios R and plotted it in Fig. 5-8. Although the resistance ratio for copper may be as high as 1400 under ideal laboratory conditions, large quantities of copper

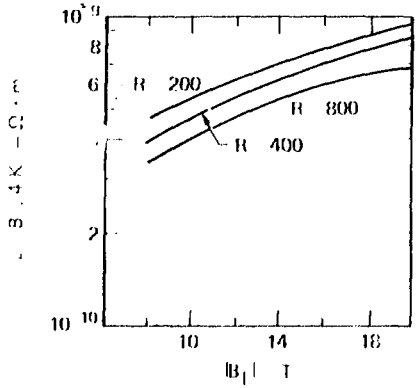

Fig. 5-8. Resistivity of copper stabilizing material, where

$$\Delta R = \frac{\rho(|B|,T) - \rho(0,T)}{\rho(0,T)}$$

$\Delta R = f\left(\frac{|B|}{\rho(0,T)}\right)$ Kohler's law,[5-6]

$R = \rho(0,2/3\ K)/\rho(0,4\ K)$, and

$\rho(|B|,T) = (1 + \Delta R)/R$.

with resistance ratios of over 200 are difficult to obtain in practice.[5-7] Thus, for this analysis we assume that the resistivity of the copper stabilizing material is given by the curve in Fig. 5-8 for a resistance ratio of 200.

Having chosen a conductor design configuration and evaluated the necessary material properties, we can estimate the maximum allowable bulk current density and compare it with the value initially assumed in developing the preliminary plug coil design. For this analysis, we divide the total thickness of the solenoid winding ($T_t = 0.957$ m) into four conductor layers of equal thickness t_i. (As previously discussed, the current density in each conductor layer J_i is equated to the smallest value of the maximum allowable current density in that layer.) We then estimate the maximum bulk current density for the entire solenoid by averaging the current densities in each of the four equal-thickness layers of conductor:

$$J = \frac{1}{4t_i}\sum_{i=1}^{4} t_i J_i = \frac{1}{4}\sum_{i=1}^{4} J_i. \quad (5\text{-}10)$$

The maximum magnetic field strength values $|B(r_i)|$ and the current densities for each layer of conductor J_i are given in Table 5-2 along with the maximum allowable bulk current density calculated with Eq. 5-10. To check the validity of the assumed linear variation of magnetic field strength across the winding, we used the computer code EFFI to calculate the actual variation of the magnetic field strength for the current density values given in Table 5-1 and the winding geometry shown in Fig. 5-1.

In Fig. 5-9, the field variation across the solenoid winding obtained with EFFI is plotted at several different axial locations and compared with the assumed linear variation. The sharp discontinuities in the calculated variation of the field

across the solenoid winding result from removing the region occupied by the inner coil-support structure (Fig. 5-1) from the abscissa of Fig. 5-9. Since the linear approximation doesn't model the radial field variation across the support structure, its removal from Fig. 5-9 facilitates the comparison of the actual and assumed field variation.

From Fig. 5-9, it may be seen that the linear approximation overestimates the field strength in the first layer and part of the second while underestimating the field strength in the remaining portion of the second winding and throughout the third and fourth winding layers. Since it appears that the linear approximation on the whole underestimates the actual field strength, a more detailed analysis incorporating a better approximation to actual variation of the field across the winding would tend to reduce the allowable bulk current density in the winding. From the values given in Table 5-2, the maximum bulk current density (J_{max} = 2975 A/cm^2) is seen to be very close to the value *initially chosen* (3000 A/cm^2) to develop the plug coil design shown in Fig. 5-1. Thus, the value initially guessed for the bulk average current density is seen to have been a reasonable choice, and the coil design developed around it appears viable with respect to this preliminary analysis of the cryostatic stability criterion.

SOLENOID SUPPORT STRUCTURE

To estimate the magnitude of the magnetic forces for this first cut structural analysis, we used a simplified model to approximate the complex magnetic field configuration within the solenoid coils. Since the Yin Yang coil set causes only a small perturbation in the magnetic field

Table 5-2. Current density/cryostatic stability (where $J_{max} = 1/4 \sum_{i=1}^{4}$ = 2975 A/cm^2.

Conductor layer	Maximum field strength (T)	Fractional area of superconductor, F_{sc}	Superconductor current density, J_{sc} (A/cm^2)	Current density in conductor layer, J_i (A/cm^2)
1	19.00	0.567	2900	1640
2	14.25	0.346	7000	2420
3	9.50	0.226	15,000	3390
4	4.25	0.135	33,000	4450

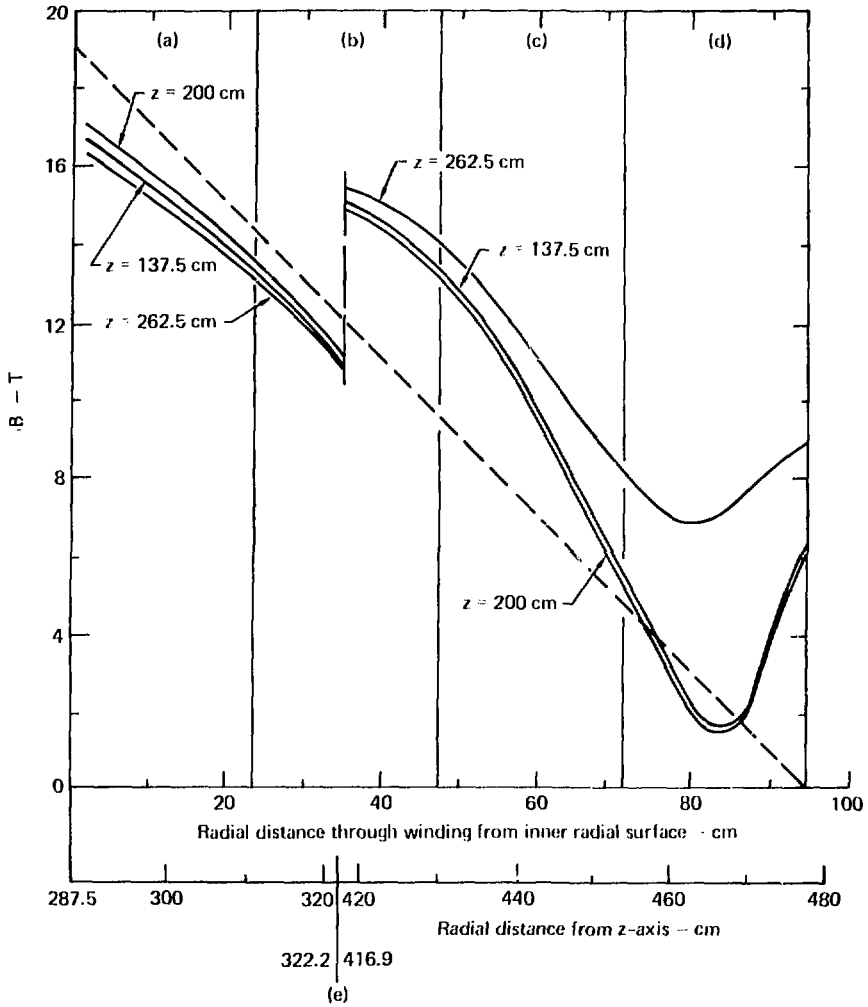

Fig. 5-9. Variation in the magnetic field across the winding of the solenoid coils in the plug coil system, where (a) is the first layer of conductors, J_1 = 1640 A/cm^2; (b) is the second layer, J_2 = 2420 A/cm^2; (c) is the third layer, J_3 = 3390 A/cm^2; and (d) is the fourth layer J_4 = 4450 A/cm^2. The solid lines are for calculated |B| with variable J_1 at three different axial locations. The dashed line is the linear approximation from Eq. 5-7. Line (e) marks the discontinuity resulting from the omission of the region occupied by the structure.

generated by the solenoid coils, the magnetic field may be reasonably approximated as axisymmetric (no tangential component, Fig. 5-1) about the z-axis. In addition, to further simplify this analysis and to be consistent with the approximations utilized in other chapters of this report, we have also neglected the radial component of the magnetic field. Thus, for this preliminary analysis we assume that the magnetic flux density vector is always directed along the z-coordinate direction ($\vec{B} = |B| \hat{k}$). To be consistent with the cryostatic stability criterion developed earlier in this chapter, we assume that the magnitude of the flux density vector varies linearly from a maximum value at the inner surface of the solenoid winding to a null value at the outer surface of the winding:

$$|B| = B_z = (|B_{mc}|)\ (1-\beta/t_t), \qquad (5\text{-}11)$$

where

β = the distance through the winding from the inner surface, neglecting the inner coil-support structure, and

t_t = the total winding thickness, neglecting the inner coil-support structure.

Since the field configuration assumed for this analysis [Eq. (5-11)] is only correct for a solenoid of infinite axial length and constant current density, it provides only a first-order approximation to the complex geometry of the actual field configuration within the solenoid.

Each differential volume of the solenoid winding experiences a body force given by the vector cross product of the local current and magnetic flux density vectors:

$$\vec{dF}/dv = \vec{j} \cdot \vec{B}. \qquad (5\text{-}12)$$

Since the flux density vector is assumed to have only a z-direction component, and the current density vector is always directed along the tangential coordinate direction, the body force is always radially directed. Thus, by neglecting the radial field density component we have eliminated the axial component of the magnetic body force. The small relative size of the axial component of the magnetic body force allows it to be neglected in this preliminary analysis.

The radially directed, magnetic body force is transmitted through the volume of each winding layer to the interface of the winding layer and its associated supporting structure. For a given current and flux-density distribution, the compressive stress σ_{cc} on the interface between the

winding layer and the support structure is determined by the sum of all the contributions made by each differential conductor layer across the entire thickness of the winding layer t. Thus, for a given maximum allowable compressive stress limit

$$\sigma_{cc} = \int_0^t |\vec{j}| \times |\vec{B}| \, dx,$$

the thickness of a particular winding layer is determined by the average value of the product of the current and the magnetic flux densities across the winding layer.

With the current density values given in Table 5-1 and the winding layer thickness shown in Fig. 5-1, the maximum compressive stress of the conductor is about 15 ksi for the high-field design ($|B_0|$ = 18 T). Although this peak stress level is probably slightly above the yield point of fully annealed, high-purity copper (~10 to 11 ksi, Fig. 5-10), a very modest amount of strain hardening will raise the yield point above 15 ksi (Fig. 5-10). Since (as will be discussed shortly) the conductor must be strain hardened by drawing in order for it to withstand the tensile loading along its axis, the compressive yield stress transverse to the conductor may well exceed the fully annealed value. If compressive stress levels of 15 ksi are

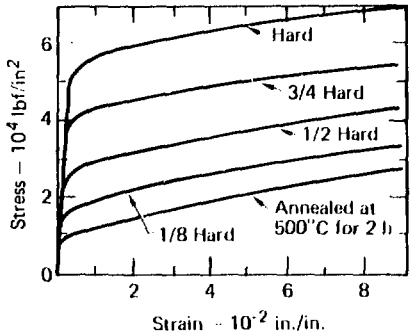

Fig. 5-10. Stress/strain properties of OFHC copper at 4 K, [5-7] where $E_{4\ K} = 17.2 \times 10^6$ lbf/in^2.

determined to be too high, they may be reduced with little design penalty by dividing the solenoids into a larger number of proportionally thinner conductors and structure layers.

In addition to the transverse compressive stress exerted on the conductor, the deflection of its supporting structure under the magnetic loads will load the conductor in tension. Unlike the transverse compressive stress previously considered, it is not clear that this axial tensile stress can be substantially reduced by separating the solenoid windings into more layers. Since the cylindrical structure supporting the second conductor layer can be made very thick, and since the magnetic forces are smaller in the second conductor layer, the maximum tensile stress experienced by the

conductor will occur in the first layer of conductors.

To estimate the maximum tensile stress level in the first conductor layer, we developed two simplified calculational models of the first conductor layer and its support structure. In the first model, we neglected the strength of the conductor and applied the entire radial magnetic force exerted on the first conductor layer to the inner surface of the supporting structure. We then calculated the conductor stress level σ_{ct} from the deflection of the support structure by equating the conductor hoop strain ε_c with the support structure hoop strain ε_s,

$$\sigma_{ct} = E_c \varepsilon_c = E_c \varepsilon_s \quad , \qquad (5\text{-}13)$$

To further simplify this analysis we use membrane theory to calculate the support-structure hoop strain for a cylindrical pressure vessel. Thus, besides neglecting the strength of the winding layer, this simple calculation also neglects the finite thickness of the support structure itself;

$$\varepsilon_s = \frac{\sigma_s}{E_s} = \left(\frac{1}{E_s}\right)\left(\frac{p\bar{r}_s}{t_s}\right) \quad , \qquad (5\text{-}14)$$

where

$\bar{r}_s$ = mean radius of structure,

p = pressure on inner surface of structure = σ_{cc}, and

t_s = radial thickness of structure.

Although this model overestimates the conductor tensile stress level by neglecting the strength of the conductor itself, it greatly simplifies the structural calculations by replacing the actual, statically indeterminate coil structure with a simplified, statically determinate calculational model. From Eq. (5-14), we obtain a hoop strain of less than 0.2% for the high-field case ($|B_0|$ = 18 T) with the current densities given in Table 5-1.

In the second structural model, we develop a somewhat more advanced analytical approximation by modeling the first winding layer and its supporting structure as concentric cylindrical tubes of linearly elastic material. The inner tube representing the first winding layer is loaded on its inner radius with a pressure equal to the maximum compressive conductor stress σ_{cc} [Eq. (5-11)], while its outer radius is loaded with the contact pressure p between the conductor layer and its supporting structure. The load σ_{cc} on the inner radius of the cylindrical tube simulating the conductor layer models the magnetic body force distributed throughout the conductor volume. Since the structural strength of the conductor has not been neglected in

this model, the contact pressure between the structure and winding layer will be less than the maximum compressive stress. How much less will depend on the relative stiffness of the winding layer and its support structure. The outer tube representing the support structure is loaded on its inner radius with the contact pressure between the winding layer and the support structure.

Although this model is more sophisticated than the preceding one, the replacement of the magnetic force distributed throughout the volume of the winding layer with an equivalent load applied to the inner surface of the winding layer appears to underestimate the deflection of the support structure and the conductor tensile stress level. Since the conductor and its support structure form a statically indeterminate structural system, the contact pressure between the winding layer and its supporting structure must be determined from an auxiliary condition.

The contact pressure may be analytically determined by equating the relationships developed from the theory of elasticity for the displacement of the outer surface of the coil winding layer with the inner surface of the supporting structure:

$$\left[\left(\frac{m+1}{m-1}\right)+1\right]\left\{\left[\frac{G_c}{G_s}\right]\left[\frac{R_c^2-1}{R_s^2-1}\right]\left[\left(\frac{m-1}{m+1}\right)+R_s^2\right]\right.$$

$$\left.\left[\left(\frac{m-1}{m+1}\right)R_c^2+1\right]\right\}^{-1}$$

$$= f\ (m, G_s, G_c, R_s, R_c), \qquad (5\text{-}15)$$

where

R_c = outside radius of winding layer / inside radius of winding layer,

R_s = outside radius of structure / inside radius of structure,

G_s = shear modulus of structure,

G_s = shear modulus of winding layer, and

$m = \frac{1}{N\upsilon} = \frac{1}{\text{(Poisson's ratio)}}$.

With the contact pressure determined, the maximum hoop strain in the winding layer may be analytically determined from the solutions of the equations of elasticity for a cylindrical pressure vessel

$$\varepsilon = \frac{[f\ (m, G_s, G_c, R_s, R_e)\ \sigma_{cc}]}{E_s} \cdot \left[\frac{1 + R_s^2 + \frac{1}{m}}{\left(R_c^2 - 1\right)}\right]. \qquad (5\text{-}16)$$

From Eq. (5-16), we determined that the hoop strain for the high-field case with the geometry given in Fig. 5-1 is approximately 0.14%.

As anticipated, the second structural model yields a lower conductor hoop strain than the first model. Since the hoop strains calculated with either the first or second structural model imply stress levels of about 25 to 35 ksi, far above the yield stress of annealed copper (11 to 12 ksi), either the copper stabilizer material must be work hardened or a method must be developed to prestress the coil support structure. Since work hardening the copper stabilizing material will substantially increase its electrical resistance at cryogenic temperatures (between 2 to 4 times, see Fig. 5-11), the maximum allowable current densities calculated earlier would decrease. However, since the increase in resistance due to the magnetic field at high field strengths is much greater ($\Delta R \approx 10$ at $|B| = 18$ T, Fig. 5-8) than the work-hardening effect, the reduction of the maximum allowable current density by work hardening will be more noticeable in the low-field regions of the solenoid winding.

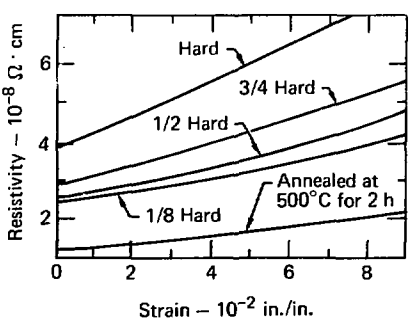

Fig. 5-11. Resistivity/strain properties of OFHC copper at 4 K.[5-7]

Thus, when the work-hardening resistance increase is added to the magneto-resistance effect previously considered, the current density in the high flux density regions of the solenoid winding is not greatly affected. However, the maximum allowable current density in the low flux density regions of the solenoid winding is substantially reduced if the copper stabilizing material is work hardened. If we are to maintain the central field strength, a reduction in the solenoid current density necessitates an increase in the solenoid winding cross section from the design illustrated in Fig. 5-1.

In addition to the strength of the copper stabilizing material, the brittle nature of the Nb_3Sn superconductor material also imposes limitations on the conductor hoop strain. It was experimentally determined that multifilamentary conductors of Nb_3Sn could withstand tensile strains of approximately 0.6% without degradation in the critical current density. The ability of the conductor to withstand such large strain values was attributed to an initial prestressing of the conductor resulting from the difference between the thermal expansion coefficients of the niobium filaments and

the copper stabilizing material. Thus, it appears that prestressing the support structure to reduce conductor strain is not necessary.

INTERNAL STRUCTURE OF THE YIN-YANG COIL

We shall now determine the maximum value of the average current density for the cryogenic-aluminum Yin-Yang winding shown in Fig. 5-1 as a function of the maximum allowable value of the local current density. For a given maximum local current density and magnetic field strength in the conductor, the average current density is determined by the fraction of the current-carrying conductor that is displaced by the noncurrent-carrying internal-support structure. From the structural analysis discussed here, the fraction of the Yin-Yang coil cross section that must be reserved for the internal structure is determined for all three of the magnetic designs. For the high-field case ($|B_0|$ = 18 T, Fig. 5-1), we consider the design of the internal structure in more detail in order to determine the thickness of the plates between adjacent layers of conductors. With the fraction of the winding cross section occupied by the internal structure (average structural fraction $\bar{f}$) determined from the analysis contained here and with the average current density values initially utilized to develop the magnetic design, we may determine j, the local value of the current density in the cryogenic-aluminum conductor necessary to achieve the desired magnetic performance:

$$j = \bar{j}/\bar{f} \ . \qquad (5\text{-}17)$$

After determining the thermal design implications (coolant passage length and area fraction, pumping power, coolant pressure, etc.) of operating at the desired conductor current density from the conductor thermal analysis described later under "Thermal Analysis of the Cryogenic Yin-Yang Coil," we can assess the feasibility of the magnetic design based on the initially assumed average current density values.

Because it greatly simplifies this preliminary analysis and because it represents a reasonably valid approximation, we estimate the magnitude and direction of the magnetic forces acting on the conductors by assuming that they are immersed in a spatially uniform, axial-direction (Fig. 5-1) magnetic field at the field strength of the mirror point. This assumption neglects the perturbations in the magnetic field strength and geometry caused by the finite length of the solenoid windings and the Yin-Yang coils themselves. Since the magnetic force system exerted on the TMR Yin-Yang coil differs considerably from

a conventional Yin-Yang coil system, a sketch of the magnetic force system is presented in Fig. 5-12. The sketch was developed by applying the Lorentz force law to the Yin-Yang coil winding immersed in the assumed uniform axial field.

To estimate the average structural fraction for the Yin-Yang coil winding, we used the internal structure configuration for the winding cross section of the major arc where the magnetic forces are strongest (xz - plane, Fig. 5-12) to size the internal structure over the entire length of the coil winding. Since with this assumption the internal structure is sized by the maximum value of the magnetic forces, whereas in an actual design it may be possible to reduce the size of the internal structure where the magnetic forces are smaller, this estimation process is probably conservative. However, a more sophisticated analysis of the average structural fraction would require a more detailed design of the internal structure involving consideration of the important and difficult problems associated with fabricating and

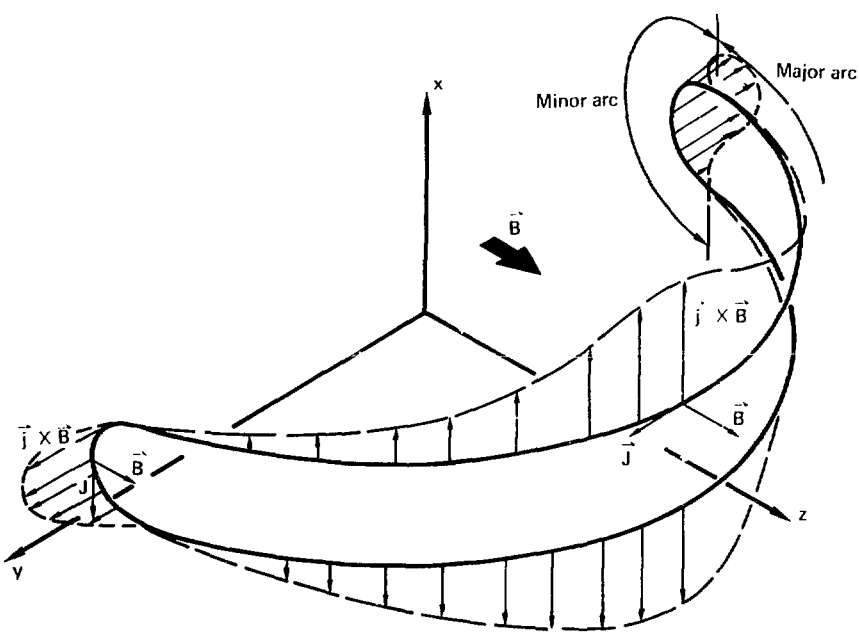

Fig. 5-12. Magnetic force system in the TMR Yin-Yang coil.

assembling an actual winding. Such a design effort is beyond the scope of this preliminary design study.

Another serious design problem neglected in this analysis is caused by the abrupt change in the directional orientation of the local magnetic force with respect to the Yin-Yang winding cross section between the major and minor arcs. If the columns of the internal structure are oriented in the direction of the magnetic force along the major arc (x-direction, Fig. 5-1), the magnetic arc will be transversely oriented to the columns of the internal structure along the minor radius. Thus, either the orientation of the internal structure columns relative to the winding cross section must be changed between the major and minor arcs, or the plates separating adjacent conductor layers must be redesigned to support the magnetic forces along the minor arcs. Although this change in loading poses a formidable structural challenge, the very small magnitude of the magnetic forces in the transition region between the major and minor arcs may allow the relative orientation of the internal structure columns to be rotated along the direction of the magnetic forces.

We determined the average structural fraction for the Yin-Yang winding cross section in the xz-plane. In this structural design, the winding conductors are divided into a series of layers (Fig. 5-1, detail C) whose thickness is chosen to limit the compressive stress in the conductors. The magnetic forces distributed over each layer are transferred by the internal structure to an external structure. The internal structure in a layer of conductors consists of a series of compressively loaded columns that transfer the total magnetic force distributed over all the proceeding conductor layers through the conductor layer under consideration. Since the columns do not contact the conductors in the layers they pass through, the conductors in each layer are subjected only to the magnetic forces distributed throughout their own volume. A flat plate is used between each layer of conductors to transmit to the columns the total magnetic force distributed over the preceding layer of conductors.

After passing through the last layer of conductors, the columns transmit the load from the preceding conductor layers to the external structure supporting the Yin-Yang coil winding. Since the columns are carrying the cumulative total of all the magnetic forces distributed over all the preceding layers of conductors, they must become larger and larger as they approach the external structure (Fig. 5-1). Thus, because of the increasing amount of current-carrying

conductor displaced from each additional conductor layer by the internal structure, each additional conductor layer lowers the average current density. In addition, as the winding thickness is increased by adding additional conductor layers, the internal structure eventually displaces the conductors, thus setting an absolute limit to the current-carrying capacity of a conductor of fixed width.

The thickness of each conductor layer t is determined by the requirement that the compressive stress on the outer surface of the conductor layer be equal to the maximum allowable design stress of the conductor σ_c. Since the annealed, high-purity aluminum used in the cryogenic-aluminum conductor is very weak ($\sigma_{yp} \approx 2$ to 3 ksi), we treat it as an incompressible fluid that transfers the magnetic body forces to the internal structural system and the external case surrounding the coil winding. Thus, the maximum allowable conductor design stress is determined by the strength of the coolant passage ducts located inside each conductor rather than by the high-purity conductor material itself.

In this analysis, we assume that the coolant passage ducts are constructed of high-strength, aluminum-alloy tubes around which the low-strength, high-purity conductor material is extruded into a conductor of square cross section (as shown later in Fig. 5-15). If we neglect buckling and assume a ratio between coolant-passage wall thickness and the coolant-passage radius of about 0.15, the maximum allowable conductor stress value is about 1.10^8 N/m^2 (15 ksi). With the assumed constant magnetic field strength $|B| = |B_{mp}|$ and with the local current density in the conductor constant at the maximum allowable value j, the thickness of each layer of conductors is constant and may be determined by the following relationship:

$$t = \sigma_c/(j\beta) \quad . \tag{5-18}$$

The fraction of each conductor layer occupied by the internal structure (local structural fraction f_{si}) may be determined in terms of the local structural fraction of the preceding layers by the following relationship:

$$f_{si} = (\sigma_c/\sigma_s)\left[(i - 1) - \sum_{i=1}^{i-1} f_{si}\right] . \tag{5-19}$$

Equation (5-19) was derived by requiring that the internal structure in a conductor layer support the magnetic forces distributed over all the preceding layers without exceeding σ_s, the maximum design stress of the structural material. Since the structural fraction of the first layer

of conductors is always known ($f_{s1} = 0$), Eq. (5-19) may be applied successively beginning with the first conductor layer to determine the structural fractions of each layer of conductors. The average structural fraction f of a given winding design, which will not in general consist of an integer number of equal-thickness winding layers [t, Eq. (5-18)], is given by the following relationship for a winding of total thickness T:

$$f = \left[\sum_{i=1}^{n^*} (1 - f_{si})\right] + [(n - n^*)(1 - f_{sn^*+1})] \quad (5\text{-}20)$$

n number of winding layers = T/t,

n^* largest integer less than n, and

f_{si} structural fraction of conductor layer i.

The second term on the right-hand side of Eq. (5-20) represents the contribution to the average structural fraction from the last conductor layer, which in general is not as thick as the preceding layers. When the simultaneous system of equations formed by Eqs. (5-18) and (5-20) is iteratively solved with the appropriate material property values σ_c, σ_s, and the field-strength B value, we can determine the local conductor current density value j required to attain the average current density j used in the magnetic design.

Table 5-3 lists the required local current density values for all three design cases along with the local average current density and structural fraction in each conductor layer as calculated from Eqs. (5-18) and (5-20). Before considering the viability of the required local current density values given in Table 5-3, we shall consider the design of the internal structure for the high-field case in somewhat greater detail.

In evaluating the average current density, we have tacitly assumed that the flat plates which transfer the magnetic force on each conductor layer to the columns passing through the following conductor layer are sufficiently thin that they have no significant effect on the average current density. To investigate the validity of this assumption, we estimate the required thickness of the plates t_p from the following analysis.

Since the plates are loaded in bending by the magnetic forces exerted on the conductor layer between adjacent columns, their thickness is determined for a given maximum design stress σ_{sp} by the spacing between adjacent columns (a, Fig. 5-13). To estimate the relationship between the plate

Table 5-3. Average current density of aluminum Yin-Yang winding [where t_{total} = 60 cm, σ_{sp} = 3.4 × 10^8 N/m²(50 Ksi), and σ_c = 1 × 10^8 N/m²(15 Ksi)].

Field, $\|B_0\|$ (T)	Layer, j	Layer thickness t_j(cm)	Structural fraction f_{sf}	$\|I_j(1-f_{sf})$ (kA/cm)	I/W (kA/cm)	J (A/cm²)	J_j (A/cm²)
15	1	25.70	0.000	62.45	116.91	1950	2430
	2	25.70	0.294	44.09			
	3	8.57	0.502	10.37			
16.5	1	18.94	0.000	56.87	128.6	2141	4000
	2	18.94	0.294	40.12			
	3	18.94	0.502	28.30			
	4	3.18	0.648	3.36			
18	1	14.19	0.000	52.08	140.28	2337	4949
	2	14.19	0.294	36.77			
	3	14.19	0.502	25.94			
	4	14.19	0.648	18.31			
	5	7.25	0.752	7.10			

stress level and the plate thickness, we model the plate as a pin-jointed beam of unit width loaded by the conductor design stress σ_c spanning the 'open space' between adjacent columns [$a(1 - f_{j+1})$]. From this model and Bernoulli-Euler beam theory, we develop the following relationship for the required plate thickness of the 'j' plate (t_{pj}; the plate separating the 'j' and 'j + 1' conductor layers):

$$t_{pj} = \left(\frac{\sqrt{3}}{2}\right) a \left(\frac{\sigma_c}{\sigma_{sp}}\right)^{1/2} (1 - f_{j+1}). \qquad (5\text{-}21)$$

This relationship neglects the effects of the plate geometry and of the actual end conditions that depend on the constructional details of the internal structure design. The center-to-center spacing of the columns (a) is set by the elastic stability limitations imposed on the compressively loaded columns. Both experimental and analytical studies have confirmed that the maximum nominal stress $\sigma_u = P/A$ that an aluminum column can support before collapsing is a function of the ratio of the length of the column ℓ to its radius of gyration $r = (I/A)^{1/2}$. In the linear elastic loading range, the maximum nominal stress is given as a function of the elastic modulus and the dimensionless geometric parameter $K\ell/r$ by the Euler relationship

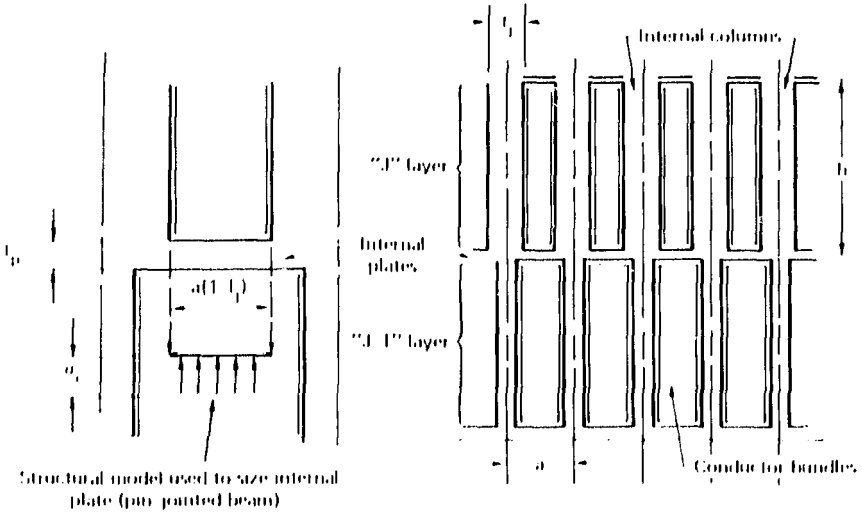

Layer no.	t_1	t_1 (cm)
1	0.000	N.A.
2	0.294	1.33
3	0.502	2.27
4	0.648	2.93
5	0.752	3.40

Fig. 5-14. Internal structure of the TMR Yin Yang winding. The inset table gives values of t_j and t_1 for the case of $|B_0|$ = 18 T, where the dimensions of the internal structure are as follows:

a = 4.52 cm,
t_c = 1.78 cm,
h^p = 13.19 cm, and
ψ = 1.00 (pin jointed).

(Fig. 5-14). In the nonlinear elastic loading range, experimental data[5-8] suggest that the maximum nominal stress is approximately linearly related to the geometric parameter K^p/r. The nondimensional parameter E is determined by the end conditions imposed on the column; the material parameters B,C,D, and E are determined from the uniaxial stress-strain curve.

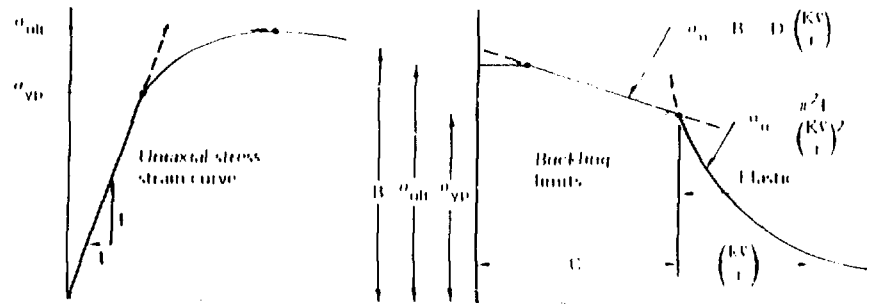

Fig. 5.14. Criteria for buckling failure of the Yin Yang structure. For the structure considered here, values for 2014-T6 aluminum at 20 K are as follows[5.1]:

B = 114.45 ksi,
C = 16.9,
D = 0.561 ksi,
E = 11,300 ksi,
σ_{ult} = 110.6 ksi, and
σ_{yp} = 95.5 ksi.

The values of the material parameters at the appropriate cryogenic temperature (20 K) are estimated from material stress-strain data contained in Ref. 5.9 and are given in Fig. 5.14. We determined the maximum allowable value of the geometric parameter F^2/t = 95 from Fig. 5.14 by requiring *that the design stress level* (41.4×10^8 N/m^2, 49 ksi) be one-half the maximum nominal stress (68.8×10^8 N/m^2, 98 ksi) that the column could support before it collapsed. This buckling safety factor of two is consistent with structural *safety factors implied by the design* stress values utilized throughout the internal structure.

If the geometric parameter is expressed in terms of the variables used to describe the internal structure in the 'j' conductor layer, we may develop the following relationship for the minimum allowable center-to-center distance between adjacent columns (a_j):

$$a_j = \left(\frac{2^3}{95}\right)\left(\frac{Nb}{t_j}\right). \qquad (5.22)$$

The minimum allowable spacing of adjacent columns is desirable because it minimizes the required plate thickness [Eq. (5.21)].

To apply this analysis to a multiple layer winding, we assume that the

columns in each conductor layer are located on common centers (Fig. 5-1) whose spacing is set by the minimum allowable spacing in the second conductor layer [a_s, Eq. (5-22)]. With this arrangement, the second conductor layer is operating with a buckling safety factor of two, whereas the other conductor layers have buckling safety factors greater than two. The calculated dimensions of the internal structure components are tabularized in Fig. 5-13. From the plate thicknesses given there, it may be seen that the assumption that the plates did not significantly reduce the average current density is justified.

Next, we shall develop a thermal analysis of the cryogenic-aluminum conductor in order to determine the feasibility of the local current density values required to attain the average current density values used in the magnetic design.

THERMAL ANALYSIS OF THE CRYOGENIC YIN-YANG COIL

In this section, we shall evaluate feasibility of operating the cryogenic Yin-Yang coil at the desired local current density values (Table 5-2).

The feasibility of operating the coil at a particular current density level is primarily determined by the thermal design implications of the associated Joule dissipation power density. For a given current density, the Joule dissipation is determined by the electrical resistance of the aluminum conductor ρ_{Al}. Since for a given level of impurities, the resistance of the aluminum conductor material increases very abruptly if the conductor temperature is raised above about 20 K (Fig. 5-15), the

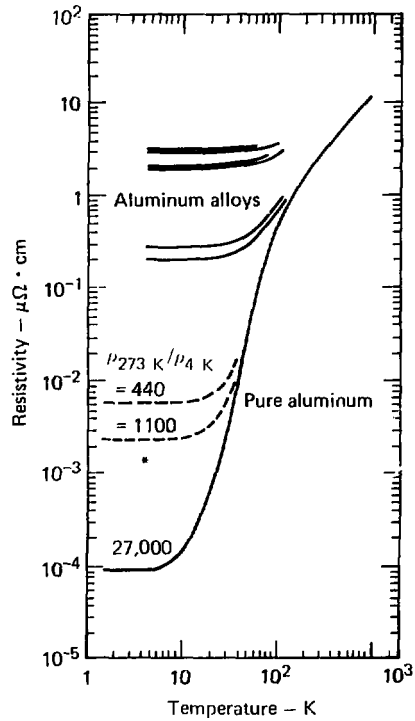

Fig. 5-15. Electrical resistivity of pure aluminum and of aluminum alloys as a function of temperature (from Ref. 5-10). The asterisk marks the data point [$\rho(0,4) \approx 1.2 \times 10^{-3}$ μA•cm] used in preparing Fig. 5-17.

outlet temperature T_0 of the helium coolant must not be over about 20 K. The inlet temperature of the helium coolant is limited by the rapid degradation of the refrigerator coefficient of performance as the coolant temperature is lowered. Because of this, the refrigerator power requirements appear to limit T_i, the inlet temperature of the helium coolant, to temperatures above about 12 to 15 K. Thus, compared to many other more conventional heat-transfer systems, the cooling system for a cryogenic-aluminum coil must operate within a very narrow temperature range ΔT = 5 to 8 K.

We can express the thermal design implications for a cryogenic-aluminum Yin-Yang coil in terms of a local and a global design requirement. Locally at each point along the conductor, the total temperature rise required to transfer the Joule dissipation from the interior of the conductor to the helium coolant itself must not cause the conductor temperature to substantially exceed 20 K. Because of the high conductivity of the aluminum conductor and its small physical size, the temperature difference required for the conductive transfer of the Joule dissipation energy to the surface of the helium-coolant passage appears to be insignificant relative to the convective film drop. Thus, for this preliminary analysis it appears that the conductive temperature difference can be neglected and only the film drop ΔT_f need be considered in formulating the local criterion.

In addition to the local design requirement discussed above, the cooling system for a nonsuperconducting, steady-state coil winding must be designed so that the global temperature rise ΔT of the coolant over the entire length ℓ of each coolant passage is not excessive. Since the global temperature rise is severely constrained in a cryogenic-aluminum coil system ΔT = 5 to 8 K, there is a severe limitation on the length ℓ of the coolant passages between inlet and outlet manifolds. Although the impact of the coolant passage length on the coil design is difficult to quantify without performing a much more detailed design study, the design of the inlet and outlet manifolding will probably become much more difficult as the coolant passage length becomes shorter.

To analytically evaluate the design requirements discussed above, we must choose a conductor configuration. For this study, we developed the conductor design shown in Fig. 5-16 where we assume that the square, high-purity aluminum conductor has been extruded around a thin, high-strength, aluminum-alloy cooling tube in the center of the conductor. The geometry

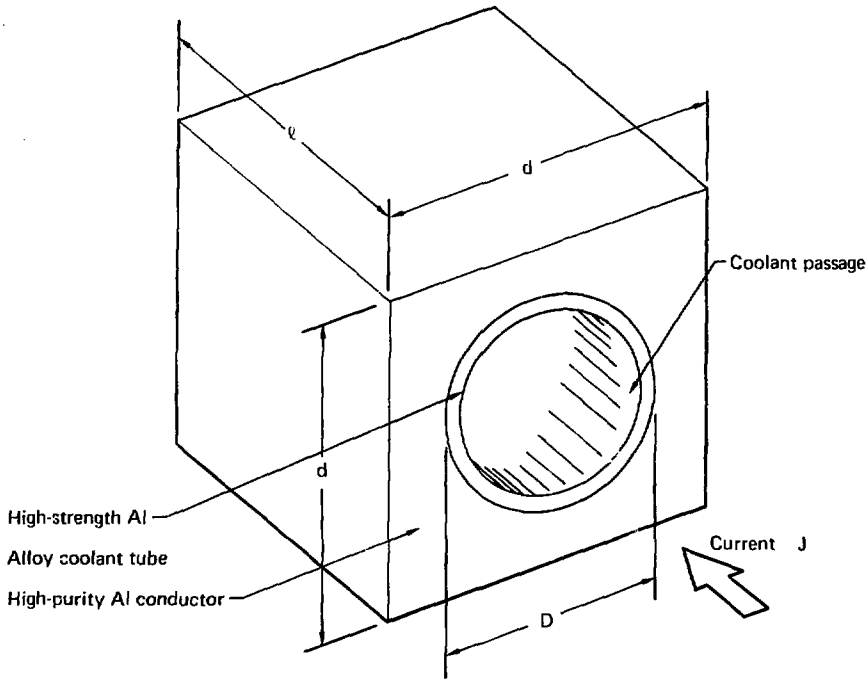

Fig. 5-16. Cryogenic aluminum conductor the Yin-Yang coil, where

$$f \equiv \frac{\text{cross-sectional area of the coolant duct}}{\text{total cross-sectional area of the conductor}} .$$

of the conductor assembly (cooling tube and surrounding conductor) is determined by the ratio of the coolant duct to the conductor cross-sectional areas f, the dimension of the conductor side d, and the length ℓ of the coolant passage between inlet and exit manifolds.

To analytically evaluate the thermal implications of the local design criterion, we develop a relationship between the current density and the film drop,

$$\Delta T_f = \left[\frac{(1 - f)d}{(\bar{u}f)^{1/2}}\right]\left(\frac{\rho_{Al}}{2h}\right) j^2, \qquad (5\text{-}23)$$

where the Joule dissipation power in a differential length of conductor is equated to the rate of convective heat transfer to the helium coolant.

Since the conductor cross section is assumed constant along each conductor, the terms enclosed by the brackets on the right-hand side of Eq. (5-23) are constant along a given coolant passage. The convective heat transfer coefficient h is determined from the coolant parameter values with the following version of the Reynold's analogy:

$$\left(\frac{hD}{K}\right) = 0.023 \left(\frac{D\overline{\rho u}}{\mu}\right)^{0.8}, \qquad (5\text{-}24)$$

where

k ≡ thermal conductivity of helium coolant,

C_p ≡ specific heat of helium coolant,

μ ≡ viscosity of helium coolant, and

$\overline{\rho u}$ ≡ mass velocity of helium coolant.

The electrical resistivity of the aluminum conductor ρ_{Al} is a function of its purity, temperature, and flux density. Thus, for a particular current density, coolant parameter values, and conductor design, the film drop is fixed for a given conductor temperature T_c. Since the outlet temperature of the coolant is approximately determined by subtracting the film drop from the maximum conductor temperature ($T_0 \approx T_c - \Delta T_f$), the film drop must be kept quite low ($\Delta T_f \lesssim 1$ K) to prevent a significant reduction of the already small global temperature rise. A decrease in the global temperature rise reduces the length of the coolant passages. The local thermal design requirement expressed by Eq. (5-23) is conceptually similiar to the cryostatic stability criterion developed for the superconducting solenoid windings [Eq. (5-3)].

To analytically evaluate the implications of a particular current density value with respect to the global design requirement, we develop the following relationship between the coolant passage length and the global coolant temperature rise from the first law of thermodynamics:

$$\Delta T = \left(\frac{2h\Delta T_f}{\overline{\rho u}\, C_p}\right)\left(\frac{1}{d}\sqrt{\frac{\pi}{f}}\right)\ell \, . \qquad (5\text{-}25)$$

In developing this relationship, we neglect frictional dissipation and evaluate the bulk properties of the coolant at the mean coolant temperature.

To evaluate the film-temperature drop and coolant-passage length for a given current density, we must determine the value of several coolant parameters. Since the coolant entrance and exit temperatures are largely determined by the use of cryogenic-aluminum conductor material, only the coolant pressure must be

specified to determine the thermodynamic properties of the helium coolant. In this first-cut analysis, we somewhat arbitrarily limit the coolant pressure to about 4 atm.

In addition to the thermodynamic properties of the helium coolant, to evaluate the film temperature and the length of the coolant passage the mass velocity ($\overline{\rho u}$) of the helium coolant must also be specified. The mass velocity of the coolant is limited by the large refrigerator power required to remove the friction dissipation power from the coolant at those very low temperatures. To evaluate this limitation, we develop an analytical expression from the first law of thermodynamics for the ratio P of the pumping power to the Joule dissipation power for an entire coolant passage. This relationship assumes an isentropic reversible pumping process:

$$P = \left(\frac{\overline{\rho u}\, C_p T_i}{j^2 \rho_{Al}}\right)\left(\frac{f}{1-f}\right) \cdot \left[\frac{1 - (P_0/P_i)^{\frac{\gamma-1}{\gamma}}}{\ell}\right], \qquad (5\text{-}26)$$

where

$P_i \equiv$ entrance coolant pressure,

$P_0 \equiv$ exit coolant pressure, and

$\gamma \equiv C_p/C_v$ for helium coolant.

We determine the ratio of outlet to inlet coolant pressures, neglecting compressibility effects, from the following relationships:

$$P_i^2 - P_0^2 = 2R\bar{T}(\overline{\rho u})\left(\frac{f_m \ell}{2r_h}\right), \qquad (5\text{-}27)$$

$$f_m = 0.00140 + 0.125/Re^{0.32}, \qquad (5\text{-}28)$$

where

$\bar{T} \equiv$ mean coolant temperature,

$R \equiv$ perfect gas constant,

$r_h \equiv$ hydraulic radius, and

$Re \equiv$ Reynold's number $= \frac{D\overline{\rho u}}{\mu}$.

Since the pumping power ratio calculated with Eqs. (5-26) through (5-28) does not include either the nonisentropic behavior of a real pump or the pressure losses in the coolant passage manifolding, the calculated pumping power ratio must be very small ($P \leq 0.1$) to avoid significantly increasing the refrigeration costs. We determine the resistivity of the high-purity cryogenic aluminum conductor as a function of flux density for a representative conductor temperature (20 K) from a previous analysis in Ref. 5-6 (see Fig. 5-17).

To determine the thermal design implications of operating the cryogenic-aluminum Yin-Yang coil at the desired current density level ($\bar{j}$ = 3949 A/cm^2,

Table 5-3), we calculate the global temperature rise ΔT, film temperature ΔT_f, pumping power fraction P, pressure ratio P_0/P_i, exit coolant T_0, and conductor temperatures T_c from the previously developed relationships for typical coolant parameters (Table 5-4). All these calculations are based on the current density required for the high-field case ($B_0 \approx 18$ T illustrated in Fig. 5-1. From Table 5-4, it is seen that for the high-field current density the length of the coolant passage is less than the circumferential distance around the coil winding ($\bar{\ell} \approx 13.8$ m). This in combination with the relatively small size of the conductors — 576 conductors are required to fill the Yin-Yang cross section — implies a large number of parallel coolant paths. If the 13.8-m circumference of the Yin or Yang coil is divided into two 6.9-m coolant paths, then about 1150 parallel coolant paths are required for each coil winding (Yin or Yang).

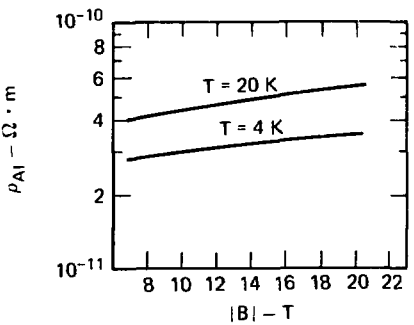

Fig. 5-17. Resistivity of high-purity aluminum (using magnetoresistance data from Ref. 5-6, where

$$R \equiv \frac{\rho(0,273)}{\rho(0,4)} = 2100, \text{ and}$$

$$\rho(0,273) = 2.5 \times 10^{-8}\ \Omega\cdot M.$$

In addition to the large number of coolant passages, the inaccessible location of the passages, which are deep within the winding, will further complicate the coil design. Although we have not considered it in this preliminary study, the development of a manifolding system capable of servicing a large number of often inaccessible flow passages while

Table 5-4. Coolant passage length in cryogenic-aluminum coil [where d = 0.025 m, f = 0.15, $p_i = 4.04 \times 10^5$ N/m^2 (4 atm), $\overline{\rho u} = 220.3$ kg/m^3, $T_i = 15$ K, $\bar{j} = 3949$ A/cm^2, and $j = 4700$ A/cm^2].

ℓ(m)	ΔT(K)	T_0(K)	P_0/P_i	p	T_c(K)
7.5	4.30	19.30	0.945	0.082	20.11
10.0	5.73	20.73	0.926	0.083	21.54
12.5	7.16	22.16	0.907	0.084	22.97

satisfying the additional requirements imposed by structural, electrical, and constructional considerations appears very difficult. Thus, although a cryogenic-aluminum Yin-Yang coil design with the required current density appears thermally feasible, the relatively short allowable coolant passage length – probably less than one circumferential length around the coil – renders the development of a complete design for a cryogenic-aluminum coil a formidable and as yet unsolved design challenge.

REFERENCES

5-1. F. H. Coensgen, *MX Major Project Proposal*, Lawrence Livermore Laboratory, Rept. LLL-Prop-142 (1976).

5-2. G. A. Carlson, *Parametric Design Study of Tandem Mirror Fusion Reactors*, Lawrence Livermore Laboratory, Rept. UCRL-79092 (1977); see also Chapter 10 of this report.

5-3. H. Hillmann, H. Kuckuck, H. Pfister, G. Rupp, E. Springer, M. Wilhelm, K. Wohleben, and G. Ziegler, "Properties of Multifilamentary Nb_3Sn Conductors," in *Proc. Superconductivity Conf., Stanford, CA, 1976* (in preparation).

5-4. C. E. Taylor, Lawrence Livermore Laboratory, private communication (1977).

5-5. Z. J. J. Stekly, "State of the Art of Superconducting Magnets," *J. Appl Phys.* 42, 66 (1971).

5-6. F. R. Fickett, "Magnetoresisitivity of Copper and Aluminum at Cryogenic Temperatures," in *Proc. Fourth International Conf. Mag. Tech. 1972* (p. 540-1).

5-7. D. N. Cornish, Lawrence Livermore Laboratory, private communication (1977).

5-8. *Alcoa Structural Handbook*, Aluminum Company of America, Pittsburg PA (1958).

5-9. *Handbook on Materials for Superconducting Machinery*, (1974) p. 4.2 1-10.

5-10. S. J. Wells, *Chemical Composition and Electrical Resistivity of Aluminum Alloys*, Hughes Aircraft Company, Rept. AFML-D5161.

CHAPTER 6. TMR NUCLEONICS

SUMMARY

We have completed preliminary nucleonics appraisals of the shielding required for the Yin-Yang magnets in the TMR plugs and of the central-cell blanket composition that would provide a tritium-breeding ratio of 1.10. It was specified that shielding for the plug coil must:

- Limit total nuclearly induced heating in the coil and cold structure to 10% of the I^2R heating in the unirradiated coil,
- Limit local nuclearly induced heating to three times the unirradiated values, and
- Allow a 1-year operational time between room-temperature anneals of the cryogenic aluminum in the Yin-Yang magnets. Calculations showed that an ~64-cm-thick, tungsten-based shield would meet these requirements.

Requirements for the central-cell blanket and shielding would be met by a 84-cm-thick, stainless-steel blanket that contains liquid lithium. Such a blanket would have a tritium-breeding ratio of 1.10 and would provide an energy multiplication of 1.20.

INTRODUCTION

Tritium breeding, conversion of thermonuclear neutrons to heat, radiation damage, activation, and component and biological shielding are all important nucleonics subjects that must be considered in the design of a fusion reactor. For this initial appraisal of the tandem mirror reactor (TMR), the limited nucleonics effort expended was concentrated in two areas:

- Shielding required for the end-plug Yin-Yang coils.
- Central-cell blanket.

Protecting the Yin-Yang plug coils, which are made of aluminum and designed to be used at cryogenic temperatures, is the major shielding challenge in this TMR design. The critical area appears to be at the inner mirror of the plug where DT plasma extending from the central cell generates 14-MeV neutrons at a significant rate.

The enhanced Q and favorable geometry of the central cell allow us to contemplate a blanket of modest performance. The enhanced Q eliminates the need for energy multiplication; and the very low area for neutron streaming (from the large length-to-diameter ratio of the cylindrical central cell) coupled with no requirement for energy multiplication leads to only a minimal requirement for neutron multiplication in the blanket. Our overall objective is to keep the blanket as simple and inexpensive as possible. Shielding for the superconducting coils of the central cell is in the 90 cms between the blanket and the coils. Ninety cm of steel- and lead-based shielding

plus the blanket should provide more than enough protection for these coils.

SHIELDING THE YIN-YANG COILS

The plasma plugs at either end of the TMR are confined by minimum-B magnetic fields. The field of each plug is generated by a pair of cryogenic-aluminum, Yin-Yang coils surrounded by two superconducting solenoids. To limit nuclear heating and radiation damage to acceptable levels, both sets of coils must be shielded from the fusion neutrons generated in *both the plasma plugs and in the* central cell.

The overall geometry of the plug is shown in Fig. 6-1. Figure 6-2(a-d) shows the Yin-Yang coils, the plasma, and the space available for shielding. Note where the magnetic flux bundle containing the plasma passes between the faces of the Yin-Yang coil. Shielding there is a major challenge because space is at a premium. Also, the thickness of the shield required between the coil faces will have an important effect on the overall size of the plug and thus on its cost. Figure 6-2 shows a 90-cm separation between the faces of the Yin-Yang coil, a plasma thickness of 50 cm, and a plasma width of 90 to 100 cm. A 5-cm-thick vacuum boundary around the plasma provides room for the 3.5 MeV alpha particles with their 1.5-cm gyroradius that are generated on the outer field lines. The remaining space (30 cm) is available for shielding. These dimensions are approximately consistant with the plug design assumed in the other chapters of this report and are a starting point for the shield analysis.

Both DD (2.45-MeV) neutrons and DT (14.1-MeV) neutrons are produced in the plug plasma. Figure 6-3 shows an estimate of the source distributions

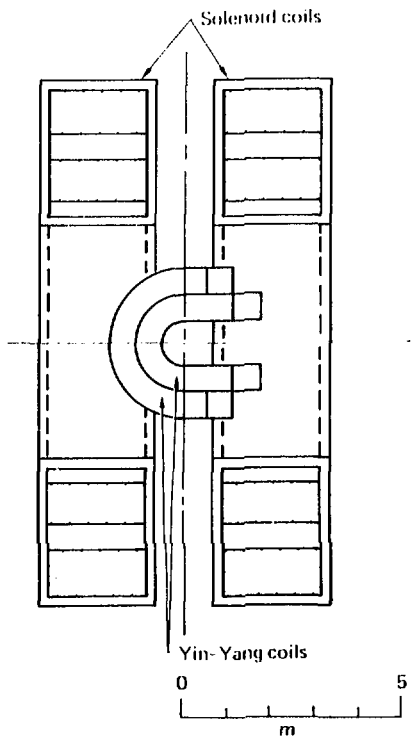

Fig. 6-1. Geometry of the TMR plug.

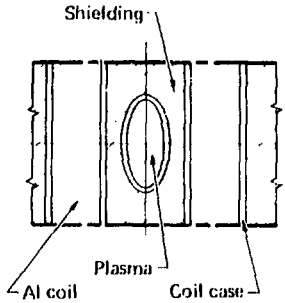

(a) Sect. A-A

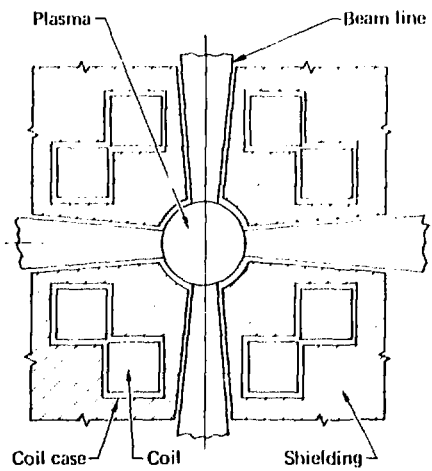

(b) Sect. B-B

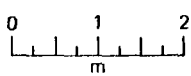

Fig. 6-2. Cross sections through the TMR plug, showing space available for shielding.

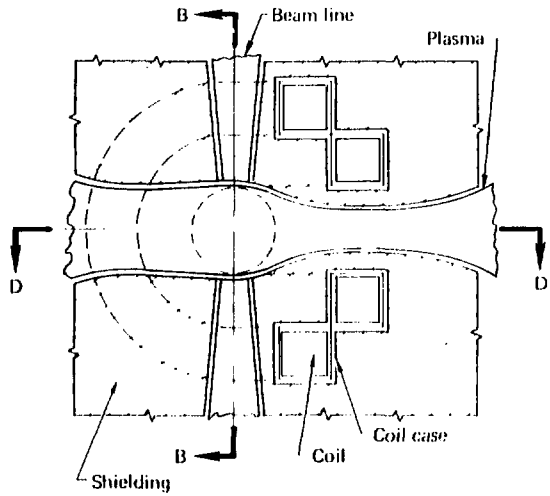

(c) Sect. C-C

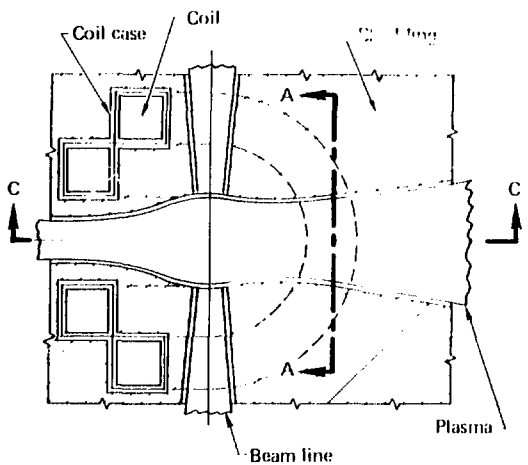

(d) Sect. D-D

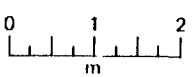

Fig. 6.2 (Continued)

for these DD and DT neutrons. The zero point on the z-(horizontal) axis is the plug center; the 140-cm point is a point in the center of the Yin-Yang coil located between the plug and the central cell. The nonsymmetric distribution of the DT reaction rate results from DT plasma extending from the central cell into the plug. Beyond z = 140 cm, the DT reaction rate remains constant at 1.9×10^{12} neutrons/cm^3·s. Plasma area and neutron source strengths versus 'z' are listed in Table 6-1. The rates at which DD and DT neutrons are generated in the inner half of the plug and between the faces of the inner Yin-Yang plug are listed in Table 6-2. The DT neutrons produced between the inner faces of the Yin-Yang coils plus

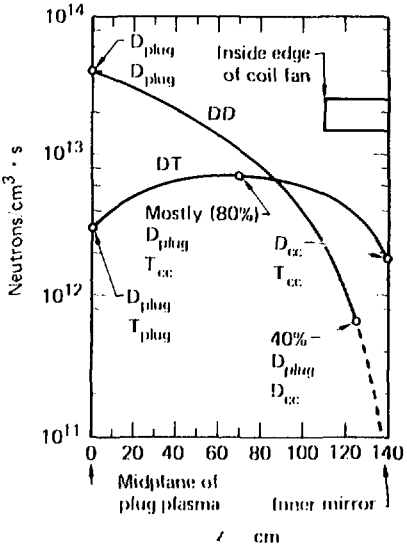

Fig. 6-3. Estimations of DD and DT neutron production in the inside half of the TMR plug (where cc indicates central cell).

Table 6-1. Neutron production in inner half of a TMR plug.

Distance z (cm)	Plasma area, A_p (10^3 cm^2)	n_{DD} (10^{17} cm^{-3} s_m^{-1})	n_{DD} (10^{16} cm^{-1} s_m^{-1})	n_{DD} (10^{17} s_m^{-1})	n_{DT} (10^{-1} s_m^{-1})	n_{DT} (10^{16} cm^{-1} s_m^{-1})	n_{DT} (10^{17} s_m^{-1})
0	7.1	40	29	20	5.0	2.2	1.5
14	6.9	32	22	31	4.5	3.1	4.3
28	6.5	26	17	24	5.7	3.7	5.2
42	6.1	20	12	17	6.5	4.0	5.6
56	5.7	15	8.6	12	6.9	4.0	5.6
70	5.4	11	5.9	8.3	7.0	3.7	5.2
84	5.0	7.1	3.3	4.9	6.7	3.3	4.6
98	4.6	4.2	1.9	2.7	6.0	2.7	3.8
112	4.2	2.1	0.88	1.2	5.0	2.1	2.9
126	3.8	0.67	0.25	0.35	3.6	1.4	2.0
140	3.4	0	0	0	1.9	0.65	0.91
154	3.8	0	0	0	1.9	0.72	1.0
168	4.2	0	0	0	1.9	0.80	1.1

Table 6-2. Generation rates of DD and DT neutrons.

	Generation rate (neutrons/s)	
	Inner half of plug; x = 0 to 170 cm	Between faces of inner Yin-Yang coil; z = 110 to 170 cm
DD neutrons	1.21×10^{19} (4.76 MW of 2.5-MeV neutrons)	1.14×10^{17} (0.05 MW)
DT neutrons	4.34×10^{18} (9.74 MW of 14-MeV neutrons)	6.5×10^{17} (1.46 MW)

the limited space for shielding in this region combine to form the dominant shielding problem for the TMR.

Shielding is required to limit heating and radiation (fast-neutron) damage in the coils to acceptable levels.

- Heating of the coils and cold structure must be limited to keep required refrigeration power to acceptable levels.

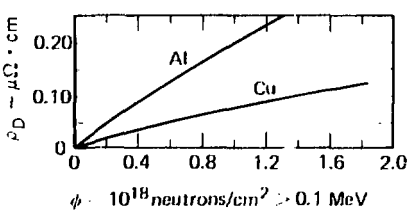

Fig. 6-4. Radiation-induced resistivity ρ_D increase for copper and aluminum vs fast neutron fluence ($E_n > 0.1$ MeV). Initial resistivities were 7.7×10^{-7} Ω•cm and 3.3×10^{-7} Ω•cm, respectively. The irradiation temperature was 4.9 K. (From Ref. 6-1.)

- Radiation damage to the aluminum conductor and other coil components must also be limited; fast-neutron damage to the conductor increases its electrical resistance.

Figure 6-4 shows (1975) data for the increase in irradiation-induced resistivity ρ_D as a function of neutron fluence (with a very slightly degraded fission spectrum) for copper and aluminum at 4.9 K. Annealing at room temperature produces 85% recovery in copper and complete recovery in aluminum. The influence of cyclic annealing on the production of damage-induced resistivity is uncertain.[6-1] The temperature and resistivity assumed for the aluminum conductor in the Yin-Yang coils are 20 K and 5.4×10^{-9} Ω•cm. The resistivity increase versus neutron fluence ($E_n > 0.1$ MeV) for this conductor is assumed to be the same as shown in Fig. 6-4. Since conductor current must remain constant, an increase in conductor resistance manifests itself as an increase in Joule (I^2R) heating.

We must consider local conductor heating as well as heating of the total conductor plus that of the cold coil structure. Local conductor heating is important because the variation of conductor resistivity with temperature is nonlinear. Because above 20 K resistivity increases rapidly, the temperature of the conductor must be kept below 20 K.

Both the shielding and coil designs will probably play important and interdependent roles in keeping coil refrigeration power and local conductor temperature to acceptable levels while keeping critical shield thicknesses and thus the overall plug size as small as possible. At this early stage in the TMR design effort, we developed the design of the plug coil without considering shielding. To see if shield requirements influence the design of the plug coil, we have completed an initial appraisal of the shielding. For this appraisal, we specified three objectives:

- Limit total nuclearly induced heating (neutron and gamma heating plus neutron-induced I^2R heating) in the coil and cold structure to 10% of the I^2R heating in the unirradiated coil. The I^2R heating in the unirradiated Yin Yang coil pair is 475 kW;
- Limit local nuclearly induced heating to three times the unirradiated value of 0.0834 W/cm^3 [$P = J^2\rho$ = (4930 A/cm^2)^2 × 5.4 × 10^{-9} Ω·cm]; and
- Allow a 1-year operational time between room-temperature anneals of the cryogenic aluminum.

To estimate nuclear heating and neutron and gamma fluxes in the mirror regions, we ran a series of coupled, neutron-gamma Monte Carlo calculations.[6,2,3] To do this, we subjected a model of the mirror region to an isotropic source of 2.45- and 14.1-MeV neutrons generated between the Yin Yang coil faces of the mirror. The calculational model (shown to scale in Fig. 6-5) is one quadrant of the mirror region. All its outer boundaries are reflecting, and it is 60 cm in depth. These calculations were performed for shield thicknesses of both 15 cm and 25 cm, where shield thickness refers to the space above and between the plasma and the coil available for shielding. The initial coil design allows for a 15-cm-thick shield in this region.

Results of the Monte Carlo calculations are listed in Table 6-3. Columns 4 through 8 list nuclear heating and neutron and gamma path lengths per source neutron. "Local" refers to the inner coil zone located above the plasma zone (see Fig. 6-5). "Total" refers to all four coil zones (plus coil case zones for heating). Columns 9 through 13 of Table 6-3 list heating rates plus neutron and gamma

Table [illegible]. Summary of [illegible] results and limits, [illegible]

Case No.	Source neutron energy, E_n MeV	Steel target thickness, cm	Neutron flux [illegible]		[illegible]	[illegible]	[illegible]	[illegible]	[illegible]	[illegible]

[illegible]

[illegible]

Note: [illegible]

[illegible]

[illegible]

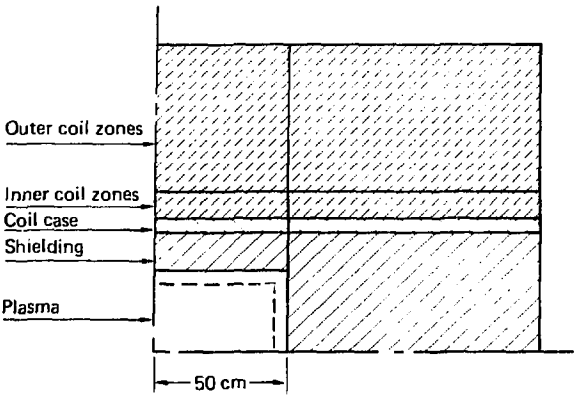

Material	Composition
Outer coil	Al 50% + Fe 50%
Inner coil	Al 100%
Coil case	Fe 100%
Shielding	W 80% + H_2O (borated) 20%

Fig. 6-5. Model used for Monte Carlo calculation of nuclear heating and neutron and gamma fluxes in the mirror regions of the TMR plug.

fluxes at the specified DD and DT neutron-source strengths. Calculated local integral flux spectra for neutrons and gammas are given in Fig. 6-6 and 6-7, respectively.

With only 15 cm of shielding, these calculations predict that direct nuclear heating is 107 kW. Also, at the calculated local neutron flux [ϕ_{DT+DD} ($E > 0.1$ MeV) = 1.96×10^{13} neutrons/cm^2•s], the allowable local radiation-induced resistivity increases in aluminum of $3 \times \rho$ = 0.0162 μΩ•cm is reached after only 3,780 s (1 h) of operation [$t = \Delta\rho / \frac{\Delta\rho}{\Delta\phi}/\phi = 0.0162/2.21 \times 10^{-19}/1.94 \times 10^{13}$ s].

It is clear that shield thickness must be increased and that the local allowable fast-neutron flux from DT neutrons will dictate what that shield thickness must be to allow 1 year of operation between anneals. The allowable local flux ($E > 0.1$ MeV) is:

$$\phi_{allowable} = \Delta\rho \times \frac{1}{\frac{\Delta\rho}{\Delta\phi}} \times \frac{1}{t}$$

$$= 0.0162 \ (\mu\Omega\cdot cm) \times \frac{1}{2.21 \times 10^{-19}}$$

$$\frac{\mu\Omega\cdot cm}{neutrons/cm^2} \times \frac{1}{3.15 \times 10^7 s}$$

$$= 2.33 \times 10^9 \ neutrons/s\cdot cm^2$$

Thus, our calculations show that the local neutron flux must be reduced four orders of magnitude below that achieved with the 15-cm-thick shield.

To estimate how thick the shield must be, we must know the attenuation properties of the shield. These

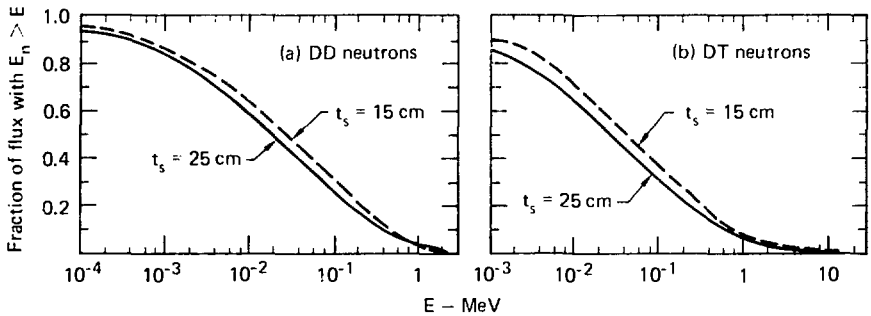

Fig. 6-6. Local neutron flux spectra from DD and DT neutrons.

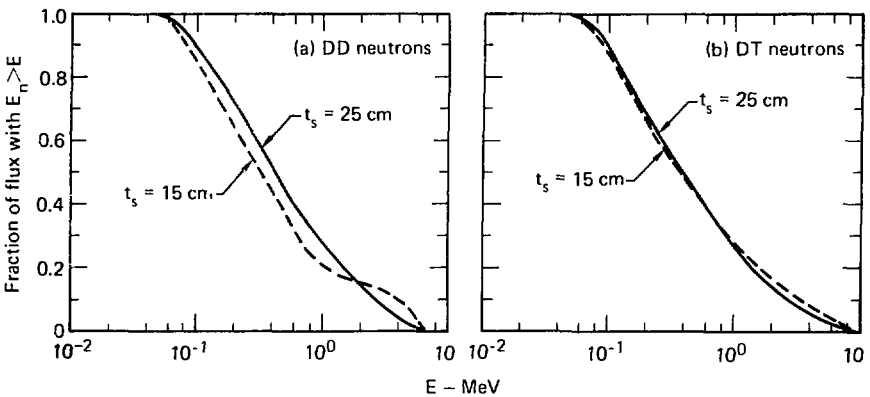

Fig. 6-7. Local gamma flux spectra from DD and DT neutrons.

properties are estimated by repeating the Monte Carlo calculations with a 25-cm-thick shield. Results of these calculations are listed in Table 6-3. Comparing the 15- and 25-cm cases gives scaling relationships by which we can estimate the required shield thickness. These relationships are listed in Table 6-4 as decade attenuation lengths (thickness of shield needed for a factor of 10 reduction in nuclear heating and neutron fluxes). With a 12.5-cm decade attenuation length for the local fast fluence from DT neutrons, the estimated shield thickness needed to protect the Yin-Yang coil from DT neutrons is

$$t_s = 15 \text{ cm} + \log\left(\frac{\phi_{ts=15}}{\phi_{allowed}}\right) L_{\phi \text{ local}}$$

$$= 15 + \log\left(\frac{1.85 \times 10^{13}}{2.33 \times 10^{9}}\right) \quad 12.5$$

$$= 63.7 \text{ cm}.$$

Our assumption that DT fusion in the inner mirror dominates the shielding requirement for the plug coil appears to be correct. Providing the coils with ~64-cm-thick shields in the inner mirrors will require a significant increase in plug size, because the initial plug design allows for only 15 cm of shielding.

Another potential problem area is where beam lines pass close to coils. We have not examined beam-line shielding; however, we assume that a plug sized to provide the ~64-cm-thick shielding for the inner coil will have more than enough room to allow shielding the beam lines also. This assumption must be checked when a more exact and complete TMR shielding study is undertaken.

We used a tungsten-based shield for this shield analysis. Since tungsten is quite expensive, a cheaper iron plus lead shield should be used for most of the plug, where ~1 m of shielding can be accommodated. (If the latter were used in the inner region, ~90-cm-thick shielding would be needed.)

CENTRAL-CELL BLANKET AND SHIELDING

The fusion neutrons (effectively all 14-MeV DT neutrons) produced in the central plasma cell are converted to useful heat and used to breed tritium in the blanket. This blanket plus shielding must limit the nuclear heating and radiation damage in the superconducting coils of the central cell to acceptable levels.

The principle nucleonics objective for the blanket is the provision of adequate tritium breeding at low cost: energy amplification in the blanket is not a primary objective. Although

Table 6-4. Shield attenuation lengths.

Source neutron energy (MeV)	Shield attenuation length (cm/decade)			
	For energy deposition		For neutron flux (E > 0.1 MeV)	
	Local	Total	Local	Total
14.1	12.7	12.2	12.5	12.2
2.45	9.42	9.21	8.84	9.34

there are many conceptual blankets that might meet this objective, we have chosen to look first at one consisting of a stainless-steel structure, a liquid-lithium (natural) tritium-breeding medium, and helium coolant. This choice does not imply that this blanket is best, only that it is a reasonable starting point. A breeding ratio T/n of 1.10 tritons per DT fusion in the central cell is considered adequate. An excess of 0.10 tritons per DT fusion would cover losses and allow for uncertainties in the calculations and nuclear data.

To determine the performance envelope of a cylindrical, stainless-steel blanket containing lithium, we performed a series of neutronics calculations in which the blanket was modeled as a cylindrical annulus 119 m long with an inner radius of 154 cm. Calculations were made for various combinations of first-wall thicknesses (0 or 2 cm) and ratios (0 to 0.3) of stainless-steel volume fraction to lithium volume fraction.

Results of these calculations are plotted in Fig. 6-7 for three effective lithium thicknesses. (Effective thickness is geometric thickness times volume fraction.) For these calculations, the lithium volume fraction is held constant at 0.649 while the stainless-steel volume fraction is varied. For these calculations, we used 316 stainless steel (SS-316) having a density of 7.97 g/cm^3 composed of 68.5wt% Fe + 12wt% Ni + 17wt% Cr + 2.5wt% Mo. A cylindrical volume source of isotropic, 14-MeV neutrons, 2.3 m in diameter and 119 m long, approximated the plasma.

The curves in Fig. 6-7 are used to examine the tradeoffs in blanket mechanical design (e.g., first-wall thickness, ratio of structure to lithium, and blanket thickness) needed to achieve the desired T/n = 1.10. To use the curves, specify two of the three variables and find the third variable by a linear interpolation between the appropriate curves.

After a number of iterations, we evolved an acceptable mechanical design for the blanket that meets the tritium-breeding requirement. This design has a 0.5-cm-thick wall, a lithium volume fraction of 0.691, and a SS-316 volume fraction of 0.179. From Fig. 6-8, the thickness required for T/n = 1.10 is 84.1 cm. Energy multiplication in this blanket is 1.20.

The conceptual design of the central cell allows for 90 cm of shielding between the blanket and blanket coolant plena and the superconducting coils of the central cell. Based on an early shielding study,[6-4] the blanket plus 90 cm of iron- and lead-based shielding should provide sufficient protection for the central-cell coils.

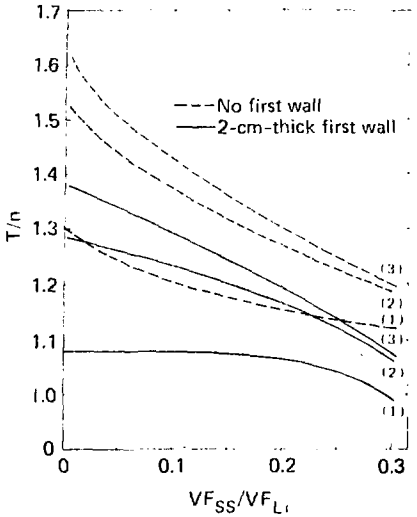

Curve no.	Blanket thickness X fuel volume fraction:
1	90 cm X 0.649 = 58.4 cm
2	135 cm X 0.649 = 87.6 cm
3	180 cm X 0.649 = 116.3 cm

Fig. 6-8. Tritium breeding ratio T/n in a lithium and stainless-steel blanket vs the ratio of the volume fraction of stainless steel to that of lithium VF_{SS}/VF_{Li}. Blanket geometry: cylindrical; inner radius = 156cm; Length = 119 cm.

REFERENCES

6-1. J. F. Guess, R. W. Boom, R. R. Coltman, Jr., and S. T. Sekula *A Survey of Radiation Damage Effects in Superconducting Magnet Components and Systems*, Oak Ridge National Laboratory, Rept. ORNL-TM-5187 (1975).

6-2. E. F. Plechaty and J. R. Kimlinger, *TARTNP: A Coupled Neutron-Photon Monte Carlo Transport Code*, Lawrence Livermore Laboratory, Rept. UCRL-50400, Vol. 14 (1976).

6-3. R. J. Howerton *et al.*, *An Integrated System for Production of Neutronics and Photonics Calculational Constants*, Lawrence Livermore Laboratory, Rept. UCRL-50400, Vol. 6, (1975) and Vol. 16 (1976).

6-4. R. W. Moir, Scientific Editor, *Standard Mirror Fusion Reactor Design Study*, Lawrence Livermore Laboratory, Rept. UCID-17644 (in preparation).

CHAPTER 7. A NEUTRAL-BEAM INJECTOR FOR THE TANDEM-MIRROR FUSION REACTOR DELIVERING 147 MW OF 1.2-MeV D°

*J. H. Fink** *and G. W. Hamilton*

*On loan from Westinghouse Electric Corp.

SUMMARY

We present a conceptual design of a high-current, 1.2-MeV D^0 injector with an anticipated operating efficiency of 73%. Major advances in beam technology are needed to meet these requirements, including a continuous source of negative ions, an efficient electron-stripping cell, and the development of associated power conditioning and control equipment. All components in our proposed beam line are elaborations of physics experiments already reported in the literature; therefore, we believe the neutral-beam requirements of the tandem mirror reactor (TMR) can be realistically satisfied in the not too distant future.

INTRODUCTION

The TMR[7-1] requires four neutral-beam injectors, each capable of delivering a continuous 122.5 A of 1.2-MeV deuterium. Considerable development must be expended to make these injectors reliable, efficient, and at reasonable cost. No revolutionary inventions are needed to meet these goals because suitable beam-line components can be made from extrapolations of current experimental apparatus. In this study of neutral-beam injectors, we shall therefore consider the general characteristics of the beam line and the nature of the components best suited to it, analyze each component in detail, and evaluate the performance of the ensemble.

GENERAL CONSIDERATIONS

High-energy neutral beams are formed by neutralizing ions, previously extracted from a plasma source, which are accelerated to the desired energy and aimed at an appropriate focus. As a consequence, the power efficiency of a neutral-beam line is highly dependent upon the ion neutralization efficiency.

Neutral beams of 100 keV or less can be efficiently made from positive ions that have been neutralized by charge exchange in a gas or vapor cell however, this process is so ineffective at higher energies that efficiency enhancement techniques become attractive. For good performance, we must have either continuous recirculation of unneutralized ions through the neutralizer cell[7-2] or energy recovery from the remaining unneutralized ions.[7-3]

At 1.2 MeV, less than 0.04% of an atomic deuterium ion beam is neutralized in a gas or vapor cell.[7-4] Because enhancement techniques are not much help, we must turn to other, more effective sources of neutrals. Beams of molecular ions could be considered for this purpose.

About 10% of a beam of 2.4-MeV of D_2^+ ions can be neutralized in a gas cell to split into two 1.2-MeV atomic components. Similarly, 23% of a 3.6-MeV beam of D_3^+ ions can be neutralized to dissociate into three 1.2-MeV atomic components; however these high voltages introduce insulation problems. Only 1.2 MV is required when negative ions are used as a source of very high-energy neutral beams.

The extra electrons can be detached from negative deuterium ions.[7-5] This detachment could be done for a beam of 1.2-MeV ions with either an electric field of about 4 MV/cm or a magnetic field of approximately 36 T; however, these fields are excessive. Although photodetachment could achieve 95% stripping, the required optical cavity is too large to be practical.

The optimum stripping efficiencies of gas, vapor, and plasma cells are insensitive to the target composition and are relatively independent of the beam energy above 100 keV. A well designed plasma cell of proper thickness could strip 85% of an incident negative-ion beam; a gas or vapor cell of suitable thickness could strip 65% of a corresponding beam.

If the size of the optical cavities required for photodetachment cannot be significantly reduced, plasma stripping of negative ions will be the most favorable method for forming 1.2-MeV neutrals. Plasma stripping offers the highest neutralization efficiency in a practical stripping-cell design.

The stripping-cell plasma considered here is generated by ionizing cesium vapor on two hot, tungsten plates — one on each side of the ion-beam line — in a process similar to that employed in a Q machine.[7-6] The tungsten temperature must be high enough to support electron emission for space-charge neutralization of the cesium ions.

Although negative ions are easy to strip, their large stripping cross section creates problems in the accel region of the beam. The ions and electrons generated from charge exchange and ionization of the background gas in the wake of the high-energy beam will bombard the grid, causing it to sputter and overheat. To obtain an acceptable grid loading which can be sustained continuously, the background gas density must be low and the beam current density held down, thereby reducing the rate of background ion and electron production.

The current density of the beam in a Pierce extraction geometry[7-7] is already limited by the maximum tolerable voltage stress between adjacent grids. In addition, a low-pressure environment must be maintained above the accel column.

Suitable pressure can be obtained if the injector walls at ground potential are covered with cryopump panels.

The cryopumps should be rotated occasionally so that they can be outgassing on the outer side while still pumping on the inside.

Forming negative ions via double-charge exchange in a cesium-vapor cell helps to reduce the gas load. This cell converts about 20% of an incident 2-keV positive ion beam into negative[7-8] ions and acts as a gas curtain to block the flow of low-temperature neutral gas streaming out of the positive-ion sources.[7-9] As a result, the gas flowing out of the positive-ion source can be pumped independently from that in the negative-ion accel region.

In this study, we use a Lawrence Berkeley Laboratory/Lawrence Livermore Laboratory ion source with hollow-tungsten, barium impregnated cathodes to provide a long, continuous operating life. We extract a beam 8 cm wide and 5 m long. This cross section facilitates gas removal and simplifies the design of the cesium double charge-exchange cell and the plasma-stripping cell. The narrow beam also makes it possible to use short grid laterals, which are easier to maintain at a uniform temperature.

The extraction grids are 40% transparent and have hollow molybdenum laterals that are cooled to 500°C by a flow of liquid metal. The source, mounted inside a large vacuum duct, is supported by high-voltage insulators above and below the beam line. Gas is removed from this region by two large mercury ejector pumps mounted at the upper and lower ends of the pump duct.

Maintaining reliable high-voltage vacuum insulation is a critical problem in the design of an MeV injector. Experience shows there is less likelihood of breakdown across a series of low-voltage gaps than there is across a single high-voltage gap. Therefore, electrostatic shields are introduced at various intermediate potentials between the high-voltage components and ground. These shields are at the same potential as the various grids in the accel column. The source is at -600 kV with respect to ground; the stripping cell is at +600 kV. Background pressure in this region is reduced by pumping through 80% transparent electrostatic shields.

The capacitance between adjacent shields stores many joules of energy. Thus any incidental discharge can easily turn into a catastrophic arc. This arc can be inhibited by forming the shields out of many small sections. These sections can be isolated by using resistors which impede the transfer of energy from section to section.

Auxiliary components are housed above and below the beam line in large, high-pressure SF_6 vessels that are shielded from the neutron and gamma fluxes emitted by the reactor. These

vessels hold electrical power supplies, isolation transformers, high-voltage insulators, liquid-metal heat exchangers, and gas and water services for the ion source. Although the design of power supplies is not a trivial task, we shall not address that problem in this study.

THE SOURCE OF NEGATIVE IONS

As part of an operating reactor, the source must deliver a continuous beam of negative ions for thousands of hours while permitting very little low-temperature gas to flow into the accel region. This can be accomplished with a suitably designed double charge-exchange cell. If the cell has the proper thickness (i.e., vapor density-length product), the cesium vapor converts 20% of a 2-keV beam of positive ions into negatives; the remainder of the beam exits as 2-keV neutrals. The cesium vapor also acts as a curtain that blocks the flow of low-temperature gas along the beam line.

To facilitate pumping low-temperature gas from the source, the ions are formed into a large beam of narrow width. The source (Fig. 7-1) delivers 800 A of positive ions (at a current density of 0.5 $A \cdot cm^{-2}$) through a sequence of four 40% transparent grids that are 8 cm wide and 5 m long. Average current density in the extracted beam is 0.2 $A \cdot cm^{-2}$.

A version of the LBL/LLL source (described elsewhere[7-5]) can be modified to use indirectly heated, hollow cathodes made of two tungsten, barium-impregnated emitters mounted face to face. The source plasma originates from a series of 45-V discharges, requiring 1.93 kW of arc power per extracted ampere, and the heaters operate at 5 V with 0.19 W/A.

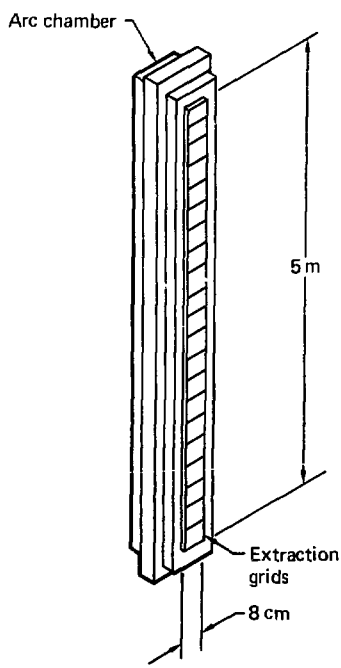

Fig. 7-1. Details of a 800-A ion source where η_1 = 40%, η_2 = 50%, η_3 = 10%; P_{htr} = 0.15 MW (5 V), and P_{arc} = 1.54 MW (45 V).

Thus, the total arc power is 1.54 MW and the filament power is 0.15 MW.

Gas seeping out of the ion source plasma flows through the aperture in the grids and is pumped away via a large vacuum duct behind the source (see Fig. 7-2). Although the LBL/LLL source delivers an ion beam with a composition of η_1 = 75% D^+, η_2 = 15% D_2^+, and η_3 = 10% D_3^+, we can assume that the beam composition, in the absence of hot-tungsten filaments, will be η_1 = 40% D^+, η_2 = 50% D_2^+, and η_3 = 10% D_3^+, with a gas efficiency ξ_G = 30%, the extracted ion current (D^+) is accompanied by a gas flow of

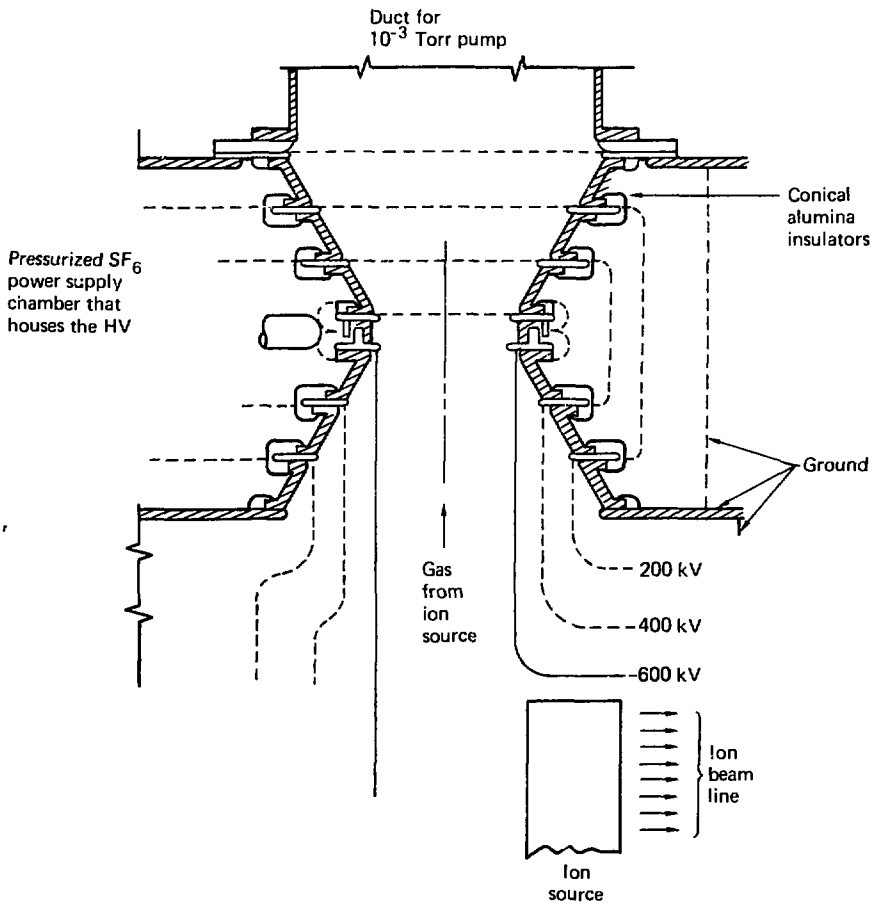

Fig. 7-2. Pumping through the high-voltage insulators.

$$Q_p = (0.19)\left(\frac{1}{\xi_G} - 1\right)\left(\frac{1}{2}\eta_1 + \eta_2 + \frac{3}{2}\eta_3\right) I^+ = 302 \text{ Torr}\cdot\text{l}\cdot\text{s}^{-1} .$$

This gas is removed by two large mercury ejector pumps located at the upper and lower ends of the pump duct. The throat pressure of the pump is assumed to be 10^{-3} Torr; the pressure in the vicinity of grid 4 is maintained at 2×10^{-3} Torr. To accommodate the gas at 500 K, the pump duct radius must be at least

$$R = \left[\frac{Q_p}{7.28\ \pi\ \Delta\rho}\right]^{1/2} \left(\frac{M}{T}\right)^{1/4} = 30 \text{ cm}.$$

Grid 1 floats (see Fig. 7-3), drawing a net zero current of ions and electrons from the plasma; grid 2, at -11.75 kV with respect to the source, extracts 0.5 $A\cdot cm^{-2}$ of positive ions from the plasma. These ions are subsequently decelerated to -1.75 keV at

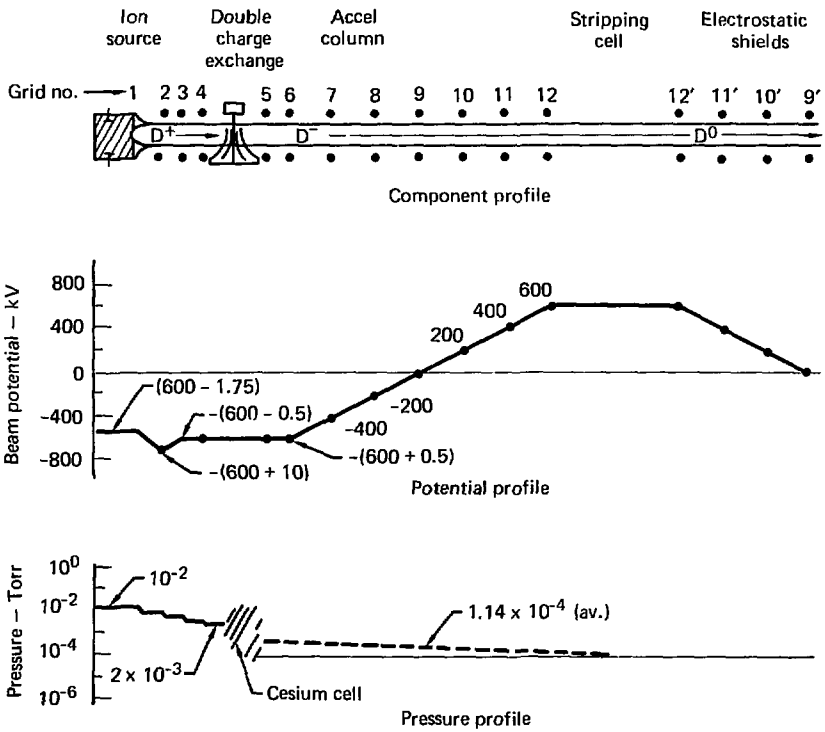

Fig. 7-3. Beam-line profiles (component, potential, and pressure).

grid 4 for injection into the cesium-vapor cell. To prevent ions from being drawn into the grid 2-3 region, grid 3 is biased at +500 V with respect to grid 4. Extraction grids 1 through 4 are curved to aim the positive ions at a line focus in the plane of grid 6. The maximum theoretical peak current density that can be obtained at the focus of a two-dimensional beam is

$$\hat{J}_{max} = J_K \left(\frac{4\ eV}{\pi\ KT}\right)^{1/2} \alpha, \qquad (7\text{-}1)$$

where J_K is the emitted current density, V is the beam energy in the region of the focus, KT is the ion energy, and α is the half angle that encompasses all ion trajectories passing through the focus. If 20% of the positive ion current is converted into negative ions in the cesium cell and the grid is 40% transparent, the virtual source of negative ions has a current density of 0.04 $A \cdot cm^{-2}$. The potential at grid 6 is 2.25 keV relative to the ion source; the angle α equals the ratio of half the beam width (4 cm) to the distance from the ion source to the focus (50 cm).

We can assume from Eq. (7-1) that the ions have a distribution of velocities normal to the beam axis that is a function of their temperature in the source. However, allowance should be made for the transverse energy imparted to the ions by the curvature of the electric fields, by scattering, and by the dissociation of the D_2^+ and D_3^+ molecules in the beam. The effective transverse energy of ions emitted from an LBL/LLL source operating at 15 kV is observed to be 4.6 eV, and the corresponding energy of the ions emitted from this source will be at last twice that value. Therefore, the peak current density of negative ions in the plane of grid 6 must be about 0.056 $A \cdot cm^{-2}$, with an average value of somewhat less than that.

Extracted positive ions in transit from the ion source to the cesium-vapor cell are subject to charge exchange with the background gas. The fraction of the beam lost in this way can be estimated by

$$F_{10} = n_b\ \sigma_{10}\ X,$$

where n_b is the density of the background gas, σ_{10} is the average cross section of neutralization, and X is the path length. If one assumes an equal pressure drop across each grid, then a source pressure of 10^{-2} Torr and a pressure beyond grid 4 of 2×10^{-3} Torr will result in a pressure of 8×10^{-3} Torr in the grid 1-2 region. With the gas at 1000 K, the background density between grids 1-2 will be 8×10^{13} cm^{-3}. Ions can be extracted from the plasma at 0.5 $A \cdot cm^{-2}$ with a bias of -11.75 kV if the grid 1-2 spacing is 0.28 cm

(according to Child's Law). The neutralization cross section corresponding to the mean ion energy across the gap is estimated to be 6×10^{-16} cm^2/D_2, so that F_{10} equals 1.5%. Conditions between grids 2-3 are similar; hence, another 1.5% of the beam is lost there.

The above values are recorded in the second and third lines of Table 7-1, along with an estimated background ionization rate that is equivalent to 0.1% of the positive-ion beam. Only 776 A of the 800 A of ions emitted from the source enter the double charge-exchange cell.

Table 7-1. Distribution of currents along the beam line.

Line	Region along beam line	Beam neutralization (%)	Beam current[a] D^+ (A)	D^- (A)	D^0 (A)	Background ionization (%)	Background current[b] Ion (A)	Electron (A)
1	*Ion source*	–	*799.7*	–	–	–	–	–
	Extractor: between grids							
2	1-2	1.5	*787.7*		(12.0)	0.1	0.8	-0.9
3	2-3	1.5	*775.9*		(11.8)	0.1	9.8	-0.8
4	Double charge-exchange cell	80.0	–	*155.2*	(620.7)	10.0	-15.5	1.5
	Between grids							
5	3-6	–	–	–	–	0.2	-0.3	0.3
6	6-7	1.3	–	*153.2*	(2.0)	0.24	0.4	0.4
7	7-8	0.5	–	*152.4*	(0.8)	0.24	-0.4	0.4
8	8-9	0.3	–	*152.0*	(0.4)	0.16	-0.2	0.2
9	9-10	0.2	–	*151.7*	(0.3)	0.11	-0.2	0.2
10	10-11	0.2	–	*151.4*	(0.3)	0.09	-0.1	0.1
11	11-12	0.1	–	*151.2*	(0.2)	0.07	-0.1	0.1
12	Stripping cell: between grids 12-12'	81.5	(27.2)	(0.8)	*123.2*	0.2	0.2	-0.2
13	Drift region through electrostatic shield and beyond)	0.6	(0.7)	–	*122.5*	0.6	0.7	0.7

[a]The main beam current is italicized; numbers in parentheses represent beam loss.

[b]The positive current flow is in the direction of the beam.

The combined reaction of cesium and background gas between grids 3-6 constitutes the double charge-exchange cell. Thus, 20% of the positive ion beam is converted to negatives and the remaining 80% exits as neutrals. This is shown in the fourth and fifth lines of Table 7-1, along with an estimated electron drain (equal to 10% of the beam current) out of the cesium to grid 3 and a corresponding drain of positive ions (equal to 0.2% of the beam current) to grid 6. Consequently, 155 A of D^- and 621 A of neutrals enter the accel region at ~2 keV.

THE HIGH-VOLTAGE ACCEL COLUMN

A Pierce-type accel system accelerates the negative ions as though they were part of a beam of infinite cross section. This is done by varying the potential along the beam line in accordance with Child's Law for planar geometry; i.e.,

$$J = q \frac{V^{3/2}}{X^2} ,$$

where J is the beam-current density, q is a constant, and V is the potential at any distance X from the ion source.

The potential along a beam of finite size is controlled, in practice, by a sequence of grids placed around the beam at suitable voltages. If this potential is to be effective, the spacing between adjacent grids (ΔX) must be about the same as the beam width. Therefore, if ΔV is the potential between adjacent grids, the average stress between them is

$$\left(\frac{\Delta V}{\Delta X}\right) = 4/3 \left(\frac{J}{q}\right)^{1/2} V^{1/4} . \quad (7-2)$$

The greatest stress occurs between grids at the highest potential. If we specify a mazimum tolerable stress (E_M) to be permitted between grids, we can establish a maximum current density that can be used in the accelerator. By rearranging Eq. (7-2), we find

$$J_M = (9/16) q E_M^2 V_O^{-1/2} . \quad (7-3)$$

Equation (7-3) shows that the maximum allowable current density in a Pierce column varies inversely with the square root of the desired energy beam. If we apply Eq. (7-3) to a deuterium negative-ion beam with no molecular components, we have

$$q = (4/9) \varepsilon_0 \left(\frac{2e}{M}\right)^{1/2}$$

$$= 3.88 \times 10^{-8} \text{ A} V^{-3/2} .$$

Thus, if E_M is assumed to be equal to or less than 50 kV/cm, the current density in a 1.2-MeV accelerator should not exceed 0.05 $A \cdot cm^{-2}$.

If we rewrite Child's Law, we can find the appropriate grid location at any potential from

$$X = (q/J)^{1/2} V^{3/4}$$

$$= 8.81 \times 10^{-4} V^{3/4} \text{ cm}, \qquad (7\text{-}4)$$

where J equals $0.05\ A \cdot cm^{-2}$. We have used Eq. (7-4) to estimate the location of grids 6-12, arbitrarily setting the grid potentials at multiples of 200 kV. Had we chosen to conduct a more detailed study, we would have used computer analysis to verify the grid potentials, location, and shape.

The positive-ion beam extracted from the source is driven through the cesium double charge-exchange cell, where 20% of it becomes negative and the remainder becomes neutral. As a result, all ions extracted from the source enter the accel region, but only those atoms in the high-energy neutral beam leave the injector. A gas load equivalent to their difference must be pumped away by the cryopump panels surrounding the beam line.

The low-temperature gas flow equivalent to the extracted ion beam (I^+) can be expressed as

$$Q_B = (0.19)\left(\frac{1}{2}\eta_1 + \eta_2 + \frac{3}{2}\eta_3\right) I^+$$

$$= 129.2 \text{ Torr} \cdot l \cdot s^{-1}.$$

The gas flow equivalent to 122.5 A of neutral beam D^0 is

$$Q_N = (0.19) D^0 = 23.3 \text{ Torr} \cdot l \cdot s^{-1}.$$

The cryopumps must therefore handle the difference:

$$Q_{cp} = (Q_B - Q_N) = 105.9 \text{ Torr} \cdot l \cdot s^{-1}.$$

A baffled cryopanel has a pumping speed of $9\ l \cdot s^{-1}/cm^2$. This will be reduced in practice to about $2\ l \cdot s^{-1}/cm^2$ to allow for the pumping restriction created by the electrostatic shields between the beam line and the pumping walls. Thus, two 5-m by 5-m walls of cryopanels — one on each side of the beam line — will establish a pumping speed of $10^6\ l \cdot s^{-1}$, and the average pressure in the injector will be less than

$$P = \frac{Q_{cp}}{S} \approx 10^{-4} \text{ Torr}.$$

The fraction of negative ions that becomes neutral as a result of electron stripping between the various grids of the accel system can be estimated by

$$F_{-10} = n_b \int_{\Delta X} \sigma_{-10}\, dX.$$

The ionization rate of the background gas can be similarly evaluated in terms of a fraction of the incident beam; i.e.,

$$F_i = n_b \int_{\Delta X} \sigma_i\, dX.$$

The stripping cross section for negative ions (σ_{-10}) and the ionization cross section (σ_i) are both known

to be functions of the energy of the incident ion beam (see Fig. 7-4); the variation of the beam potential along the beam path has been previously evaluated. This enables us to determine that the cross sections are a function of the beam path (see Fig. 7-5). We have calculated the area under each section of curves, corresponding to particular grid gaps. The fractions F_{-10} and F_i are computed from an assumed background gas density of $n = 2.3 \cdot 10^{12}$ cm^{-3}. These values are tabulated as the beam neutralization and the background ionization in lines 6 through 11 of Table 7-1. From these values, we determine that only 151 A of D^- enters the stripping cell.

THE STRIPPING CELL AND BEYOND

The fractions of the incident negative-ion beam that remain negative, become neutral, or become positive can be represented by the same equations for both a vapor cell and a plasma cell; i.e.,

$$F_0 = \left(\frac{\sigma_{-10}}{\sigma_{-10} - \sigma_{01}}\right)\left[\exp(-\sigma_{01}\pi) - \exp(-\sigma_{-10}\pi)\right], \quad (7\text{-}5)$$

$$F^- = \exp(-\sigma_{-10}\pi), \quad (7\text{-}6)$$

$$F^+ = \left(1 - F_0 - F^-\right), \quad (7\text{-}7)$$

where σ_{-10} is the stripping cross section of the negative ion, and σ_{01}

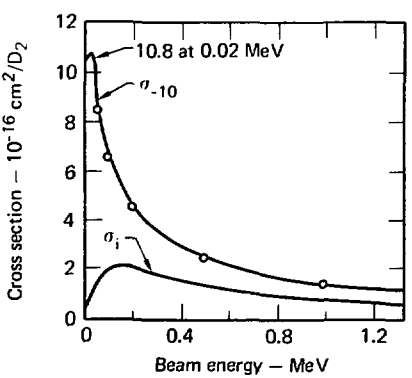

Fig. 7-4. Ionization and charge-exchange cross sections as a function of beam energy.

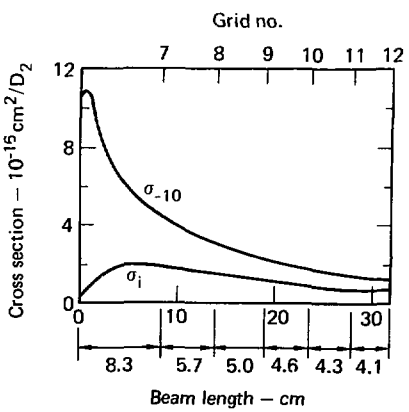

Fig. 7-5. Ionization and charge-exchange cross sections along the beam path.

is the corresponding ionization cross section of the neutral. At high energy, we neglect the cross sections σ_{1-1}, $\sigma_{-1,1}$, and σ_{0-1}.

The appropriate cross sections for a 1.2-MeV negative ion beam are listed below for both vapor and plasma.

Cross section (10^{-16} cm^2/atom)	Vapor	Plasma
σ_{-10}	1.2	14.0
σ_{01}	0.26	0.66

The solutions to Eqs. (7-5) through (7-7) are plotted as a function of target thickness in Figs. 7-6 and 7-7. An optimum stripping of 65% is obtainable with a vapor target that is 1.6×10^{16} cm^{-2} thick; an optimum 85% stripping can be obtained with a plasma target 2×10^{15} cm^{-2} thick. The high efficiency of plasma stripping has been experimentally verified.[7-10]

The unneutralized portion of the beam at the optimum vapor- and plasma-cell thickness is composed of almost equal densities of positive and negative ions. This composition introduces problems when one attempts to recover the energy from the ions. To circumvent this difficulty, we propose to use an over-dense plasma cell. The stripping efficiency of this over-dense cell would be reduced to 81.6%, 18.0% of the beam would change to positive ions, and the remaining 0.5% would remain negative. This is shown in the twelfth line of Table 7-1.

The positive ions, generated from negatives by the loss of two electrons, have a 2.4-MeV energy relative to the ion source, or a 1.8-MeV energy relative to ground. The beam cross-sectional area is somewhat larger than 8×500 cm and has a positive-ion current of 27.2 A. This corresponds to a positive-ion current density of less than 6.8×10^{-3} A•cm^{-2} and a power density of less than 12.2 kW•cm^{-2} at the ground-potential beam dump. If the beam were allowed to expand to about four times its original size, it could be readily collected in a grounded beam dump at an intensity of ~3 kW•cm^{-2} (see Fig. 7-8). A power savings of 17.1 MW could be realized, assuming a 35% efficient thermal recovery.

A plasma thickness of roughly 2×10^{15} ions/cm^2 is required in the stripping cell to obtain the desired efficiency. This creates a need for a cell, 20 to 200 cm long, with a plasma density of 10^{14} to 10^{13} cm^{-3}. The plasma ion density in the stripping cell must be sufficiently high — 80% or better — to prevent a significant fraction of the high-energy neutralized beam from being re-ionized by collisions with background neutrals.

These requirements can be satisfied in a metal-vapor plasma produced by surface ionization if the ionization potential of the vapor is low and the

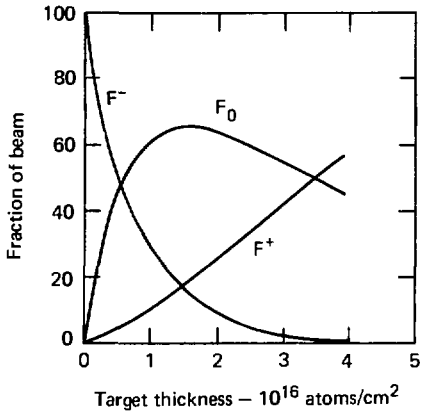

Item	Optimum	Preferred
F_0 (%)	65.5	60.3
F^+ (%)	19.8	34.7
F^- (%)	14.7	5.0
Target thickness (10^{16} cm^{-2})	1.6	2.5

Fig. 7-6. Beam composition in a cesium-vapor stripping target.

surface has a high work function. Surface ionization for the impingement of metal vapor on most refractory metals has been studied, and the theory for cesium vapor in contact with hot tungsten is well known.[7-11] Numerous experiments[7-6] on "Q machines" and the like have shown that atom, ion, and electron fluxes are a function of surface ionization and thermionic electron emission, not volume effects. The stripping cell must therefore have

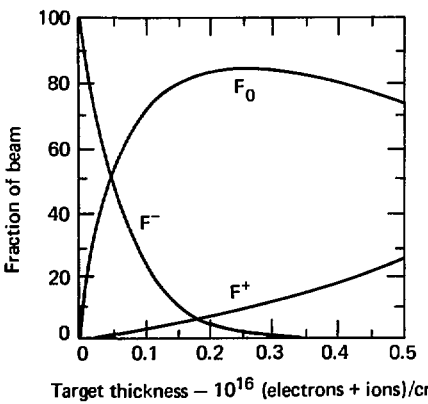

Item	Optimum	Preferred
F_0 (%)	85.7	81.5
F^+ (%)	8.4	18.0
F^- (%)	5.9	0.5
Target thickness (10^{16} cm^{-2})	0.2	0.38

Fig. 7-7. Beam composition in a cesium-plasma stripping cell.

a cesium ion density equal to the electron density. This requires an emitted electron current density of 10 to 100 $A \cdot cm^{-2}$ and a corresponding tungsten temperature of 1400 to 3300 K, depending on what fraction of the surface (θ) is coated with cesium. Since the evaporation rate of cesium atoms and ions from the tungsten surface depends upon the temperature and θ, an 80% ionized plasma implies a value of θ that is no greater than 0.1. Experiments[7-6] have shown that these requirements can be met for plasma densities of 10^{13} to 10^{14} cm^{-3} when the temperature of the tungsten is at 2300 to 2800 K.

For several reasons, stripping cells should be designed at relatively low density (10^{13} cm^{-3}) and greater length (200 cm):

- Structural and thermal problems are simplified at the lower temperature;
- The ion and electron recombination rate is reduced in the lower-density plasma volume; and
- If several layers of heat shields surround the stripping cell, the only significant heat loss will be through the open ends; therefore, the heat loss depends primarily upon the temperature of the wall and not upon its length. An estimated 1 MW of heating should be made available for this application.

The openings at the ends of the cell correspond to the beam cross section — roughly 8 by 500 cm. Barriers can be added along the beam line to restrict the flow of cesium that streams out of the stripper and

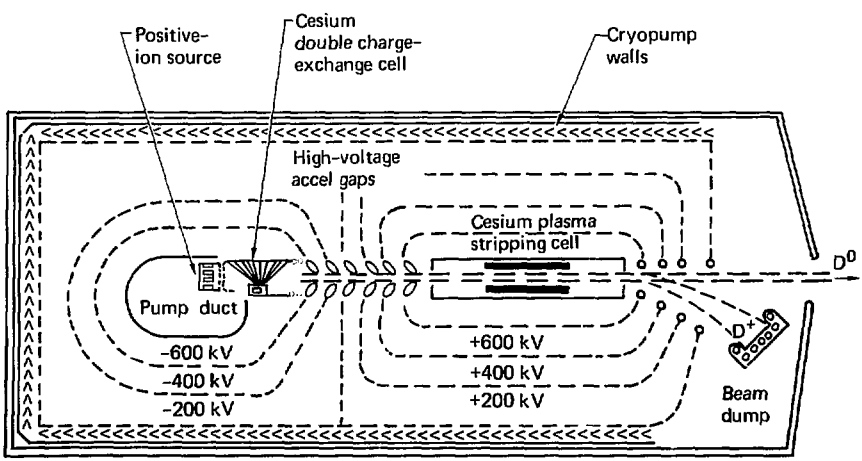

Fig. 7-8. A 1.2-MeV neutral-beam injector.

along the beam line into the ion source or the reactor. Cesium losses in a Q machine are prevented by a transverse magnetic field of about 0.1 T. If such fields were introduced at the entrance and exit to the stripping cell, no serious deflection of the ion beam would result at 1.2 MeV. Hot-tungsten sheets can be hung vertically in the injectors, thus limiting the severity of the structural problem.

If the background pressure beyond the stripping cell is 10^{-5} Torr or less and the gas temperature is 500 K, the density will be about 2×10 cm^{-3}. The ionization cross section of the neutral beam at 1.2 MeV will be $\sim 0.32 \times 10^{-16}$ cm^2/D_2, and the background ionization cross section will be about the same. The fraction of the neutral beam lost in a 10-m drift region will correspond to $F_{01} = n\sigma_{01}X = 0.6\%$, while the background ionization corresponds to 0.7 C/s. These values are shown in the last line of Table 7-1.

SYSTEM PERFORMANCE

Throughout this study, we have estimated the background charge-exchange and ionization currents along the beam line (see Table 7-1). Table 7-2 shows the corresponding grid currents that result when every background ion goes to its closest positive electrode and every electron goes to its closest negative electrode. The power supplies needed to sustain these currents are shown in Fig. 7-9. Table 7-3 shows the power dissipation derived from Table 7-2 at each of the grids.

All electrodes (including the ion source) are maintained at about 500°C by removing the dissipated heat via circulating liquid metals. This allows recovery of some waste heat by means of high-voltage, insulated, heat exchangers located in the pressurized SF_6 chambers. Some of this thermal energy can be used to heat the mercury ejector pumps and to evaporate the cesium in the double charge-exchange cell. The remainder, converted to electricity at 35% efficiency, results in a savings of 15.5 MW, as shown in Table 7-4. From the net result shown in Table 7-5, we determine that the neutral-beam injector has an overall power efficiency of 73%.

It is impossible to establish accurately the cost of each injector from the data we have presented. However, we can estimate the cost on the basis of \$320/kW divided by the beam efficiency. This gives an estimated total of \$65 million for the entire injector system for the TMR.

Table 7-2. Estimates of grid currents. The odd-numbered lines represent the beam loss due to charge exchange; the even numbered lines show the background current caused by ionization.

Line	Region between grids	Grid No. G 1	G 2	G 3	G 4	G 5	G 6	G 7	G 8	G 9	G 10	G 11	G 12	Beam dump	Wall	Line from Table 7-1
1			12.0 D^+													2
2	1-2	0.8 e	0.8 D^+													
3			11.8 D^+													
4	2-3		0.8 D^+	0.8 e												3
5					-931.1 e[a]											
6	3-6			15.5 e	15.5 D^+	0.3 e	0.3 D^+									4, 5
7								2.0 D^-								
8	6-7						0.4 D^+	2.4 e								6
9									2.8 D^-							
10	7-8							2.4 D^+	2.4 e							7
11										0.4 D^-						
12	8-9								0.2 D^+	0.2 e						8
13											0.3 D^-					
14	9-10									0.2 D^+	0.2 e					9
15												0.3 D^-				
16	10-11										0.1 D^+	0.1 e				10
17													0.2 D^-			
18	11-12											0.1 D^+	0.1 e			11
19													177.6[b]			
20	12-12'											0.2 D^+	0.2 D^-	27.2 D^+		12
21	Drift region														0.7 D^+	13
	Total (A):	0	25.4	16.3	946.3	0.7	2.0	4.8	3.0	0.4	0.4	0.1	177.1	27.2 D^+	0.7	

[a] Secondary emission from bombardment by 620.7 A of neutrals. In addition, 310.4 A of electron current is required to convert the positive ion beam to negative. Grids 4 and 5 are electrically common.

[b] 123.2 A of electrons is removed from the negative-ion beam to form 123.2 A of neutrals and 54.4 A of electrons is removed to form 27.2 A of positive ions — for a total of 177.6 A of electrons.

Table 7-3. Grid dissipation data taken from Table 7-2.

Grid	Potential (kV)	Electrode current (A)	Particle energy (keV)	Source of current	Dissipated power (kW)	Line from Table 7-2
1	Floats	Net −0.8	6.0	Electrons from grid 1-2 gap	4.8	
		Zero +0.8	Negligible	Ions from source plasma		2
2	−11.75[a]	12.0	6.0	Charge-exchange from grid 1-2 gap		1
		0.8	6.0	Ions from gap 1-2 gap		2
		11.8	6.0	Charge-exchange ions from gap 2-3 gap	138.9	3
		0.8	6.0	Ions from grid 2-3 gap		4
3	+0.5[b]	0.8	6.0	Electrons from grid 2-3 gap	11.8	4
		15.5	0.5	Electrons from charge-exchange cell		6
4-5	−600[c]	931.0	Negligible	Ions in charge-exchange cell		5
		15.5	Negligible	Ions in charge-exchange cell	Negligible	6
		0.3	Negligible	Electrons in charge-exchange cell		
6	−0.5[b]	0.3	0.5	Ions from charge-exchange cell		6
		0.4	100	Ions from grid 6-7 gap	40.2	8
7	−400	0.4	100	Electrons from grid 6-7 gap		8
		2.0	100	Neg. ions from grid 6-7 gap	280	7
		−0.4	100	Pos. ions from grid 7-8 gap		10
8	−200[c]	0.4	100	Electrons from grid 7-8 gap		10
		0.8	100	Neg. ions from grid 7-8 gap	140	9
		−0.2	100	Pos. ions from grid 8-9 gap		12
9	Grnd	0.2	100	Electrons from grid 8-9 gap		12
		0.4	100	Neg. ions from grid 8-9 gap	80	11
		−0.2	100	Pos. ions from grid 9-10 gap		14
10	+200	0.2	100	Electrons from grid 9-10 gap		14
		0.3	100	Neg. ions from grid 9-10 gap	60	13
		−0.1	100	Pos. ions from grip 10-11 gap		16
11	+400[c]	0.1	100	Electrons from grid 10-11 gap		16
		0.3	100	Neg. ions from grid 10-11 gap	50	15
		−0.1	100	Pos. ions from grid 11-12 gap		18
11'	+400[c]	−0.2	100	Pos. ions from grid 11-12 gap	20	20
12	+600[c]	0.1	100	Electrons from grid 11-12 gap		18
		0.2	100	Neg. ions from grid 11-12 gap	30	17
12'	+600[c]	177.6	Negligible	Neg. ions from stripping cell	Negligible	19
		0.2	Negligible	Neg. ions from ionization in cell		20
Beam dump	Grnd	27.2	1800	Pos. ions from stripping cell	41,960	19
Wall	Grnd	0.7	1200	Ions from drift region	840	21

[a] Relative to source.

[b] Relative to charge-exchange cell.

[c] Relative to ground.

CONCLUSIONS

We have described a neutral-beam injector that consists of five components, each entailing a significant development effort. These components are

- A continuously operating source of negative ions. This source uses a gas-tight, cesium-vapor cell equipped with a flowing, liquid-metal cooling system.

- A high-voltage, negative-ion accel system design with conservative grid loadings and an acceptable level of high-voltage stress.

- A plasma-stripping cell modeled after a "Q machine" and a beam dump to collect the unstripped ions.

- A large injector assembly whose walls are covered with continuously regenerating cryopanels and a complex set of high-voltage electrostatic shields that inhibit voltage breakdown.

- Reliable power supplies with associated protective equipment and diagnostic display and control components.

The prospect of a 122-A injector of 1.2-MeV neutral deuterium atoms

Table 7-4. Energy recovery.

Electrode	Electrode area (cm^2)	Dissipated power (kW)
P_{fil}	10,000	150
P_{arc}		1,540
Grid		
1	2,000	5
2	2,000	140
3	2,000	12
4,5	2,000	—
6	2,500	40
7	2,500	280
8	2,500	140
9	2,500	80
10	2,500	60
11	2,500	50
12	2,500	30
12'	2,500	—
11'	2,500	20
Beam dump	18,000	48,960
	Total:	52,347

Total waste heat (from table above)		52,347 kW
Direct use of waste heat:		
Mercury ejector pump	6,000	
Cesium double charge-exchange cell	2,000	
Total: less direct use of waste heat		8,000
Waste heat		44,347
Electric power obtained from waste heat (at 35% conversion efficiency)		15,521 kW

may be awesome, but we have identified no basic constraints that would prevent its construction. The model we present is, in fact, based upon successful physics experiments. Translating these ideas into a reliable operating machine will, nevertheless, be an impressive undertaking.

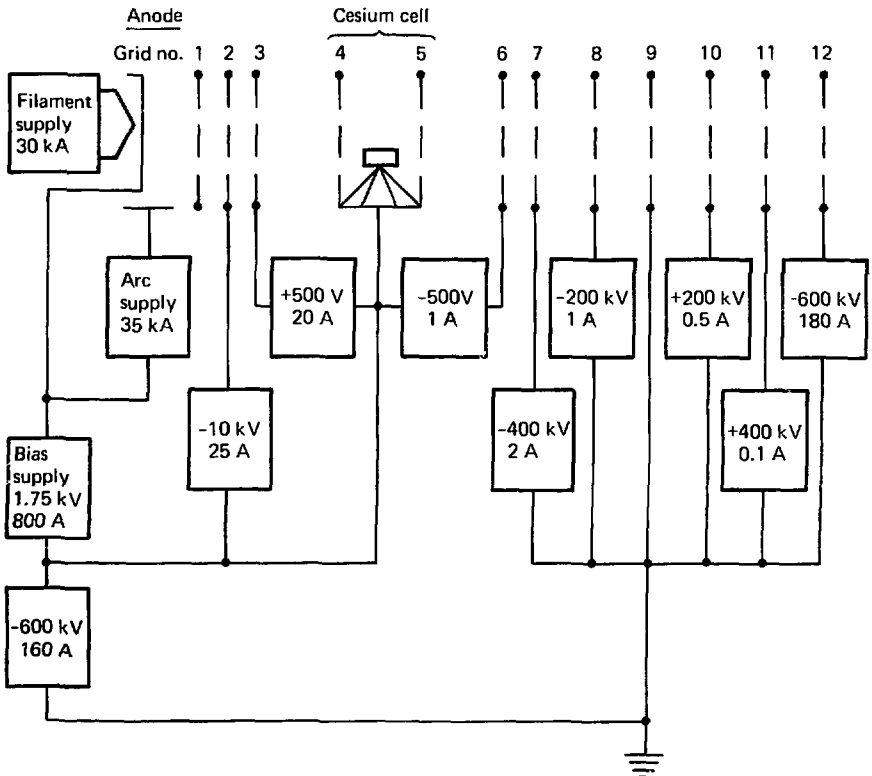

Fig. 7-9. Power supplies needed to sustain the currents in a 1.2-MeV neutral-beam injector.

Table 7-5. Power distribution.

Power supply	Voltage (kV)	Current (A)	Power output (MW)	Efficiency (%)	Power input (MW)
Filament	5[a]	30[b]	0.15	90	0.17
Arc	45[a]	35[b]	1.58	90	1.76
Bias	1.75	800	1.40	90	1.56
Grid					
2	10.0	25	0.25	90	0.28
3	500	20	0.01	90	0.01
6	-500	1	—	90	—
Cathode	-600	160	96.00	97	98.97
Grid					
7	-400	2	0.80	90	0.89
8	-200	1	0.20	90	0.22
10	200	0.5	0.10	90	0.11
11	400	0.1	0.04	90	0.04
12	600	180	108.00	97	111.34
Total power supply input:					215.35
Auxiliary equipment:					
Mercury ejector pumps (operate from waste heat)					0.00
Roughing pump (negligible)					0.00
Cryopumps (at 0.7 $W/l.s^{-1}$)					0.70
Double charge-exchange cell (operates from waste heat)					0.00
Plasma-stripping cell					1.00
Total power:					217.00
Energy recovery (from Table 7-4):					15.50
Beam power output (122.5 A at 1.2 MeV):					147.00
Injector efficiency $\frac{\text{beam power output}}{\text{total power} - \text{energy recovery}}$:73%					

[a]Expressed as volts.

[b]Expressed as kiloamps.

REFERENCES

7-1. T. K. Fowler and B. G. Logan, "The Tandem Mirror Reactor," *Comments on Plasma Phys. and Controlled Fusion Res.* 2 (6), 167 (1977).

7-2. J. W. Beal and V. K. Neil, *A Method for Achieving Complete Neutralization of a High Energy Charged Particle Beam*, Lawrence Livermore Laboratory, Rept. UCRL-76505 (1974).

7-3. W. L. Barr and R. W. Moir, "A Review of Direct Energy Conversion for Fusion Reactors," in *Proc. Second Topical Meeting Technology of Controlled Nuclear Fusion, Richland WA*, 1976 (ERDA, CONF-760935, 1976), p. 1181.

7-4. K. H. Berkner, R. V. Pyle, and J. W. Stearns, "Intense, Mixed-Energy, Hydrogen Beams for CTR injection," *Nucl. Fusion* 15, 249 (1975).

7-5. J. H. Fink, W. L. Barr and G. W. Hamilton, *A Study of Efficient High-Power, High-Energy Neutral Beams for the Reference Mirror Reactor*, Lawrence Laboratory, Rept. UCRL-52173 (1976).

7-6. N. Kynn, Princeton University, private communication (1977) and *A Test on Neutral Beams, A Preliminary Study*, Princeton University, Princeton, N. J., Technical Memorandum No. 81 (1959).

7-7. T. J. M. Sluyters, R. A. Mari, V. Kovarik, R. Lockey, and S. Senator, "A Bright High-Gradient 750-keV Ion Gun," *Particle Accelerators* 1, 15 (1970).

7-8. A. S. Schlachter and J. W. Stearns, "Equilibrium Yield of D^- by Charge Exchange of 0.5-3keV D^+ in Cesium Vapor," *Bull. Am. Phys. Soc.* 21, 1135 (1976).

7-9. O. A. Anderson, *A Compact High-Energy Neutral Beam System*, Lawrence Livermore Laboratory, Rept. UCID-16914 (1975).

7-10. G. I. Dimov and G. V. Roslyakov, "Conversion of a Beam of Negative Hydrogen Ions to Atomic Hydrogen in a Plasma Target at Energies Between 0.5 and 1.0 MeV," *Nucl. Fusion* 15, 551 (1975).

7-11. J. B. Taylor and I. Langmuir, "The Evaporation of Atoms, Ions and Electrons from Cesium Films on Tungsten," *Phys. Rev.* 44, 423 (1933).

CHAPTER 8. DIRECT ENERGY CONVERTER FOR THE TANDEM MIRROR REACTOR

W. L. Barr

SUMMARY

Direct converters to recover power from the plasma lost from the ends of the Tandem Mirror Reactor (TMR) can be very effective. The high ambipolar potential and the low ion temperature result in good efficiency even with a single collector stage. About 60% of the total efflux power (carried by escaping fuel ions, alpha particles, and electrons) can be directly recovered after allowing for losses due to plasma electrons, grid interception, secondary and thermionic electrons. The two types of region in the TMR — the central cell and the end plugs — result in two distinct energy groups of ions and suggest a two-stage direct converter. The addition of a second collector stage in the direct converter raises its efficiency to about 70%. The direct converter would also serve to control the recycling of cold electrons from the end walls. Problems associated with space charge, voltage holding, and capacitively stored energy appear to be solvable.

INTRODUCTION

A TMR produces a set of conditions at the ends that is quite different from that of other mirror reactors. In particular, the high ambipolar potential in the end plugs results in a high minimum energy for the efflux ions when they reach the direct converter (DC). Also, the high potential in the end plugs enhances the confinement of the alpha particles. Methods for preventing the buildup of alphas are discussed in the chapter on plasma physics (Chapt. 3). Here, we assume for simplicity that the alphas thermalize and finally escape to the DC in a manner similar to the escape of fuel ions from the central cell. If in fact the efflux alphas are concentrated in a particular flux tube, this should not require any major change in the DC. The large potential difference between the plasma in a plug and the grounded grid at the DC is not expected to be a problem. The plasma density at the magnetic mirror is low compared to the density at the center of the plug ($10^9 cm^{-3}$ *vs* $10^{15} cm^{-3}$). For electron density to be equal to the ion density at both places, the potential at the mirror must be down about 1/13 from the value at the center. Therefore, because the potential at a mirror is less than kT_e = 42 keV, only a modest potential difference exists between the mirror and the end wall.

Even so, there remains a small gradient in potential outside of the mirrors that tends to pull cold

electrons from the end walls into the plasma. These electrons are produced on the end walls almost entirely by ion rather than electron impact, because the energy of the primary electrons is so high (~42 keV) that their coefficient for the production of secondary electrons is extremely small. Therefore, by collecting the ions on positive collectors in a direct converter, the only electrons produced at the end walls will be those from the grids in front of the DC. The direct converter thus can play the dual role of recovering power from the ions and of controlling the release of electrons from the ends.

The magnetic field at the DC is low, only about 100 G, because of the large expansion ratio that is required to reduce the power density from the 1400 MW/m^2 in each mirror throat to the allowed 1 MW/m^2 at the DC.

Other novel features of the TMR that affect the DC are the high value of Q and the two distinct groups of ion energies, as discussed next.

PARTICLE ENERGIES AT THE DIRECT CONVERTER

The performance of the DC depends on the energies of the various charged particles at the entrance to the DC. The energies there are determined by the energies and the ambipolar potentials inside the plug and central-cell regions. Although the DC actually consists of two units (one at each end), the currents and powers to the DC are calculated here for the combined DC system. Quantities evaluated at the DC will be indicated by a prime to distinguish them from the corresponding values inside the reactor. Otherwise, the notation used here is the same as that used in the section on plasma physics.

The total charge particle power P'_{dc} at the DC is given by the sum

$$P'_{dc} = I'_p \bar{E}'_p + I'_c \bar{E}'_c + \frac{1}{2} I'_\alpha E'_\alpha + I'_e \bar{E}'_e \quad , \tag{8-1}$$

where $I'_p = 438.5$ A is the ion current from the plugs, which is just equal to the trapped fraction (89.6%) of the neutral-beam equivalent current injected into the plugs. The average energy $\bar{E}'_p$ of these ions at the DC is equal to the injection energy, 1200 keV, first reduced by the loss due to electron drag during the containment time of an average plug ion, and then increased by the difference in potential between plug and DC. The amount ΔE_p by which electron drag reduces the energy of a plug ion during its lifetime is estimated here by multiplying the average rate of energy transfer by the average lifetime of a plug ion. That is,

$$\Delta E_p = (\bar{E}_p - 1.5\ T_e)(n\tau)_p/(n\tau)_{ie}$$

$$= 743\ \text{keV},$$

because $\bar{E}_p = 878$ keV in the plugs and the equipartition time $(n\tau)_{ie} \approx 10^{12}\ T_e^{3/2}$ in these units. The potential drop from plug to DC is $\phi_e + \phi_c = 350$ kV. Therefore, $\bar{E}_p' = 807$ keV. The current I_c' from the central cell to the DC can be determined from the power balance (below) to be $I_c' = 1284$ A. The mean energy of these ions as they clear the potential barrier in the end plugs has been shown to be equal to T_c there, and $T_c = 30$ keV. They are then accelerated by the 350-kV potential difference, giving $\bar{E}_c' = 380$ keV.

The electrical current due to alpha particles, $I_\alpha' = 288$ A, is obtained directly from the rate of fusion reactions: $I_\alpha' = 2eP_F/E_F$, with $P_F = 2532$ MW and $E_F = 17.58$ MeV. All of the alphas are assumed to thermalize ($f_\alpha = 1.0$, see Chapt. 3), so that the mean energy of the alphas at the DC is $\bar{E}_\alpha' = 30 + 2 \times 350 = 730$ keV by the same reasoning as for $\bar{E}_c'$. Since the electrons are also electrostatically confined, their mean energy at the DC is just $\bar{E}_e' = T_e = 42$ keV. The electron current I_e' must be equal to the sum of the ion currents:

$$I_e' = I_p' + I_c' + I_\alpha' . \qquad (8\text{-}2)$$

When Eqs. 8-1 and 8-2 are combined, I_c' is determined in terms of P_{dc}', and P_{dc}' is known:

$$P_{dc}' = P_{in} + 0.2\ P_F - 0.8\ I_c'\bar{E}_c . \qquad (8\text{-}3)$$

Here, $P_{in} = 526$ MW is the power that is injected and trapped, and $P_F = 2530$ MW is the fusion power. The second term in the right-hand side of Eq. 8-3 gives the power carried by the alphas, and the last term represents the 80% of the residual kinetic energy, $\bar{E}_c = \frac{3}{2} T_c$, of the reacting D^+ and T^+ ions that is carried away by the resulting neutrons and is not available for direct conversion. This last term has only a 1% effect here and is therefore ignored in determining P_{dc}' and I_c'. When these three equations are combined, the result is that $I_c' = 1284$ A and $I_e' = 2011$ A.

It is interesting to check the self-consistancy of the parameters. From Table 2-2 in Chapt. 2, the volume of plasma in the central cell is $V_c = 452\ m^3$, the density is $n_c = 1.1 \times 10^{20}\ m^{-3}$, and $(n\tau)_c = 7.7 \times 10^{20} s/m^3$. Combining these values gives I_c', the loss current from the central cell, as

$$I_c' = V_c n_c^2 e/(n\tau)_c = 1140\ \text{A}.$$

This is only about 10% lower than the value obtained from P_{dc}' and serves as

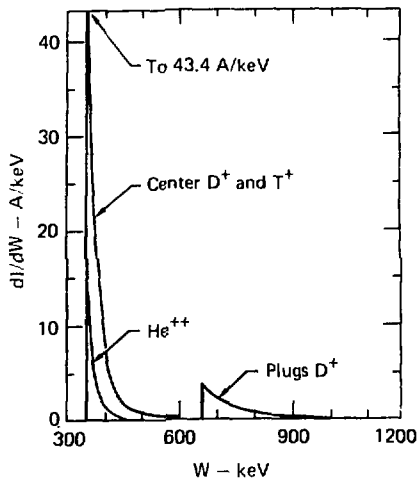

Fig. 8-1. The distribution in ion energy at the direct converter. For He^{++}, the energy per unit charge is plotted.

a satisfactory check on the various quantities involved. In analyzing the DC, we use $I_c' = 1284$ A.

The approximate energy distributions for these three groups of ions at the DC are sketched in Fig. 8-1. For the fuel ions from the central cell, we take a two-dimensional Maxwellian

$$\frac{dI_c'}{dE_c'} = (5.06 \times 10^6 \text{ A/keV}) \cdot \exp(-E_c'/30.0), \quad 350 \leq E_c',$$

where the low-energy cutoff is set by the minimum energy that an ion can have after passing over the potential barrier in the plugs. Similarly, for the alpha particles we take

$$\frac{dI_\alpha'}{dE_\alpha'} = (1.35 \times 10^{11} \text{ A/keV}) \cdot \exp(-E_\alpha'/30.0), \quad 730 \leq E_\alpha' .$$

The distribution function for the ions from the plugs is different. Neutral atoms injected with energy $E_{p,in}$ are ionized and trapped in the plugs. Once ionized, they begin to lose energy to the electrons, which have a lower mean energy. As the ion energy decreases due to the electron drag, the frequency of elastic collisions with other ions increases, with the result that as its energy is lowered an ion has an increasing probability of finding the loss cone and escaping from the plug. The energy distribution of the ions escaping from the plug is therefore peaked at low energy. At the DC, the entire distribution is shifted up in energy by the difference in potential.

An expression that fits this description and gives the known total current and power from the plugs is

$$\frac{dI_p'}{dE_p'} = 3.47 \times 10^9 \times (E_p' - 350)^{-3.6}, \quad 658 \leq E_p' \leq 1550 .$$

The lower limit on E_p' is determined by the ambipolar potential $\phi = 350$ kV

and the mirror ratio R = 2.14 in the plugs:

$$E'_{p,min} = \frac{R\phi}{R - 1} = 658 \text{ keV}.$$

The upper limit is just the 1200-keV injection energy increased by the 350-kV difference in potential.

Figure 8-1 shows a plot of the combined energy distribution for the three groups of ions at the DC. The two distinct energy groups suggest that to recover both groups efficiently the DC should have two collector stages. The possible efficiencies of both a single-stage and a two-stage DC are evaluated here.

GRIDS

The direct converters that are evaluated here use immersed grids to control the electrons and prevent them from reaching the positive ion collectors (see Figs. 8-2 and 8-3). Two grids are used: the first is held at ground potential and the second is held negative to reflect the electrons. Therefore, the sink for the electrons is the grounded grid, which must be designed to handle all of the power from the electrons plus the power from those ions that are intercepted. It can be seen from the immediately preceding discussion of particle energies that the electrons carry about 8% of the power to the DC. To provide an adequate sink for the electrons and to handle the large thermal power, the grounded grid is about 5% opaque to the beam. It therefore receives about 13% of the total power to the DC.

The thermal load on the negative grid results only from the ions that it intercepts. It is therefore desirable to keep this grid as transparent as possible. Considerations of heat transfer and of voltage holding set the minimum practical opacity at 1 to 2% for this grid.

Neither grid can be allowed to reach a temperature where thermionic electron emission is significant, because neither the DC nor the reactor can tolerate a large flux of cold electrons. It is this restriction that sets the limit on the power density that can be handled by the DC.

Convectively cooled grids can be used up to equivalent input power densities of about 500 W/cm^2 if the span is less than about 3 m. Beyond these ranges, the grid becomes too opaque to be practical. Both water and high-pressure helium have been studied as coolants. Smaller tubes can be used for water than for helium, but the heat is removed from water at a temperature that is too low to allow efficient recovery in a thermal cycle. However, because of

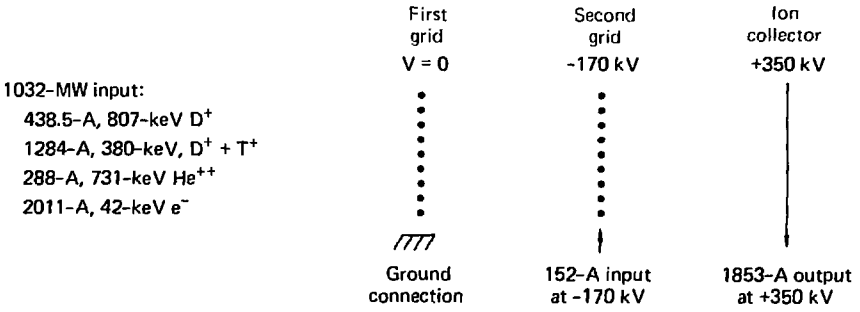

Fig. 8-2. Power and current flow in a single-stage direct converter on the TMR, where the efficiency is $\eta_{DC} = [(1853 \times 350) - (152 \times 170)]/1.032 \times 10^6 = 0.603$.

the danger of failure among the many tubes operating close to their mechanical limits, convectively cooled grids of all kinds should probably be avoided.

Here, we postulate radiatively cooled grids. Grids made from a carbon/carbon composite material appear able to handle the highest power density of any of the possible materials for radiatively cooled grids. Besides having a high emissivity and a relatively high work function (for lower temperature and decreased thermionic electron emission), the carbon grids appear strong enough to span large distances, thus reducing interception

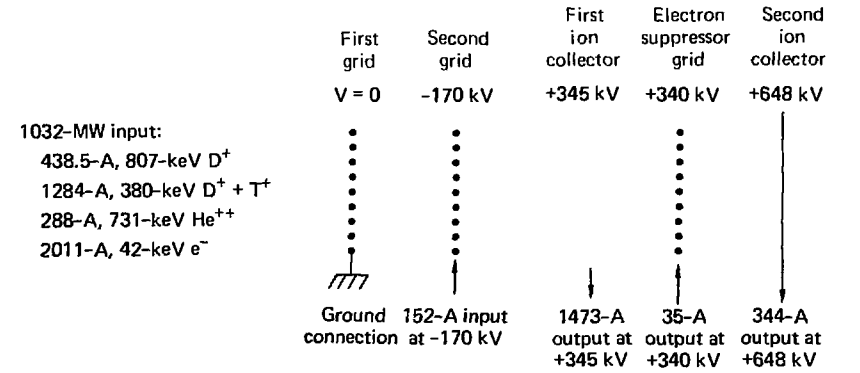

Fig. 8-3. Power and current flow in a two-stage direct converter on the TMR, where the efficiency is $\eta_{DC} = [(1473 \times 345) + (35 \times 340) + (344 \times 648) - (152 \times 170)]/1.032 \times 10^6 = 0.695$.

of the beams by support structure. Since the efflux plasma is guided by the magnetic field that exists outside the Yin-Yang coils at the ends, the beam is fan shaped with a cross section that is thin compared to the width. By orienting the coils so that the two efflux fans are both horizontal, the grids can be supported above and below across the smaller dimension. No support structure need be immersed in the beam.

The lengths of the fan-shaped expanders are determined by the amount of expansion required to reduce the power density to values that the grids can tolerate. Studies of radiative heat transfer in similar grid structures have shown that graphite grids whose elements have circular cross sections are useful up to about 200 W/cm^2 when the energy of the incident D^+ and T^+ ions is about 170 keV. Here, the mean energy is $\overline{W}_i$ = 472 keV, with the result that the collector voltages are about three times higher and the loss of power due to thermionic emission at 200 W/cm^2 is also about three times higher than at 170 keV. However, thermionic emission decreases rapidly as the beam power density is decreased. A power density of 100 W/cm^2 appears to be reasonable, and that is the value that was chosen for this preliminary study.

Because the grounded grid receives all of the primary electrons and most of the secondary and thermionic electrons in addition to the intercepted ions, it actually receives about three times as much power as it simply intercepts from the ions. Thus, the effective power density at the grounded grid is about 330 W/cm^2. To radiate this increased power without heating to thermionic emission temperatures, the elements in the grid can have a noncircular cross section. This can give an increased surface area for radiating away the heat without increasing the beam interception. Maintaining the alignment of such elements may be a serious problem.

The spacing between grids must be small enough to avoid space-charge limitation of the input beam current. Since the input power density is 100 W/cm^2 and the mean ion energy is 472 keV, the current density is 2×10^{-4} A/cm^2. In Fig. 8-1 note that there are two groups of ions; those with a mean energy of 380 keV per unit of charge, and those with 807 keV. Also in Fig. 8-1, note that the first ion collector should be set at 350 kV. When retarded by 350 kV, these two groups of ions have the same density as a 1.6×10^{-4} A/cm^2 beam of mono-energetic ions with 380 keV of initial energy. Such a beam

is space-charge limited at 350 kV when the spacing is 3.0 m from the V = 0 equipotential. Therefore, the spacing between negative grid (-170 kV) and first collector (+350 kV) need only be less than 4.5 m.

Such a large spacing is easily compatible with voltage-holding requirements. According to the Paschen curve, gas breakdown in H_2 is avoided if the pressure is kept below 2×10^{-4} Torr. Data on surface-initiated breakdown indicates that the 520-kV difference can be held across gaps in vacuum as small as 10 cm.

Although the interelectrode spacing could be reduced to a few tens of cm, the stored electrostatic energy that could be released in a spark is reduced if the spacing is large. Sparks that are driven by less than about 10 J of capacitively stored energy tend to heal the surface and help to prevent other breakdowns, whereas much more than 10 J damages the surface and makes other breakdowns more likely. The energy stored in the capacitor formed by the collector and the negative grid is 0.30 J/m^2 when the spacing is 4.0 m and the voltage difference is 520 kV. Therefore, 10 J is stored in 33 m^2 of area, and since each DC has 516 m^2 of frontal area, each must be divided into about 16 sections to keep the energy stored in each section below 10 J. It was partly to facilitate this division into sections that both of the fan-shaped expander tanks were oriented horizontally. Separate supports for the different sections can be located about and below the beam without increasing the interception.

The actual design of the DC is left for future work. This preliminary analysis simply indicates that a design is possible and it predicts the performance of the DC. A much more detailed study is required to select the materials and design the structure. Additional thought must be given to the design of the heat-transfer system, of the high-voltage insulators, of the cryopanel vacuum pumps, and of the plasma scrape-off region. (The scrape-off region acts as a dump for high-Z impurities on the outer flux lines.)

DIRECT CONVERTER EFFICIENCIES

The efficiency of the DC can be determined by tabulating the amount of power that is lost to each of the various loss mechanisms. Table 8-1 itemizes the amounts of power that are made unavailable for direct conversion by each mechanism in the approximate order that they are encountered by the incident beam. In the following text, a single-stage DC is considered first; a two-stage DC

is then analyzed by comparing it with the single-stage unit.

Efficiency of a Single-Stage Direct Converter

The first loss from the 1032 MW of incident power is that of the primary electrons. A 2011-A electron current arrives at the DC with a mean energy of 42 keV per electron. This amounts to 85 MW of incident power that is dissipated on the first grid. Since the first (grounded) grid is 5% opaque, it intercepts 47 MW of the 947 MW of ions. Similarly, the negative grid intercepts 2%, or 18 MW, of the remaining ions. This 18 MW of ions amounts to 38 A, which also contributes to the drain on the negative power supply listed near the bottom of the table.

Loss of ions by charge exchange with gas in the expander is negligible at these relatively high energies if the pressure is held below 5×10^{-5} Torr.

A single collector can recover all 1872 A of ions that pass through the grids if the collector potential is not greater than the minimum ion energy per unit of charge. In Fig. 8-1, note that the minimum energy is 350 keV. Since the recovered power is proportional to the collector potential, it is set at the maximum value, 350 kV. Then, the recovered power is 350 kV × 1.872 kA = 655 MW from the 882 MW of ion power that reaches the collector. The 227-MW difference is removed as heat from the collector.

We mentioned earlier that 38 A of ions are intercepted on the negative grid. Each ion releases about two secondary electrons from the grid. Also, a small emission current of thermionic electrons will result from the heating of the grid by the ions. Thus, the total drain on the negative power supply is about four times (allowing one unit of 38 A for emission) the ion current, or 152 A. At a grid potential of -170 kV, this is a power loss of 26 MW. Grid potential is set at $-4T_e$ to stop nearly all primary electrons.

The final loss mechanism in a single-stage DC is due to that part of the 38 A of thermionic electrons from the negative grid that is accelerated onto the collector. About half of the electrons will go each way because they are emitted uniformly over the surface of a grid element. Secondary electrons are created only on one-half of the surface, and they all exit away from the collector and, together with half of the thermionic electrons, deposit another 16 MW of heat on the grounded grid. Half of 38 A collected at 350 kV results in a loss of 7 MW of power. Finally then, 622 MW of net electric power is recovered from the

incident 1032 MW. A single-stage DC can therefore be expected to recover 60.3% of the total incident power.

Table 8-1 summarizes the losses and Fig. 8-2 shows schematically the recovered and supplied power. The table shows that the largest loss is due to the rather poor match of a single collector potential to a spread in energy. However, all 227 MW of ion heating plus 10 MW of electron heating at the collector is available for thermal conversion. (This includes 3 MW listed as a drain on the negative supply.) The 173 MW of heat radiated from the grids is difficult to recover because of the large area that receives it. In the chapter on parametric analysis (Chapt. 10), it is assumed that all 410 MW of heat is used in a thermal cycle.

Efficiency of a Two-Stage Direct Converter

The presence of two distinct groups in the ion energy distribution (see Fig. 8-1) suggests that a DC

Table 8-1. Summary of losses from the one- and two-stage direct converters for a 1032-MW input power.

Loss mechanism	One-stage Loss (MW)	One-stage Remains (MW)	Two-stage Loss (MW)	Two-stage Remains (MW)
Unrecovered primary electrons	85	947	85	947
Interception of ions by grounded grid	47	900	47	900
Interception of ions by negative grid	18	882	18	882
Charge exchange	0	882	0	882
Remaining kinetic energy of ions when collected	227	655	101	781
Loss due to the mean angle of incidence	0	655	11	770
Loss due to the spread in angle of incidence	0	655	13	757
Drain on negative grid power supply	26	629	26	731
Collection of thermionic electrons	7	622	7	724
Suppressor grids	0	622	7	717
Recovered power:		622		717
Lost power:		410		315
Efficiency (%):		60.3		69.5

with two collectors could be more efficient that a single-stage unit. A two-stage Venetian-blind (VB) DC is similar to the single-stage DC just examined, but has an added collector and suppressor grid (see Fig. 8-3). As shown in Table 8-1, losses to the first two grids and to charge exchange are the same for one- and two-stage direct converters. The main advantage of the VB comes from its two collectors, whose potentials can be adjusted to fit the energy distribution of the ions.

Figure 8-1 suggest that with ideal energy sorting it should be possible to collect all central-cell ions and α-particles at 350 kV and all plug ions at 658 kV. The currents of these three groups of ions after allowing for grid interception are 1195 A, 268 A, and 408 A, respectively. The recovered power then could be 512 MW on the first collector and 269 MW on the second, for a total of 781 MW recovered and the remaining 101 MW appearing as heat.

To sort the ions according to energy, the VB must be tilted at an angle whose optimum value is 6.9° to give the ions a mean incident angle of 83.1°. This tilting requires the reduction of the collector potentials by a factor $\cos^2(6.9°) = 0.986$ and reduces the recovered power by the same factor to 770 MW. Also, the energy sorting is not perfect because the spread in incident angle causes some high-energy ions to be intercepted by the low-energy collector. The larger expansion in the magnetic expander reduces this spread and the resulting interception on lateral surfaces to a small but significant value. This interception results in about 10% of the 408 A of plug ions being collected at 350 kV instead of 658 kV, for a loss of about 13 MW.

As in the single-stage DC, the drain on the negative power supply amounts to 26 MW. Also, because we assume that all thermionic electrons that reach the collectors are caught on the first collector at 350 kV, the 7-MW loss is the same as for a single-stage collector.

One additional loss in the VB results from the emission of secondary electrons from the suppressor grid (see Fig. 8-3). This grid is directly behind the first collector assembly and is held at a slightly lower potential than that collector to prevent secondary electrons produced on the first collector from flowing to the higher potential of the second collector. About 80% of the 1463 A of ions collected on the first stage is first transmitted by it and then passes through the suppressor grid from behind. If the grid is 1% opaque and if the secondary emission coefficient is

about 2, then 23 A of electrons will be released from the rear surface of the grid and pulled into the second collector. Since the potential difference is about 310 kV, the power loss is 7 MW.

Finally then, the net power recovered by the two-stage VB out of the total incident 1032 MW is 717 MW, for a net efficiency of 69.5% (compared to 60.3 % for the single-stage direct converter (see Table 8-1 and Fig. 8-3). The 142 MW of heat generated on the two ion collectors is available for processing in a thermal cycle because both collectors are convectively cooled. This 142 MW is composed of 101 MW from ion kinetic energy, 11 MW plus 13 MW from interception due to angles of incidence, 3 of the 26 MW from the negative grid, 7 MW of thermionic electrons, and 7 MW from the suppressor grid (see Table 8-1). In the single-stage DC, 237 MW (227 + 3 + 7) of heat is generated on the single collector.

CHAPTER 9. POWER SUPPLIES FOR THE TANDEM MIRROR REACTOR

W. L. Dexter

SUMMARY

In this chapter, we describe the power requirements and supplies for the Tandem Mirror Reactor (TMR) ion sources, direct converters, and magnets. The efficiencies of the power supplies are also estimated.

POWER SUPPLIES FOR THE ION SOURCES AND THE DIRECT CONVERTER

The TMR has four ion sources and a one-stage direct converter at each end. Figure 9-1 shows the direct converter and a single ion source with its associated power supplies.

In normal operation, a substantial amount of power for the ion sources comes from the direct converters; however, before plasma buildup, the direct converters consume rather than supply power. Also, the heaters in the cesium cell require power during startup. During startup, the entire system requires 887 MVA; during running, 229 MVA.

The output of the direct converter is positive 350 kV at 1853 A. The positive accel grid of the ion source requires 700 kV; to utilize the output of the direct converter for this grid, a 268-kV topping power supply is provided. A series tube modulator provides isolation between the four sources. A total of 712 A is required for the four ion sources; the remaining 1141 A from the direct converter is converted to 60 Hz and returned to the 230-kV ac power bus.

Ion Source Power Supplies

The power supplies and associated equipment for the ion sources can be broken down into the following major categories:

- Filament and arc power supplies powered from an 800-Hz power source.
- Low-capacity insulating transformers.
- 60-Hz to 800-Hz converters.
- Negative 600-kV power supply.
- Positive topping power supply.
- Modulator regulator.
- Intermediate power supplies for the positive and negative grid of the ion source.
- Q-machine power supply.

The filament and arc power supplies are mounted on the high-voltage structure of the ion source. To reduce the physical size and weight, they are powered from a 800-Hz power source. The size of both transformers and filters can be substantially reduced by using high-frequency power. Because laminated transformer cores can be used, 800 Hz was chosen as a logical frequency. Smaller power supplies offer an additional advantage: because they have a reduced capacity to ground and therefore less stored energy, damage to the ion source grid during

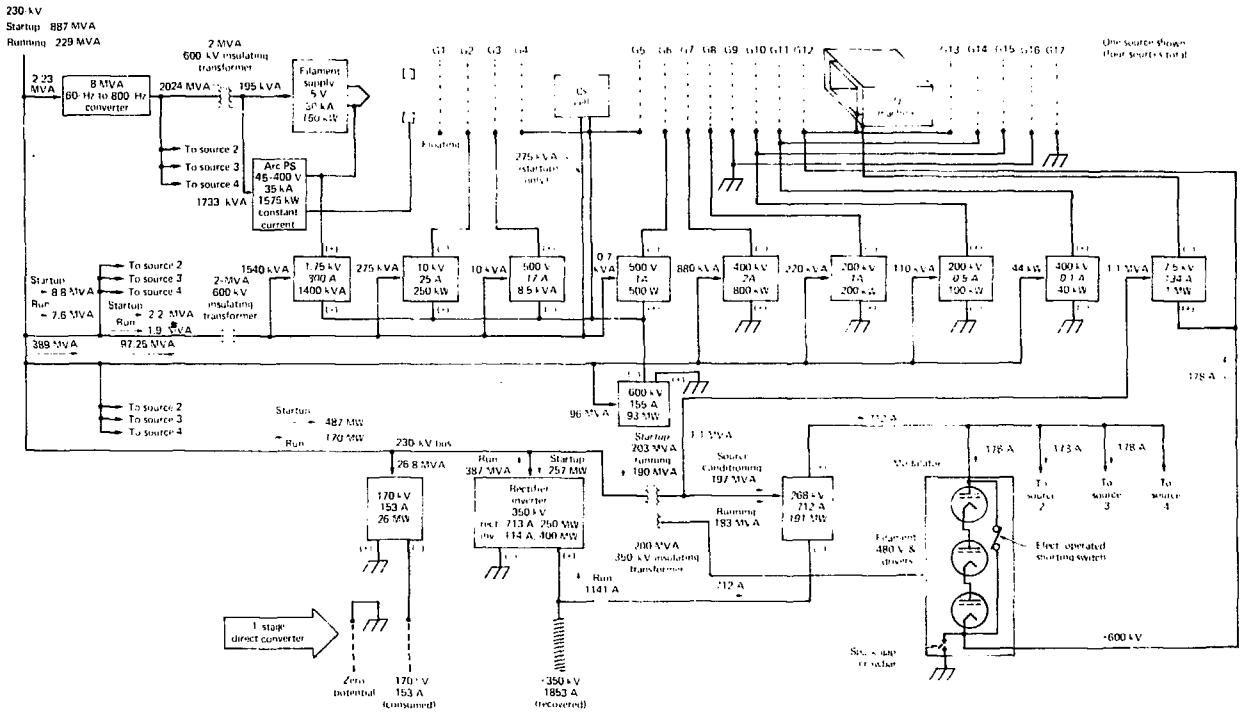

Fig. 9-1. Direct converter and a single ion source plus associated power supplies.

sparking is reduced. The filament supply is a low-voltage, high-current transformer having built-in reactance to limit the turn-on current when the filaments are cold. The arc supply is a transformer-thyristor arrangement in which the thyristor control provides constant-current characteristics. The arc supply has a turn-down feature that reduces the arc current whenever a spark discharge is detected in the accel power supplies.

The high-voltage insulating transformers are designed for low interwinding capacity. This is achieved by making small coils with high current density and by providing large windows in the core. The insulation is pressurized sulfur-hexafloride gas.

The 60-Hz to 800-Hz converters are a conventional rectifier-thyristor, inverter-transformer arrangement that is optimized for low losses by running low current densities in the transformer windings.

The negative 600-kV accel power supply is a transformer-rectifier-filter arrangement having a series tube modulator in the output and thyristors in the primary line to adjust the output voltage. A sensitive current detector in the output detects sparking in the source electrodes and signals the arc supply to reduce the arc current.

The positive topping power supply is similar in design to the negative power supply except that it does not have a modulator and it is large enough to power four sources.

The positive 600-kV modulators are a series high-vacuum tube arrangement and provide precise voltage control of the accel voltage during source conditioning. After the sources are baked in, a remotely operated switch bypasses the series tubes, thereby reducing the power loss caused by the tube drop. A spark-gap crowbar diverts the output of the accel power supply in the event of a spark breakdown in the ion source grids.

The power supplies for the negative grid of the ion source are relatively low-voltage power supplies electrically stacked on the main accel voltage to achieve the required grid potentials. These power supply cabinets are at 600-kV accel potential; therefore, power is supplied to them by an insulating transformer.

The power supply for the Q-machine is at 600 kV above ground; therefore, power is provided to it from an insulating transformer that also provides power to the 268-kV topping power supply.

Direct Converter Power Supplies

The direct converters require two different power supplies: a conventional transformer-rectifier that supplies power at all times to the first grid and an inverter-rectifier

connected to the collector assembly that can supply power during start-up and also recover power and deliver it to the power lines during normal operation. The inverter-rectifier consists of a thyristor-rectifier bridge that converts ac to dc and a thyristor-inverter bridge that converts dc to ac. The inverter bridge is an electronic switching device that sequentially connects a dc bus to the appropriate lines of an ac system. The rectifier bridge and the inverter bridge each has its own firing circuits. The input signals of the two firing circuits are driven from an inverter-rectifier logic chassis that provides a continuous transition from rectifier to inverter operation by means of a single input signal.

The direct converter power supplies are mounted outdoors on a transformer pad, and the high-voltage units are insulated by high-pressure sulphur-hexafloride gas.

POWER SUPPLIES FOR THE MAGNETS

The reactor has the following cryogenic magnets:

- Two plug coil sets, each consisting of a Yin-Yang coil pair and a solenoidal pair.
- Thirty-four central-cell solenoids.

The same power-supply design is used for all coils. The inventory of power supplies for the entire reactor is as follows:

- Yin-Yang coils: 2 power supplies
- Plug solenoidal coils: 4 power supplies
- Central-cell solenoids: 17 power supplies

Total: 23

Each power supply has the following ratings:

- Output voltage: 60 V
- Output ripple: <250 mV
- Output current: 10 kA
- Power: 600 kW

The charging time of the magnet coils is 24 h. The power supplies have the following unique features:

- The output dc circuit breaker is capable of interrupting 10 kA with 10 kV across the contacts. A discharge resistor absorbs the energy stored by the magnet.
- The rate of charge into the magnet coil is precisely controlled in accordance with a prescribed plan.
- In the event of a magnetic quench or fault, the power supply would be automatically de-energized.
- The power supply contains an inverter that returns the energy stored in the magnet to the power lines when the magnet is discharged.
- The power supply has a two-loop regulator that provides a current stability of 1% and controls and limits the maximum rate of change of voltage.

• The power supply has a control system that detects the onset of a magnetic quench and continuously monitors the following parameters:

- Coil current
- Charging and discharging voltage
- Coil interturn voltage
- Lead voltage drop
- Level in liquid-helium reservoir
- Helium-gas pressure and evaporation rate
- Change in magnet coil flux.

The power supplies for the magnets, in common with all other major electrical components, have provisions for either manual or computer control. Also, computer storage is provided for taking and storing the values of various coil parameters.

POWER SUPPLY EFFICIENCIES

All power supplies in the TMR system are optimized for high efficiency by running the current densities of the transformer windings at a conservative level. The power loss in the rectifier thyristors is negligible (about 0.5%). We expect large systems of this type to have an efficiency in excess of 95%. Utility companies that operate large dc transmission systems attain an overall efficiency better than 97%. The efficiencies that we have estimated for the TMR power supplies are listed in Table 9-1.

Table 9-1. Estimated efficiencies of TMR power supplies.

Power supply (MVA)	Efficiency (%)
10	>97
4 to 10	>95
4	>90

CHAPTER 10. PARAMETRIC ANALYSIS

G. A. Carlson

SUMMARY

The results of this parametric design study illustrate the variation in Tandem Mirror Reactor (TMR) characteristics with changes in the independent design parameters, reveal the set of design parameters that minimize the cost of the reactor, and show the sensitivity of the optimized design to physics and technological uncertainties.

THE ANALYTIC MODEL

Physics

The heart of the analytic model for the TMR is the simple, self-consistent description of TMR physics given in Chapt. 3. (An almost identical physics model was presented in App. B of Ref. 10-1.) This model relates the densities, energies, and containment times of the ions and electrons in the plugs and central cell. The plugs are assumed to be mirror machines having classical end losses and sustained by the injection of high-energy neutral beams. (Since the purpose of the end plugs is to stopper the central cell and not to produce fusion power, single-species injection is proposed, e.g., either deuterium or tritium.) The central cell is fueled by low-energy neutral beams of deuterium and tritium. Electrons heated by the energetic ions in the plugs in turn heat the cold ions in the central cell.

The equations of the physics model can be self-consistently solved in a number of ways. In this first analytic model, we find it most convenient to specify the plug injection energy, the plug mirror ratio, the mirror ratio between the plugs and the central cell, the plasma β in the plugs and in the central cell, and the temperature of the central-cell ions. The physics output then consists of the various energies, containment parameters ($n\tau$'s), density ratios, the plasma volume ratio between the central cell and plugs, and Q (thermonuclear power divided by trapped injected power).

Reactor Design

Next, we specify the particular reactor design. First, specification of a single magnetic field strength (usually the central field of the plug) allows calculation of all the plasma densities and the fusion power density in the central cell. Then, specification of the blanket energy multiplication factor M and various efficiencies (of thermal conversion, direct conversion, and neutral-beam injection) allows calculation of power flows. At this point, the power quantities are only relative

because an absolute power level has not been selected.

Finally, specification of a single dimension or power quantity (we usually choose to specify the net electric power) allows complete design of the reactor. The dimensions of the cylindrical central-cell plasma and the approximately spherical plug plasmas are completely determined by the central cell-to-plug volume ratio, the fusion power density of the central cell, the desired total fusion power, and the requirement for magnetic flux conservation throughout the machine.

The plug magnets are designed to provide the specified magnetic field and to be large enough to contain the plug plasma. The scaling laws for the plug magnets were derived from the point designs described in Chapt. 5.

The design of the central cell begins at the cylindrical first wall (three alpha gyroradii away from the plasma) and proceeds outward through the blanket, shield, magnet, support structure, handling and maintenance equipment, and finally the reactor building. The scaling laws for the central cell were derived from the point design described in Chapt. 4. In all cases, the blanket and shield thicknesses are held constant at 94 and 86 cm, respectively. Thus, the primary variables in the central-cell design are the length, first-wall radius, and magnetic field strength. The plant design is completed by sizing the injectors, the direct converters, and the thermal conversion system.

Cost Estimate

Estimates of direct capital costs for all elements of the power plant permit a final estimate of the cost of power.

The cost of the central cell tends to be dominant and is therefore the most carefully evaluated. It is broken down into separate cost estimates (see Table 10-1) for the blanket, shield, vacuum vessel, solenoidal coil, coil restraining structure, coil case, main support structure, the crawler-transporter under each central-cell module, and the central-cell portion of the reactor building. The scaling laws for these costs were derived from the point design described in Chapt. 4.

The cost of the plug is broken down into separate cost estimates (see Table 10-2) for the plug coils, coil restraining structures, coil refrigerators, and the plug portion of the reactor building. The scaling laws for the coil-related costs are derived from the point designs in Chapt. 5.

Cost estimates for the thermal conversion , direct conversion, and

Table 10-1. Summary of cost estimates for central cell.

Item	Cost estimate
Blanket (estimated on a per unit mass basis):	
Stainless steel structure	$22/kg
Neutron moderator and tritium-breeding material[a]	$25/kg
Shield (estimated on a per unit mass basis):	
Stainless steel	$11/kg
Lead cement	$1/kg
Borated carbon	$5.50/kg
Vacuum vessel (estimated on a per unit mass basis):	
Stainless steel	$14/kg
Solenoidal coil (always at a low magnetic field strength (2.4 T in the point design) and conservatively sized for an overall current density of 1200 A/cm^2.)	
Conductor (density assumed to be that of copper)	$6.60/kg
Cost of winding the coil	$0.0023/A·m
Coil restraining structure and coil case (stainless steel)	$14/kg
Main support structure (steel)	$11/kg
Crawler-transporter under each central-cell module (cost assumed to scale linearly with the mass of the central-cell module)	Normalized to $600 thousand for a 3-m-long module weighing 7.2×10^5 kg.
Central-cell portion of the reactor building (cost assumed to scale linearly with the length of the central cell L_c and with the square of the outer radius of the central cell r_{outer})	Normalized to $24 million for L_c = 100 m and r_{outer} = 4.5 m

[a]The $25/kg estimate was made for lithium aluminate, one of the proposed breeding materials (see Chapt. 4). The final design choice was for an approximately equal *volume* of encapsulated liquid lithium. We believe that our blanket cost estimate is somewhat high for this case.

Table 10-2. Summary of cost estimates for plugs.

Item	Cost estimate
Plug coils (a cryogenic-Al Yin-Yang coil pair inside a superconducting solenoidal pair)	
Solenoidal pair (designed for an overall current density of 3000 A/cm^2)	\$0.0013/A•m
— plus winding	\$0.0023/A•m
Stainless-steel restraining structure for the solenoidal pair	\$22/kg
Yin-Yang coil pair (pure-Al conductor and Al-alloy internal structure)	\$22/kg
— plus winding	\$0.0023 A•m
Coil restraining structures (a stainless-steel external restraining clamp whose mass is estimated from the Yin-Yang study in Ref. 10-2)	\$22/kg
Coil refrigerators (cost of refrigeration scales with the 7/10 power of the refrigerator input power, which is estimated to be 50 W of heat per W removed from the coil. This input power — 23 MW in the point design — is also subtracted from the gross electric power of the plant when we calculate the net electric power)	\$40 million
Plug portion of the reactor building (assumed to scale with the square of the outer radius r_{outer} of the central cell)	Normalized to \$19 million of r_{outer} = 4.5 m

injection systems are summarized in Table 10-3.

The reactor systems just discussed do not include all of the systems considered in the cost estimate for our Standard Mirror Fusion Reactor as reported in Ref. 10-2. Systems not explicitly included are the cryopanel vacuum system for the injectors and direct converters, the refrigeration system for the cryopanels and the superconducting coils, the plant electrical equipment, instrumentation and controls, the tritium handling system, miscellaneous buildings, and site improvements. Our preliminary estimate for the cost of these systems for a 1000-MW(e) TMR is \$270 million.

As an economic figure of merit, we add all the above direct capital

Table 10-3. Summary of cost estimates for thermal conversion, conversion, and injection systems.

Item	Cost estimate
Thermal conversion system (includes blanket coolant loop, direct converter coolant loop, steam genetators, turbine generators, steam condensers, all steam and water piping, cooling towers, and the turbine hall).	$70/kW of thermal power handled by the thermal converter.
Direct conversion system (includes direct converter vacuum tank, collector elements, electrical conditioning equipment, and thermal panels for the radiative cooling of collector elements)	$130/kW of charged-particle power entering the direct converter.
Injection system (includes injector plus their power supplies)[a]	$200/kW of electrical power input to the injectors.

[a]The effect of a higher injection system cost will also be discussed.

costs* and divide by the net electric power to obtain the direct capital cost per unit of installed capacity [$/kW(e)]. We have used the minimization of this figure of merit to optimize the design of the TMR. (In our Standard Mirror Fusion Reactor study,[10-2] we pointed out a deficiency of the $/kW(e) figure of merit; namely, designs with higher neutron loadings on the first wall are not properly penalized for their more frequent outages for blanket maintenance. For that reason, we used the cost of net electrical energy (mills/kWh) as the economic figure of merit in Ref. 10-2. We shall adopt this method for future analytic models of the TMR. We suspect that our results will be about the same since the first-wall loading of the optimized TMR point design is only 2.1 MW/m^2 (vs 3.3 for our standard mirror reactor).

*We emphasize that the estimated costs are direct capital costs only and that no indirect costs have been added. In our Standard Mirror Fusion Reactor study,[10-2] we estimated that indirect costs (indirect field costs, engineering services, contingency, interest during construction, and general office costs) are 1.48 times the direct capital costs.

COST OPTIMIZATION

Input for the Point Design

We chose to specify a net electric power of 1000 MW(e) for the TMR point design. (Lower and higher power levels will be discussed later in this chapter.) Other input parameters held constant in our search for an optimized point design were as listed in Table 10-4.

Table 10-4. Parameters held constant in determining an optimized TMR design, for net electric power of 1000 MW(e) and deuterium plug injection.

Parameter	Value
Vacuum mirror ratio in plug	1.07
Beta of plug plasmas	1.0
Beta of central-cell plasma	0.7
Fraction of α-particles adiabatically confined	1.0
Vacuum central field of plug	16.5 T
Blanket energy multiplication	1.2
Thermal conversion efficiency	0.4
Direct conversion efficiency	0.6
Injection efficiency	0.8

Optimization of the Point Design

The remaining input parameters that must be specified in order to calculate a TMR design are the injection energy, the temperature of the central-cell ions, and the vacuum mirror ratio between the center of the plug and the central cell. We varied these three parameters in our search for an optimized point design. The results are shown in Figs. 10-1, where we plot \$/kW(e) versus the three parameters. The minimum cost of \$1260/kW(e) occurs for

Injection energy = 1.2 MeV
Central-cell ion temperature = 30 keV
Plug-to-central cell R_{vac} = 7.0

We choose this minimum cost design as the TMR point design.

In Figs. 10-2 and 10-3 we show the variations of two reactor figures of merit: the recirculating power fraction (defined as the gross electrical power minus the net electrical power, divided by the gross electrical power) and the neutron loading of the first wall. TMR optimization is always a tradeoff between a good power balance (low recirculating power fraction) and a high central-cell power density (high neutron loading of the first wall). Note that moving off-optimum results in a "good" change in one figure of merit and a "bad" change in the other.

The energy-dependent curves, (a) in Figs. 10-1,2, and 3 indicate a rather shallow cost minimum over the range of injection energy considered. This is somewhat misleading because the performance of the TMR becomes very sensitive to injection energy at lower energies. Figure 10-4(a) shows the cost of the 1000 MW(e) TMR over a wider range of injection energy.

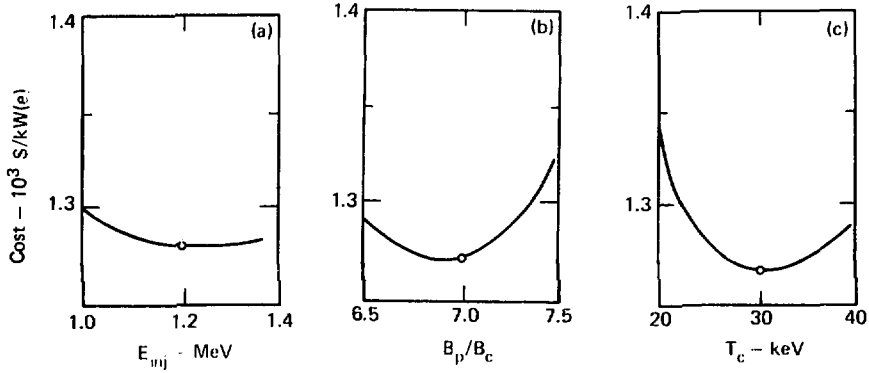

Fig. 10-1. Effect on cost of 1000-MW(e) TMR's of variation in (a) injection energy E_{inj}, (b) vacuum mirror ratio between the center of the plug and the central cell B_p/B_c, and (c) temperature of the ions in the central cell T_c. *(Note: In Figs. 10-1 through 10-10, the data points identify the values selected for the point design.)*

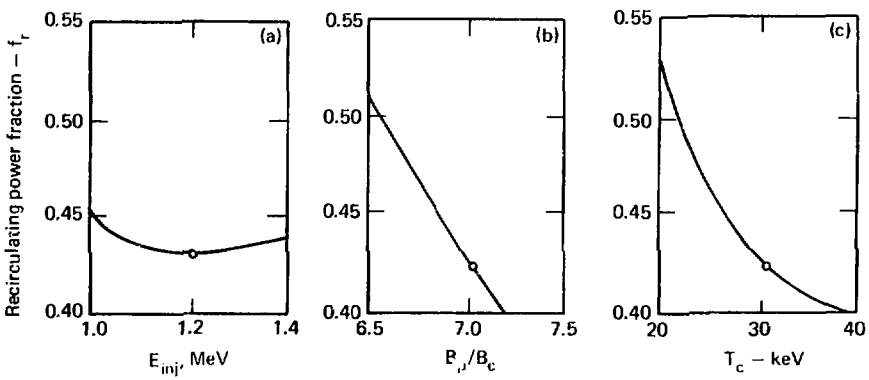

Fig. 10.-2. Effect on recirculating power fraction f_r of 1000-MW(e) TMR's of variation in the parameters defined in Fig. 10-1.

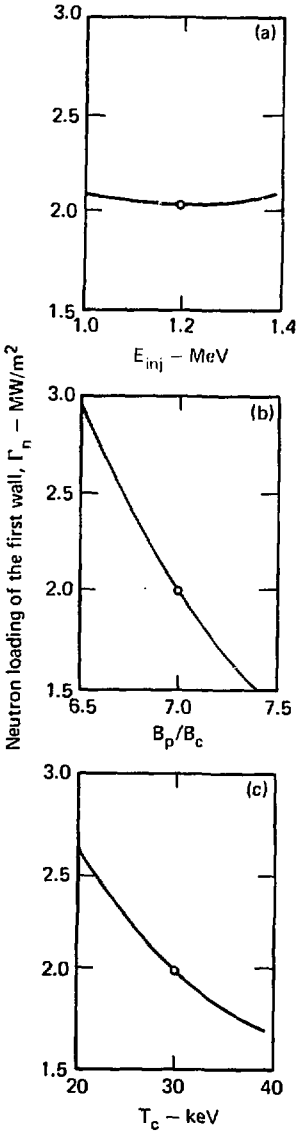

Fig. 10-3. Effect on the neutron loading of the first wall of 1000-ME(e) TMR's of variation in the parameters defined in Fig. 10-1.

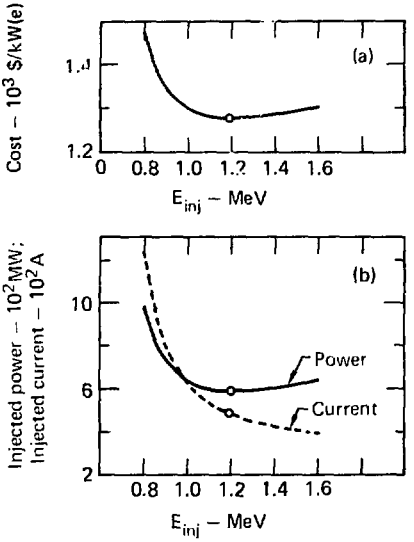

Fig. 10-4. Performance of 1000-MW(e) TMR: (a) variation in cost over a range of injection energies, and (b) variation of the total neutral-beam power and current injected into the plugs.

Shown in Fig. 10-4(b) is the variation of the total neutral-beam power and current injected into the TMR plugs. Note the sharp increase in cost with decrease in injection energy. At 800-keV injection energy, Q has dropped to 2.9 and the recirculating power fraction has increased to 0.56. At still lower injection energies, Q drops precipitously, primarily because the plugs can no longer support a large central-cell plasma at fusion temperatures. At 650-keV injection energy, Q is only 0.5 and the reactor no longer produces net power.

Table 10-5. Plasma parameters for the TMR point deisgn.

Parameter	Value
Injection energy	1.2 MeV
Average plug ion energy, E_p	878 keV
Electron temperature, T_e	42 keV
Central-cell ion temperature, T_c	30 keV
Electron potential, ϕ_c	263 keV
Central-cell ion potential, ϕ_c	88 keV
Plug β	1.0
Central-cell β	0.7
Plug particle $n\tau$	2.5×10^{14} s/cm^3
Central-cell particle $n\tau$	7.7×10^{14}
Central-cell to plugs plasma volume ratio	500
Plug-to-central cell ion density ratio	7.96
$\langle\sigma v\rangle_{DT}$	6.64×10^{-16} cm^3/s
Plug ion density, n_p	8.57×10^{14} cm^{-3}
Central-cell ion density, n_c	1.08×10^{14}
Plug plasma radius, r_p	0.48 m
Central-cell plasma radius, r_c	1.22 m
Fusion power density	5.41 W/cm^3
First-wall neutron loading, Γ_n	2.06 MW/m^2
Q	4.81

Table 10-6. Physical characteristics of the TMR point design.

Item	Value
Plug vacuum mirror ratio, $R_{vac,\ plug}$	1.07
Plug vacuum central field, $B_{0,\ plug}$	16.5 T
Plug center-to-central cell mirror ratio	7.0
Central-cell vacuum field	2.4 T
Central-cell dimensions:	
Length, L_c	101 m
First-wall radius, r_{fw}	1.56 m
Outside radius	4.52 m

Description of the Point Design

The plasma characteristics of the optimized point design are given in Table 10-5. The physical characteristics of the reactor are given in Table 10-6. The power-flow quantities are given in Table 10-7. Finally, Table 10-8 gives the breakdown for the direct capital costs of the point design.

OTHER DESIGN CONSIDERATIONS

We investigated the effect on reactor design of values other than those used in the point design.

Other Power Levels

Figure 10-5(a) shows the $/kW(e) cost of TMR's designed for net power outputs ranging from 250 to 2000 MW(e). The results plotted represent designs that have not been reoptimized; i.e.,

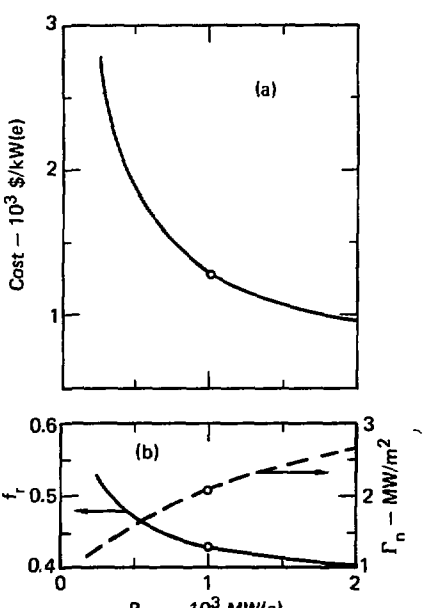

Fig. 10-5. Effect upon (a) cost and (b) recirculating power fraction f_r and neutron loading of the first wall Γ_n of variation in the net power output P_{net} of the TMR.

Table 10-7. *Power-flow quantities in the TMR point design.*

Item	Value (MW)
Electric input power to injectors	734
Injected neutral-beam power	587
Trapped neutral-beam power	526
Fusion power	2532
Thermal power into blanket	2026
Thermal power out of blanket	2431
Charged-particle power into direct converter	1033
Electric power out of direct converter	620
Thermal power into thermal converter	2844
Electric power out of thermal converter	1138
Gross electric power	1757
Auxiliary power	23
Net electric power	1000
Recirculating power fraction:	0.43
System efficiency:	0.34

they have the same injection energy, central-cell ion temperature, and plug-to-central cell mirror ratio as the point design. We found that re-optimization of the central-cell ion temperature, the plug-to-central cell mirror ratio, and the ignition energy for the 250 MW(e) and 2000 MW(e) cases had almost no effect on the costs shown in the figure. Figure 10-5(b) shows that the cost decreases with increasing power for two reasons: a decrease in the recirculating power faction and an increase in first-wall loading. The optimized 2000-MW(e) TMR has a 150-m-long central cell and costs $980/kW(e).

Table 10-8. Cost breakdown — TMR point design.

Item	Cost (millions of $)	% of total
Central cell		
Blanket	114	8.9
Shield	62	4.9
Vacuum vessel	11	0.9
Coil	35	2.7
Coil structure	21	1.6
Main structure	51	4.0
Crawler-transporter	22	1.7
Subtotal:	316	24.7
Plug coils	171	13.3
Reactor building	44	3.4
Injector system	147	11.5
Direct conversion system	134	10.5
Thermal conversion system	199	15.5
Other	270	21.1
Total:	1,281	100

Tritium Plug Injection

For the point design, we assume that deuterium is injected into the plug. However, we also investigated tritium injection because of the potential advantage it offers: at the same energy, beam penetration through the plasma is less and velocity space scattering is slower (i.e., the plug $n\tau$ is greater). A third physics effect, this one detrimental, is an increase in the equilibration time between the ions and electrons in the plugs. This effect tends to reduce the attainable volume ratio between the central cell and the plugs, and hence to reduce Q.

We recalculated the point design with tritium injection (without reoptimization) and found only a slight cost reduction [from \$1280/kW(e) to \$1240/kW(e)]. As expected, $n\tau_{plug}$ increased (to 3.4×10^{14} s), but the reduction in volume ratio (to 300) resulted in a net decrease in Q (to 3.9). However, the recirculating power fraction increased only a small amount (to 0.46) because the neutral-beam trapping fraction increased to 0.98. Finally, the neutron loading

of the first wall increased to 2.5 MW/m^2 because the smaller volume ratio resulted in a shorter, fatter reactor.

Reoptimization of the tritium injection case would result in the tradeoff of some of the increased wall loading for a lower recirculating power fraction. However, the potential for improvement is not great. For this reason and also because of the added complications of handling tritium in the high-energy injectors (for which we assessed no additional costs), we discarded the tritium option.

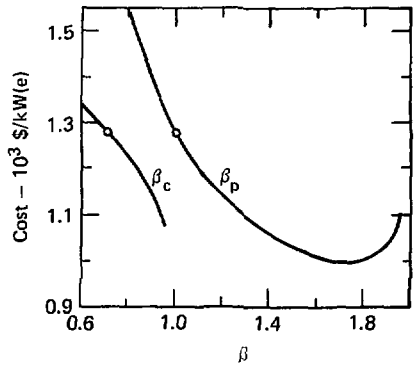

Fig. 10-6. Cost of optimized 1000-MW(e) TMR's as a function of central-cell beta β_c and plug beta β_p.

Variation of Central-Cell β

The point design value of the central-cell beta β_c was 0.7, and the central-cell plasma was assumed to obey the "long, thin" approximation; i.e.,

$$B_{plasma} = B_{vacuum} (1 - \beta_c)^{1/2} .$$

Recent physics analyses indicate that the central-cell plasma may be stable for β_c as high as 0.95. Figure 10-6 shows the cost of *optimized* (central-cell ion temperature and plug-to-central cell mirror ratio) 1000-MW(e) TMR's as a function of β_c. For $\beta_c = 0.95$, the cost of an optimized 1000-MW(e) TMR is reduced to $1080/kW(e). This reactor is considerably shorter and fatter than the point design: the central-cell length L_c is 55 m (versus 100 m) and the first-wall radius is 2.2 m (versus 1.6 m). The recirculating power fraction is reduced to 0.34, and the first-wall loading is increased slightly to 2.2 MW/m^2.

Variation of Plug β

The point design value of plug beta β_p was 1.0, and the plug plasma was assumed to obey a "short", fat" approximation for 2XIIB-like plasmas; i.e.,

$$B_{plasma} = B_{vacuum} \left(1 - \frac{\beta_p}{2}\right)$$

Note that complete exclusion of the magnetic field by the plasma (just prior to field reversal) would require

$\beta_p = 2$. Experiments on 2XIIB indicate that β_p in the range of 1 to 2 may be possible.

Figure 10-6 shows the cost of *optimized* (central-cell ion temperature and plug-to-central cell mirror ratio) 1000 MW(e) TMR's as a function of β_p. It can be seen that there is an optimum value of $\beta_p = 1.7$, for which the reactor cost is reduced to \$1000/kW(e). This reactor is much more compact than the point design: L_c is 57 m and the first-wall radius is only 0.7 m. The recirculating power fraction is reduced to 0.33, and the neutron loading of the first wall is a high (probably too high) 7.2 MW/m^2. The latter effect results because the optimum plug-to-central cell mirror ratio is only 3.5 (versus 7.0 for the point design), which results in a high ion density in the central cell (5.7×10^{14} cm^{-3}). This optimum design for high plug β would probably change if we adopted the mill/kWh minimization method, including the costs of blanket maintenance.

Variation of f_α

For the point design, we assume that f_α, the fraction of alpha particles adiabatically confined, was unity. Although this appears possible, it also appears that the confinement of these particles could be intentionally spoiled by a redesign of the transition region between the plug and the central cell. Alpha heating would then be reduced, but at the same time the reduced alpha pressure in the central cell would permit a higher fuel density in the central cell.

We investigated the design of a 1000-MW(e) TMR with $f_\alpha = 0.5$ and found that reoptimization (injection energy, central-cell ion temperature, and plug-to-central cell mirror ratio) yielded a cost of \$1350/kW(e), 5% higher than the point design. The loss of alpha heating caused this reactor to optimize at a plug injection energy of 1.5 MeV.

Variation of $B_{0,\ plug}$

The vacuum magnetic field strength at the center of the plug, $B_{0,\ plug}$, was chosen to be 16.5 T for the point design. Figure 10-7(a) shows the predicted reactor cost (without reoptimization) as $B_{0,\ plug}$ is varied from 15 to 18 T. Figure 10-7(b) shows that as $B_{0,\ plug}$ is increased, both reactor figures of merit — the recirculating power fraction and neutron loading of the first wall — improve, and thus the cost decreases. The decreasing *rate* of cost reduction with increasing $B_{0,\ plug}$ is due to the rapidly increasing cost of the plug magnets. Increasing the plug field from its point design value to 18 T reduces the reactor cost by only

1.8%. Also, we note that there is only a 3.4% increase in reactor cost if we reduce the plug field from its point design value to 15 T.

Variation of the Vacuum Mirror Ratio of the Plug

The vacuum mirror ratio of the plug coil, $R_{vac,plug}$, was chosen to be 1.07 for the point design. A plug mirror ratio this low, coupled with a maximum allowable magnetic field strength, permits either a high confining field in the central cell (high fusion power density) or a high ratio of field (and thus density) between the plugs and the central cell (good central-cell confinement). The low plug mirror ratio was chosen in the expectation that these gains were more important than better plug confinement.

Figure 10-8 shows the predicted cost of *optimized* (central-cell ion temperature and plug-to-central cell mirror ratio) 1000-MW(e) TMR's as a function of $R_{vac,plug}$ for a constant value of the plug mirror field (17.7 T). This means that as $R_{vac,plug}$ is increased from its point design value of 1.07, the vacuum magnetic field strength at the center of the plug decreases from its point design value of 16.5 T. Figure 10-8

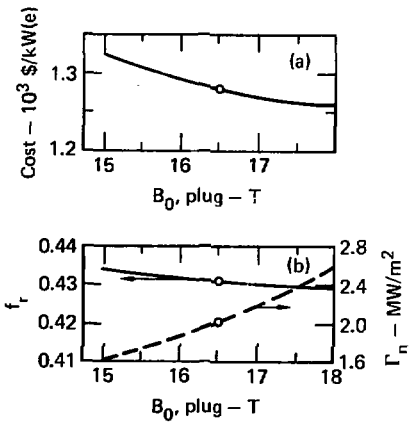

Fig. 10-7. Effect on (a) predicted reactor cost and (b) recirculating power fraction f_r and neutron loading of the first wall Γ_n of variation in $B_{0,\ plug}$, the vacuum magnetic field strength at the center of the plug, for 1000-MW(e) TMR's with vacuum mirror ratio of the plug $R_{vac,plug} = 1.07$.

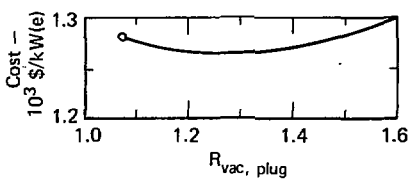

Fig. 10-8. Predicted cost of optimized 1000-MW(e) TMR's as a function of the vacuum mirror ratio of the plug $R_{vac,plug}$ for plug mirror field $B_{mirror} = 17.7$ T.

shows that an optimum mirror ratio exists at about $R_{vac,plug} = 1.25$, somewhat higher than the point design value. However, the optimum is quite shallow, and the minimum cost is only 1.5% less than that for the point design.

Variation of Blanket Energy Multiplication

The blanket energy multiplication factor, M, is 1.2 for the point design. Figure 10-9 shows the predicted cost for 1000-MW(e) TMR's (without reoptimization) as a function of M. The cost is insensitive to small changes in M.

The Effect of a Beryllium Blanket

On the basis of our conceptual design of a Standard Mirror Fusion Reactor,[10-2] we predict that an M of 1.7 to 1.9 could be achieved in TMR with a beryllium-bearing blanket, which would cost about 2.4 times as much as the non-beryllium blanket.

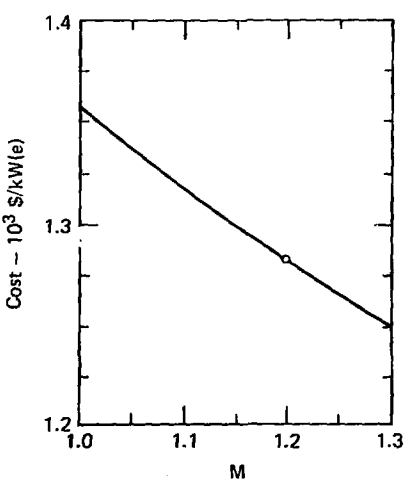

Fig. 10-9. Predicted cost for 1000-MW(e) TMR's (without optimization) as a function of the blanket energy multiplication factor M.

We investigated the use of a beryllium blanket in the 1000-MW(e) TMR, and found that with reoptimization (central-cell ion temperature and plug-to-central cell mirror ratio), a beryllium-bearing TMR would be 3% less expensive at M = 1.7 and 6% less expensive at M = 1.9. Either of these reactors would be considerably shorter than the point design (L_c = 62 m for M = 1.7; L_c = 59 m for M = 1.9).

Variation of Conversion Efficiencies

The point design values for conversion efficiencies are 0.4 for the thermal converter (including the bottoming cycle of the direct converter, 0.6 for the direct converter, and 0.8 for the injector system. (Recent work on the injector system, discussed in Chapt. 7, indicates that 0.7 may be a more accurate prediction of the injector system efficiency.)

Figure 10-10 shows the percentage change in the predicted cost of 1000-MW(e) TMR's without reoptimization) as a function of the three efficiencies. For a given percentage point change in efficiency, the change in reactor cost is the greatest for changes in the thermal efficiency and the least for changes in the direct converter efficiency.

We also investigated the effect of a simultaneous 5 percentage point change in all three efficiencies from their point design values. For a 5

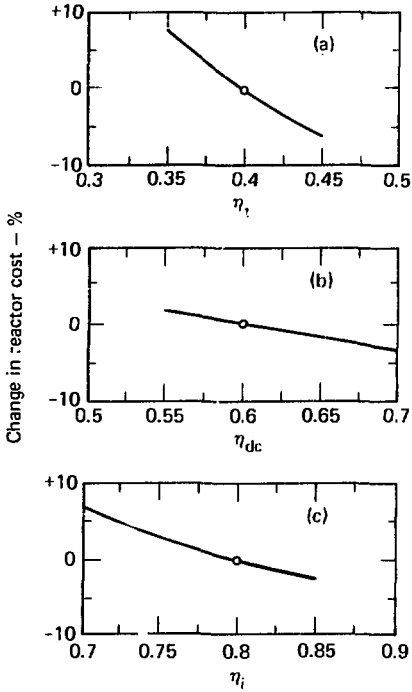

Fig. 10-10. Percentage change in the predicted cost of 1000-MW(e) TMR's (without reoptimization) as a function of the efficiencies (a) of the thermal converter η_t, (b) of the direct converter η_{dc}, and (c) of the injector system η_i.

percentage point decrease in the efficiencies, the predicted cost of the 1000-MW(e) TMR (without reoptimization) increased by 14%; for a 5 point increase, the reactor cost decreased by 9%.

Variation of Injector Cost

For the point design (and all the parametric variations discussed above) the injector system for the plug estimated to cost $200/kW of electrical power input to the injectors. (Since the point design value for injector efficiency was estimated to be 0.8, this cost is equivalent to $250/kW of neutral-beam power.) Because recent work suggests that this value may be low, we investigated the effect of a doubled cost for the injector system: $400/kW of electrical power input, or $500/kW of neutral-beam power. The result for a *reoptimized* (central-cell ion temperature and plug-to-central cell mirror ratio) 1000-MW(e) TMR is an 11% increase in the pre ted reactor cost. Thus, it is quite important to resolve the question of injector cost. In Chapt. 7, the cost estimate of $320/kW is intermediate between the $250 and $500 values; our best current estimate therefore represents a 5% increase in reactor cost.

Electron Heating

Direct heating of electrons in the TMR is an attractive idea because it would reduce the required neutral-beam injection energy in the end plugs. In our investigation of the effect of electron heating, we assume that the electrical efficiency of such heating as well as its cost per unit power is the same as for the neutral-beam injectors. Figure 10-11 shows the optimum neutral-beam energy and

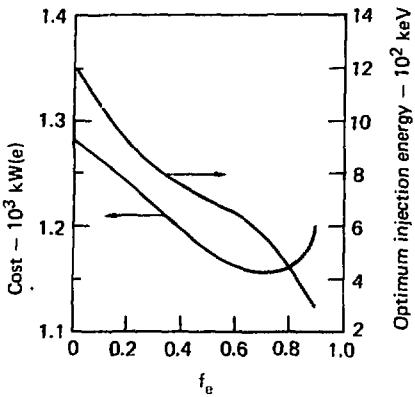

Fig. 10-11. Optimum neutral-beam injection energy and predicted cost of optimized 1000-MW(e) TMR's as functions of f_e, the fraction of the total heating that goes to the electrons.

the predicted cost of optimized 1000-MW(e) reactors as functions of f_e, the fraction of the total heating that goes directly to the electrons.

For our point design with neutral-beam injection only, $f_e \approx 0$. There is an optimum value of f_e near 0.75 for which the cost of the reactor is reduced to \$1160/kW(e). The neutral-beam injection energy for this optimized reactor is 500 keV.

REFERENCES

10-1. F. M. Coensgen, *TMR Major Project Proposal* (Appendix B: "Tandem Mirror Reactor Scaling" by B. G. Logan), Lawrence Livermore Laboratory, Rept. LLL-Prop 148 (1977).

10-2. R. W. Moir, Scientific Editor, *Standard Mirror Fusion Reactor Design Study*, Lawrence Livermore Laboratory, Rept. UCID-17644 (in preparation).

CHAPTER 11. STARTUP SCENARIO

R. G. Logan and R. W. Moir

SUMMARY

In this chapter, we present some preliminary thinking about how to start up the Tandem Mirror Reactor (TMR). Considerations include startup time, total invested 1.2-MeV neutral-beam power, and the sequence followed to achieve a steady-state power output of 1000 MW(e).

THE SCENARIO

In our preliminary thinking about the startup scenario for the TMR, we consider a startup procedure in which beams from the 1.2-MeV neutral-beam modules* impinge on a low-energy, initial plasma target of density $n_p|_{t=0} \equiv n_{p0} = 0.01\, n_{pf}$, where n_{pf} is the final (asymptotic) plug density. We neglect the initial power and energy required to provide the target plasma. The initial target density in 2XIIB is about 1% of the maximum value (plasma stream density $n_s \approx 10^{12}$; final 2X density $\hat{n} \approx 10^{14}$). We wish to calculate the startup time t_s and the total neutral-beam energy W_b invested during startup of the TMR:

$$W_b \equiv \int_0^{t_s} P_b(t)\, dt. \qquad (11\text{-}1)$$

The startup time t_s can be defined as the time required for the density in the plug (and the corresponding density in the solenoid

$$\frac{n_c(t)}{n_{cf}} = \frac{n_p(t)}{n_{pf}}$$

to reach 63% of its maximum value, at which time the gross electric power of the reactor (0.4 of that at full power) should be just sufficient to take over and power the neutral beams for a zero net power ($Q \approx 1$). Different beam power time functions $P_b(t)$ may be considered to minimize startup energy.

The rate equation for $n_p(t)$ is given by

$$\frac{dn_p}{dt} = \frac{I_{b0}}{qV_p}\left\{1 - \exp\left[-n_p(2r_p)\sigma_{eff}\right]\right\} - \frac{n_p^2}{(n\tau)_p}, \qquad (11\text{-}2)$$

where $V_p = 4/3\ \pi r_p^3$ is the volume of the plug [perhaps $r_p = r_p(t)$, but it might be taken constant with certain profiles of target plasma and beam injection].

We assume that the incident beam current I_{b0} may be approximated by a pencil beam aimed through the plasma diameter and that it is attenuated by an effective cross section $\sigma_{eff} \approx \frac{\Sigma\langle\sigma_i v\rangle}{V_0}$, which is nearly all ionization on deuterons at E_{inj} = 1.2 MeV ($\sigma_{eff} \approx 1 \times 10^{-16}\,cm^2$ at

*When any module is "on", it is on at full voltage, current density, and power.

1.2 MeV). Furthermore, we assume that the plasma confinement product $(n\tau)_p$ is independent of density, as is appropriate for classical loss rates due to ion-ion scattering and electron drag. Since the TMR plasma energy balances for T_e and T_i are also independent of n_p or n_c as long as we keep n_p/n_c constant, we can take T_e, T_i and $(n\tau)_p \quad 6 \times 10^9 E_{inj}^{3/2} \approx 2.5 \times 10^{14} cm^{-3} \cdot s$ constant to zero order.

When n_p is small, the plasma is thin to the beam, and the loss term $n_p^2/(n\tau)_p$ can be neglected. Equation (11-2) then gives

$$\frac{dn_p}{dt} \approx \frac{I_{b0}}{qV_p} (n_p) (2r_p) (\sigma_{eff}); \quad (11-3)$$

that is, n_p increases exponentially in time as

$$n_p(t) \approx n_{p0} \exp(t/\tau_0), \quad (11-4)$$

with a time constant τ_0 given by

$$\tau_0 = \frac{qV_p}{I_{b0} (2r_p) \sigma_{eff}} . \quad (11-5)$$

At high density, the plasma becomes thick to the beam, so that $\exp[-n_p(2V_p)\sigma_{eff}] \approx 0$, and the loss term $n_p^2/(n\tau)_p$ begins to dominate. Equation (11-2) predicts that the density will saturate to a maximum value n_{pf} at equilibrium ($dn_p/dt = 0$) given by

$$\frac{I_{b0}}{qV_p} = \frac{n_{pf}^2}{(n\tau)_p} ; \quad (11-6)$$

that is,

$$n_{pf} = \left[\frac{I_{b0} (n\tau)_p}{qV_p} \right]^{1/2} . \quad (11-7)$$

Starting with 0.01 n_{pf} density in the thin-plasma limit and assuming constant I_b, r_p, and τ_0, we can estimate the startup time for the density to exponentiate to 0.63 n_{pf}

$$t_s = \tau_0 \ln 63 \approx 4t \tau_0. \quad (11-8)$$

Let us consider the case where all the beam current and power required to maintain the steady state at $n_{pf} = 8.6 \times 10^{14} cm^{-3}$, $r_p = 48$ cm at $E_{inj} = 1.2$ MeV, and $n\tau_p = 2.5 \times 10^{14} cm^{-3} \cdot s$ are switched onto the target at t 0 and maintained constant during the buildup. For these parameters, Eq. (11-6) gives $I_{b0} = 219$ A for all beam trapped and $I_{b0} = 244$ A for 10% beam transmission in the steady state. Then Eq. (11-5) gives an exponentiation time constant $\tau_0 \approx 32$ ms and a startup time $t_s \approx 0.13$ s. This is a very short time. The beam energy consumed during this time is

$$W_0 \approx (2)(244 \text{ A})(1.2 \times 10^6)$$
$$(0.13) = 76 \text{ MJ}.$$

This energy is within the range of energy that can be stored in devices such as batteries or homopolar generators. In fact, however, $t_s = 0.13$ s

is too short for reactor startup because the characteristic time constant for hot alpha particles and electrons to heat solenoid ions is $n\tau_{drag}/n_e \approx (2.7 \times 10^{14}\,cm^3/s)/10^{14}\,cm^{-3} \approx 2.74$ s. Thus, fusion power will not be generated until several seconds after the plug plasmas have been built up.

The thermal time constant for the blanket is much larger:

$$t_{blanket} \approx \frac{(10^6\,cm^3)(500°C)\left(4\ \frac{J}{cm^3 \cdot °C}\right)}{2 \times 10^6\ W/m^2} = 10^3\ s.$$

Most of the neutral-beam power can be supplied by the direct converter once the plasma starts to burn (i.e., after a few seconds), so that the power that must be taken off the local grid can be a small fraction (≳25%) of the net final power put into the grid.

THE STARTUP SEQUENCE

If we assume that we shall achieve a steady-state power of 1000 MW(e) with the TMR, the startup sequence would be as follows:

1. The magnet is cooled down and the field is generated.
2. The blanket and the thermal conversion part of the direct converter are warmed up by circulating helium, which is heated externally. Assume this requires 25 MW.
3. The cryogenic magnet is energized; this requires about 25 MW of refrigeration power. A rough estimate for the energizing time is 10 s.
4. A target plasma is created from energy stored in a capacitor bank.
5. The neutral-beam modules are turned on in the plugs; this consumes 734 MW(e).
6. The plug plasma builds up to full density, and the plasma becomes steady state with 90% beam attenuation after 0.1 s.
7. The direct converter then begins to recover the injected, trapped beam power. This is 320 MW from the direct converter plus 85 MW from the thermal bottoming cycle.
8. After 3 s, the center-cell plasma reaches its steady-state density and temperature. (Because we assume a D-D mixture in the center cell, the fusion power will be low.)
9. The mixture is changed in about 10 minutes to a 50-50 D-T mixture so as to keep the power transient in the thermal conversion system less than 5% per minute, which is standard power plant operation.

Figure 11-1 shows the power that must be supplied versus time during startup of the TMR. Note that 800 MW is supplied for 0.1 s and 400 MW for a few minutes.

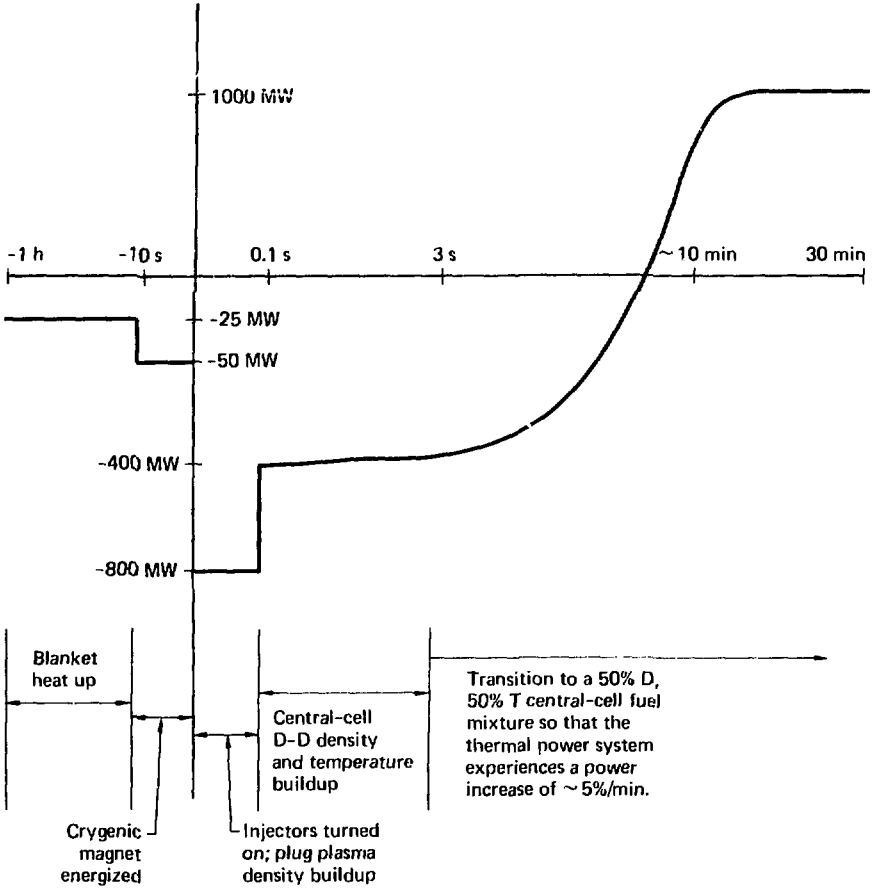

Fig. 11-1. Net electrical power from TMR during the startup sequence.

It should be emphasized that startup is an event that can be scheduled for times when excess capacity from the grid is available. Also after startup the reactor will run continuously until a scheduled maintenance or unplanned outage occurs; that could be months. It may be possible to start up with less than full power in the beams and thus reduce the 800-MW and 400-MW power requirements.

In the next study on the TMR, the question of startup will be examined more carefully in a systems context.

We shall treat questions such as the best ways to store energy during plasma buildup, the fraction of full load that can be sustained, the factors affecting transient power loading (i.e., how fast can we go from the power-consuming phase to the power-output phase), and load-following characteristics.

CHAPTER 12. ASSESSMENT OF NEEDED TECHNOLOGY

R. W. Moir

SUMMARY

Much of the technology needed for the Tandem Mirror Reactor (TMR) is either state-of-the-art or is already being developed for other fusion reactor designs. We have proposed special development programs for areas of technology not falling into either of these categories.

TECHNOLOGY REPRESENTING STATE-OF-THE-ART OR BEING DEVELOPED

Blanket

The blanket in the TMR has a simple cylindrical geometry and modest (2 $MW \cdot m^{-2}$) wall loading. Therefore, the material requirements and first-wall design are similar to if not easier to fulfill than those in other fusion reactor designs.

Central-Cell Magnet

The central-cell magnet is a Nb-Ti, 2.5-T, dc superconducting coil that could use state-of-the-art technology.

Superconducting Magnet for the End Plug

The superconducting magnet in each end plug is constructed from Nb_3Sn and has a 17.3-T field at the winding. Because this magnet is a simple solenoidal pair and has a simply curved, winding pattern with a 4- to 5-m radius of curvature, there are no special problems due to geometry. The conductor is now being developed and will probably be available within 5 years.

TECHNOLOGY NEEDING SPECIAL DEVELOPMENT PROGRAMS

Cryogenic Magnet for the End Plug

The cryogenic Yin-Yang magnet used in each end plug is made of aluminum, produces an incremental 1-T field superimposed on the 17.3-T field of the solenoidal pair, and is about 3 m in diameter. This coil represents a modest extension of state-of-the-art technology and could probably be built in 10 years. See Ref. 12-1 for the magnet development program plan.

End-Plug Injector

A high-energy (1200-keV) high-efficiency (80%) neutral-beam injector is used for the end plugs. The negative-ion technology that is the basis for this injection system does not now exist, and only a small development program is underway. However, the basic processes are well known and each individual step has been demonstrated. Rapid progress is likely once a sizable effort is mounted. A program plan for the development of a neutral-beam injector whose design is based on the production of negative-ion beams is discussed elsewhere.[12-2]

Direct Energy Conversion

The direct converter on each end of the TMR is beyond the state of the art. Small-scale experiments at 100 keV are underway that are relevant to the 300- to 400-keV conditions in TMR. Also, we plan to mount a small plasma direct converter on each end of the Tandem Mirror Experiment (TMX). The development plans for direct energy conversion are discussed in a draft program plan for direct conversion.[12-3]

Plasma Production and Control

A great deal of experimental information is needed on techniques for plasma production, impurity control, pumping, etc. It is partially in response to this need that we have initiated the TMX.[12-4]

REFERENCES

12-1. *Program for Development of High-Field Superconducting Magnets for Fusion Research*, Lawrence Livermore Laboratory, Rept. Misc-2007 (1975).

12-2. E. B. Hooper and R. V. Pyle, *Negative Ion Program Plan*, Lawrence Livermore Laboratory, Rept. (in preparation).

12-3. R. W. Moir, G. W. Hamilton, and W. L. Barr, *Preliminary Program Plan for Direct Energy Conversion*, Lawrence Livermore Laboratory, Rept. UCRL-52141 (in preparation).

12-4. G. H. Coensgen, Project Leader, *TMX Major Project Proposal*, Lawrence Livermore Laboratory Rept. LLL-Prop-148 (1977).

CKM GPO 789-086/4962